The Dissertation Committee for Donald Timothy Slottke certifies that this is the approved version of the following dissertation:

SURFACE ROUGHNESS OF NATURAL ROCK FRACTURES: IMPLICATIONS FOR PREDICTION OF FLUID FLOW

Committee:

John M. Sharp, Jr., Supervisor

Richard A. Ketcham

M. Bayani Cardenas

Stephen E. Laubach

Robert E. Mace

SURFACE ROUGHNESS OF NATURAL ROCK FRACTURES: IMPLICATIONS FOR PREDICTION OF FLUID FLOW

by

Donald Timothy Slottke, B.S.; B.S.

Dissertation

Presented to the Faculty of the Graduate School
of The University of Texas at Austin
in Partial Fulfillment
of the Requirements
for the Degree of

Doctor of Philosophy

The University of Texas at Austin
May, 2010

ACKNOWLEDGEMENTS

I would like to gratefully acknowledge the U.S National Science Foundation (Grant EAR-0439806) and the Geology Foundation of The University of Texas at Austin for support of this research

SURFACE ROUGHNESS OF NATURAL ROCK FRACTURES: IMPLICATIONS FOR PREDICTION OF FLUID FLOW

Donald Timothy Slottke, Ph.D.

The University of Texas at Austin, 2010

Supervisor: John M. Sharp, Jr.

Where open, connected fractures are present, they dominate both fluid flow and transport of solutes, but the prediction of hydraulic and transport properties *a priori* has proven exceedingly difficult. A major challenge in predicting solute transport in fractured media is describing the physical characteristics of a representative surface that is appropriate to modeling. Fracture aperture, roughness, and channeling characteristics are important to predict flow and transport in hard rock terrains. In areas with little soil cover, fracture mapping can indicate areas or directions of greater permeability but not the magnitudes. Both cover and complex geology can limit mapping. Hand samples are generally available and upscaling from their properties would be highly beneficial. Assessing the impact of roughness on field-scale fluid flow through fractured media from samples of natural fractures on the order of 100cm^2 assumes a relationship between fracture morphology and discharge is either scale invariant or smoothly transformable. It has been suggested that the length scale that surface roughness significantly contributes to the discharge falls within the size of a typical hand sample, but few data exist to support extension of small-scale relationships to larger scales. I analyze the results of flow tests on a single fracture through a 60 x 30cm block of rhyolitic tuff. The results are compared with relationships of smaller samples in a similar tuffs and granites. The data are processed to yield regularly gridded surface elevations. Describing roughness as a ratio of surface area to footprint, variances of the roughnesses of surface covering equivalently sized square samples are plotted against sample size to determine if a representative surface exists. For specimens of fractures measuring up to 25 x 29cm, a 3.2 x 3.2cm sample of granite with an iron oxide/clay fracture skin yields a reasonable expression of the roughness of the entire surface. The number of data points included in a sample of this size transcends skin type, composition and grain/crystal size. The results suggest that the unmodified cubic law is valid for the range of gradients expected in the field using the geometric mean of areal aperture data to estimate hydraulic aperture. The data also indicate that fracture aperture is not well predicted by single aperture measurements or even by averaging along a particular scan line; three-dimensional laboratory analysis and/or field testing are required. There may be a suitable scale of data for upscaling fracture roughness on the order of $10cm^2$. However, due to mismatch between top and bottom surfaces inherent in natural fractures, aperture samples are not consistent across the specimen and cannot be scaled. Upscaling of other factors, such as flow channeling, remain to be tested.

TABLE OF CONTENTS

LIST OF TABLES

LIST OF FIGURES

SYMBOLS

∇, gradient operator.

$\Delta x, \Delta y, \Delta z$, spacing in the x, y, or z direction.

α, β, ξ, arbitrary linear correction [L].

δx, incremental adjustment to x [units of x].

ε, absolute roughness [L].

ϕ, γ, θ, arbitrary angular correction [radians].

μ, dynamic viscosity [cp], or arithmetic mean.

ρ, density, [g/cm^3].

ρ_w, density of water $\approx$ 1g/cm^3.

σ, stress [F/L^2]

σ^2, variance.

τ, shear stress.

A, area, [L^2]

b, aperture or separation between surfaces, [L].

b_a, arithmetic mean aperture, [L].

b_e, hydraulic (effective) aperture, [L].

b_g, geometric mean aperture, [L].

b_h, harmonic mean aperture, [L].

b_m, mechanical aperture, [L].

$\mathbf{F}$, body force (gravity), [L/t^2].

g, gravity equal to 980cm/s^2.

h, head [L].

i, hydraulic gradient [L/L].

K, hydraulic conductivity [L/t].

K_I, stress intensity factor $\left[Pa \cdot \sqrt{m} \right]$.

l, length of specimen in the direction of flow, [L].

p, reduced pressure equal to fluid pressure plus elevation pressure head, [M/L·t^2].

$\hat{p}$, fluid pressure, [M/L·t^2].

Q, discharge [L^3/t].

q, specific discharge [L/t].

q_w, discharge per unit width [L^2/t]

Re, Reynolds Number [-].

S, surface area [L^2].

S_0, 2D footprint of rough surface [L^2].

t, time.

T, temperature or transmissivity.

$\mathbf{u}$, velocity vector.

v, velocity [L/t].

w, width perpendicular to boundary head gradient [L].

x,y,z, Cartesian coordinates with x horizontal and perpendicular to boundary head gradient, y increasing from up gradient to down gradient, and z vertical elevation [L].

x,y,z non-specific variable.

1 FLUID FLOW IN NATURAL FRACTURES

1.1 Introduction

Fluid flow through fractured media is an important line of research in hydrogeology. From managing groundwater resources in hard rock aquifers to analysis of flow paths of contamination plumes to estimates of storativity in doubly porous media, the participation of fractures in fluid flow mechanics must be carefully considered in interpreting field hydrologic data. Yet while the physics of fluid flow is well understood, equations used to predict fluid flow through fractured media commonly fail to characterize the system accurately.

What is the data requirement to estimate fluid flow through a discrete fracture? With natural fractures, roughness and contact points contribute to flow in the form of tortuosity, constriction, and opening of flow paths and eddy effects. Thomas (1998) detailed exponential growth in the publication of research into surface roughness. However, examination and quantification of real surfaces in relation to their ideals fall largely into the realm of engineering (e.g., applications in lubrication and heat production, structural stability, and manufacturing standards). For geologists, fluid flow problems through fractured media tend to be solved backwards; empirical data define a modifier to the applicable flow law that assumes homogeneous conditions.

When modeling fluxes of fluids, solutes, or colloids in natural subsurface environments, the integral role of fractures is the rule rather than the exception. The ease with which a particular fluid moves through a porous medium defines permeability (k), and is commonly expressed as hydraulic conductivity (*K*), which relates fluid properties and medium permeability. Fluid flow is mathematically described by Navier-Stokes equations:

$$\begin{aligned}&\frac{\partial \mathbf{u}}{\partial t}+(\mathbf{u}\cdot\nabla\mathbf{u})=\mathbf{F}-\frac{1}{\rho}\nabla\hat{p}+\frac{\mu}{\rho}\nabla^2\mathbf{u}\\&\nabla\cdot\mathbf{u}=0,\end{aligned} \tag{1.1}$$

where the change in velocity $\mathbf{u}$ with respect to time plus an advection term $(\mathbf{u}\cdot\nabla\mathbf{u})$ is related to a body force **F**, the pressure gradient $\nabla\hat{p}$, and inertial forces $\frac{\mu}{\rho}\nabla^2\mathbf{u}$, where μ is fluid viscosity and ρ is fluid density. Conservation of mass is maintained. The body force can be eliminated by defining a reduced pressure p:

$$p=\hat{p}+\rho g z, \tag{1.2}$$

where g is the gravitational force and z is elevation.

At steady state, Equations 1.1 and 1.2 reduce to:

$$\mu\nabla^2\mathbf{u}-\rho(\mathbf{u}\cdot\nabla)\mathbf{u}=\nabla p\,. \tag{1.3}$$

For smooth parallel plates, the advective term identically vanishes. With constant head boundaries up and down gradient and no flow boundaries laterally, $\mathbf{u} \neq 0$ only in the y direction (Figure 1.1) and varies only with z. Then, integrating $\mathbf{u}$ twice with respect to z and making use of the boundary conditions yields an equation for discharge through a fracture of width w:

$$Q=w\int_{-b/2}^{b/2}\mathbf{u}_y z\,dz=w\int_{-b/2}^{b/2}\frac{\left|\overline{\nabla p}\right|}{2\mu}[z^2-(b/2)^2]\,dz=\frac{-\left|\overline{\nabla p}\right|wb^3}{12\mu}\,. \tag{1.4}$$

This is the common form of the cubic law. From Darcy's Law:

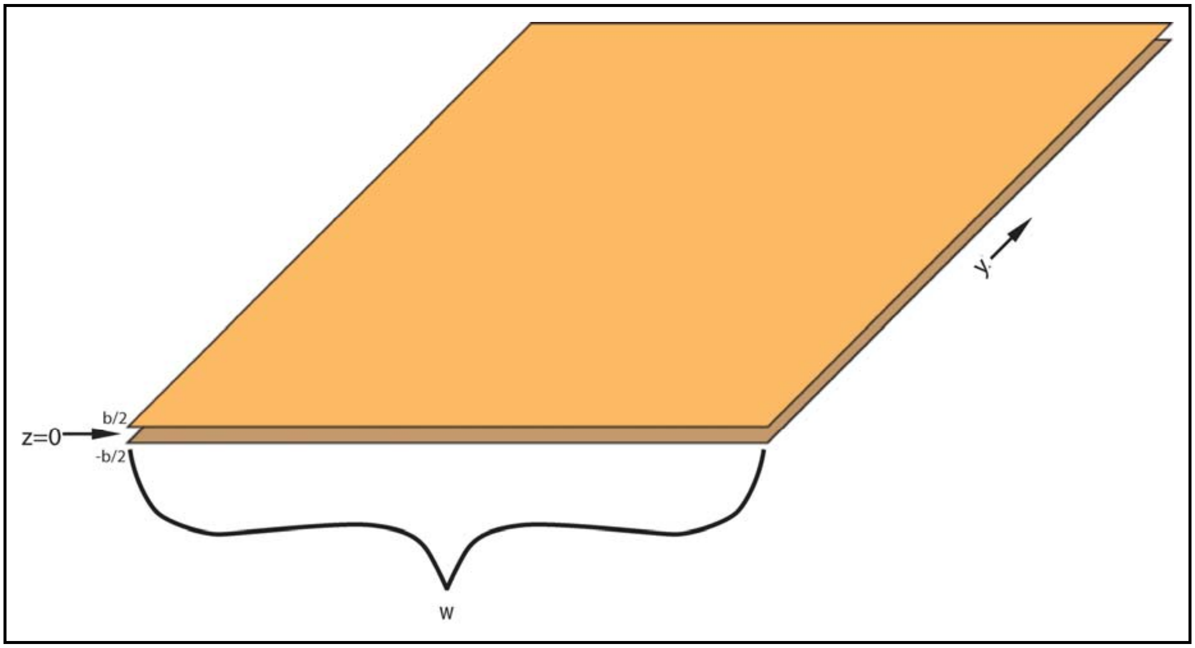

Figure 1.1 Representation of ideal parallel plate fracture. Head decreases into the page. v=0 at z=b/2 and z=-b/2.

$$Q = -KAi, \tag{1.5}$$

where A is the cross-sectional area perpendicular to flow and i is the hydraulic gradient. It is apparent that:

$$K = \frac{\rho_w g}{12\mu} b^2 . \tag{1.6}$$

For smooth, parallel, no slip "fractures," this is the exact solution to fluid flow. However, this is also a preferred equation when fracture surfaces are not smooth. Just how much surface roughness causes deviation from ideal discharge has been the subject of much research over the past 60 years. A number of corrections to the cubic law account for surface roughness in the form of tortuosity, constriction and opening of flow paths, and nonlinear effects in the laminar flow regime. The seminal efforts of Louis (1969) and Lomize (1951) independently modified hydraulic conductivity as:

$$K_{rough} = K_{cubic} \cdot \frac{1}{\left[1 + C\left(\frac{\varepsilon}{b_m}\right)^{1.5}\right]} , \tag{1.7}$$

where ε/b_m is a measure of relative roughness, ε is the mean asperity height (Figure 1.2) sampled at 1mm increments along specimen profiles, and b_m is the mechanical aperture. Lomize used engineered metal plates, and with a maximum relative roughness of 0.85, reports C=6. Louis' poured concrete of differing sized sands corresponds to a maximum relative roughness of 0.72 and yields C=3.1.

For natural fractures, the assignation of a roughness coefficient bears some scrutiny. Many studies have shown that the cubic law holds where velocity is low and

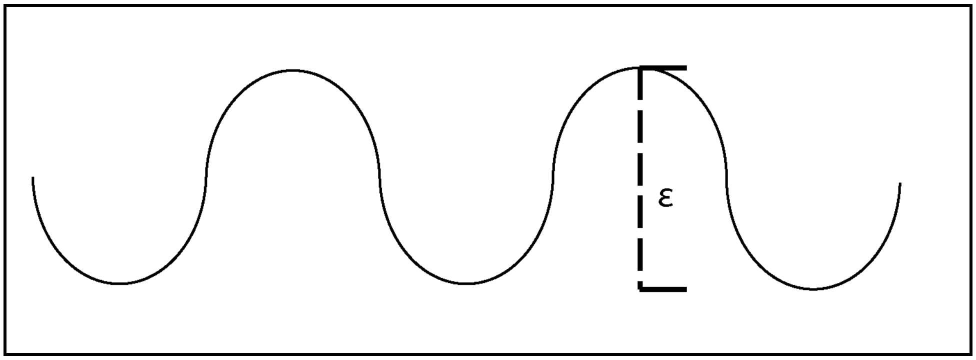

Figure 1.2 For an idealized fracture surface, the absolute roughness equals the mean asperity height— the difference between the elevation of the peaks and troughs.

the arithmetic mean aperture $b_a >> \varepsilon$ or where $b_a < \varepsilon$ such that the roughness defines the fracture channel rather than modifies it (e.g., Brown 1987, Zimmerman and Bodvarsson 1996, Ge 1997, Méheust and Schmittbuhl 2000). However, when aperture is on the order of roughness significant deviation from discharge predicted by the cubic law results. Witherspoon et al. (1980) find the friction factor of Lomize works well for fractured samples of basalt, granite, and marble. However, this comparison falls short on two fronts: 1) the roughness of the natural surfaces is not evaluated and 2) while the range of friction factors for the natural surfaces satisfies the Lomize equation for a valid roughness, it requires a relative roughness of less than 0.23, or an aperture greater than 4 times the mean asperity height. Thompson (2005) shows that the for a granite with $\varepsilon / b_m \approx 4$ the constant C in the Louis and Lomize equation falls 2 orders of magnitude, making this an unlikely tool for natural fractures.

Another complication to the use of the cubic law for prediction of flow in fractured media is the assumption of laminar flow. The Reynolds Number (Re) relates inertial forces to viscous forces defined here as:

$$Re = {}^{\rho v \cdot 2b}\!\big/_{\mu} . \qquad (1.8)$$

Theoretically, at $Re \approx 2000$ the physics of fluid flow through smooth channels indicates the onset of turbulence (Lamb 1932). However, the validity of the cubic law has been set numerically at $Re < 1$ (e.g. Zimmerman and Bodvarsson 1996, Nicholl et al. 1999). Physically, from interpretation of flow tests for the data of Louis and Lomize, transitional flow begins at $Re \leq 500$. The physical flow tests conducted in this study indicate no appreciable nonlaminar hydraulic behavior up to $Re = 100$.

In this study, I isolate and quantify discharge through discrete natural fractures. The samples used to refine the technique presented include a parallel plate proof of methodology, a fine-grained granite from Fredericksburg, TX, consecutive vertical fractures of semi-welded Santana Tuff from Trans-Pecos Texas, and a large fracture in welded Paintbrush Tuff from Yucca Mountain in Nevada. I process computed tomography data to produce digital representations of these fractures in the flow configuration. Modeling discharge through the digitized fractures, I show good agreement between empirical results and an unmodified cubic law using geometric mean aperture.

1.2 Hypotheses

My hypotheses include:

- The unmodified cubic law is valid for the laminar flow regime using an appropriate representative physical aperture.

In Chapter 5, I show the results of matching physical flow test results to numerical models using transmissivity calculated from computed tomography derived aperture distributions. Chapter 6 discusses the merits of using point, profile, and areal aperture data as a predictor for hydraulic aperture. The geometric mean of aperture data from mated surfaces adequately predicts fluid flow in the laminar flow regime.

- A representative elemental surface (RES) can be used to assign a roughness value for much larger surfaces.

Surface roughness is expected to affect fluid flow at the scale of aperture. For this study, I use approximately 0.25mm spaced data to assign a roughness value to surfaces of nominal 0.5mm aperture fractures. From these data, I look for a sample size that shows stationarity across the entire surface in the form of a mean value among all samples approximating the roughness of the entire surface, and near zero variance among samples. In Chapter 7, I report the roughness statistics for 25 surface–scale pairs and propose a data requirement for an RES.

- A representative elemental volume (REV) exists for discrete fractures at a similar size to the RES.

Discharge per unit width of a fracture is used as a metric to compare model results of differently sized fractures in an effort to find a sample volume that mimics the hydraulic properties of physical flow test results. Chapter 8 details the results of using the aperture data from a calibrated model to illustrate the limitations of scaling aperture.

- Channeling can be scaled from a fracture REV to predict the spatial extent of solute transport and breakthrough times.

Should an REV for fractures exist, channeling exhibited at small scales may transform via a branching parameter to limiting widths for solute transport for point sources. Variability in channeling at small scales discussed in Chapter 8 leaves the prospect of accurate upscaling from hand sample fractures ambiguous.

2 FRACTURE SPECIMENS

Table 2.1 describes the specimens used in this study. It was necessary to confine the study to well indurated rocks that would not deteriorate under saturated conditions. A spatially and temporally variable collection of specimens populate this study (Figure 2.1). The granites range from fine- to coarse-grained, and the tuffs include up to centimeter scale pumice and lithic fragments in a largely aphanitic groundmass.

2.1 Description of Specimens

The Yucca Mountain specimen comes courtesy of Sandia National Labs in New Mexico. It is from a moderately welded member of the Paintbrush Tuff, a quartz poor, alkali-calcic welded to densely welded ash-flow tuff (Byers et al. 1976).

The Elberton Granite is a pink fine-grained granite emplaced from several kilometers northeast of Elberton, GA to approximately 16km west southwest of Lexington, GA. The particular specimen included in this study is from an exfoliation joint with a clay and iron oxide coating.

Two medium-grained specimens of Town Mountain Granite, part of the Llano Uplift in central Texas, are included. In outcrop, the Town Mountain Granite exhibits four major types of fracture skins: weathering rind, pyrolusite coating, slickensides, and iron oxide coating. One specimen has a 1cm leached weathering rind that imparts significant roughness to its surface. The second is coated with pyrolusite. Both were collected from just north of Fredericksburg, TX.

Two coarse-grained granites are included from South Australia. Calca Granite is a massive Mesoproterozoic (1.6BYa) granite dominantly composed of alkali feldspar and

Table 2.1 Specimens used in this study, their provenance, character, sizes and published ages.

Specimen	Location	Rock Description	Size	Age
YM01-02	Yucca Mountain, Nevada	Paintbrush Tuff, alkali-calcic moderately welded tuff.	$2080cm^2$	13.2-12.5MYa
El01-3	Elberton, GA	Fine grained granite with iron oxide and clay coating.	$1600cm^2$	320MYa
Fr-Wr	Fredericksburg, TX	Medium grained granite with 1cm weathering rind.	$154cm^2$	1.2BYa
Fr-MnO	Fredericksburg, TX	Medium grained granite with pyrolusite coating.	$266cm^2$	1.2BYa
Pad	Padthaway, South Australia	Coarse grained green granite with 3cm weathering rind		Ordivician
Calca	Calca, South Australia	Coarse grained granite with 1mm weathering rind and 1cm iron oxide band		1.6Bya
Oatman Creek	Llano, TX	Fine grained unweathered granite fracture (2 surfaces).	$52cm^2$	1.2BYa
Brushy Canyon	Culberson County, TX	Fine grained sandstone, bedding plane fracture (2 surfaces).	$69cm^2$	Permian
CC01-1	Big Bend State Park, TX	Welded rhyolitic tuff, unweathered surface.	$29cm^2$	28MYa
CC01-2	Big Bend State Park, TX	Welded rhyolitic tuff, weathered surface.	$54cm^2$	28MYa
CC01-3	Big Bend State Park, TX	Impact fracture in welded rhyolitic tuff (2 surfaces), unweathered.	$134cm^2$	28MYa
CC02-1	Big Bend State Park, TX	Semi-welded rhyolitic tuff (2 surfaces), clay coating.	$120cm^2$	28MYa
CC02-2	Big Bend State Park, TX	Semi-welded rhyolitic tuff (2 surfaces), clay coating.	$142cm^2$	28MYa

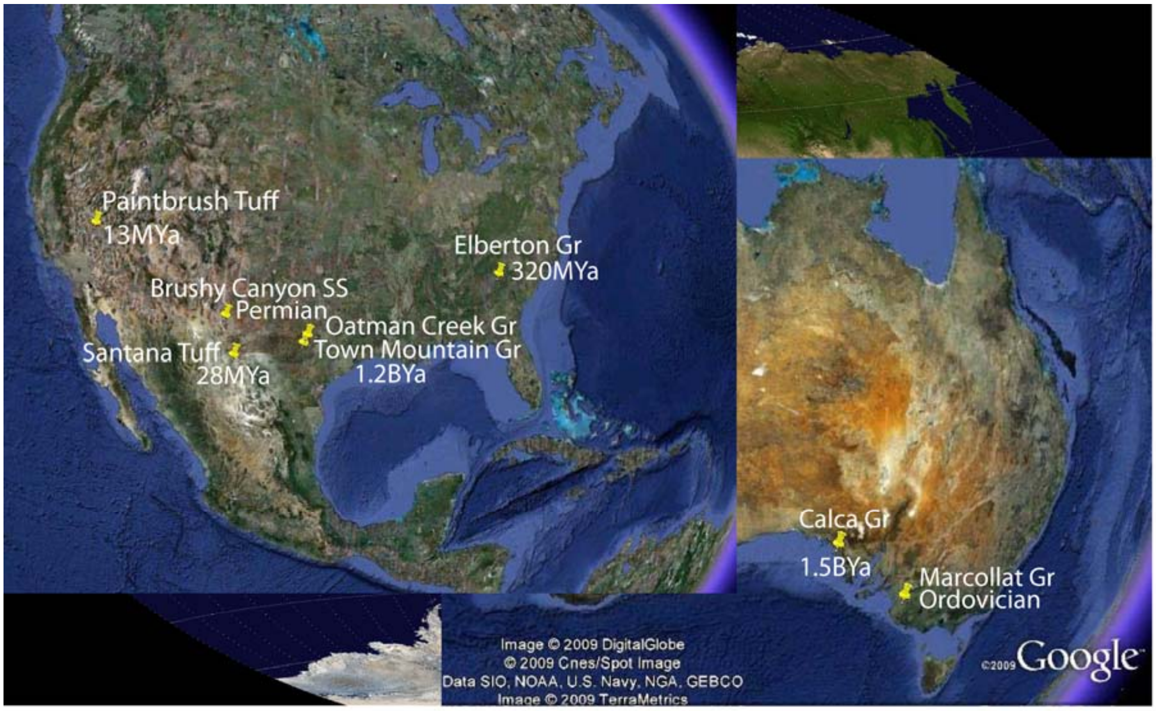

Figure 2.1 Specimen rock types and ages.

quartz and mined for dimensional stone (Budd et al. 2001). I collected a weathered vertical fracture specimen from an abandoned quarry that exhibits a 1mm leached weathering rind external to a 1cm iron oxide band. The Ordivician age Marcollat Granite presents as green to olive-green, composed of green feldspars, smoky quartz and amphibole (Drexel et al. 1995). The collected fracture specimen exhibits a 3cm leached weathering rind.

The Oatman Creek Granite is a fine-grained late differentiate of the Town Mountain Granite of the Llano Uplift (Conrad 1982). This particular fracture specimen is from an unweathered fractured road-cut east of the city of Llano. Preparation of the Oatman Creek Granite and the fine-grained, thin bedded Brushy Canyon Sandstone is detailed in Thompson (2005).

I collected the remaining specimens from Closed Canyon in Trans-Pecos Texas. The Santana Tuff is a semi-welded to welded rhyolitic, vitric-crystal tuff (Smyth-Boulton 1995). Samples CC02-1 and CC02-2 are consecutive vertical cooling joints from the wall of Closed Canyon. Samples CC01-1 though CC01-3 are from a float sample on the floor of the canyon. The transport properties of the skins of Elberton Granite, Town Mountain Granite, the green Marcollat Granite from Padthaway, and the Calca Granite specimens are examined by Garner (2007).

2.2 Sample Preparation

The limits of the High Resolution X-ray Computed Tomography (CT) Facility at The University of Texas at Austin (UTHRXCT) dictated the maximum size of the samples cut from collected specimens, which expanded from approximately 13cm to 30cm over the course of this study based on the method of data acquisition (Ketcham and Carlson 2001). I cut the raw specimens down to an appropriate dimension using a combination of rock slab and lapidary saws. The slab saws are either water-cooled or oil-cooled with 16-inch (41cm) or 24-inch (61cm) diamond blades. The lapidary saw is water cooled with an 8-inch (20cm) diamond blade. Finished sample mean fracture surfaces are orthogonal to the base and at least two sides; the top was squared digitally. Mated fracture specimens were cut in their mated configuration to yield a rectangular sample through which the mean fracture plane is approximately horizontal.

The fracture specimens were cut to maximize the sample surface (or fracture volume) while respecting the width requirement for CT imagery. Orientation of the fracture guided my initial cut, but stabilizing the rock mass during the cut was of primary importance. Therefore, mean fracture plane is a subjective quality rather than a quantitative one. Once a flat reference was achieved, the remaining cuts were precisely registered to the fracture surface. Though fine corrections are beyond the capability of the flexible saw blades, a final cut that rectifies the initial estimate was possible.

The Elberton Granite specimen yielded three 13cm wide samples. Successful use of the samples as one unit preceded bisection of the Paintbrush Tuff sample subsequent to physical flow testing. The Paintbrush Tuff sample was cut in two by Southwest Marble and Granite Works in Austin, TX

3 PHYSICAL FLOW EXPERIMENT

The apparatus used for the physical flow experiment is modified from Thompson (2005). Figure 3.1 represents the model for the experiment. There are four requirements for a successful experiment using this configuration: 1) steady state in terms of a constant reduced pressure (head) gradient, 2) a constant fracture volume, 3) an incompressible fluid, and 4) accurate measurement technique. The first two represent well controlled boundary conditions. The third satisfies conservation. The fourth simply requires practice, but does enter into uncertainty analysis. Reservoirs up and down gradient maintain a constant head gradient across the fracture sample. Once steady state is achieved, discharge and temperature are recorded to satisfy calculation of hydraulic aperture and Reynolds Number.

3.1 Flow Test Sample Preparation

The Santana Tuff specimens (Figure 3.2) came out of the field in a best fit configuration. Qualitatively, this means that the two sides fit together with no slip and such that one side is approximately the cast of the other. This is the assumed registration of the surfaces at the time of fracturing as all fractures used in the study have no indication of shear. The surfaces were registered to each other in the field, and this registration was maintained throughout sample preparation, flow testing, and computed tomography (CT) imagery.

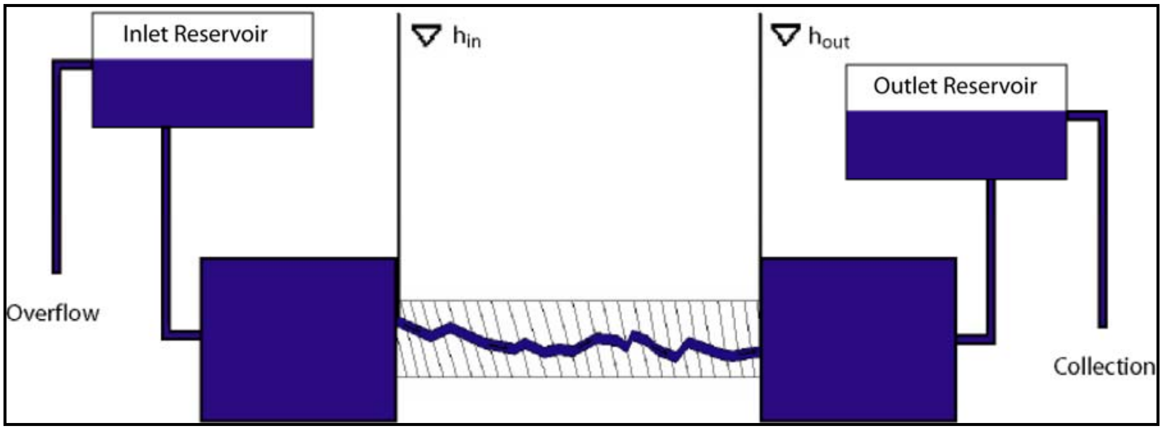

Figure 3.1 Cartoon model of flow experiment. Reservoirs above sample maintain head gradient across fracture. Reservoirs adjacent to sample allow transition from pipe flow to slot flow external to fracture. Head is measured at inlet and outlet of fracture sample. Overflows allow collection of discharge and regulation of head.

Figure 3.2 Santana Tuff fracture specimens cc02-1 (left) and cc02-2 (right) in best fit configuration from the field.

With two consecutive fractures, and owing to the nature of using a wet saw to prepare the samples, I chose to preserve the morphology of the weathering products on the top and bottom surfaces of the second Santana Tuff fracture, sample CC02-2, using an epoxy spray before cutting the specimen to size. After cutting, the samples were dried completely in an oven not exceeding 75°C. The exterior surfaces of the samples were then sealed with Minwax® polyurethane. To define precisely the lateral boundaries of the experiment for the fracture samples used in this study, a minor addition to the best fit configuration was made with parallel strips of 3mm thick closed cell foam. This foam compresses to 0.25mm between flat surfaces without significant deformation, therefore justifying an assumption that the edges of the foam remain parallel after mating the two surfaces of a fracture. The 0.25mm addition to the overall mechanical aperture should be considered an ideal case maximum. In practice, the edges of the fracture samples are rarely in contact, so the effect of the foam does not warrant consideration of the configuration of the mated surfaces as being other than best fit.

Faceplates constructed of 0.5-inch (1.27cm) gray PVC (Figure 3.3) act as an interface between the fracture sample and the flow test apparatus and provide a measuring point for pressure head. The same closed cell foam used between the fracture surfaces acts as a gasket that conforms to any irregularities between a faceplate and its corresponding fracture face. All seams are sealed with GOOP® plumbing contact adhesive. This product flows easily, stays flexible, and bonds dissimilar surfaces extremely well.

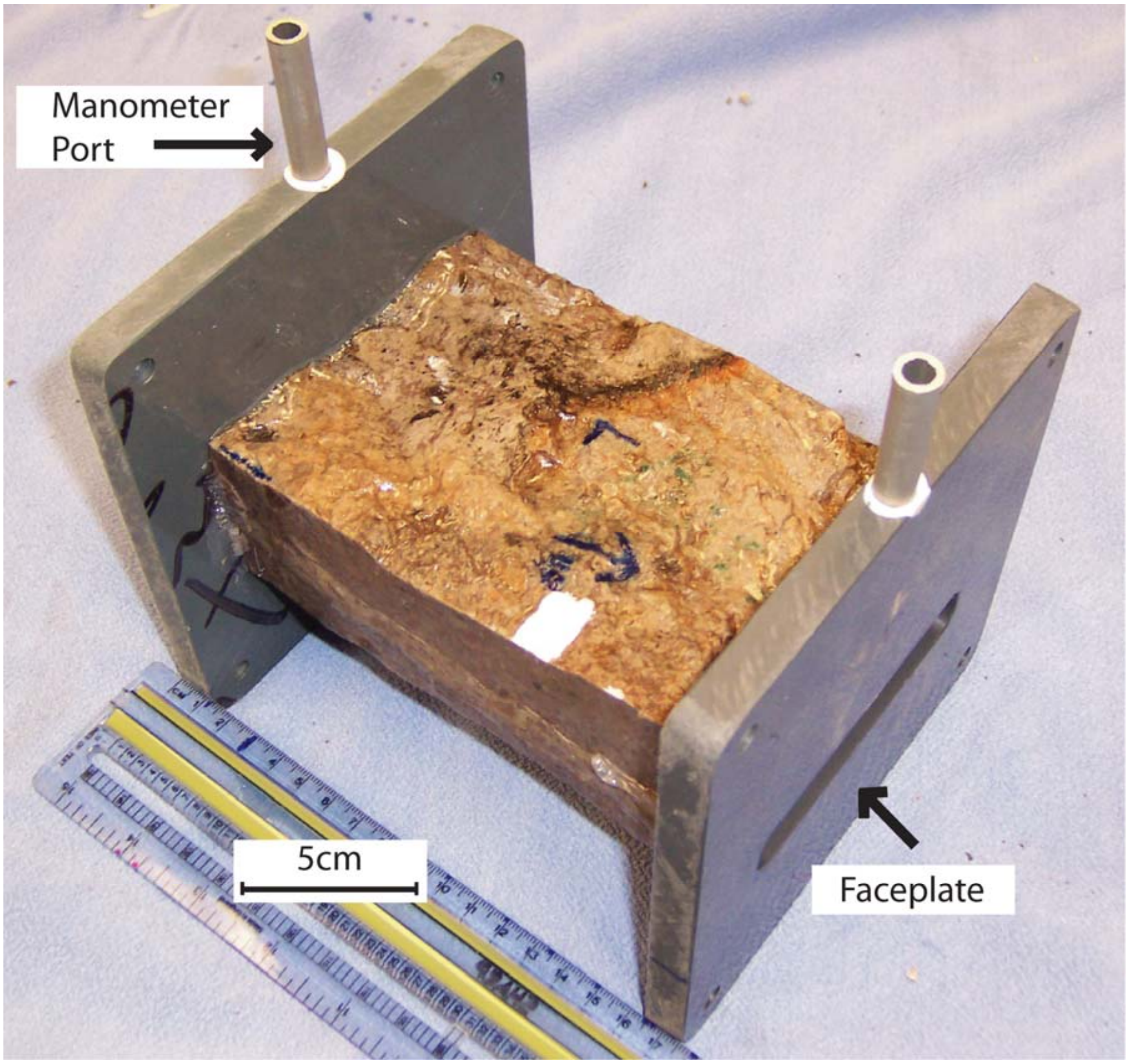

Figure 3.3 Santana Tuff fracture sample CC02-2 prepared for flow testing. The faceplates bolt to the flow test apparatus conditioning reservoirs. Surgical tubing connects the 3/8in OD manometer ports to the manometers of the flow test apparatus.

3.2 Experimental Procedure

Accurate physical flow testing is a laborious process subject to inaccuracy stemming from many sources. First, water will find a way through any permeable zone. Thus, sealing the actual fracture system between the measuring points is of primary importance to ensure that only flow through the fracture is considered in further analysis. Beyond that, a good deal of trial and error went in to devising the following procedure as the most efficient, given the constraints of steady-state and the general configuration of the apparatus, for developing the discharge per unit gradient data for the final iteration of this study.

3.2.1 Delivering a constant head gradient

The experimental apparatus pictured in Figure 3.4 and associated flow test procedure is modified from Thompson (2005) in a number of ways. These are necessary to ensure consistency in flow tests within a sample run and between samples, and include the method of water delivery, quality checks to maintain constant head to the fracture, chlorination and monitoring of the water to retard algae growth and keep pH equilibrated with the rock matrix, and changes to the range of gradient tested and the actual data collection procedure.

From a mechanical standpoint, the water supply is delivered to the saturated system from a 55-gallon (210L) storage reservoir via a Rule 360 submersible pump with output of approximately 380cm^3/s. This stream is split using a y-adapter with one side full open that returns to storage. The other allows a gross adjustment to a 5-gallon (19L) reservoir that supplies the experimental system by gravity drainage. This upper reservoir

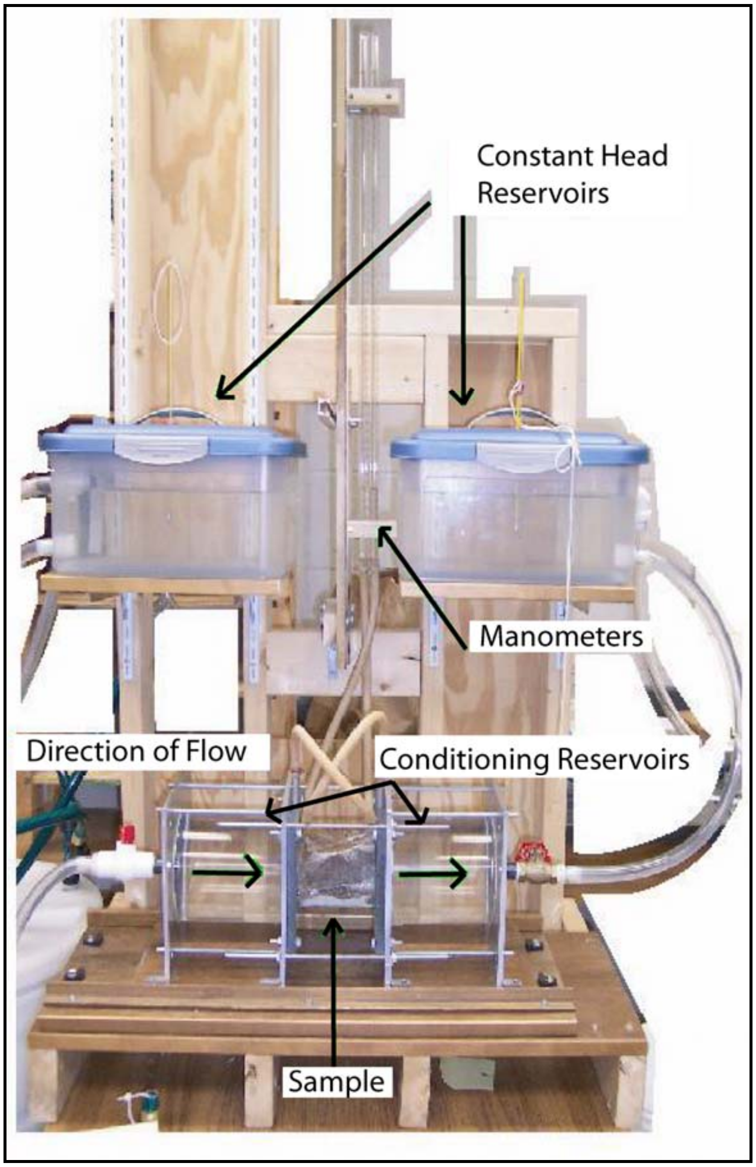

Figure 3.4 Actual flow apparatus. Water gravity supplied to inlet reservoir. Overflow capacity is twice that of supply to maintain head. Manometer is graduated at 1.07mm intervals.

accomplishes two tasks. First, it eliminates any temperature fluctuation induced by the pump. Second, with an overflow return to storage and a common hose bib, a constant level is maintained in the reservoir that delivers a constant flow rate to the inlet reservoir of the experimental system (Figure 3.1).

Originally, the inlet reservoir had the same capacity overflow as its output to the fracture sample (1.27cm ID). Observing the effects of surface tension at the overflow in the form of fluctuations in the level of the inlet reservoir by as much as 5mm for what should have been steady state, I added a second overflow port (Figure 3.5). This doubling of the overflow capacity allows constant head to be maintained even under high gradients by ensuring significant and constant overflow is maintained.

To accommodate fracture samples of up to 10.5cm width, Thompson's stilling chambers, conditioning reservoirs, were modified by enlarging the end plate opening from 6.5cm slots to 10.5cm diameter circles. Two additional sets of conditioning reservoir boxes were fabricated to accommodate larger samples.

3.2.2 Preserving fracture volume

The sample used for the pilot project for this study served as a model for how to hold the fracture surfaces in their configuration against the vertical fluid pressure exerted during physical flow testing. Figure 3.6 contains a picture reprinted from Thompson (2005) showing how the fracture volume is maintained via confining plates. This methodology was put to use for the parallel plate proof of concept flow test runs and the flow test for the first Santana Tuff fracture sample (CC02-1). Upon completion of the CC02-1 flow tests, it was noted that the rigidity of the bond between the fracture sample

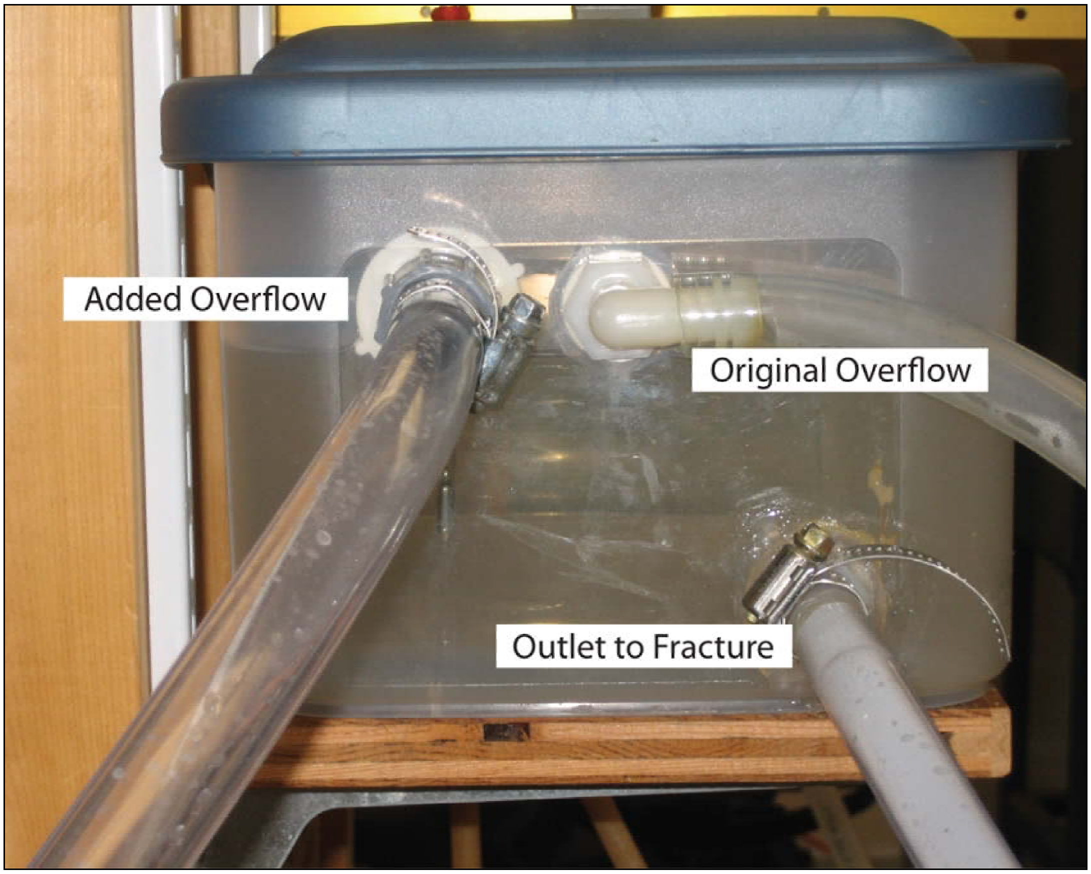

Figure 3.5 Inlet reservoir showing additional overflow capacity.

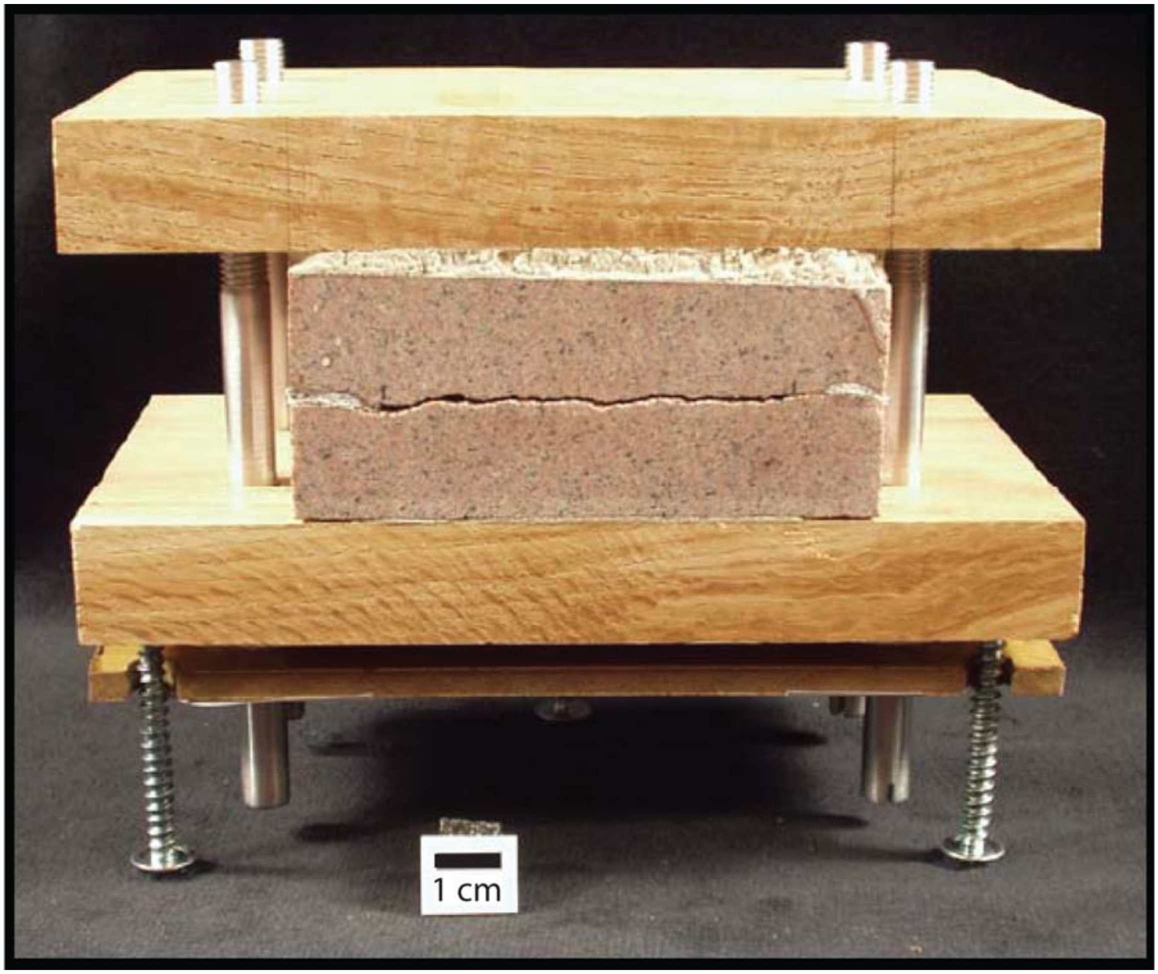

Figure 3.6 Sample fracture from Oatman Creek Granite used in pilot program for this study reprinted from Thompson (2005).

and the faceplates is sufficient to withstand the pressure fluctuations induced by cycles of flow testing. Therefore, no confining pressure beyond that supplied by the mounting of the fracture sample and by the flow test apparatus was deemed necessary for subsequent samples.

3.2.3 An incompressible fluid

For the fracture volumes, gradients, and confining pressures used in this study, the deionized (DI) water used is assumed incompressible. Care is required, however, to ensure that all air is expelled from the fracture at the time of flooding the system and that the fracture remains saturated for the duration of flow testing. This was initially accomplished by filling the system from the bottom up and then using time and agitation to minimize air pockets. The latter condition includes loss of saturation due to a breakdown in procedure and the introduction of a gas phase from water-rock interaction.

The interaction between rock, water, and algae, ubiquitous in a system open to the atmosphere, is considered in this study. The use of approximately 0.25m^3 of DI water to run the experiment precludes draining the system each day, so to keep algal growth down, I added Cl^- in the form of dichloro s-triazinetrione dihydrate ($C_3HCl_2N_3O_3 \cdot 2H_2O$), keeping free chloride to 3ppm. Along with Cl^- levels, I also monitored pH to avoid conditions favorable to matrix dissolution or flocculation and aggregation of clays. For the tuff specimens, pH was maintained at neutral to slightly basic (7.0 – 7.2) by adjustments to the Cl^- levels alone.

During a cycle of flow testing, the system is initiated from the pump forward. Once the pump is started, the upper reservoir is opened allowing flow to the inlet reservoir. Then the valve to the inlet conditioning reservoir is opened followed by the outlet conditioning reservoir discharge valve. This process ensures no introduction of air to the system. The shut-down procedure reverses this process.

3.2.4 Measurement techniques

At the point of data collection, seven factors contribute to accurate measurement:

- constant head maintained throughout test,
- visual measurement of head gradient,
- visual measurement of temperature,
- timing operation,
- coordinating discharge collection with timing,
- visual measurement of volume, and
- mass measurement.

The error introduced by each of these is independent of the others. All errors are procedurally minimized as detailed in the following discussion.

The flow test apparatus is designed to run indefinitely as specified; all overflows and discharges return to storage. The one necessary requirement is that the upper reservoir must have a constant overflow. This is accomplished via adjustment of the pump and monitoring of a float in the upper reservoir that extends beyond the rim of the reservoir as a warning that overflow is approaching (Figure 3.7). When approximately 1cm is showing between the lines on the float and the top rim of the upper reservoir, visually evaluating the change in water level is simplified. Adjustment of the flow from

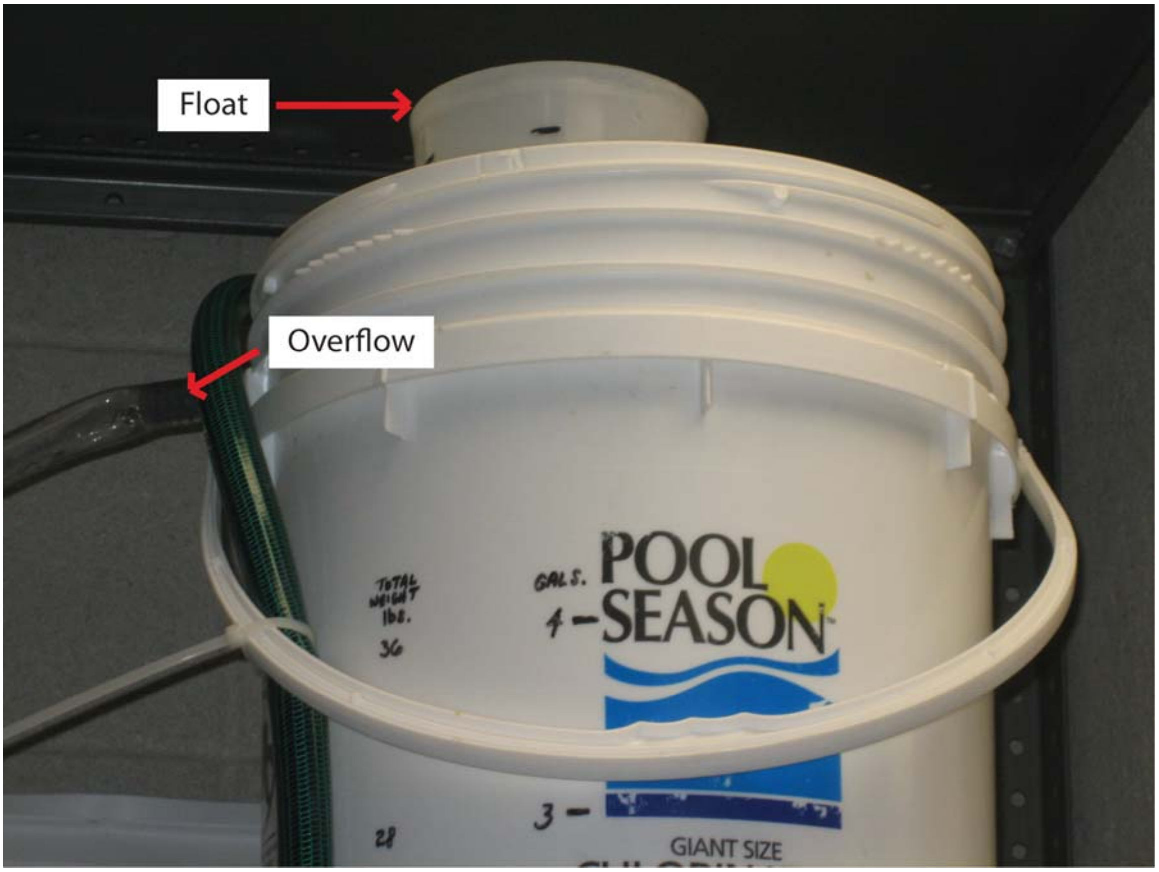

Figure 3.7 Upper reservoir. Lines on float give approximately 3cm warning before catastrophic overflow. The reservoir will discharge through the overflow valve when lines are just visible.

the pump to the reservoir is made until the water level holds steady. Then fine adjustment can be made to the output of the upper reservoir to the inlet reservoir (Figure 3.1) until the level of the inlet reservoir and the levels of the manometers all hold steady for at least 5min. This defines steady state for this experiment.

Head gradient is composed of two elements: the difference in head at the outlet from the inlet and the distance between the two measurements. Several graduated burettes were evaluated to serve as manometers for the flow test apparatus. While the manufacture of burettes may yield precise volumetric instruments, the cross sectional area from one to the next apparently is variable batch to batch as it took a special request to acquire two that had equal gradation spacing. This results in reported head heights being converted from visual measurements at a spacing of 1.07mm. Discretizing readings on a continuous scale is commonly expected to 1/10 of a gradation (Pinskii et al 1969). While I report partial gradations to the tenth, I conservatively estimate accuracy to one quarter gradation. Therefore, for the two readings for each flow test, maximum error is estimated at 1.07mm. As the shortest flow path for any sample is 90mm, the error from head measurement propagates to a maximum of 1.2%. For the length measurement, my estimate of visual error corresponds to 0.5mm. This adds a maximum of 0.6% to the overall error attributable to head gradient.

Viscosity of water over 20–30°C varies by 20%. With a temperature range for all flow tests of 22°C to 26.125°C it is appropriate to include a temperature corrected viscosity in the calculation of hydraulic aperture. One reading from the inlet reservoir and one from the outlet reservoir are recorded at 0.125°C precision and averaged. This yields a maximum error associated with the temperature readings of 0.25°C. Many curve fitting equations have been proposed for relating the viscosity of water to temperature. I use an equation that simplifies the International Association for the Properties of Water and Steam (IAPWS) formulations to achieve calculation of viscosity at 1atm with respect to temperature as proposed by Patek et al. (2009). Equation 3.1 uses the constants and exponents in Table 3.1:

$$\mu/\left(10^{-6}\,Pa\cdot s\right)=\sum_{i=1}^{4}a_i\left(T^*\right)^{b_i} \tag{3.1}$$

where T^* is dimensionless temperature equal to T/(300K) and a_i and b_i are matching parameters. The viscosities calculated using Equation 3.1 have an uncertainty in the range of interest of 1% attributable to disparities in the experimental data matched. Propagating temperature uncertainty into viscosity uncertainty yields a maximum error associated with viscosity of 3.2%.

Synchronizing the timing operation with the collection of discharge was accomplished easily because of the configuration of the flow test apparatus. The discharge tubing from the outlet reservoir reaches the storage reservoir so the system can run continuously without user intervention. This allows flexibility in where and how discharge is collected for a flow test. Time duration for each test was arbitrary. Discharge collected to near capacity of either a 250ml or a 1L graduated cylinder determined the end of the test. Prior to initiating a test, the dry graduated cylinder is placed on a platform in the middle of a 5-gallon (19L) bucket and the discharge hose is transferred to the same bucket. Timing information was acquired using *Online-Stopwatch*, a self contained Adobe Flash application. Errors in timing are solely due to lack of coordination between the hand holding the discharge tube and the one pressing

Table 3.1 The leading constants and exponents for equation 1.9 to calculate viscosity of water from temperature at 1atm (Patek et al. 2009).

a_i	b_i
280.68	-1.9
511.45	-7.7
61.131	-19.6
0.45903	-40

the mouse key. Keying the stopwatch as fast as possible yields a conservative 0.2s reaction time. This corresponds to a maximum error of 1.2% at a gradient of 2.0. At a gradient of less than 0.5, which includes the full laminar flow regime under the experimental condititions, the maximum error falls to 0.4%.

Errors associated with volume readings resulted from two independent phenomena: visual inspection and cross contamination from one flow test to the next. Volumes from the 250ml graduated cylinder used in this study were recorded to 1/4 gradation precision (0.5ml). Allowing the conservative 1/8 gradation accuracy gives a nominal error estimate of 0.2% for 250ml flow tests. Completely drying the interior of the graduated cylinder between flow tests was critical to maintain the accuracy of the volume measurements. As much as 4ml could remain in the graduated cylinder due to surface tension effects upon pouring out the collected discharge. As the drying of the graduated cylinder was accomplished systematically, no associated error is attributed to this cause.

Closely related to the possible errors in volume are those associated with mass measurements. The dry empty 250ml graduated cylinder was tared on an Ohaus Scout Pro 2000g capacity digital scale before each flow test. As the discharge tube crossed the edge of the graduated cylinder twice during each test, some water did get on the exterior. Thus, the exterior of the graduated cylinder was dried thoroughly before being placed on the scale. Again, this source of possible error is discounted. However, although a 200g calibration weight regularly affirmed the accuracy of the scale, after drying the graduated cylinder, the zero reading of the scale varied between -0.2g and 0.2g. Using this range as the error propagates a 1.6% error in mass of discharge at the lowest gradients. More often, individual flow tests accumulated more than 230ml discharge yielding a ≤0.2% error attributed to mass.

Plugging Equation 1.6 into Equation 1.5 and rearranging to solve for hydraulic aperture b_e yields:

$$b_e = \left(\frac{\rho_w g w i}{12\mu \cdot Q} \right)^{1/3} . \tag{3.2}$$

In terms of uncertainty, this can be expressed as:

$$\frac{\delta b_e}{b_e} = \frac{1}{3}\left(\frac{\delta \rho_w}{\rho_w} + \frac{\delta w}{w} + \frac{\delta i}{i} + \frac{\delta \mu}{\mu} + \frac{\delta Q}{Q} \right), \tag{3.3}$$

where δx/x equals the relative error attributed to x. The maximum error for width is 0.8% using the same constraints as that for length. Thus the overall maximum error in hydraulic aperture calculation from the physical flow test experiment is:

$$\frac{\delta b_e}{b_e} = \frac{1}{3}\left(0.4 + 0.8 + 1.8 + 3.2 + 0.6\right) = 2.4\% . \tag{3.4}$$

3.3 Parallel Plates

The first iteration of this study verified the procedural setup using parallel plates made from 0.5-inch (1.27cm) clear polycarbonate (Figure 3.8). The separation between the plates was maintained by 18 gauge (1.02mm diameter by American Wire Gauge standards) copper wire running the full length of the "fracture" along both sides immediately distal from the foam used to isolate the fracture volume. The confining plates top and bottom in Figure 3.8 reduce to insignificance the possibility of medial flex of the rigid plates. The physical dimensions of the fracture volume are 101.6mm x 151.6mm x 1.02mm. The results of the flow tests conducted on the parallel plates are

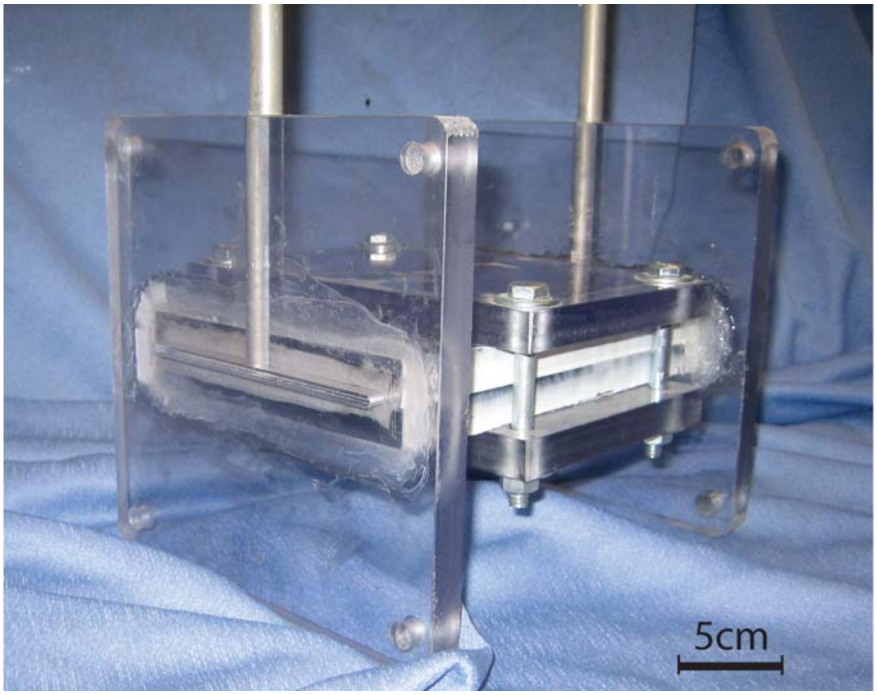

Figure 3.8 Parallel plate sample configuration. Sample is 10.2cm wide with a 15.2cm long slot flow channel propped open by 1.19mm 18 gauge copper wire.

reported in Table A.2. The discharge per unit gradient for these same results is graphically displayed in Figure 3.9.

With the common assumption that predicting flow through fractured media was at best an order of magnitude proposition, an approximately 10% reduction of b_e from b_m seemed within tolerance at first glance. However, several procedural failings came to light from this first attempt. Most important for future flow tests was the realization that 25L of supply water to start is insufficient to maintain a constant head for the duration of a single flow test. This is evident especially at the higher gradient tests on Figure 3.9. What might be considered nonlaminar effects at the beginning of a transitional flow regime can be explained by falling discharge in response to falling head up gradient.

Second, temperature and density were spot sampled throughout a day of flow testing rather than systematically as part of each test. Conceivably, the anomalous calculation of ρ_w at 1.03g/ml caused an underestimation of hydraulic aperture near 3% for that day's flow tests. This result precipitated institution of the procedural steps measuring mass, recording volume, and drying then taring the graduated cylinder for each flow test.

Finally, although initiating the flow tests with fresh DI water, delay in completion of the full suite of flow tests resulted in significant algae growth in the system at one point. To combat this effect and to address the issue of constant head in the upper reservoir, water supply for the next iteration of the study used tap water filtered through a Barnstead Hose Nipple Cartridge (part number D8922 and Figure 3.10) that deionizes and removes

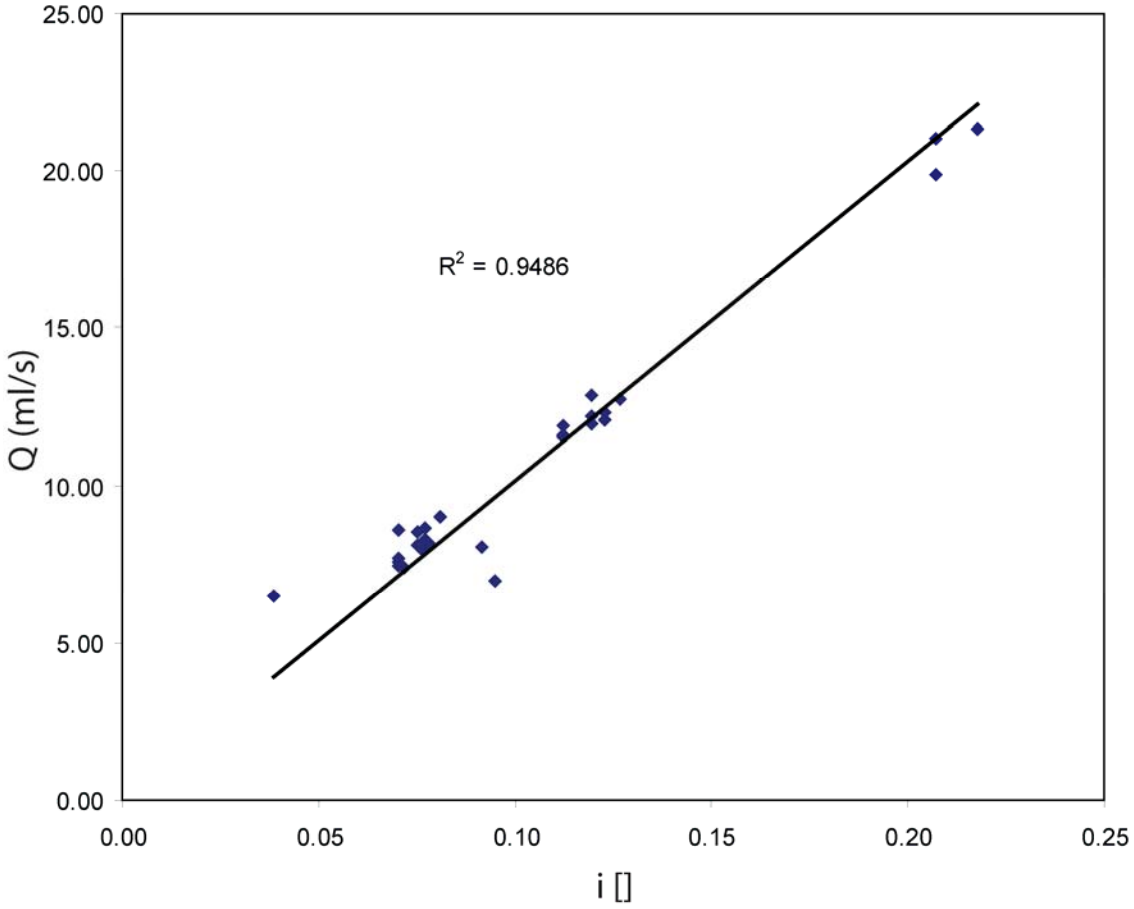

Figure 3.9 Discharge per unit gradient for the flow tests of the parallel plate sample. A zero intercept trendline is included to illustrate how a laminar flow regime should behave. Scatter and the apparent nonlaminar behavior of the data is attributed to lack of constant head during testing rather than transitional flow.

Figure 3.10 Barnstead Hose Nipple Cartridge has 3/8in nipples top and bottom. Water flows through the resins from bottom to top stripping ions and organic carbon. Supplies up to 75l/h. Color change of resins indicates filtering capacity remaining in cartridge.

organic carbon supplying up to 75l/h, more than sufficient for the discharge rates expected.

3.4 Oatman Creek Granite

With the flow apparatus modified to deliver a constant head of DI water, the fine-grained fracture sample from Thompson (2005) pictured in Figure 3.6 was fitted with new faceplates and flow tested again. Flow test data includes that reported in Thompson (2005) and a series of 31 additional flow tests conducted by Robertson (Table A.4, written communication 2006). Disagreement between the two data sets can be explained by flow test methodology with further refinement of the parallel plate flow test procedure warranted. Further, the data as they pertain to laminar versus transitional flow are ambiguous.

Table A.3 contains the Thompson flow test data. The tests were run from a minimum gradient of 0.26 to a maximum of 3.26. The range of Reynolds number for these tests is 47.1 to 540.6. Looking at the data in Figure 3.11a, an assumption of laminar flow might be made with the linear relationship between gradient and discharge. However, upon closer observation of best fitting trends, it is apparent that a curve to the data exists at gradients greater than one (Figure 3.11b). This effect is not necessarily due to a transition away from a laminar flow regime. Figure 3.11c adds the Robertson flow test results. These data have a strong linear correlation between hydraulic gradient and discharge through a gradient of 0.85 and can be considered to be in the laminar flow regime. However, they also show a marked increase in discharge per unit gradient at all gradients tested from the Thompson data.

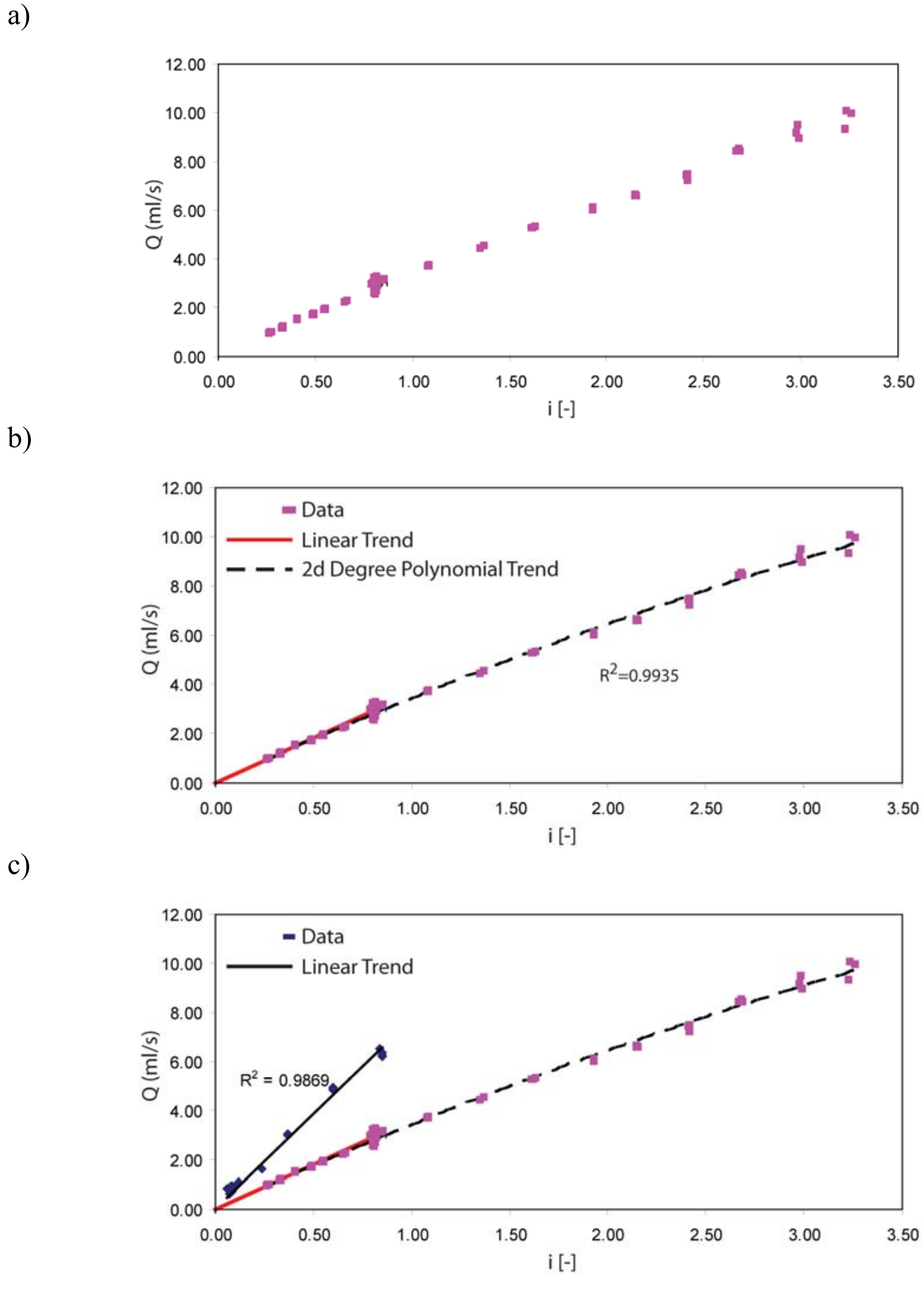

Figure 3.11 Discharge versus gradient data for Oatman Creek Granite: a) data from Thompson (2005) without trend line , b) with linear and 2 degree polynomial trends, and c) adding Robertson (2007) data and associated linear trend. Differences in shift and slope due to changes in experimental methodology.

The differences between the two methodologies for flow testing lie in the manner by which flow is controlled and in the assumption of steady state. Thompson used the flow control on his stilling chamber to regulate the discharge of the outlet reservoir to match the overflow of the inlet reservoir. This creates a variable conductivity for the apparatus that does not appear in any of the data and accounts for the upward shift of the new data. Failure to maintain a constant head in the upper reservoir throughout the flow test could account for the curve in Thompson's data. As the gradient and discharge increase, head in the upper reservoir decreases faster, thereby showing more effect at larger gradients.

3.5 Santana Tuff

Two consecutive fractures (Figure 3.2) from the wall of Closed Canyon outside of Big Bend National Park were cut to maximize rectangular fracture samples for the next iteration of this study. The fractures are assumed cooling joints; they are weathered and subject to episodic saturation. I hypothesize that the flow tests of these related fractures will exhibit similar characteristics, which will allow extrapolation to fracture sets.

3.5.1 CC02-1

For the suite of flow tests on fracture sample CC02-1 (Figure 3.12), I strove to delineate a transition out of the laminar flow regime. Data from all flow tests on CC02-1 is reported in Table A.5. A strong linear relationship between discharge and gradient was found at low gradients (0.02 through 0.6), so I increased the gradient by large increments looking for a break from linearity. Figure 3.13a shows the linear trend and an abridged data set that corresponds to these tests.

Figure 3.12 Fracture sample CC02-1.

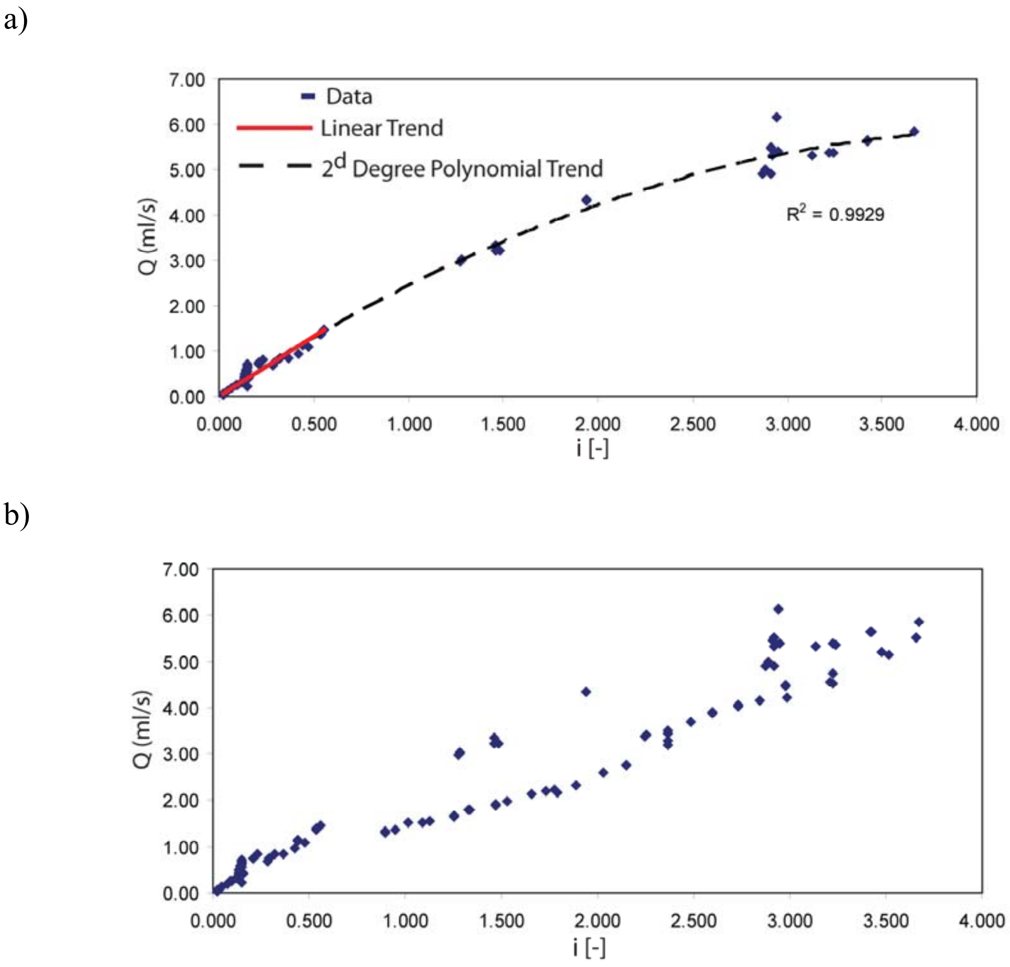

Figure 3.13 Flow test data from sample CC02-1. a) Abridged data set showing a linear trend between discharge and gradient exists at gradients <0.6. A smooth rounding trend described by a second degree polynomial shows a departure from strictly laminar flow at higher gradients. b) Inclusion of late data indicating degradation of the sample fracture volume due to overload of the DI filter and possible flocculation and redeposition of clays present in the weathered sample.

Following exposition of the general nature of the discharge to gradient relationship, I used a series of intermediate flow tests to fill in the gaps in gradient. Data from these tests is included in Figure 3.13b. Once the data were plotted, I saw no alternative to disassembling the sample to gain insight into the nature of the apparent blockage. While disassembly does not necessarily mean destruction of the sample, in this case the two halves of the fracture were sealed in such a manner that part of the top half adhered to the bottom surface (Figure 3.14). There was also significant bridging of the fracture with white precipitate. Therefore, I conclude that the degradation of fracture volume was due to an overload of the water purification filter as well as possible flocculation and redeposition of clays present as weathering products on and within the original fracture surfaces.

3.5.2 CC02-2

To avoid fracture degradation, remaining iterations of flow testing rely on starting with DI water, adding free chloride to nominal pool concentrations, and monitoring pH to keep it stable relative to the saturated fracture. Further refinement would include pulverizing discarded pieces of the original fracture specimen, enclosing the resulting powder in a filter and adding it to the storage reservoir allowing the water to equilibrate with the rock prior to initiating flow tests. This was deemed likely to accomplish little considering the time investment over monitoring and maintaining stable conditions.

The flow tests on the second Santana Tuff fracture sample incorporated the best practices developed through previous trials, which serve as a benchmark procedure for

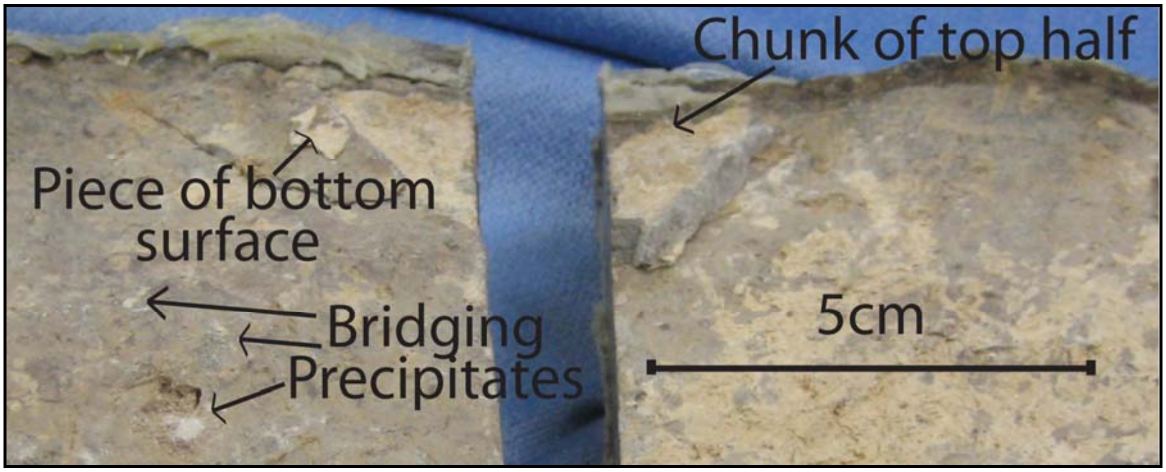

Figure 3.14 Left side of inlet to fracture sample CC02-1 after flow testing (top surface on left). Significant degradation of the fracture volume is evidenced by the adherence of a portion of the top half of the fracture to the bottom surface, also replicated on the top surface with adherence of portions of the bottom skin. White precipitate bridged the fracture in numerous locations.

recording flow test data under controlled conditions for further studies using the described apparatus. Discharge versus gradient data for 73 flow tests are displayed in Figure 3.15a and listed in Table A.6. Again, a linear trend can be drawn through data points at low gradients, while a second degree polynomial closely matches a transition away from laminar flow at higher gradients. I set the transition point from laminar flow at a gradient of 0.5 arbitrarily; from a visual inspection of the data I extracted a best linear fit and took the average of hydraulic apertures from those data points. This corresponds coincidentally to velocities yielding a Reynolds number less than 100. From these data, I surmise that the transition from laminar flow to full turbulence is a continuous function of velocity as might be expected.

Figure 3.15b confines the data to the laminar flow regime. These data set the hydraulic aperture at 0.53mm under laminar conditions. It could be argued that these data have a curve to them as well, and that the cutoff for the linear trend should be made at a gradient of 0.25. This would increase the mean hydraulic aperture by 2% to 0.54mm for comparison sake and result in a 6% increase to expected discharge.

3.6 Paintbrush Tuff

With a satisfactory experimental procedure in place, the latest iteration of this study examines flow through a fracture sample an order of magnitude greater in volume than any previously tested. This sample of Paintbrush Tuff from Yucca Mountain, measuring 64cm inlet to outlet by 30cm wide, came courtesy of Sandia National Laboratories in New Mexico. It was fitted with six ports arranged in two rows of three a)

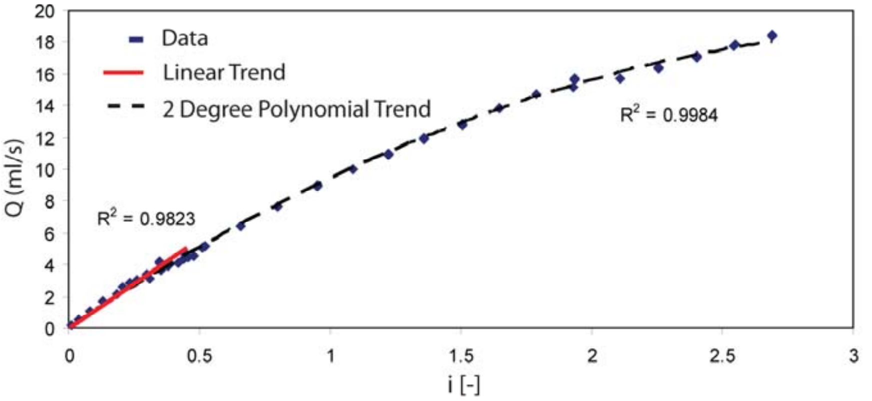

b)

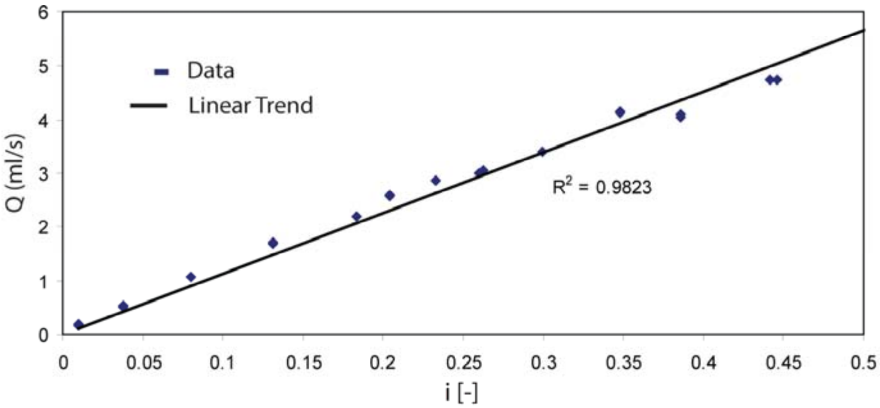

Figure 3.15 Flow test data from Santana Tuff sample CC02-2. a) Data from 73 flow tests show a linear trend at low gradients followed by a gentle rounding over as flow transitions away from laminar conditions. b) Data from flow tests at a gradient less than 0.5 yield a mean hydraulic aperture of 0.53mm.

down the overall gradient (Figure 3.16). This provides a means to develop a flow field within the fracture in addition to total discharge measurements.

Ideally, the flow tests results from this sample would show a similar linear trend between discharge and gradient at gradients less than 0.5 with a gentle roll over at higher gradients. The data listed in Table A.7 and plotted in Figure 3.17 tell a different story. While there is scatter in the data, the overall trend is linear through a gradient of 0.75, the maximum allowed by the configuration of the flow test apparatus for a fracture sample this long.

This raises several questions regarding fluid flow under natural fracture conditions and scale:

- What factors contribute to the scatter?
- Is the lack of a second degree polynomial trend indicative of competing nonlinear effects?
- Does the transition point away from a linear trend increase with scale?

At first glance, there seems to be a good deal of scatter to the data points in Figure 3.17. But taking the extreme discharge per unit gradient values and drawing $y=mx$ lines through those points yields an envelope for all data with 0.64° separating the boundaries. There are, however, still issues surrounding the use of a natural fracture at this scale.

When the sample was first saturated, I left the fracture vertical for more than a day, agitating it on occasion, to allow time for air to migrate to the outlet reservoir. Only when I was confident that little air remained in the system did I begin taking data. However, for the first several days of flow testing, the measurement ports on the top of the sample had to be bled, as a significant accumulation of gas presented overnight. This

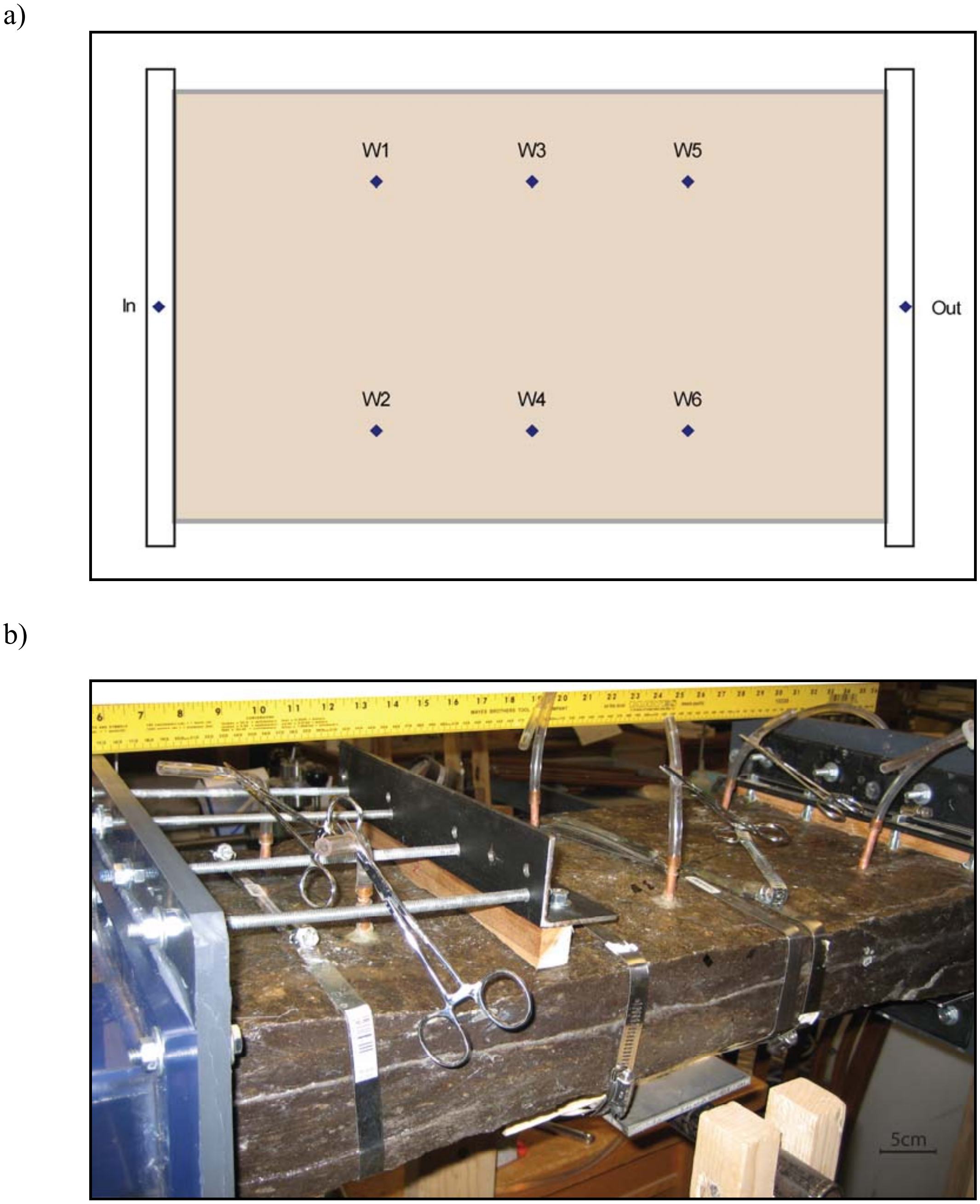

Figure 3.16 a) Schematic of monitoring ports for Paintbrush Tuff fracture sample. b) Sample mounted between inlet and outlet reservoirs and on a stand that allows rotation of the sample to vertical.

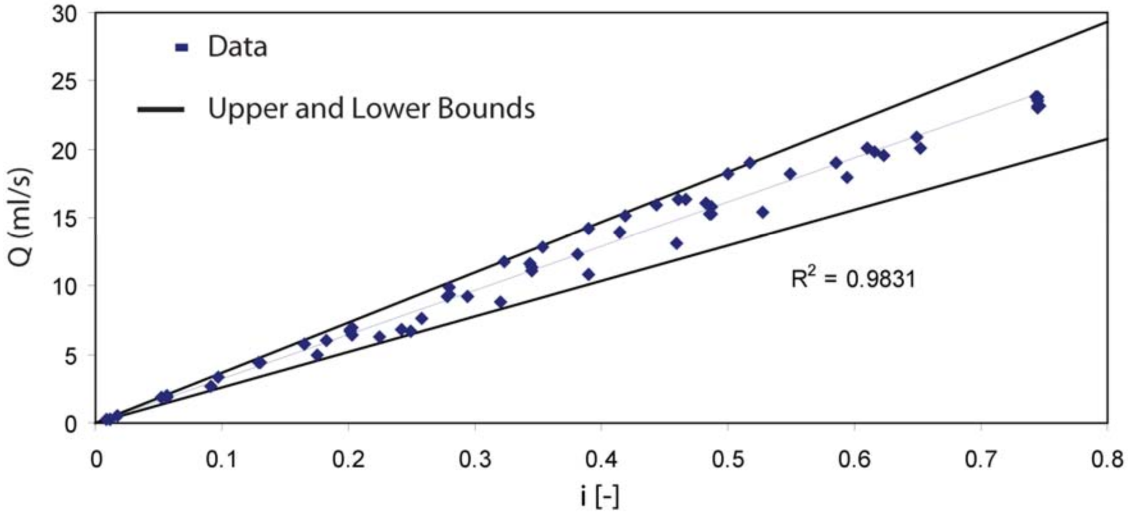

Figure 3.17 Data from 63 flow tests on sample fracture in Paintbrush Tuff. Scattering of data points is bracketed by a 0.6o angle defined by the slopes of the extremes with the origin (no flow with no gradient). Therefore, I conclude that all data are from laminar flow conditions and the scatter present is due to factors outside the procedural control of this experiment.

was either due to equilibration of the rock matrix and the fluid, or migration of trapped air during or immediately subsequent to flow testing. I reject the latter hypothesis, as in two phase flow the discontinuous phase does not migrate independently of the continuous phase; compressibility, miscibility and buoyancy are the primary drivers in response to the flux of the continuous phase. Therefore, one would expect episodic appearances of air at one or more measuring ports over the course of a day of flow testing, not accumulation under no external hydraulic gradient.

So an unforeseen and unquantified gas phase within the fracture volume may have flattened a curve in the relationship between discharge and gradient. Figure 3.18 displays the head difference across the sample versus hydraulic aperture for all flow tests discretized by day of data collection. Under ideal laminar flow conditions, there should be no variation in hydraulic aperture with an increase of head difference across the sample. The data collection on days one and two exhibit this invariant behavior with a mean b_e of 0.51mm. Beginning with day three, b_e showed variability with little change in Δh, signifying a mobile restriction to flow. The system showed little response to bleeding the manometer ports until days six through eight. The flow tests during these days exhibit the expected behavior of a nominal discontinuous gas phase where the continuous phase is under a variable hydraulic gradient. Under low flow conditions, the gas phase is minimally compressed, reducing the apparent volume of the fracture and corresponding discharge. As gradient and velocity increase, the gas phase compresses, increasing apparent fracture volume and approaching the discharge expected of a fully saturated fracture. The remaining flow tests appear to be under equilibrium conditions

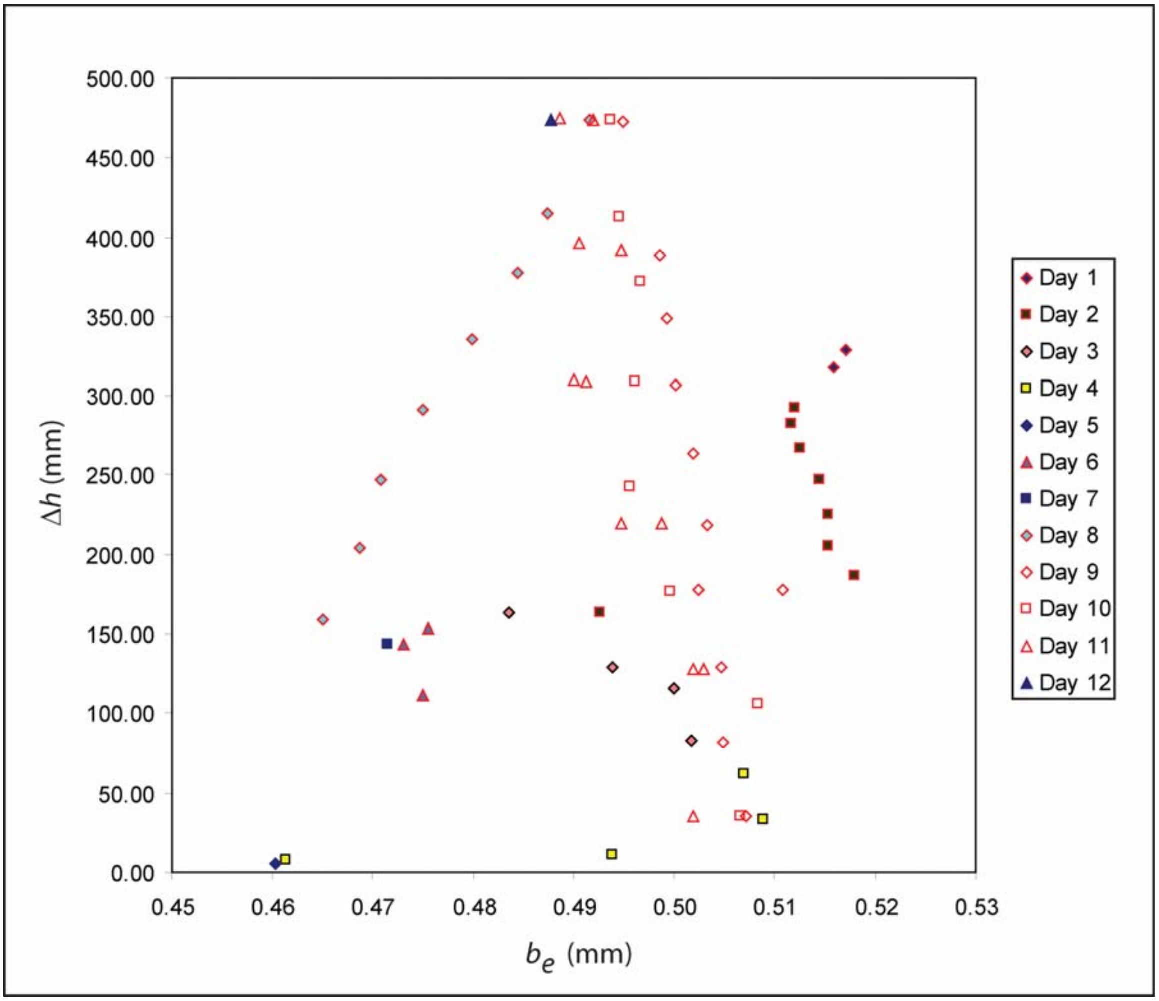

Figure 3.18 Variation in hydraulic aperture for Paintbrush Tuff sample by day of flow testing. Ideally, in the laminar flow regime b_e would be insensitive to the change in head across the sample. Days 1,2,6, and 9–11 exhibit relatively insensitive behavior in b_e with change in head among flow tests. Days 3 and 4 show considerable variation in b_e with little change in Δh. The flow tests from Day 8 seem to support the hypothesis of compression of a discontinuous gas phase increasing b_e with increasing Δh.

with respect to fluid and rock chemistry as no gas presented at the manometer ports and b_e stabilized with variation in Δh to a mean value of 0.50mm.

An additional source of uncertainty for this fracture sample lies in measuring discharge. I calibrated a bucket with a diameter that varied with height for use with total discharges up to 20L. Figure 3.19 shows the heights of water in the bucket at full liter intervals along with the extrapolated curve that could be used for intermediate volumes. The purpose of using volume targets in the multiple liter range for this sample is to reduce the effect of error attributable to measurement accuracy. A number of measurements went into creation of the curve in Figure 3.19, however. Each water height measurement is independent of the others, so a 1mm error range that incorporates actual measurement reading and deviation of the scale from vertical. The one liter increments were subject to the same error as is the flow test procedure regarding volume measurements. Establishment of the one liter benchmark consisted of filling a 250ml graduated cylinder four times (with drying cycle included). This yields a maximum error associated with each liter increment of 4ml and an error range for the full 20L of 80ml or 0.4%. While these errors are minimal with respect to the calculation of hydraulic aperture, they could contribute to the scatter present in the data.

The question of competing nonlinear effects resulting in a smoothed curve is more appropriately addressed in Chapter 5 with results from numeric modeling. As to whether increasing scale relates to an increase in the hydraulic gradient at which a nonlinear trend emerges, the data from previous samples suggest this is not the case. The Oatman Creek sample, smallest of those flow tested, behaved linearly up to a gradient of 0.85, while the Santana Tuff samples both showed a nonlinear trend at gradients exceeding 0.5.

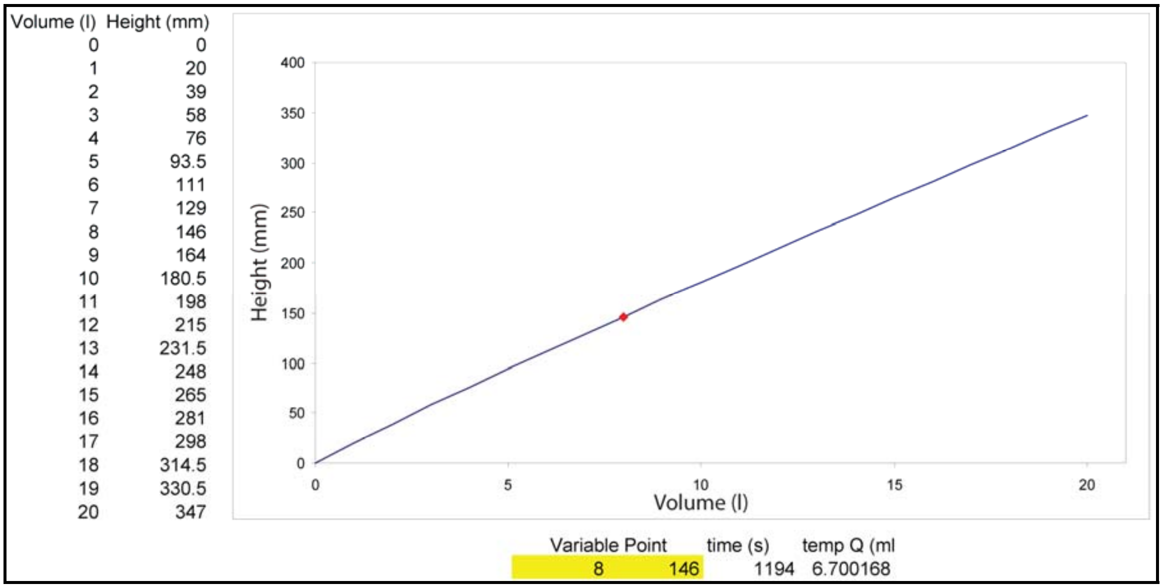

Volume (l)	Height (mm)
0	0
1	20
2	39
3	58
4	76
5	93.5
6	111
7	129
8	146
9	164
10	180.5
11	198
12	215
13	231.5
14	248
15	265
16	281
17	298
18	314.5
19	330.5
20	347

Variable Point		time (s)	temp Q (ml
8	146	1194	6.700168

Figure 3.19 Water height/Volume curve for calibrated discharge bucket used during Paintbrush Tuff fracture sample flow testing. A single point is added that can be used to convert water height to volume at interstitial height measurements. I also included a discharge calculation to spot check the accuracy of the calibration and the measurement procedure during long time duration flow tests.

4 DIGITAL REPRESENTATIONS

Pairing physically derived experimental data to a numeric model requires an accurate representation of the fracture boundaries. Accuracy is required not only in the method used to define the top and bottom surfaces of a sample, but it is also imperative to register the two surfaces as they were configured for the physical flow test. A slight alignment change, due to offset or rotation of one surface relative to the other away from the best fit configuration used for flow testing, results in dramatic changes to the resulting fracture volume. The need for non-destructive acquisition of fracture surface data in flow test configuration motivated the use of computed tomography to transform the physical samples into digital arrays of surface elevations. The registration issue was learned, and serves as a warning to researchers of the difficulties inherent in fitting regularly gridded data sets scanned separately.

4.1 Computed Tomography

The High Resolution X-ray CT Facility at The University of Texas operates a custom built tandem scanner by Bio-Imaging Research Inc. capable of 10μm resolution. For the purposes of this study, the field of view divided by 512 detectors, or 1024 depending on configuration, defines the horizontal resolution, while the vertical spacing is set to 0.25mm. Output from the CT scanner consists of a sinogram (Figure 4.1) depicting the density differences of the sampled material through a continuous 360^{o} cycle for each vertical increment. This configuration for this type of data collection is depicted in Figure 4.2. Each sinogram is reconstructed to produce a 512 or 1024 pixel diameter 2D slice of grayscale values representing average density of the voxel, or incremental

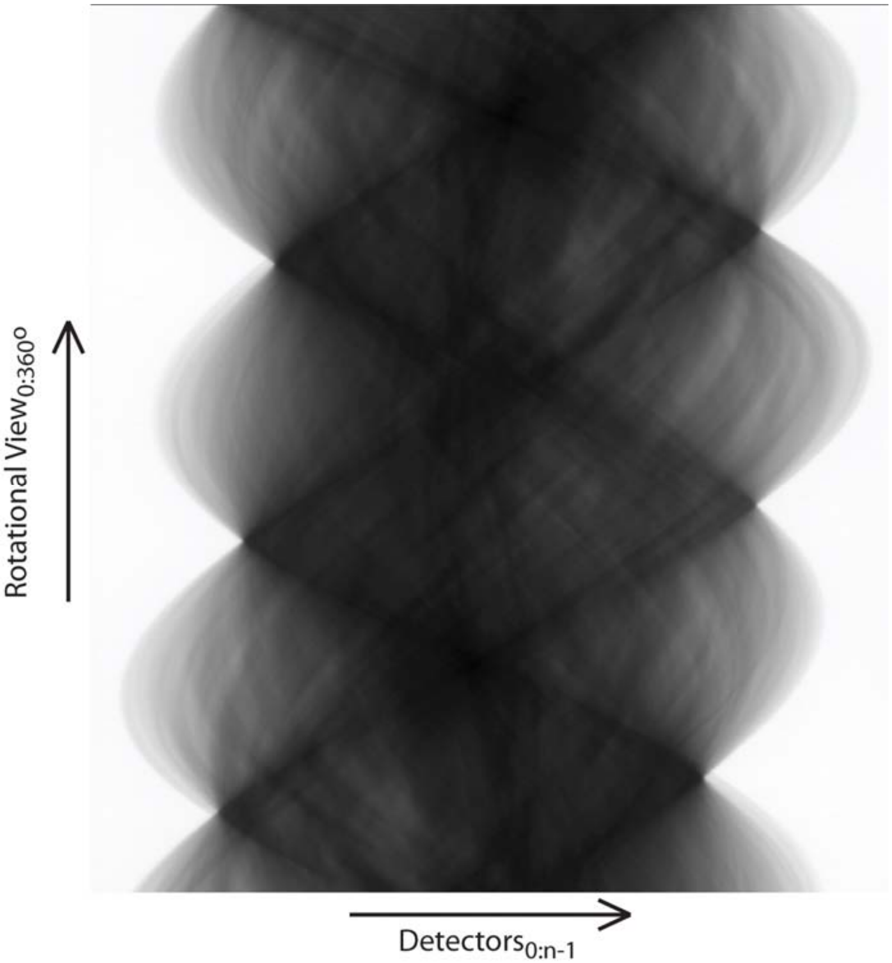

Figure 4.1 Sinogram of one slice of a small cube of migmatite. Color indicates apparent density at the detector array (horizontal axis). Before processing, dark colors represent dense material, white corresponds to air. Views are taken as the sample rotates. Distinct views are plotted on the vertical axis.

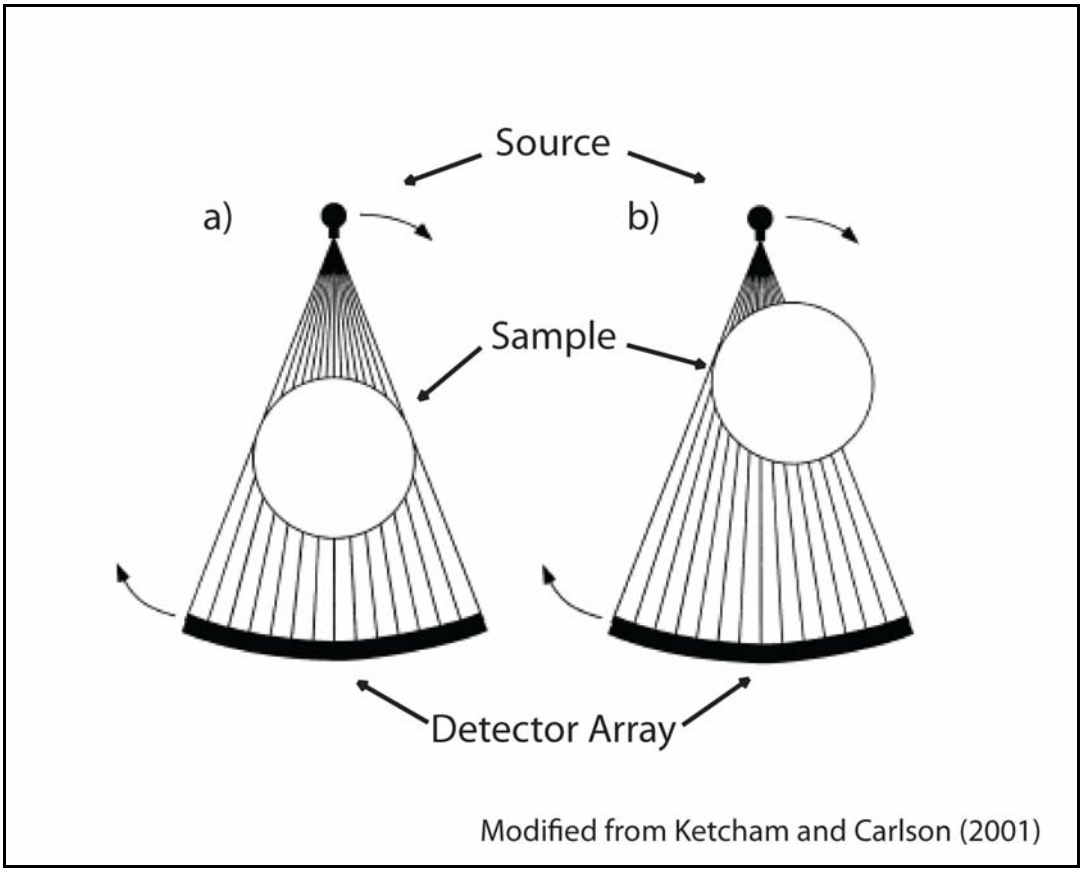

Figure 4.2 Computed tomography scanning configuration consists of a fan x-ray source that either fully encompasses the sample (a), or is offset from the sample (b). In either case high energy x-ray attenuation through the sample referenced to position over a full revolution of the sample or the source/detector array pair is to a first order a linear function of density.

unit of volume, through the sample (Figure 4.3). This averaging of density at the scale of a voxel is an advantage of CT imagery over mechanical measurements; though each voxel is singularly valued, it is weighted by the extremes of the continuous volume sampled.

While data from the scans of single surfaces are straightforward, there are considerations necessary to acquire the desired data from paired surfaces. Here I detail the differences in the configurations of the mated fracture samples as they were prepared for scanning.

The Oatman Creek Granite sample from Thompson (2005) was scanned in its sample holder (Figure 3.5) in a horizontal orientation. The adjustable aperture was backed off from the flow configuration to a nominal 1mm separation. Also, the vertical offset between slices is 0.2mm as opposed to 0.25mm for all other scans. The resulting 32 slices depict the rock and air spatial variation in the plane of the fracture (e.g. Figure 4.4).

Santana Tuff fracture sample CC02-1 is pictured in Figure 4.5 as it was prior to scanning. After processing the CT raw data, the entry to the fracture is digitized in Figure 4.6. From this figure, it is apparent that the two halves of the fracture are not oriented in exactly the same manner; the space between top and bottom surfaces is greater on the left side than on the right. Further, there is a subtle hint from this slice that were the two halves to come together, the top half would settle to the left. This configuration has deleterious effects on modeling considerations. Differing orientation of the two halves results in slightly different spacing in the mean surface plane of the top and bottom surfaces. Meaning, for an arbitrary point on the bottom surface $z(x)$, the

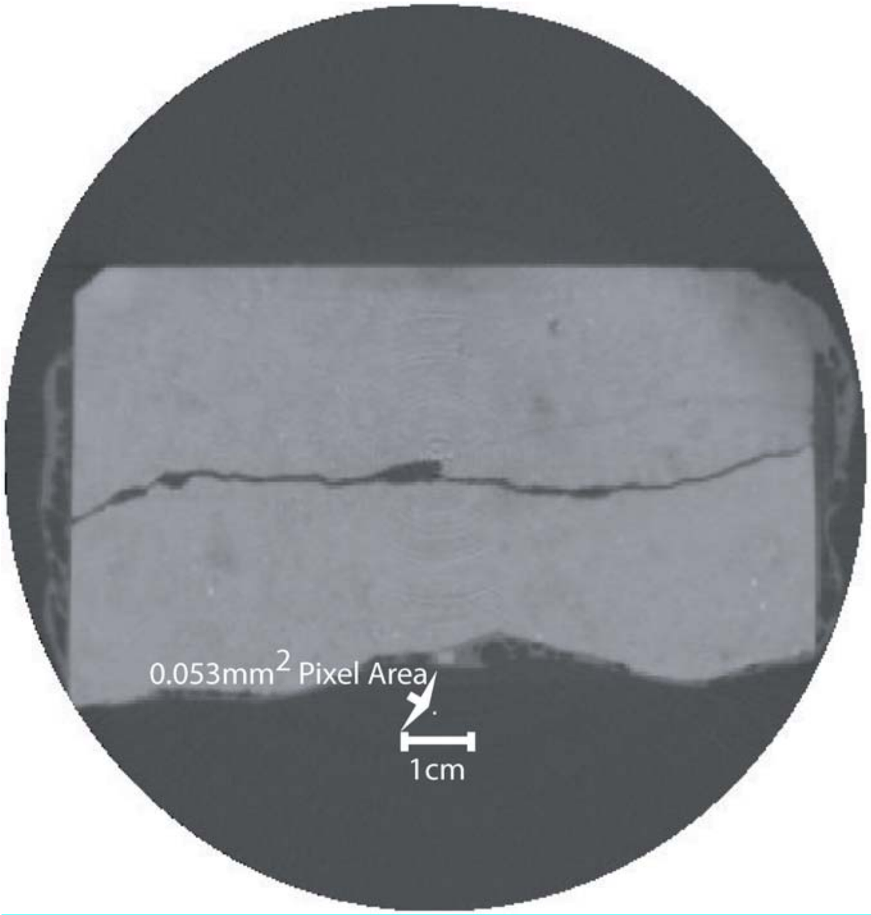

Figure 4.3 One 512 pixel diameter CT slice of fracture sample CC02-2. The fracture surfaces made up of 603 of these slices are defined by 0.23mm spaced elevations for this sample.

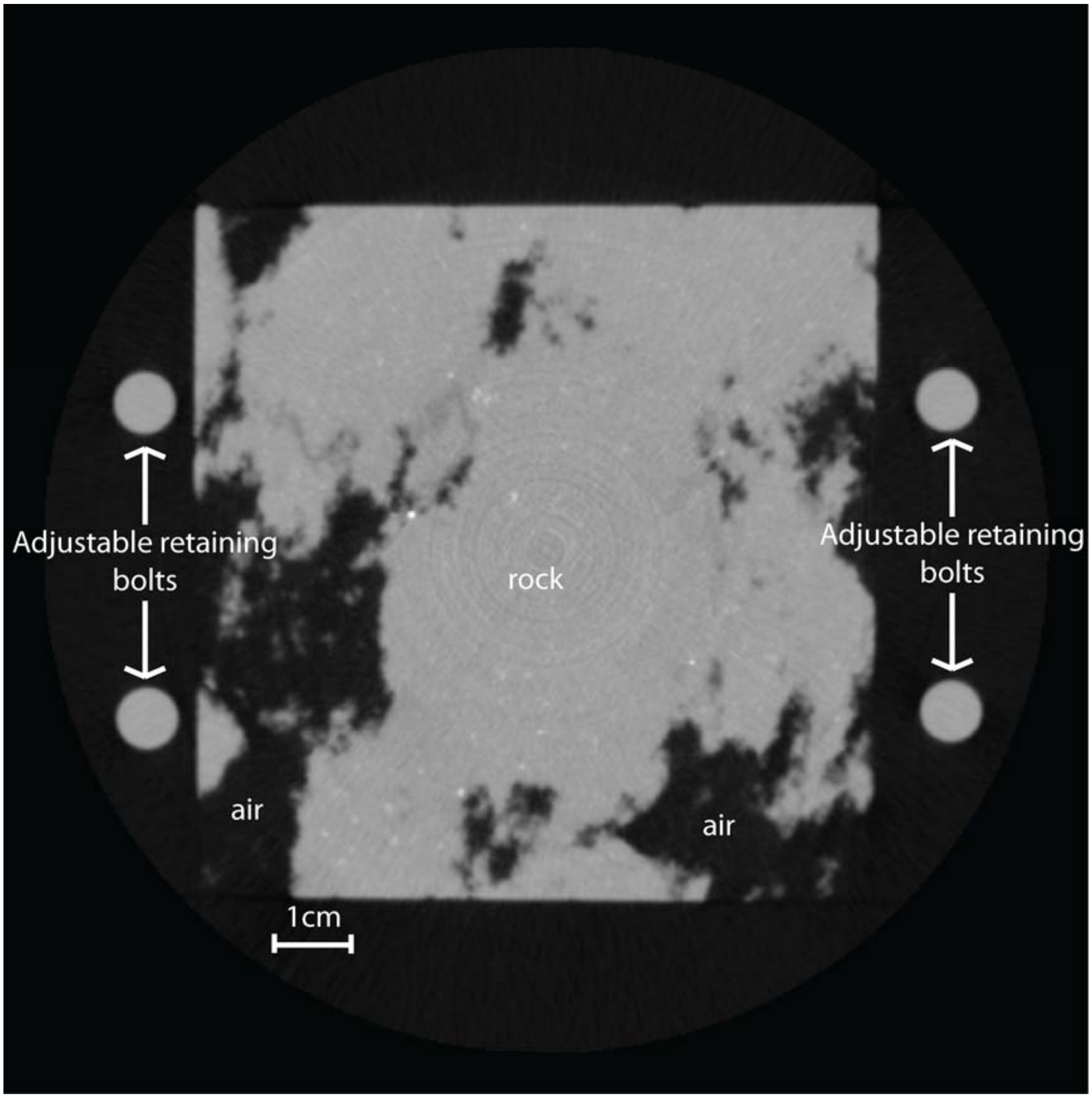

Figure 4.4 Horizontal CT slice through Oatman Creek Granite fracture sample. The adjustable retaining bolts can be seen outside the rectangle of the actual sample. The variation between black and gray represents the spatial arrangement of air and rock in the plane of the fracture at this particular relative elevation.

Figure 4.5 Santana Tuff fracture sample CC02-1 as prepared for scanning.

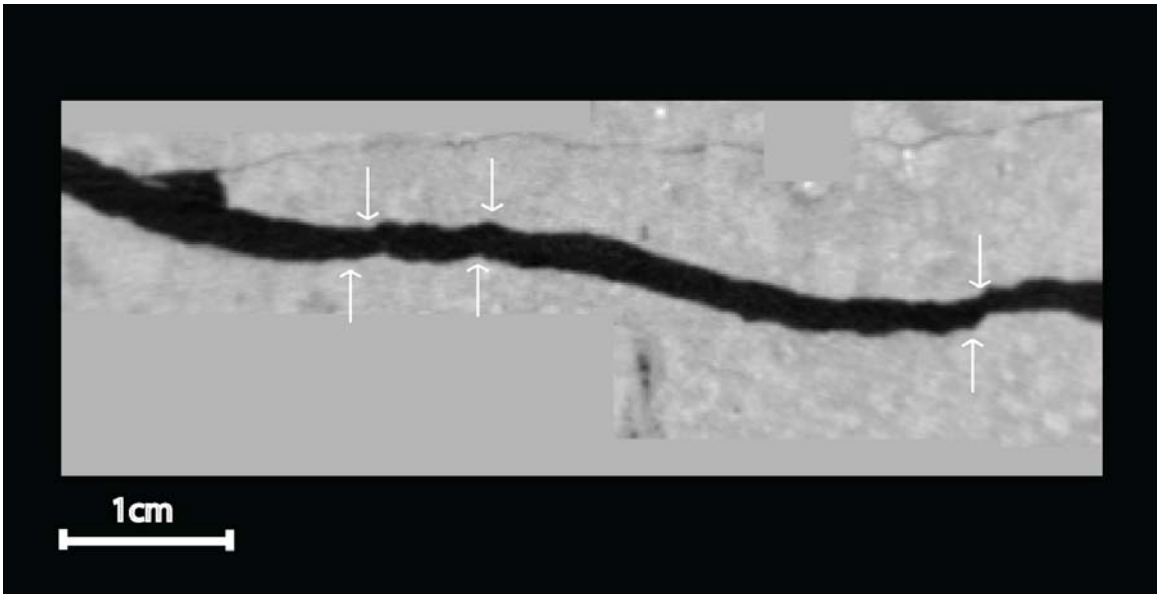

Figure 4.6 CC02-1 fracture entry slice resulting from CT imagery. Notice the subtle mismatch between the surfaces (e.g. as referenced by the white arrows), also the arbitrary spacing between the right and left edges.

corresponding point on the top surface is defined at some intermediate horizontal location $z(x+x\cdot\delta x)$, where $|\delta x|<\Delta x$. Any offset, whether lateral or rotational, between the two fracture halves promotes bridging of the fracture opening, increasing any measure of aperture, and artificially creating the need for a friction correction factor to match physical data.

Unfortunately, the lesson of scanning fractures in the same configuration as flow test conditions was not learned before the scan of CC02-2. However, the results of the first scan compared to a second scan with the sample in the flow test configuration more dramatically illustrate the problem. In Figure 4.7, the first and last slice of each scan is manipulated to show the difficulties in reconciling the unregistered scan to the actual fracture volume. Let $S_{top}(x,y,z)$ and $S_{bot}(x,y,z)$ represent a set of top and bottom fracture surfaces. In general terms, six shifts are necessary to reproduce a best fit fracture from an unregistered scan:

$$S_{top}\left(x,y,z\right)\leftarrow S_{top}\left(x,y,z+y\cdot\sin\phi\right), \tag{4.1}$$

where ϕ is the angular difference between the two halves in the yz plane;

$$S_{top}\left(x,y,z\right)\leftarrow S_{top}\left(x+y\cdot\sin\gamma,y,z\right), \tag{4.2}$$

where γ is the angular rotation in the xy plane necessary to match the two halves;

$$S_{top}\left(x,y,z\right)\leftarrow S_{top}\left(x,y,z+x\cdot\sin\theta\right), \tag{4.3}$$

where θ is the angular rotation in the xz plane necessary to match the two halves;

$$S_{top}\left(x,y,z\right)\leftarrow S_{top}\left(x+\alpha,y,z\right), \tag{4.4}$$

where α is the horizontal offset;

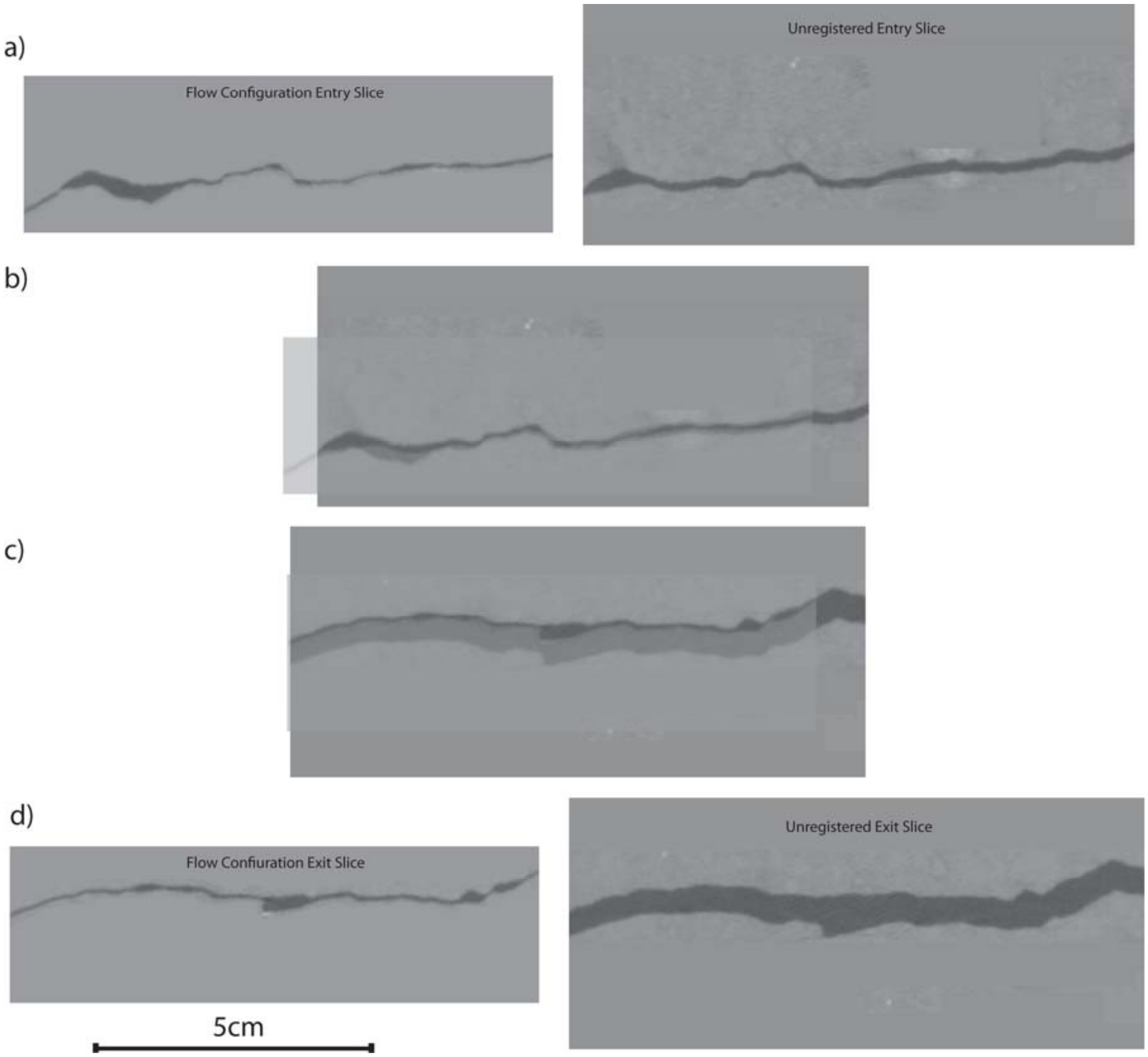

Figure 4.7 Comparison of CT scans of Santana Tuff fracture sample CC02-2. a) Entry slice of fracture. The actual flow configuration is on the left, the results from an unregistered scan are on the right. b) Entry slices from the two scans overlaid. c) The exit slices overlaid. Notice the counter clockwise rotation in the direction of flow and the plane of the fracture of the unregistered data in relation to the flow configuration; also, the obvious widening of the apparent aperture down the fracture. These effects are due to failure to preserve an orthogonal set of reference planes for the two fracture halves during the unregistered CT scanning process. d) Exit slice of the fracture. Again, the actual flow test configuration is on the left and results of the first scan on the right. Notice the views of the bottom surface of the exit slice do not match. This results from the accumulation of 600*δx from the entry to exit slice.

$$S_{top}\left(x,y,z\right) \leftarrow S_{top}\left(x,y+\beta,z\right), \qquad (4.5)$$

where β is the vertical offset; and

$$S_{top}\left(x,y,z\right) \leftarrow S_{top}\left(x,y,z+\zeta\right), \qquad (4.6)$$

where ζ is the residual separation between the two surfaces.

Equations 4.1 through 4.5 are all subject to the spacing bias as described, promoting an increase in the apparent aperture due to slight mismatches between corresponding gridded points on the surfaces. Error associated with Equation 4.6 is due to the surface picking algorithm and the volume averaging inherent in CT imagery. Since *z* values are elevations at exact points, there is no issue of spacing because of a shift. CT scans of the Paintbrush Tuff sample and future samples use the best fit configuration.

4.2 Data Processing

The computed tomography data output from the HRXCT facility is processed further according to specific need. The tuffs used in this study contain a number of voids within the rock volume that are not connected and did not participate in flow during the flow test experiment (Figure 4.8). These were masked systematically in a number of ways throughout the course of the study. The top and bottom surfaces were picked using an evolving algorithm designed to be accurate to approximately 1/10 of a voxel width. Finally, for the cases where the fracture sample was scanned unregistered, I implemented an algorithm to produce a best fit data set for comparison purposes.

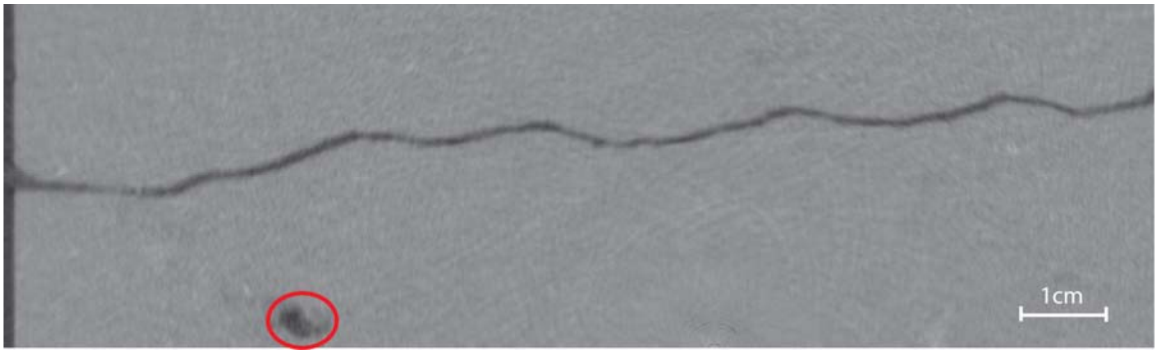

Figure 4.8 Processed CT data from half of Paintbrush Tuff sample. The void circled can defeat the surface picking algorithm and is masked in the final data set.

4.2.1 Masking voids

For CC02-1, I first masked obvious voids with rectangular areas of a grayscale value similar to the host rock using ImageJ, an open source image processing program (Rasband 2006 and Figure 4.9). Even with the ability to repeat actions automatically, this became tedious. Then, after running the first iteration of the surface picking algorithm produced a number of anomalous surface elevations, I returned to ImageJ to mask those as well.

For the raw CT data from fracture sample CC02-2, I used a feature of ImageJ that allows definition of a polygon using an arbitrary number of points to mask the entire rock volume except for a strip just beyond the actual fracture volume as seen on the flow configuration slices in Figure 4.7. This procedure still demanded visual inspection of each slice, but one time through eliminated all extraneous voids.

The CT data from the Paintbrush Tuff sample contained additional anomalies. The copper manometer ports in the top surface and the anchor bolts used to hold the bracket securing the inlet and outlet reservoirs to the fracture sample deflect beam energy, leaving areas within the matrix with apparent zero density as well as leaving linear features that would be considered air by the surface picking algorithm (Figure 4.10). As there are also a great deal of voids in this tuff, over 5000 slices must be inspected and masked appropriately prior to defining the fracture volume. This led to development of an IDL routine that interrogates the data set for anomalous minimum values, provides a user interface to deal with only the anomalies, and provides feedback

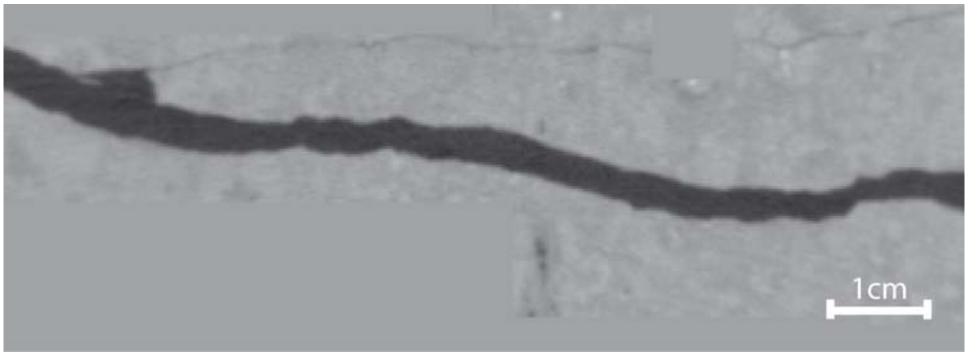

Figure 4.9 Masking of fracture sample CC02-1 entry slice.

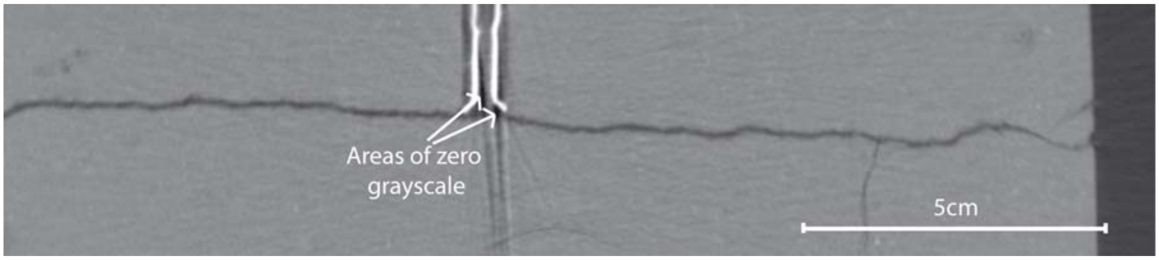

Figure 4.10 Anomalous areas in CT image of Paintbrush Tuff fracture sample (left side) due to copper manometer port. Linear features have apparent reduced density and would be considered part of the fracture by the surface picking algorithm if not masked.

to ensure that the changes requested by the user addressed the anomaly correctly. The user guide for the algorithm *AutoMaskStack.pro* is provided in Appendix B.6.

4.2.2 Surface picking algorithm

The algorithm used to define a fracture volume from a 3D data set of grayscale values has evolved over the course of this study. A data set of CT values is arranged as depicted in Figure 4.11. For each xz slice, there are 0 to $x_{\max}$-1 lines of 0 to $z_{\max}$-1 grayscale values. The preprocessing of the data set to mask anomalous areas ensures that the minimum grayscale value of each line occurs within the fracture. The general sequence of steps for the algorithm is then to begin at the minimum value of each line and traverse to the first pixel that crosses the air-rock boundary up and down from that minimum, and then to calculate the actual position of the interface within those boundary pixels. The values returned from the algorithm include 2D arrays of z elevations of the top and bottom surfaces and an aperture array.

For the data sets from the CT scans of the Oatman Creek Granite fracture sample and the unregistered surfaces of fracture samples CC02-1 and the first scan of CC02-2, the guarantee that at least one pixel in each line contained a grayscale value equivalent to all air is the necessary condition for accurate placement of the top and bottom fracture surfaces using the initial surface picking algorithm. Scans of fracture samples in a best fit configuration have points of contact and lines where the minimum value is well above that of all air due to the volume averaging effect of CT imagery (Ketcham et al. submitted 2009). To accommodate this, I use a missing attenuation algorithm to integrate

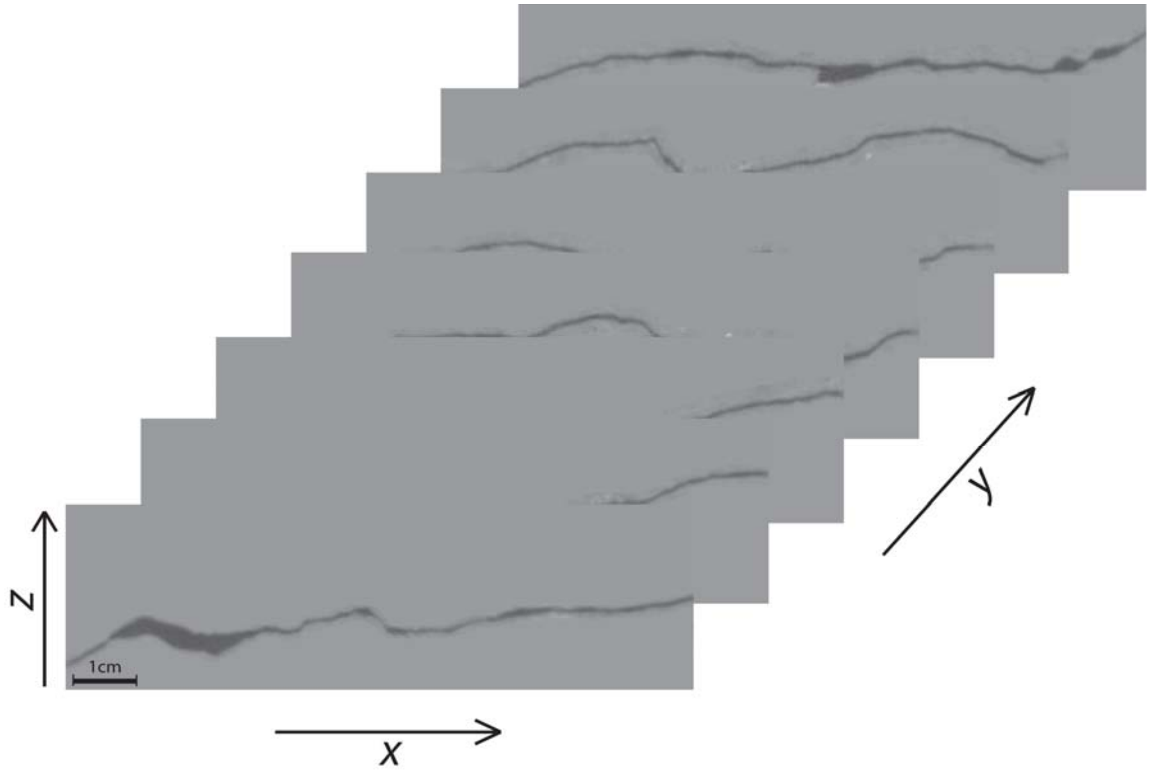

Figure 4.11 Orientation of the 3D axes as discussed in text regarding CT data sets.

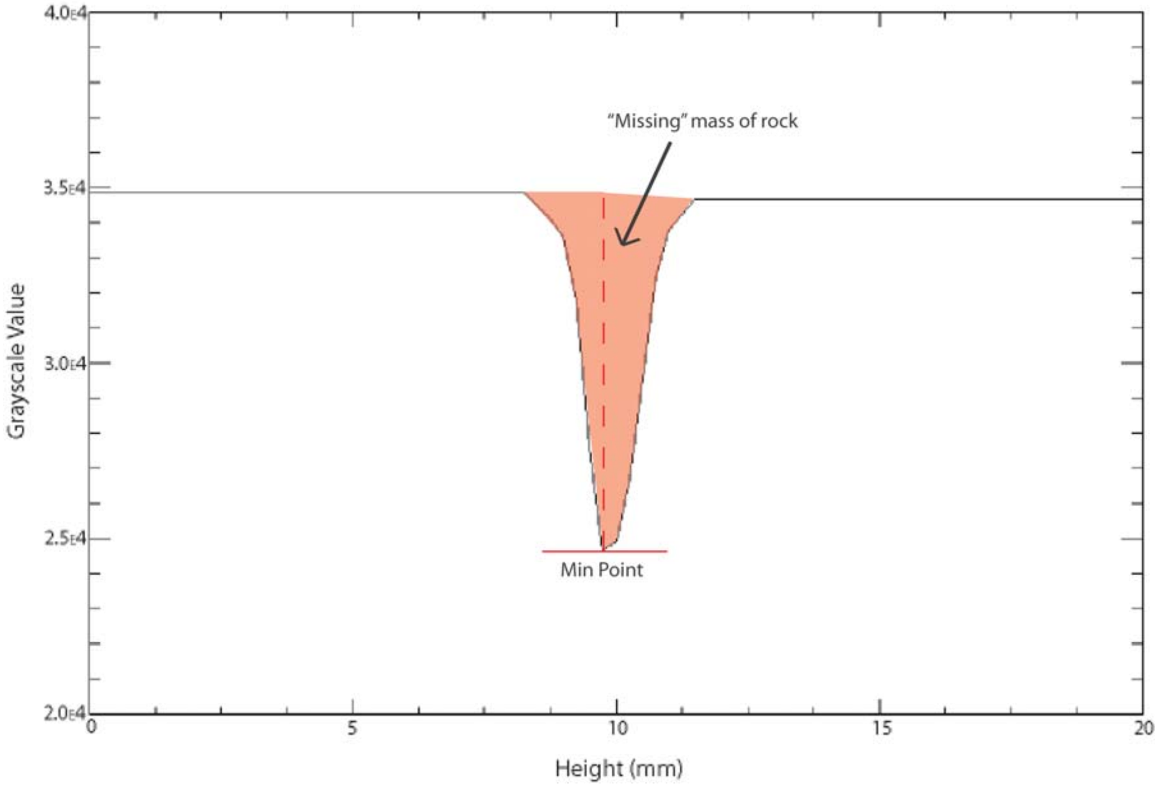

Figure 4.12 Missing attenuation method of calculating aperture. The value for rock at either side of the fracture is variable and defined as the grayscale value of the pixel immediately distal of the first pixel with a grayscale value greater than that of the average of all air and all rock on the traverse from the minimum. Therefore, in practice, the integration of Equation 1.19 is carried out on the two half apertures defined from the minimum grayscale value within the fracture to these end points.

the volume of rock "missing" from the fracture (Figure 4.12). The generalized solution for aperture then becomes:

$$b = \int_{z=\min(f(z)<all\_rock)-1}^{z=\max(f(z)<all\_rock)+1} \frac{all\_rock - f(z)}{all\_rock - all\_air} dz, \tag{4.7}$$

where z is a position on each line of CT values within the fracture, and $f(z)$ is the grayscale value at that position. This requires only that the grayscale value at the boundary of the fracture is greater than the average of the grayscale values of all air and all rock. The full algorithm *GetVertCrackOptimize.pro* with usage information is provided in Appendix B.1.

4.2.3 Best fit algorithm

Where in a continuous sense, best fit refers to a condition of maximum shear strength, discrete sampling of the surfaces onto regular grids constrains the possibilities to a weaker condition. Assuming the surfaces are approximately aligned, I define a digital best fit as three points of contact and a local minimum arithmetic mean aperture.

The recursive IDL function *FitSurface.pro*, transcribed in Appendix B.4, takes non-overlapping top and bottom surfaces, described by 2D arrays of elevation values, and computes the best fit registration. It utilizes my algorithm *BestFit.pro* (Appendix B.5), which removes a wedge from an upper surface yielding three contact points, each in a different quadrant of the 2D grid (Figure 4.13). It then shifts the top surface relative to the bottom surface in a one pixel "radius" square searching for a better fit with the b_a metric. Once a minimum is found, the search is repeated with a doubled data set, then a tripled data set, before returning the path corresponding to the minimum mean apertures.

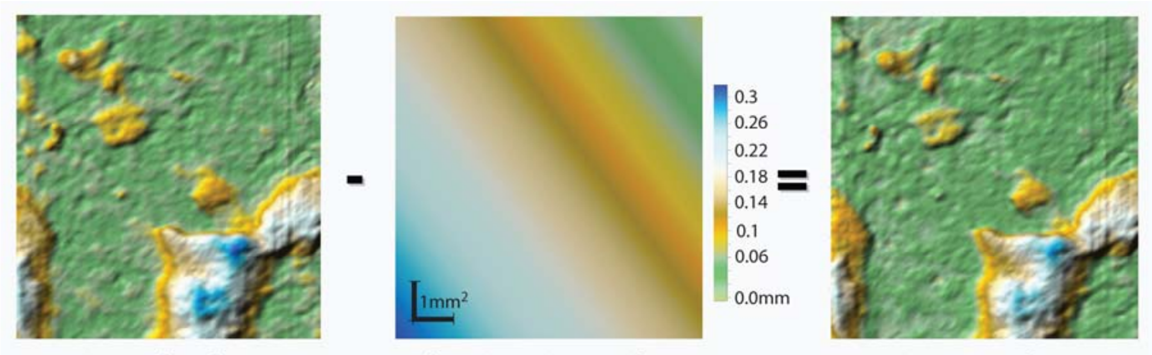

Original Surface Three Point Best Fit Plane Best Fit Surface

Figure 4.13 Example of best fit procedure. Three points of contact, each in a different quadrant of the underlying grid, define a plane, that when subtracted from the top surface of an unregistered pair, yields a mated pair with no overlap and minimized arithmetic mean aperture.

While the best fit algorithm is a novel exercise, and useful in the discussion of scaling issues by defining best fit subsets of an already registered pair of surfaces, the results of this digital manipulation of unregistered data sets do not achieve the desired result of a match in statistics to the registered surfaces (Table 4.1). The two fracture samples that were scanned in the flow test configuration approximate the hydraulic aperture from their respective flow tests reasonably well. There is an issue with the Oatman Creek Granite fracture sample, however. Thompson (2005) discusses aperture values below his nominal setting, whether it be 1.0mm for CT imagery or 0.5mm for flow testing, as aberration; he expected that the nominal separation was from a closed position at the lateral edges of the sample. In that case, my best fit algorithm sets the mean aperture on the edges coincidentally to 0.5mm with three interior points of contact, and the resultant arithmetic mean aperture of 0.61mm reasonably correlates to hydraulic aperture. If, on the other hand, the nominal separation adds 0.5mm to the apparent aperture at point of contact, no central tendency measurement on the resulting aperture field predicts actual discharge through the sample. Based on visual estimation of the separation of the sample surfaces in its current state, I accept the former premise that the 0.5mm opening of the fracture using the adjustment screws started from a closed position at those adjustment points.

Table 4.1 Comparison of the results of using best fit apertures to apertures derived from registered surfaces for estimating hydraulic aperture. Again, b_a is the arithmetic mean aperture and b_e is the hydraulic aperture calculated from Equation 3.2. Thompson (2005) reported a nominal separation of the two halves of his Oatman Creek Granite fracture sample of 0.5mm, yet a best fit solution of the CT data for this sample yields a 0.5mm mean separation of the lateral boundaries (the three points of contact are off the edges).

Specimen	b_a (mm)	Reported b_a (mm)	Best Fit b_a (mm)	b_e (mm)
Oatman	0.61	0.5*	0.41	0.54
CC02-1	——	——	1.05	0.31
CC02-2	——	——	1.33	0.53
CC02-2a	0.63	——	0.63	0.53

5 MODELING

The purpose of this study is to offer insight into effectively predicting physical flow through fractured media from limited data. Of course, prediction of fluid flow often involves some form of discrete modeling. In this chapter, I discuss the building of 2D MODFLOW models representing the 3D fracture volume of the Oatman Creek Granite fracture sample and both Santana Tuff samples using data described in Table 5.1, the results of Cardenas et al. (2007) 2D full Navier-Stokes solution to flow on one longitudinal profile of CC02-2, and the effect of spatial distribution of high transmissivity zones on discharge and channeling.

5.1 MODFLOW

The aperture and boundary data used in this study consist of regularly gridded, discrete data points. The simplest and likely most widely accepted choice for a model is the finite difference model MODFLOW made available through the U.S. Geological Survey. MODFLOW is a framework that uses one of several solvers to develop a hydraulic head field iteratively for a user defined domain. There are also a number of MODFLOW packages that allow a multitude of flow and transport problems to be explored. Details of the program, its packages, and input requirements can be found in Harbaugh et al. (2000). For modeling flow in a fracture, the head field provides sufficient data to quantify discharge and identify preferential channel charateristics. I used MFI Version 1.1 to generate the input files necessary to run the Preconditioned Conjugate Gradient (PCG) solver in MODFLOW-2000 Version 1.18.01. All input files are generated in IDL using scripts described in Appendix B.

Table 5.1 Spacing and areas from computed tomography data for the samples flow tested. The reported pixels width for YM includes area of zero aperture between the two subsets of the whole fracture data as explained in the text.

Sample Name	Δx,Δz (mm)	Δy (mm)	Pixels Wide	Pixels Long	Sample Area (cm^2)
Oatman	0.25	0.2	240	350	42.00
CC02-1	0.27	0.25	360	488	119.24
CC02-2	0.24	0.25	401	603	141.68
YM	0.23	0.25	1370*	2529	1987.82

Let C_0 be a square cell with four facing cells, C_1 through C_4, as arranged in Figure 5.1. Let properties between the facing cells and C_0 be defined in terms of the participating facing cell (X_1 through X_4). Transmissivity is defined as the flux per unit width per unit gradient for a saturated thickness:

$$T = Kb. \tag{5.1}$$

Where the experimental fracture has no flow boundaries at the top and bottom surfaces, the saturated thickness is the aperture. Using Darcy's Law (Equation 1.5):

$$Q_1 = T_1 \cdot \Delta y \cdot \frac{h_0 - h_1}{\Delta x}, \tag{5.2}$$

$$Q_2 = T_2 \cdot \Delta x \cdot \frac{h_0 - h_2}{\Delta y}, \tag{5.3}$$

$$Q_3 = T_3 \cdot \Delta y \cdot \frac{h_0 - h_3}{\Delta x}, \tag{5.4}$$

$$Q_4 = T_4 \cdot \Delta x \cdot \frac{h_0 - h_4}{\Delta y}. \tag{5.5}$$

Conservation of mass for an incompressible fluid under steady state conditions requires:

$$Q_1 + Q_2 + Q_3 + Q_4 = 0. \tag{5.6}$$

For an isotropic medium, and with Δx equal to Δy, solving for h_0 yields:

$$h_0 = \frac{h_1 + h_2 + h_3 + h_4}{4}. \tag{5.7}$$

The conceptual model for an open fracture with no flow boundaries laterally, top and bottom, using variable aperture as a proxy for one of the hydraulic properties necessary to solve the flow equation in MODFLOW is illustrated in Figure 5.2. Let T_i be the transmissivity in cell *i,* T_j be the transmissivity in cell *j*, and T_{ij} be the transmissivity between cells *i* and j. Then under confined conditions, MODFLOW uses the harmonic mean of the transmissivities of the two adjacent cells:

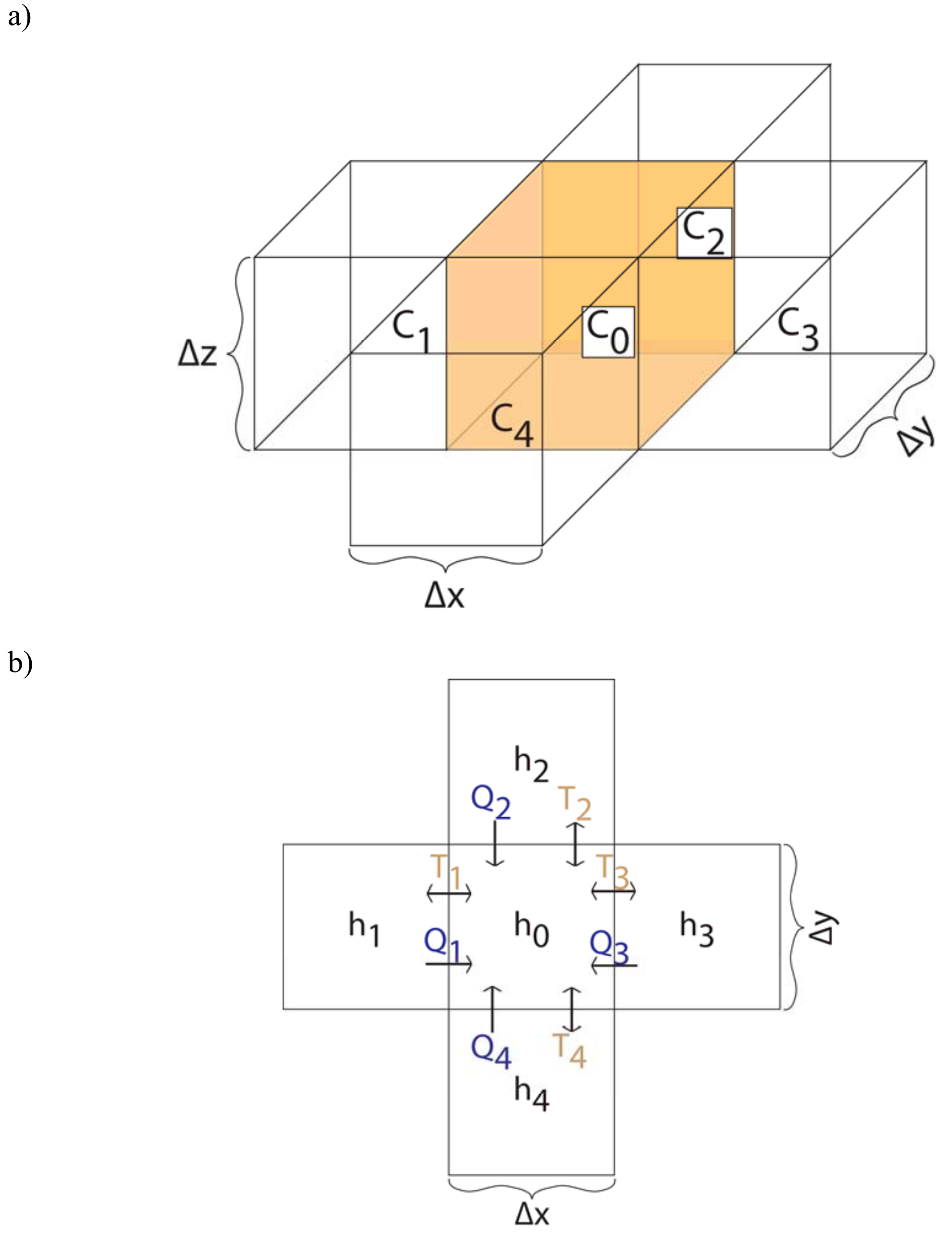

Figure 5.1 a) One layer of model cells. Solving for head in C_0 is possible using Darcy's Law and transmissivity values for all cells. b) Net discharge into cell 0 from C_1–C_4 necessarily must be zero for an incompressible fluid under steady state conditions. Head values for all cells are solved iteratively until a threshold minimum change in value is reached.

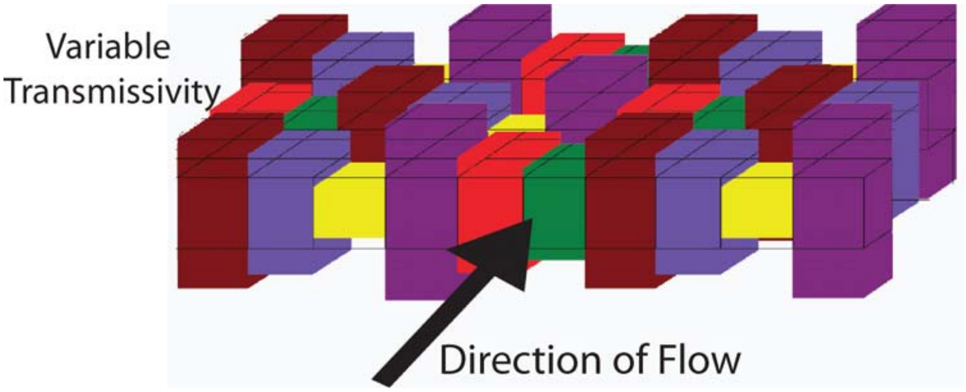

Figure 5.2 Cartoon representing discrete variability in the hydraulic properties of a modeled fracture.

$$T_{ij} = \frac{T_i \cdot T_j}{T_i + T_j}, \tag{5.8}$$

to solve the flow equation for flux between the two cells. Further, there is no requirement that Δx and Δy be equal. In this case, a more complicated solution for h_0 is:

$$h_0 = \frac{\frac{\Delta x}{\Delta y}\cdot(T_2+T_4)(h_2+h_4)+\frac{\Delta y}{\Delta x}\cdot(T_1+T_3)(h_1+h_3)}{2\left(\frac{\Delta x}{\Delta y}\cdot(T_2+T_4)+\frac{\Delta y}{\Delta x}\cdot(T_1+T_3)\right)}. \tag{5.9}$$

All h_0 are solved iteratively until a user defined threshold in change between iterations is reached. I calibrated the model for CC02-2 at a gradient of 0.08. As a general value for groundwater gradient might be 0.001, I used 1.0E-6cm as a threshold for change in head between iterations to keep error associated with model convergence below 0.1%.

5.1.1 CC02-2

The model for CC02-2 is one layer consisting of 401 rows by 603 columns. The spacing between adjacent rows is 0.024cm. The spacing between adjacent columns is 0.025cm. The model boundaries are defined as constant head in column 1 and column 603. No flow boundaries are assumed in MODFLOW when the edge of the model is reached, so no further distinction is necessary. Layer 1 is defined as a confined unit, and the input parameter *T* is defined for each cell using the discretized aperture data as:

$$T_{ij} = \frac{b_{ij}^3 \cdot \rho_w g}{12\mu}, \tag{5.10}$$

where *i* references the row and *j* references the column of each cell. The resulting transmissivity field is depicted in Figure 5.3. The low background transmissivity is punctuated by highly transmissive zones due to breakage at the time of fracture or

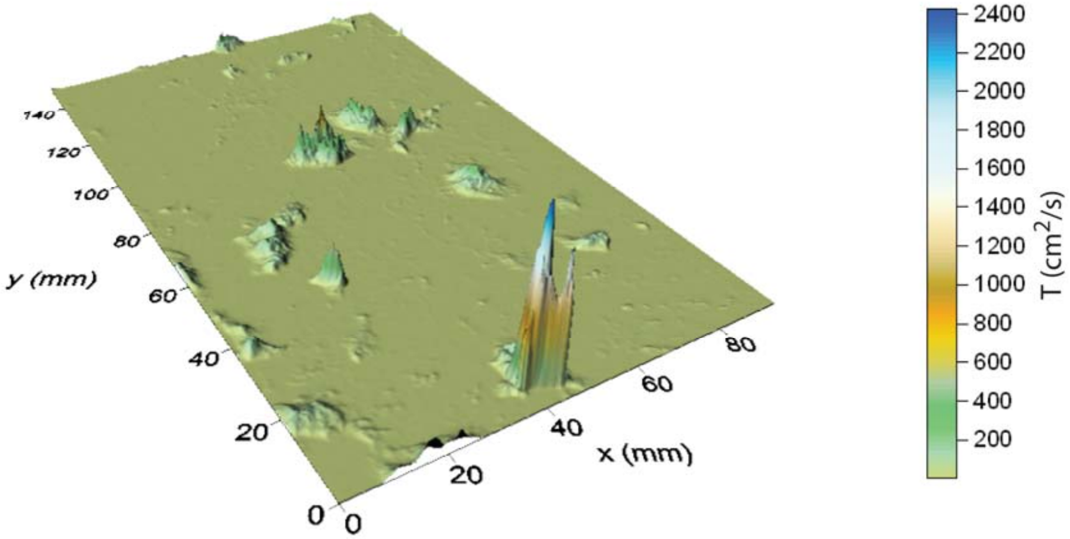

Figure 5.3 Transmissivity field for fracture sample CC02-2. This background relatively low transmissivity punctuated by highly transmissive areas is a common feature of natural surfaces with little offset.

weathering processes. Figure 5.4 shows the model output head data. While there is no obvious correlation between the high transmissivity zones and the head data, one can pick out one or two fast flow paths the may be influenced by the spatial distribution of the high transmissivity zones.

MODPATH is a post processing routine that calculates the travel times and paths of massless particles given MODFLOW model output. Note that MODPATH flow paths calculated for this model are linear; that is, there are no eddy effects, turbulence, or water-rock interactions as discussed in Cardenas et al. (2007). Placing one particle in the first cell of each row and plotting their flow paths, channels become much more apparent (Figure 5.5). Small scale channel formation is evident from zero to 1s elapsed time. It appears that the highest transmissivity zone near the fracture inlet does initiate the major channel through the center of the model, but the late time tailing in the area suggests that its impact is localized. Again, tailing effects present in this model are purely the result of the velocity distribution and not attributable to nonlinear causes.

During the period from 2 to 3s elapsed time, the dominant gradient competes with the cross-fracture channel developed by a linear spatial arrangement of high transmissivity zones. However, the persistence of the channels in shuttling the tailing particles lends credence to the supposition that the channel formation is a true effect and not just an artifact of the model.

Validation of the model lies on the match of model discharge to the empirical data. The flow test experiment achieved a 1.07ml/s discharge for each of three flow tests at gradient of 0.08. The model predicted a discharge of 1.07ml/s with a 0.29%

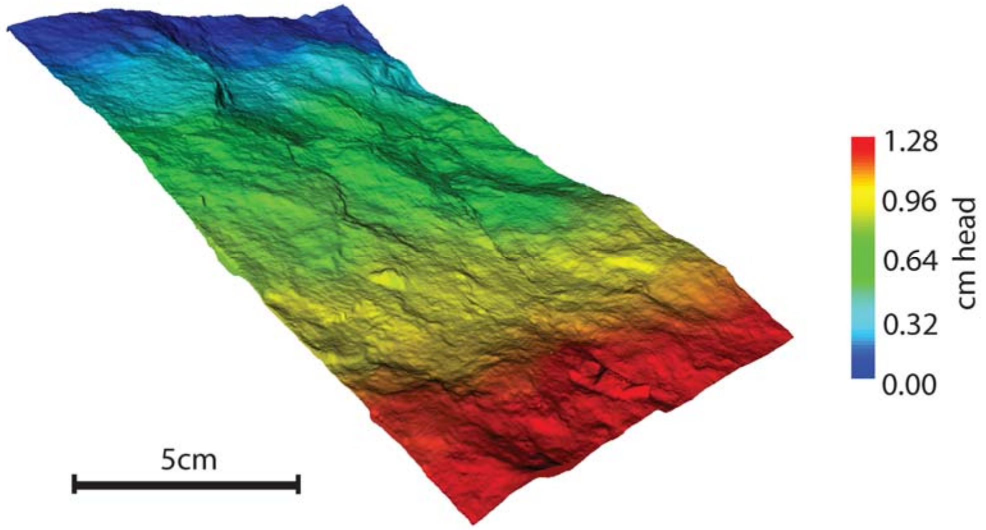

Figure 5.4 Head distribution model output for fracture sample CC02-2 at a gradient of 0.08 from inlet to outlet.

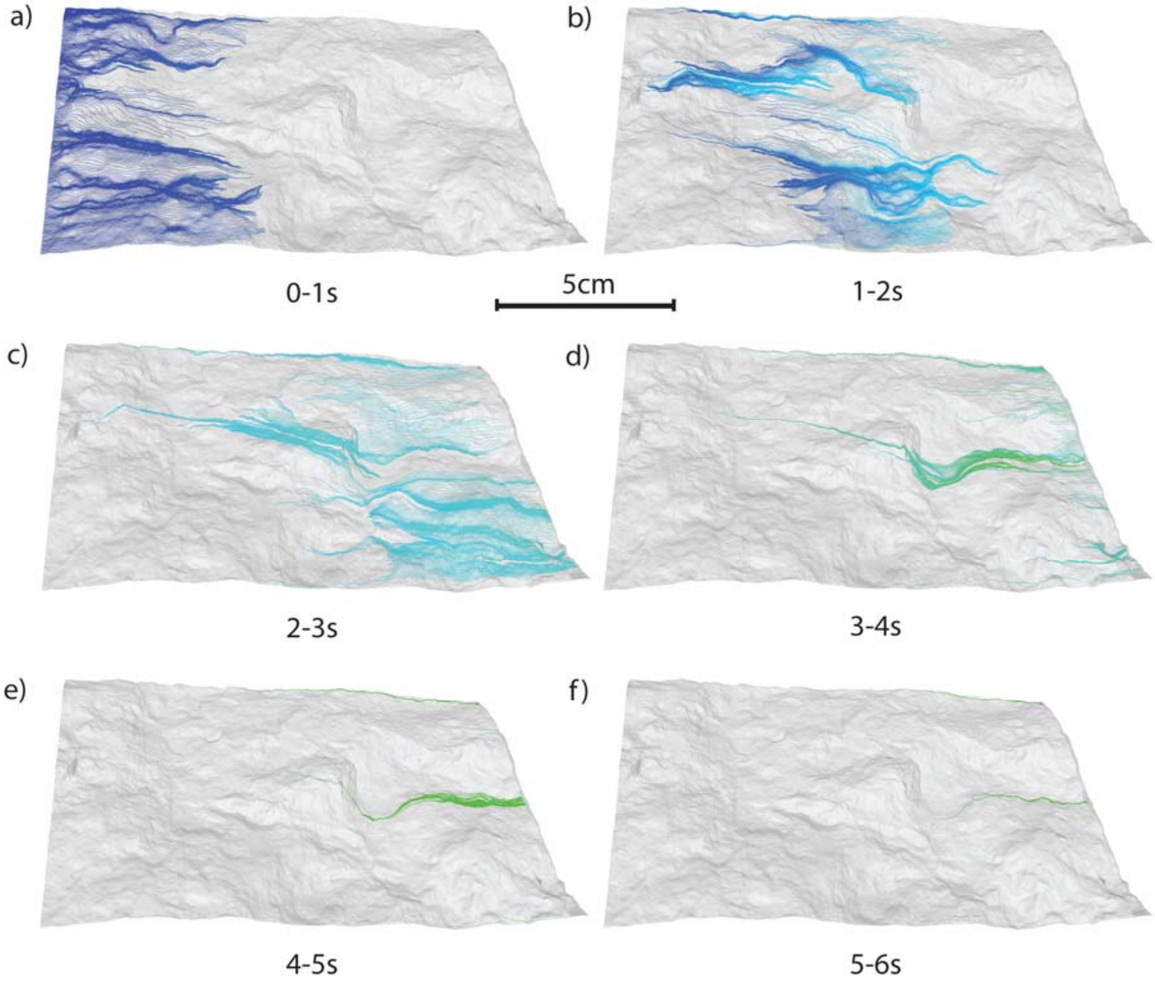

Figure 5.5 Time discretized flow paths of massless particles calculated using MODPATH on the head distribution output from MODFLOW on CC02-2. 401 particles are released at time zero, one in each upgradient cell. From 0 to 1s elapsed time, notice small channel formation. By 2s elapsed time, 3 dominant channels correspond to the spatial arrangement of the high transmissivity zones. Leakage from the high *T* zones in the direction of the dominant gradient can be seen in c). Linear tailing is evident in d) and e) suggesting the channels are persistent. By 6s elapsed time, few straggling particles remain isolated from the channels.

discrepancy. Considering a 2.4% maximum error on the flow test experiment, the model is considered to be representative of the actual flow test conditions. Meaningful calibration of this model is not possible given the single layer, steady state concept.

5.1.2 Oatman Creek Granite

The model for the Oatman Creek Granite sample consists of one layer of 240 rows by 350 columns. Columns 1 and 350 are designated constant head boundaries. The lateral boundaries of row 1 and row 240 are no flow. Spacing is 0.2mm between adjacent columns and 0.25mm between adjacent rows. Transmissivity defined by the best fit aperture using Equation 5.10 populates the MODFLOW flow equation parameter for Layer 1.

Modeled flow using the best fit configuration at full spacing yields a realistic result (Table 5.2). The uncertainty in the separation of the surfaces for the physical flow tests and possible rotation from the flow test configuration to the CT scanning configuration precludes meaningful further calibration of this model.

5.1.3 Unregistered samples

5.1.3.1 CC02-1

The best fit configuration for the first Santana Tuff sample yields an aperture field with an arithmetic mean greater than three times that of the hydraulic aperture. Therefore, the model incorporating this unregistered aperture data grossly overestimates the physical flow test results.

"Best Fit" for this data set results from several shifts and a tripling of the data. To keep the model within the limits of MFI (999 x 999 cells), I reduced the data to the original spacing, which eliminates 6 rows and 10 columns due to shifting. Therefore, the model consists of one layer of 354 rows by 478 columns. Columns 1 and 478 are constant head boundaries. Rows 1 and 354 are no flow boundaries. Spacing is 0.25mm between adjacent columns and 0.27mm between adjacent rows. The gradient is set to 0.15, as the corresponding physical flow tests were performed prior to any degradation of the sample, and therefore represent the conditions the model attempts to reproduce.

Transmissivity is set using the aperture field and Equation 5.10, and populates the block-centered flow package parameter necessary to solve the MODFLOW flow equation. Modeled discharge is 5.1ml/s, an order of magnitude greater than the expected value of 0.66ml/s.

5.1.3.2 CC02-2

The best fit aperture field for Santana Tuff sample CC02-2 has an arithmetic mean of 1.33mm, greater than twice that of the flow configuration, which is achieved with a tripled data set. I implemented a model using both a reduced data set corresponding to the original sampling, and the full tripled best fit data set to verify the concept. The model results are not expected to match the physical flow test data due to the irreproducibility of the physical flow test configuration from unregistered surfaces.

The model of the reduced data set consists of one layer of 398 rows and 618 columns. Columns 1 and 618 are constant head boundaries yielding a gradient of 0.08. Rows 1 and 398 are no flow boundaries. Spacing is 0.25mm between adjacent columns

Table 5.2 Model results compared to the corresponding flow test discharge. The model from flow test configuration CT data matched the flow test discharge within measurement error without further calibration. The Oatman Creek Granite sample, scanned under approximate flow test configuration, also achieved a reasonable model result. The two models built with best fit configurations of unregistered CT data overestimated physical discharge by an order of magnitude.

Specimen	i	Flow Test (ml/s)	Model (ml/s)
Oatman	0.08	0.75	0.65
CC02-1	0.15	0.66	5.1
CC02-2	0.08	1.07	13.67
CC02-2a	0.08	1.07	1.07

and 0.28mm between adjacent rows. With transmissivity set from the aperture data using Equation 5.10, the model produces a discharge of 13.7ml/s.

The model constructed from the full data set has one layer of 1195 rows and 1854 columns. Column 1 has a constant head of 1.28cm and head for column 1854 is set to zero, corresponding to the calibrated 0.08 gradient. Rows 1 and 1195 are no flow boundaries. Spacing is 0.08mm between adjacent columns and 0.09mm between adjacent rows. Modeled discharge with transmissivity set from plugging the aperture data into Equation 5.10 is 13.8ml/s. The disparity with the reduced data set results from the loss of an extrapolated row.

5.2 Full Navier-Stokes Simulation

Cardenas et al. (2007) subjected one longitudinal transect of the CC02-2 sample (Figure 5.6) to a full Navier-Stokes solution for two-dimensional pressure and velocity gradients at the same boundary conditions applied in the MODFLOW model for an incompressible fluid. The results, while valid in themselves, have dramatic implications for three-dimensional fluid behavior under what is considered laminar flow.

A closer view of the first 3cm of the Cardenas model (Figure 5.7a) shows an eddy zone that develops in two-dimensions under low gradient. Figure 5.7b depicts a snapshot of a modeled pulse of solute traveling through the fracture profile, with concentration greater than zero colored to show the areal extent of any solute, and to illustrate the extensive tailing due to aperture variation and roughness of the fracture surfaces. Both of these effects are generally considered nonlinear. That they occur in a 2D model without regard for aperture variation laterally implies that a linear correlation between discharge

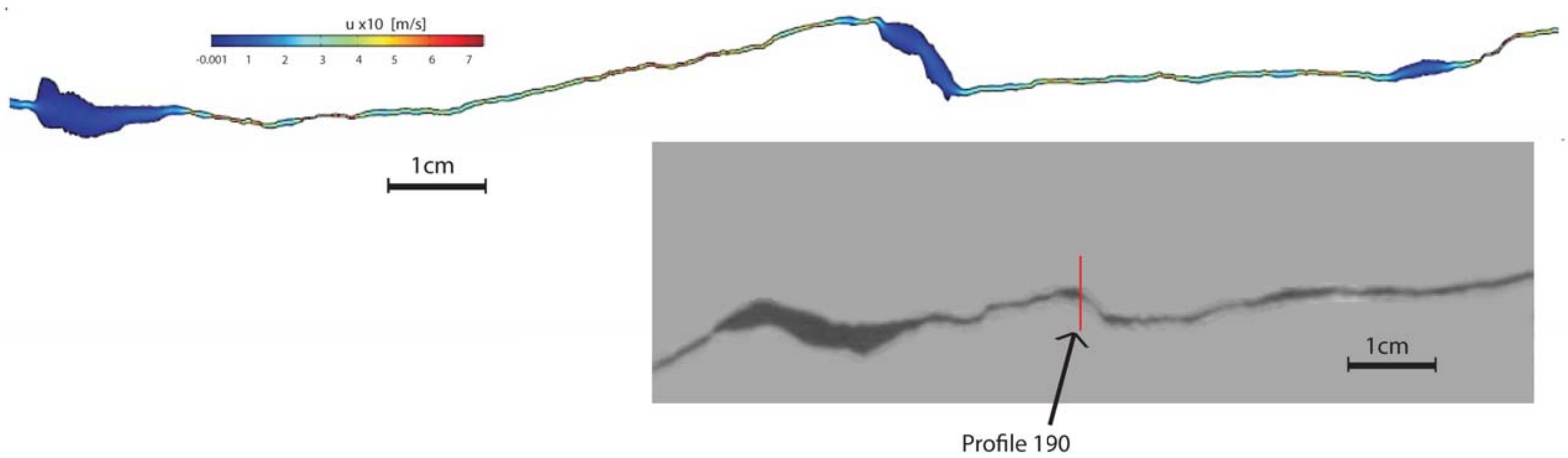

Figure 5.6 Longitudinal profile at row 190 of 401 through fracture sample CC02-2. The red line on the entry slice of the fracture marks the profile location. Displayed are the results of 2D finite element model solving Navier-Stokes Equations for pressure and velocity from Cardenas et al. (2007).

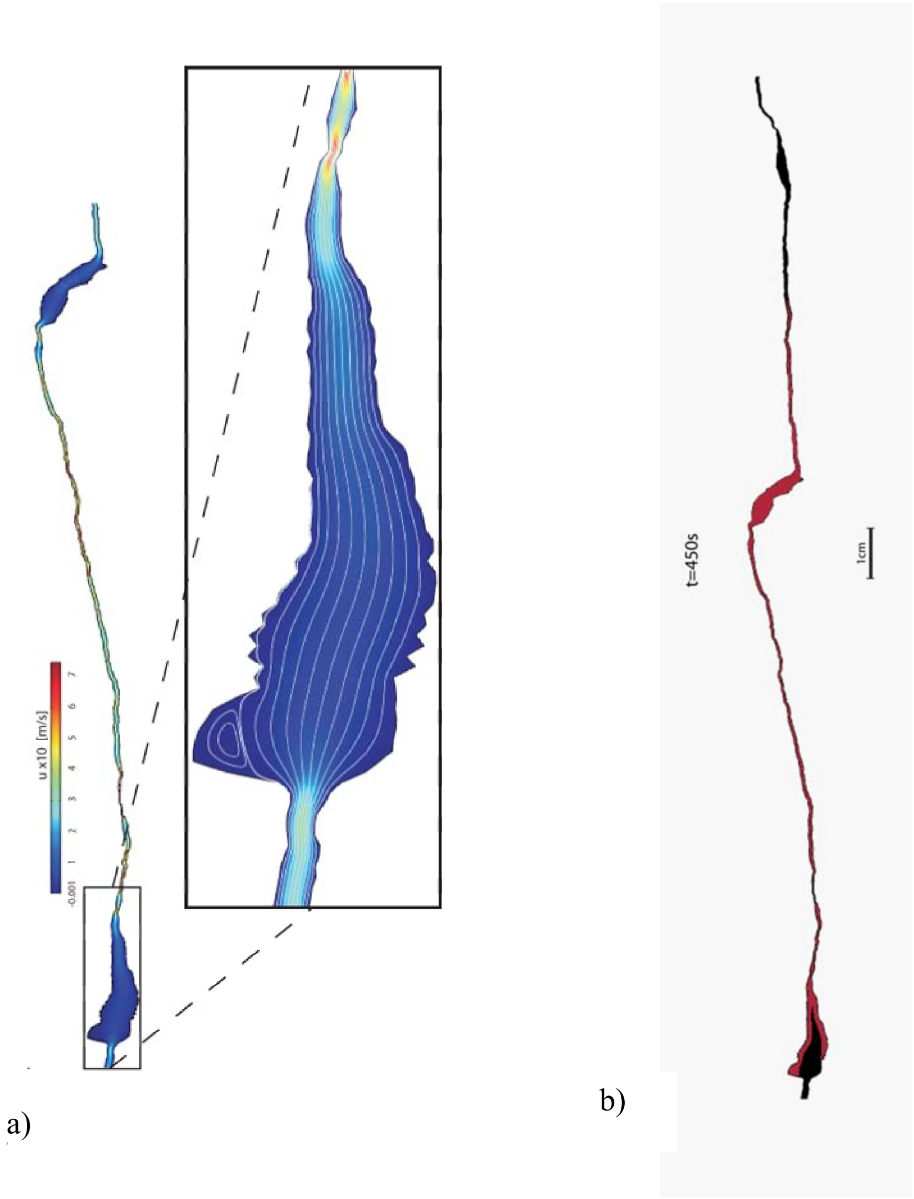

Figure 5.7 a) Flow lines and velocity profile from full Navier-Stokes solution of velocity and pressure on first 3cm of a 2D profile of fracture sample CC02-2. Notice the recirculation (eddy) zone near the inlet of the fracture (Cardenas et al. 2007). b) Presence of solute at t-450s for a pulse transport model on the same data set. Red is not indicative of concentration, but illustrates long tailing due to the roughness of the fracture surfaces and aperture variation in 2D.

and gradient masks many nonlinear behaviors that are either additive or destructive in terms of the effect on discharge from a 3D fracture volume.

5.3 Stochastic Realizations of CC02-2 Aperture Distribution

The idea that a sample of a natural fracture can be used to extrapolate to a fracture set for modeling purposes is attractive, but it is also data intensive. Further, acquisition of an appropriate sample may be problematic. In this section, I explore the applicability of using a known aperture distribution to populate a pseudo-randomly generated aperture field. Building on this technique provides a means to generate digital fracture sets with limited data investment.

Using the apertures calculated for the CT scan of the flow configuration of fracture sample CC02-2, I built stochastic fractures of 20, 30, and 40 large aperture areas and modeled the resulting transmissivity field generated with Equation 5.10. The IDL code I wrote to handle building an aperture distribution is included in Appendix B. I chose the number of peak aperture areas from visual inspection of the transmissivity field of the sample (Figure 5.8).

To build the pseudo-random aperture distributions, I broke the actual CC02-2 aperture distribution (Figure 5.9) into three sections: 1) $b>1.5$mm, high range associated with the local maximum value; 2) $0.5\text{mm}<b\leq 1.0$mm, the mid range corresponding to a transition from the high transmissivity zone to the background transmissivity; and 3) $b\leq 0.3$mm the low range used to set the minimum value between peak areas. A random value index from the high range populates a random location in the output aperture grid

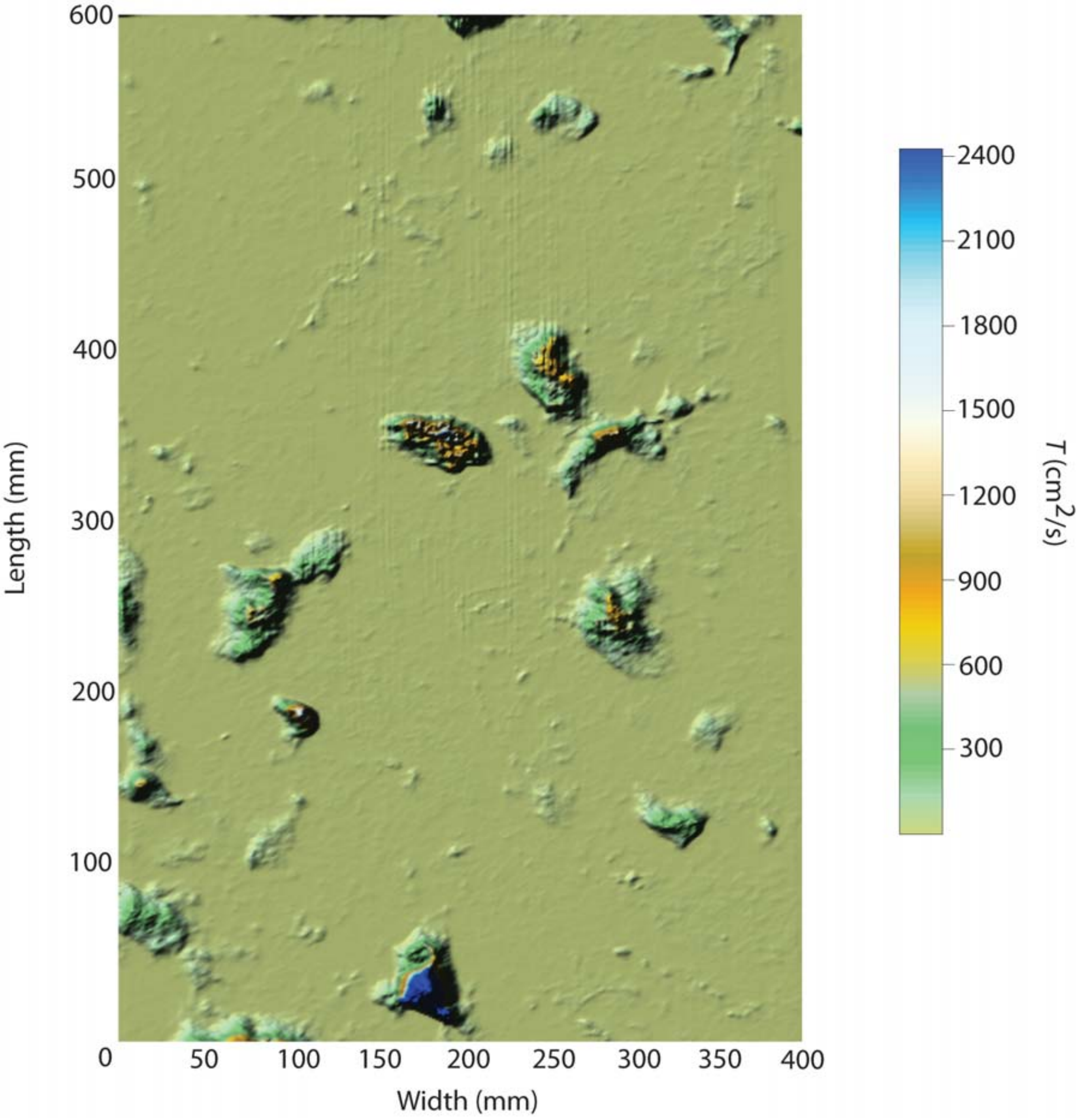

Figure 5.8 Transmissivity of the flow configuration calculated from CT data of fracture sample CC02-2. From inspection of this figure, I estimated 20 areas of peak transmissivity to begin building a pseudo-random fracture.

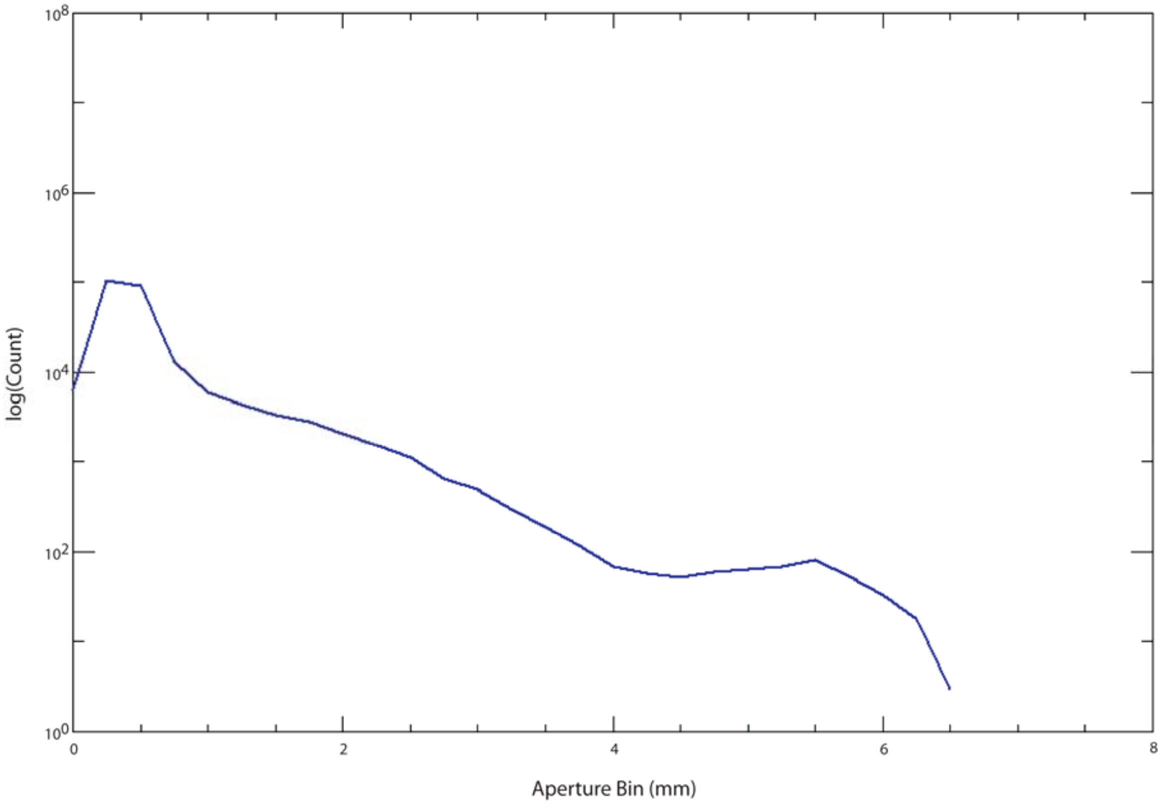

Figure 5.9 Aperture distribution calculated from CT data for fracture sample CC02-2. The number of peaks used to build pseudo-random fractures corresponds to a minimum peak value of 1.5mm.

for each peak. Four transition apertures are chosen by random index from the mid range and placed randomly within 25 pixels of the peak, one in each of the ±*x* and ±*y* directions. Next, one value from the low range is set at the midpoint between each of the peaks to provide a location for local minima for kriging purposes.

I used the IDL Krig2D function to interpolate the entire grid from the selected points using a various input parameters, in an attempt to achieve a result resembling the data set from the actual fracture, with little success. The difference in magnitude between the highs and lows, and the relatively isolated spatial distribution of the peaks invariably led to a steep descent from each peak to the background aperture value. To work around this limitation, I implemented a further randomization multiplying each peak up to 25 times, and then placing the copies randomly within a 25 pixel "radius" square of the original.

Following this procedure, I found the discharge from the calibration physical flow test bracketed by two realizations using 30 peak apertures. The aperture distributions are compared in Figure 5.10, while the transmissivity grids are displayed in Figure 5.11. One might expect that the upper bound would be BRealA and the lower bound would be BRealC due to the greater number of large aperture values in the BRealA grid. However, the opposite is true. MODFLOW and MODPATH data for all three models are reported in Table 5.3. A clue as to why can be found in Figure 5.12, showing the flowpath output of MODPATH for the three models. The fast flowpath on the left side of BRealC can be attributed to the near continuity of high transmissivity zones down the left side of that realization (Figure 5.11c), despite the relatively low magnitude of individual peaks.

While the stochastic fracture realizations for the aperture distribution of CC02-2 could be refined to look more realistic, the results of the models of the bracketing realizations yield useful insights to fracture flow behavior. It is reasonable to represent the hydraulic behavior of a natural fracture using just the aperture distribution. Areas of large aperture do not necessarily correlate to high discharge. The spatial arrangement of high transmissivity zones affect discharge to a greater extent than the magnitude of those zones.

Table 5.3 Comparison of aperture statistics and model output for bracketing built fractures with those of the actual fracture. Although all measures of the aperture of BRealA are greater than BRealC, and the average travel time of MODPATH particles is faster, BRealA is the lower bound in terms of discharge.

Specimen	min (mm)	max (mm)	b_a (mm)	Q (ml/s)	t_{min} (s)	t_{max} (s)	t_{ave} (s)
CC02-2	0.03	6.53	0.63	1.07	2.57	11.00	3.53
BRealA	0.12	5.03	0.73	1.01	1.83	13.03	3.91
BRealC	0.06	4.31	0.59	1.27	0.97	19.05	4.55

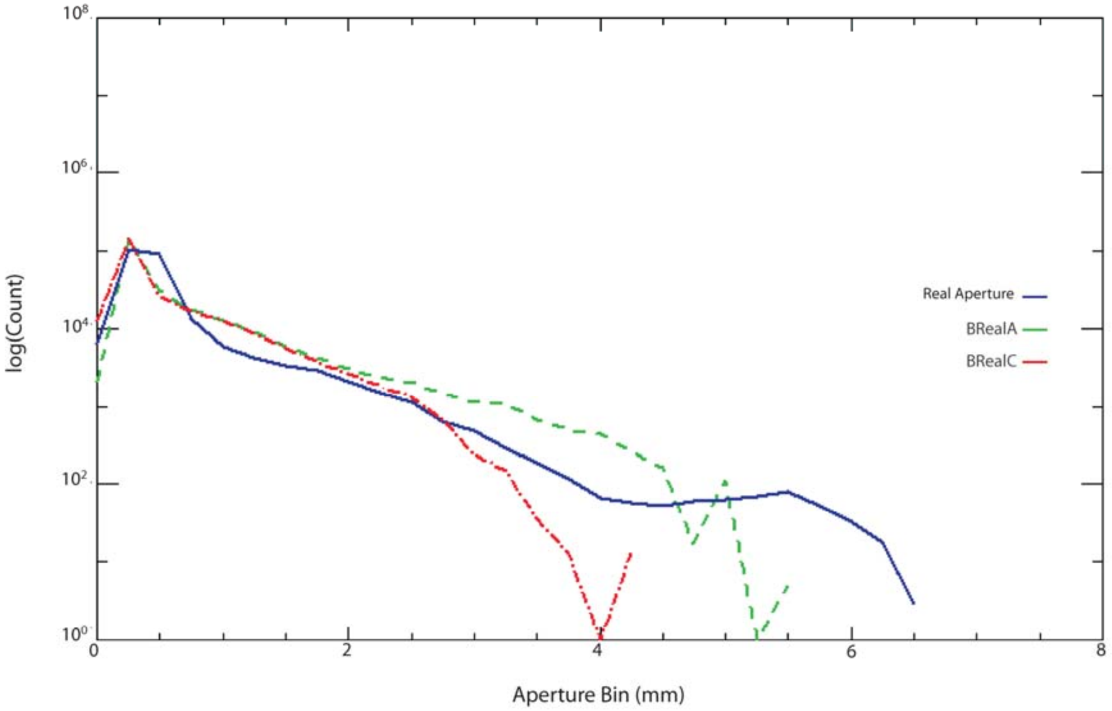

Figure 5.10 Aperture distribution of CC02-2 overlain by the distributions of the bracketing built fractures. The pseudo-random fractures BRealA and BRealC have 30 peak apertures greater than 1.5mm, with background aperture values of less than 0.3mm.

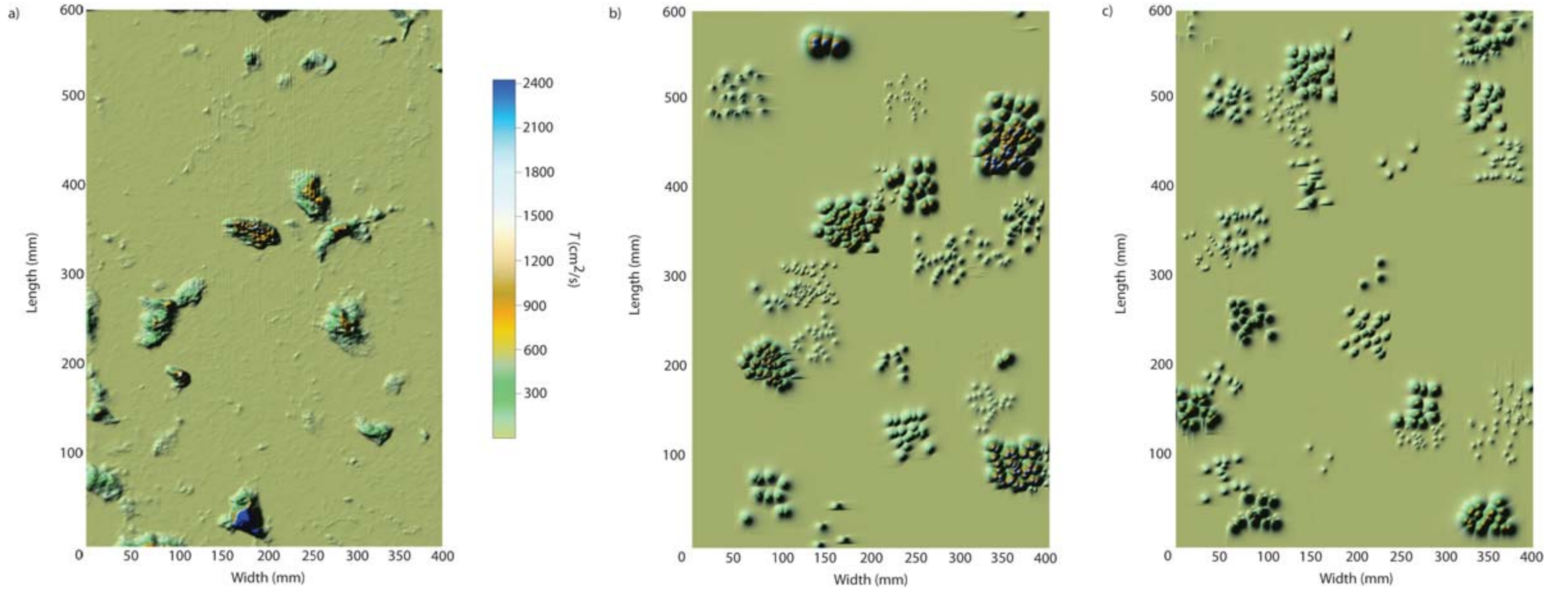

Figure 5.11 a) Original transmissivity field for fracture sample CC02-2. b) Transmissivity field for built fracture BRealA. c) Transmissivity field for built fracture BRealC. Notice the height and width differences between the high transmissivity areas in b) and c).

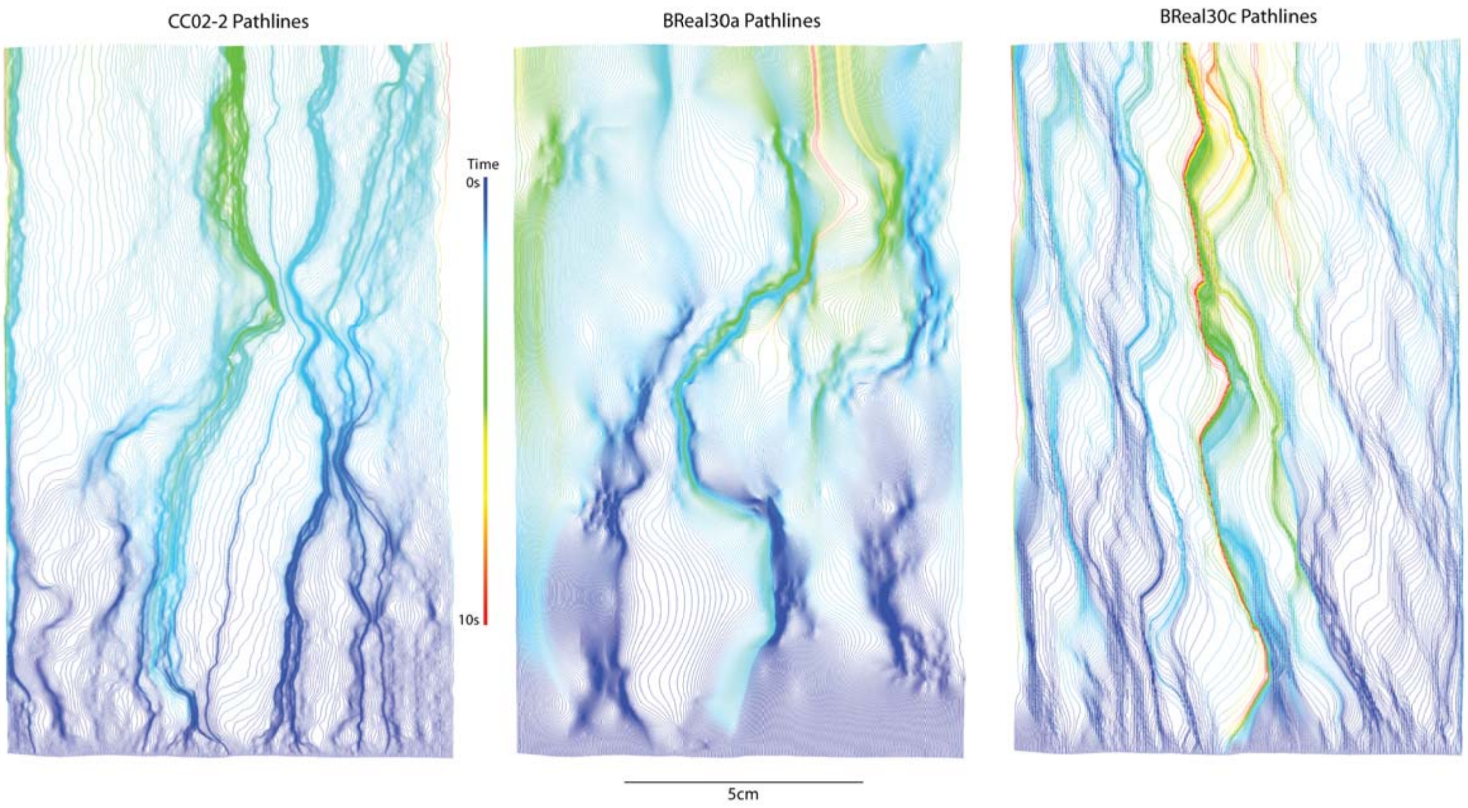

Figure 5.12 MODPATH output from MODFLOW velocity profile for fracture sample CC02-2, BRealA and BRealC. Travel time statistics are very similar between CC02-2 and BBRealA as can be visually confirmed. The fast flowpath on the left side of BRealC accounts for the increase in discharge over the other two models despite having lower magnitude high transmissivity zones.

6 PREDICTING HYDRAULIC APERTURE

Presented with the "surface expression" of fracture sample CC02-2 (Figure 6.1), what would be the best choice for a representative aperture? From the modeling results in Chapter 5, the arithmetic mean of physical aperture values is a poor predictor of hydraulic aperture even under ideal conditions. In this chapter, I take a closer look at the CT derived aperture data from the registered samples CC02-2 and Oatman.

6.1 Meaning of Means

There are three methods of defining an average value from a finite data population: 1) the arithmetic mean; 2) the harmonic mean; and 3) the geometric mean. When applied to a physical parameter of a flow system, each of these has a different physical meaning.

The arithmetic mean X_a:

$$X_a = \frac{1}{n}\sum_{i=1}^{n} x_i, \tag{6.1}$$

where x_i is a discrete data point, and n is the number of data points, describes properties that vary in parallel (Figure 6.2a). It is useful, for instance, when computing a horizontal hydraulic conductivity K_h for stacked units where vertical hydraulic conductivity $K_v << K_h$.

The harmonic mean X_h:

$$\frac{1}{X_h} = \frac{1}{n}\sum_{i=1}^{n} \frac{1}{x_i}, \tag{6.2}$$

describes properties that vary in series (Figure 6.2b). It might be used to define the hydraulic aperture of the profile described in Section 5.2.

Figure 6.1 First CT slice of sample fracture CC02-2, representing the actual fracture opening in the direction of flow.

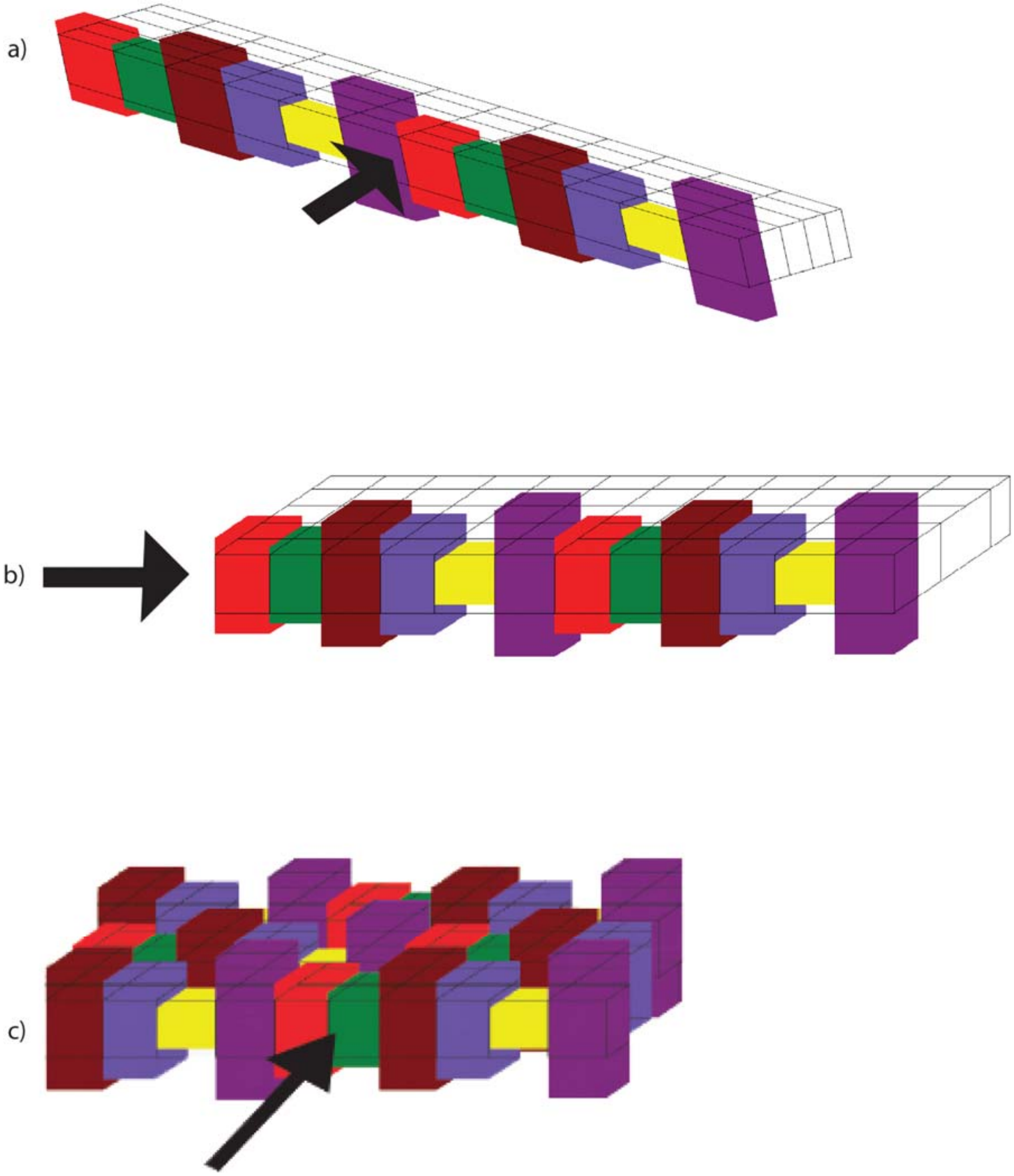

Figure 6.2 Physical representations of a) arithmetic mean, b) harmonic mean, and c) geometric mean. The arithmetic mean describes properties that vary in parallel. The harmonic mean describes properties that vary in series. The geometric mean theoretically describes properties that vary in two dimensions.

The geometric mean X_g is related to the other two in the sense that $X_h \leq X_g \leq X_a$, and is defined:

$$X_g = \left(\prod_{i=1}^{n} x_i \right)^{1/n} . \tag{6.3}$$

It theoretically describes properties that vary in two or three dimensions as in Figure 6.2c. Therefore, it is expected that the geometric mean aperture b_g will closely match hydraulic aperture b_e under laminar flow conditions.

6.2 Point Predictions

Reports of the surface expressions of fracture aperture often rely on point measurements associated with oriented scanlines. The full point aperture data from fracture sample CC02-2 allow evaluation of a point measurement as a predictor of hydraulic behavior.

Figure 6.3 graphically displays the expected error in discharge for various confidence intervals. Overall, the percentages work in the favor of a point predictor; greater than 1% of the data points fall in a 1% window about the hydraulic aperture. This pattern holds through all confidence intervals. However, looking at this another way, the 20% confidence interval provides a one in four chance of picking an aperture that predicts discharge within the range 37% less through 33% greater than actual discharge.

As a precise predictor then, the point measurement is little better than throwing darts for estimating hydraulic aperture. Aperture data sets for mated fractures have been described as lognormal (e.g. Johns 1993, Keller 1998) and Gamma distributions (Tsang and Tsang 1987). While the distribution of CC02-2 apertures may resemble a lognormal distribution (Figure 5.9), it more closely matches a normal distribution using the median

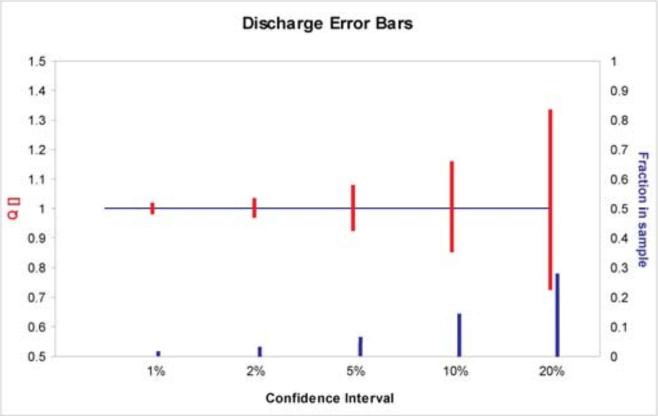

Figure 6.3 Comparison of expected percentage error in discharge for a given confidence interval using the CT derived aperture data for fracture sample CC02-2. The fraction of aperture values that fall within a given interval is greater than that interval.

aperture and a standard deviation calculated from extrapolation of the right limb of the normal curve through the positive skew of the actual distribution (Figure 6.4).

A normal distribution nicely fits truncated data of the Oatman Creek Granite fracture sample as well (Figure 6.5). Using the midpoint of the bin at the peak of the histogram of the actual aperture distribution as the mean, and calculating the standard deviation from aperture data less than or equal to 1.0mm yields a curve that overestimates small apertures and underestimates large apertures, which might be expected from loss of material due to breakage or weathering.

The mean aperture parameter for the normal curves matched to the aperture distributions of the flow configuration CT scans has no physical meaning in relation to actual fluid flow. It might be attractive to use the mean of the normal curves as a conservative estimate for hydraulic aperture, but the parametric model used to generate the curves is derived from a spatially independent subset of the source data, and better estimators of central tendency that are physically tied to the source data are available: the arithmetic, geometric, and harmonic means.

6.3 Profile Predictions

Fracture aperture estimated from profile data is another attractive method to predict hydraulic aperture. Digital images from fracture surface expressions, or from intersection with well-bores at relatively shallow depths, are readily available and easy to analyze. But is the data from a fracture profile sufficient to characterize fluid flow behavior in that fracture?

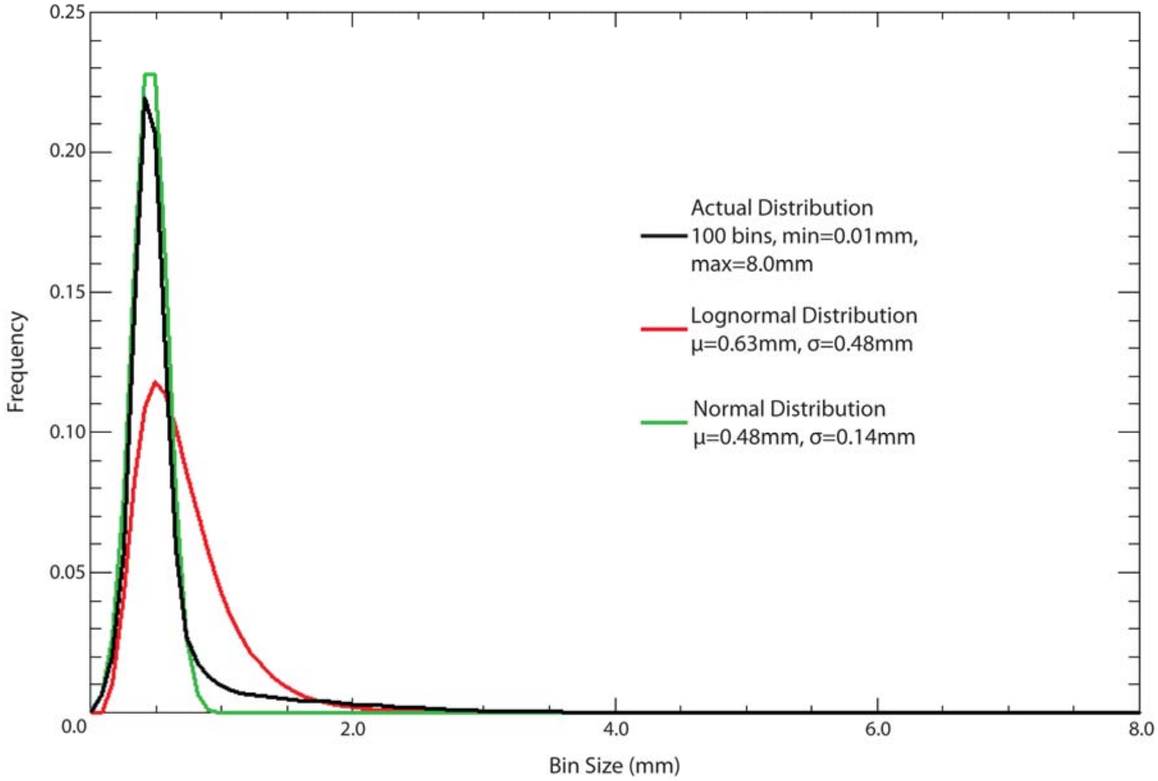

Figure 6.4 Actual aperture distribution of fracture sample CC02-2 in black. For comparison is a lognormal distribution in red, using the mean and standard deviation of the actual distribution. A normal distribution in green, constructed using the midpoint of the median bin as the mean and extrapolating the right limb of the actual distribution to 0.9mm and calculating the standard deviation from the actual apertures less than or equal to this value.

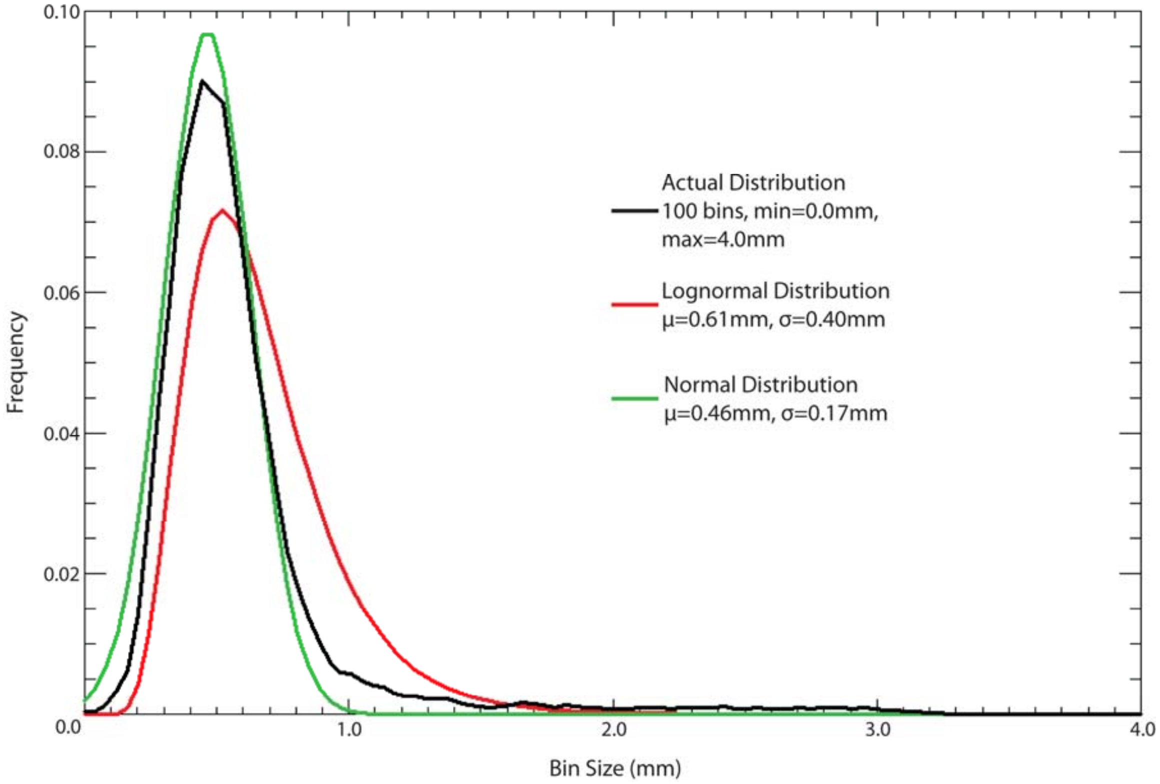

Figure 6.5 Actual and modeled aperture distributions for Oatman Creek Granite fracture sample. The mismatch from the normal distribution, using a mean equal to the midpoint of the peak aperture bin and a standard deviation calculated from aperture values less than or equal to 1.0mm, with that of the actual aperture distribution can be attributed by material loss due to breakage.

Computing the arithmetic mean aperture from the data depicted in Figure 6.1 yields a representative aperture of 0.91mm from the "surface expression". Discharge predicted from this aperture overestimates actual discharge achieved through the fracture in the laminar flow regime by more than 500% at all points (Figure 6.6). Clearly, this profile is not a good estimator of hydraulic aperture.

The results from profiles normal to flow further into the fracture are little better, and illustrate the uncertainty in using 2D aperture data to predict hydraulic behavior. Figure 6.7 shows the variation of arithmetic mean aperture normal to the overall head gradient. Out of 603 slices of CT data, no arithmetic mean aperture matches the physical hydraulic aperture. Again the percentages work in favor of the confidence interval used. As a conservative measure, 180 of the profile means fall below the physical hydraulic aperture. Greater than 10% of the profile means fall within a 5% error interval about the physical hydraulic aperture. However, one random profile, or even several, has little chance of representing the hydraulic behavior of this fracture. An areal estimator of aperture is necessary.

6.4 Comparison of Means

Also pictured on Figure 6.7 is the arithmetic mean of all aperture data points for fracture sample CC02-2. At 0.63mm for the fracture, the predicting discharge from the arithmetic mean overestimates actual discharge through the laminar flow regime from 20-110%. A comparison of the three means for the aperture data from CC02-2 with the flow test experimental results under laminar flow conditions is shown in Figure 6.8.

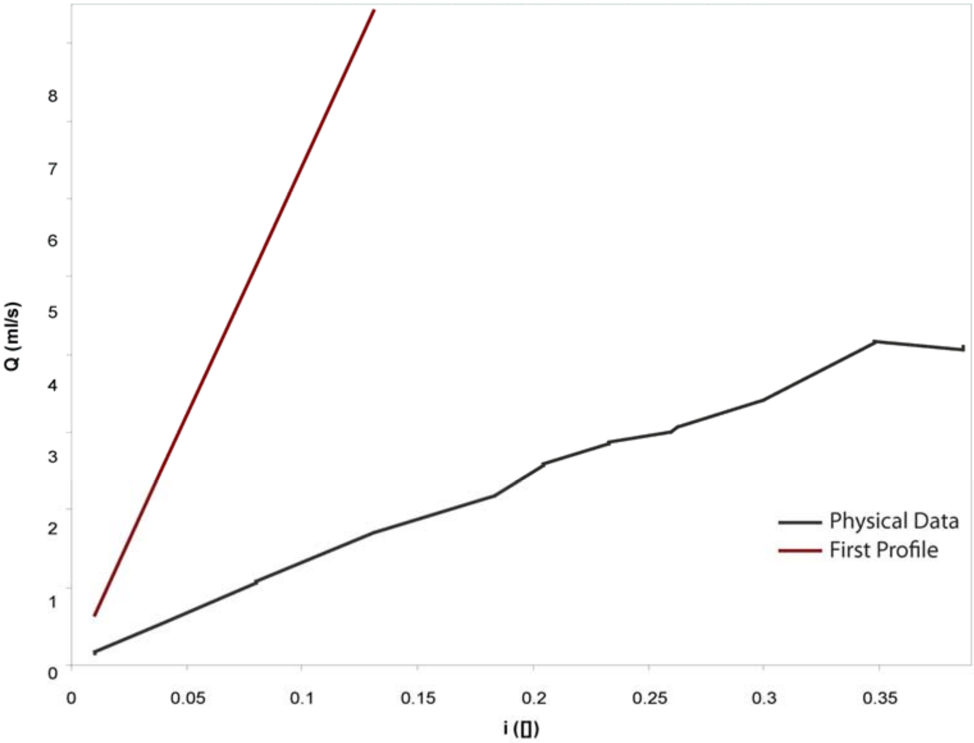

Figure 6.6 Comparison of discharge predicted from the arithmetic mean of aperture data from first profile of fracture sample CC02-2 with the physical flow test data in the laminar flow regime. At all gradients, predicted discharge is at least six times that achieved in the physical experiment.

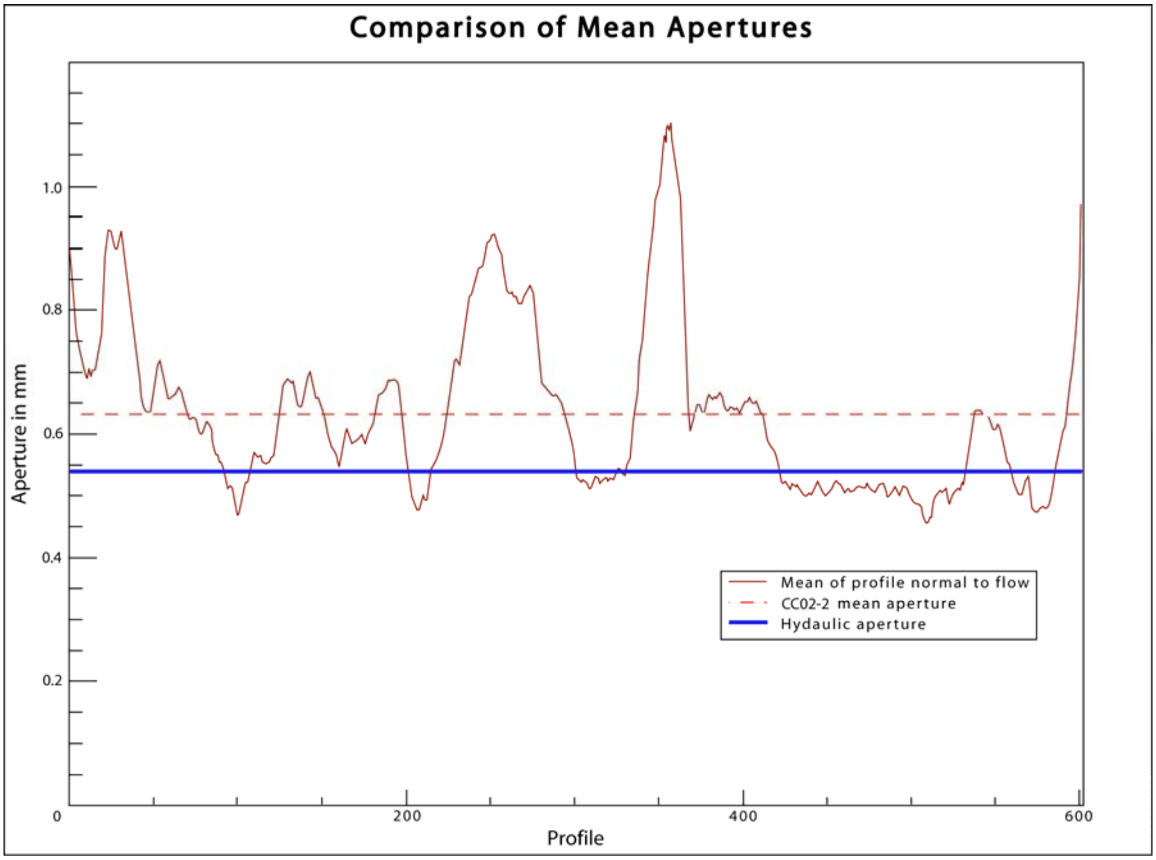

Figure 6.7 Arithmetic mean of mechanical apertures normal to flow plotted from inlet to outlet of fracture sample CC02-2. For reference, the arithmetic mean aperture of the entire fracture sample and the hydraulic aperture calculated from physical flow tests in the laminar flow regime are depicted in red and blue respectively.

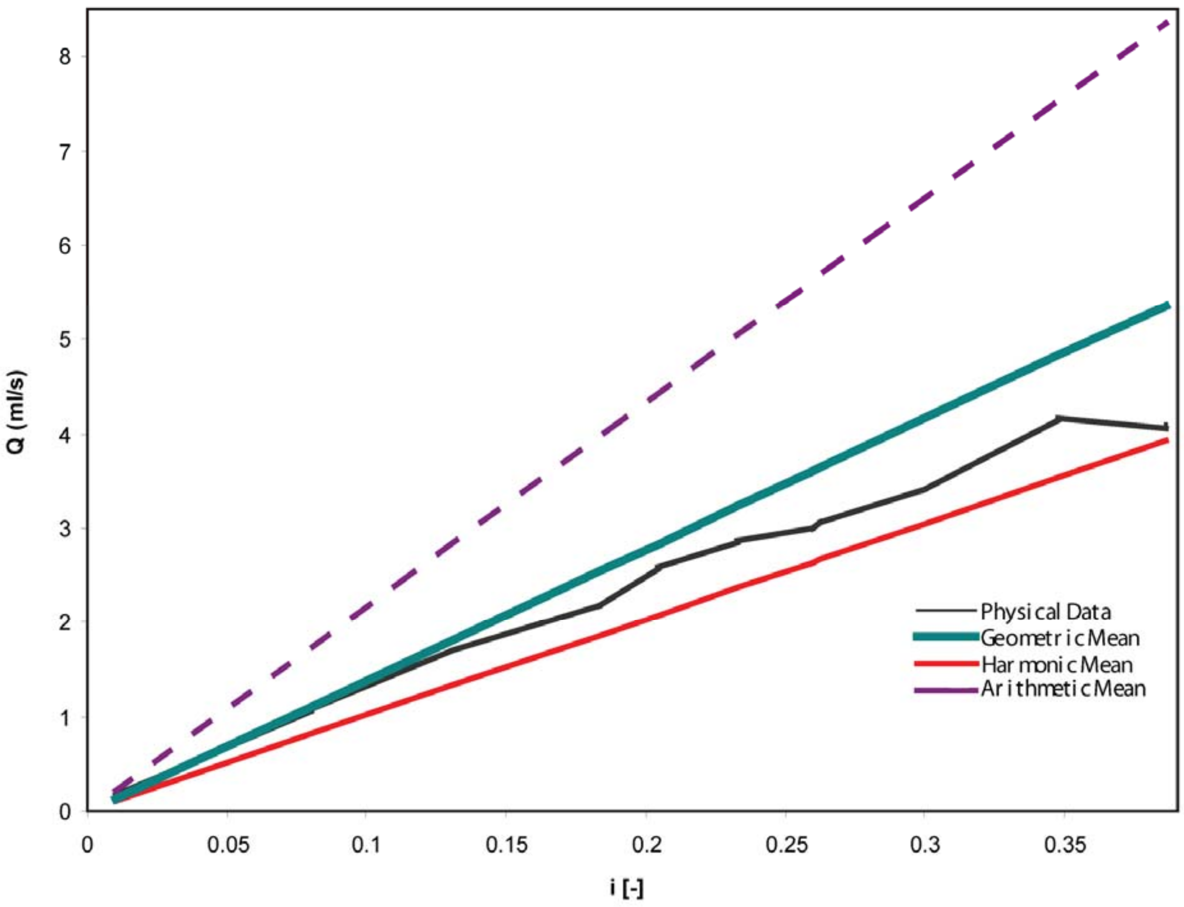

Figure 6.8 Cubic law flow predictions of arithmetic, harmonic, and geometric means of all aperture data from fracture sample CC02-2 plotted with the physical flow test experiment data for gradients in the laminar flow regime. Predictions using the geometric mean most closely match physical flow at typical groundwater gradients.

The harmonic mean, which gives weight to the smaller values, would be expected to underestimate discharge at all points. In fact, the harmonic mean of all aperture data is 0.49mm. This value calculates a predicted discharge 3 to 43% lower than flow test results.

The geometric mean respects the effect of 3-dimensional variation in properties and is expected to provide the best estimate of hydraulic aperture. For the case of fracture sample CC02-2, the geometric mean of all aperture data points is 0.55mm, corresponding to predicted discharges for the laminar flow regime that range from 22% lower to 32% greater than actual discharge. As the gradient increases, the flow regime departs from strictly laminar into a transitional regime, and the harmonic mean aperture becomes a better predictor of hydraulic aperture due to weighting the lower aperture values. However, at gradients less than 0.1, typical for most groundwater applications, the geometric mean aperture most closely matches actual discharge with no modification of the cubic law.

7 MEASURING ROUGHNESS

Often, measured physical aperture data are not available for fractured media analyzed by fluid flow modeling. In such cases, a representative mechanical aperture distribution may be used to serve as conductive pathways for flow. From the 2D model work of Cardenas et al. (2007) on a profile of the Santana Tuff fracture sample CC02-2, it was shown that surface roughness plays a significant role in fracture flow. Therefore, a modifier for the cubic law that describes the roughness of natural fractures is in order for models using stochastic aperture distributions not tied to physical areal fracture data.

The surface roughnesses of natural fractures are defined in a number of ways depending on the application. Areal descriptors most often are associated with shear strength, while modifiers to flow equations that account for rough surfaces largely depend on the results of profile measurements. In this chapter, I define a Representative Elemental Surface (RES) in terms of the number of data points that can be used to describe the roughness of a much larger surface.

7.1 Fracture Mechanics

Fractures propagate in response to differential stress. They are classified into one of three modes (Figure 7.1a). The nature of propagation is dependent on the regional stress field, the morphology of the fracture itself, and the material properties and dimensions of the enclosing rock unit. This section describes the necessary conditions for Mode I fracture propagation and the effects of these conditions on the roughness of the resultant fracture surfaces.

The field of fracture mechanics has its origin in the theory of Griffith (1920) regarding the reduction of strength in metals due to surface scratches. Equating the

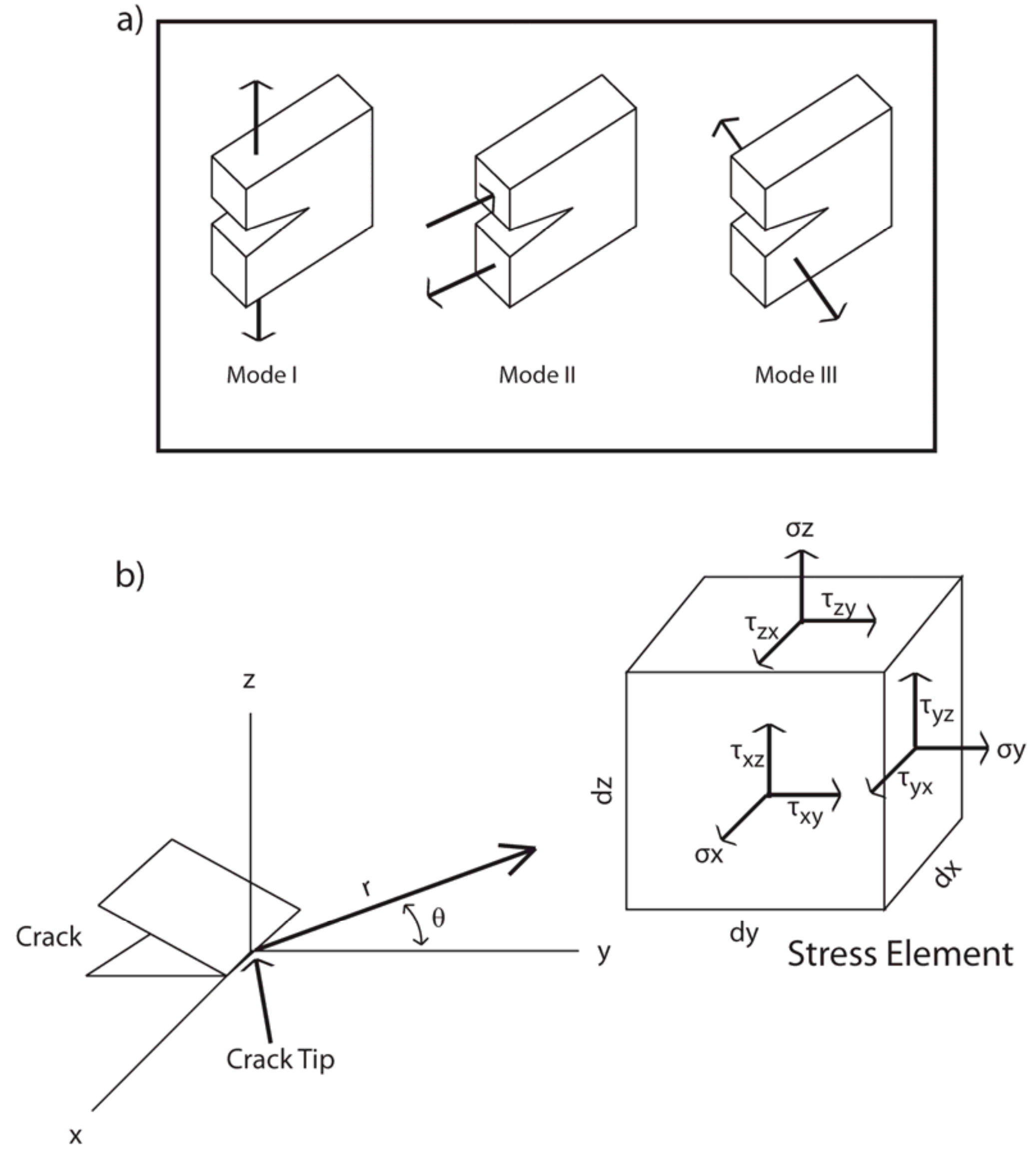

Figure 7.1 a) Modes of fracture propagation. Mode I is pure opening. Mode II is shear normal to the fracture tip. Mode III represents tearing with shear nominally parallel to the fracture tip. b) Model of the state of stress near the fracture tip within the rock body after the solutions of Westergaard (Perez 2004). The variables refer to the following: σ_i is the tensional stress in the *i* direction; $\tau_{i,j}$ indicates shear stress in the *j* direction, normal to the *i* direction; *r* is radial distance from the crack tip; and Θ is the angle about the crack tip with 0^o as the *z*-normal plane of symmetry, assuming an isotropic solid, for the fracture surfaces.

elastic strain energy released due to fracture propagation to the surface energy created, a stability condition for a fracture volume is defined. When far-field stress creates a stress field at a fracture tip that would potentially release strain energy exceeding that of the surface energy created, the solid ruptures in accordance with the near tip stress field to minimize potential energy.

Perez (2004) presents a detailed implementation of Irwin's (1958) stress intensity factor K_I into Westergaard's (1939) solutions for the stress field near a crack tip (Figure 7.1b) to account for the stress singularity as distance from the tip, *r*, approaches zero. This yields:

$$K_I = \sigma_z \sqrt{\pi a}\ , \tag{7.1}$$

where σ_z is the tensional stress normal to the plane of symmetry, assuming an isotropic solid, between the fracture surfaces through the crack tip, and $2a$ is the length of the fracture.

The onset of material failure occurs at a critical stress intensity, $K_I = K_{IC}$. This defines the material property of fracture toughness. Subcritical fracturing, crack propagation while $K_I < K_{IC}$ but greater than some threshold value, commonly occurs in the subsurface under saturated and/or corrosive conditions (Atkinson 1982, Philip et al. 2005).

For pure Mode I opening, planar fractures propagate perpendicular to the direction of minimum stress, σ_{min} (Olson et al. 2009). From Figure 7.1b, let:

$$\sigma_{\|} = \sigma_{\min} = \sigma_z, \tag{7.2}$$

where $\sigma_{||}$ refers to the stress parallel to the plane of the fracture; and:

$$\sigma_{\perp} = \frac{1}{\frac{1}{\sigma_x} + \frac{1}{\sigma_y}}, \tag{7.3}$$

where $\sigma_{\perp}$ is the effective compressive stress on the crack tip. The magnitude of the anisotropy between $\sigma_{||}$ and $\sigma_{\perp}$ suppresses deviation from planarity during fracture propagation. A weak anisotropy promotes crack-front hooking to intersect adjacent fractures, thereby creating compound fracture surfaces (Philip et al. 2005).

Locally, the crack tip must either skirt grain/crystal boundaries or propagate through them. Which occurs depends on both material properties and external forces. Weathering products, cleavage, and imbrication enhance intergranular or intercrystalline fracture propagation. High strain rate can overcome local heterogeneities, propagating fractures through relatively tough grains/crystals. Well-cemented matrix materials are more likely to exhibit transgranular fracturing, even under subcritical fracture propagation (Olson et al. 2009).

Section 7.2 describes quantification of roughness as a departure from planarity. The processes influencing propagation of fractures detailed in the preceding paragraphs can either enhance or retard roughness. Orientation of mineral cleavages and rock fabric with respect to direction of fracture propagation play a primary role in development of roughness. Data sampling density also contributes to the magnitude of calculated roughness as detailed in Section 7.5.3 with the data from the Elberton Granite samples.

7.2 Quantification of Surface Roughness

Rough fracture surfaces can be digitally represented by a number of techniques over a range of accuracies down to <1μm. Chae et al. (2004) discuss usage of stylus profilometers, scanning electron microscopy, and confocal laser scanning microscopy. Thomas (1998) provides a detailed look into the instruments used in describing rough surfaces in 2D and 3D, and describes the challenges inherent in representing a continuous surface digitally. Roughness changing with scale of measure is always an issue. The 1mm divider used by Louis and Lomize in calculating their respective absolute roughnesses does not effectively capture roughness of natural fractures (Figure 7.2). Even surface maps are no more than rectangular gridded collections of profiles at some point. Evaluation of the 0.25mm scale used in this study is presented with the results.

The structural engineering view of natural rough surfaces often lies in the stability of fractured media under increasing shear stress. The Joint Roughness Coefficient (JRC) developed by Barton (1973) scales this property. The JRC is defined by Barton et al. (1985) as:

$$JRC = \frac{\alpha - \phi_r}{\log(JCS / \sigma'_{no})}, \tag{7.4}$$

where:

α is the angle at which sliding occurs between two rough surfaces;

JCS is the joint compressive strength [Pa];

σ'_{no} is the effective normal stress at the point of sliding [Pa];

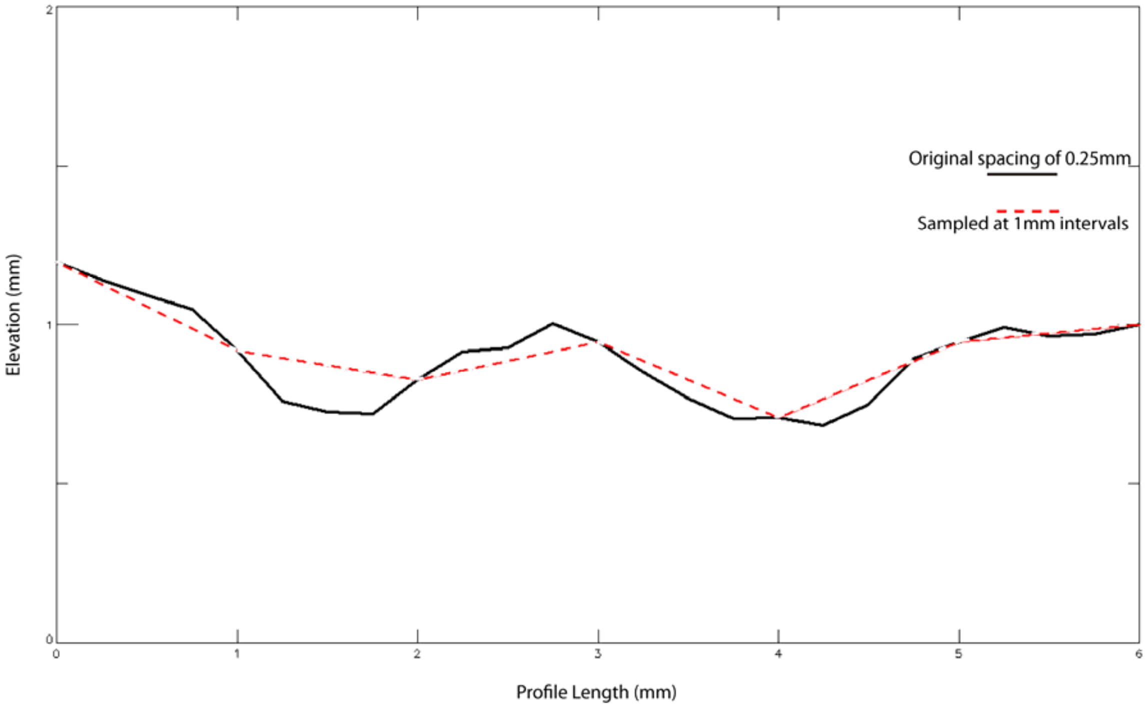

Figure 7.2 Example of undersampling of surface roughness at the millimeter scale from Santana Tuff specimen CC02-2. Both highs and lows are systematically under-represented in estimates of ε using 1mm spacing. Elevation is exaggerated by 2x to illustrate this behavior clearly.

ϕ_r is the residual friction angle, which incorporates alteration effects into the equation. The residual friction angle is estimated by Barton and Choubey (1977) to follow the empirical relation:

$$\phi_r = (\phi_b - 20) + 20\, {}^{r}\!/\!{}_{R}\,, \tag{7.5}$$

where:

ϕ_b is the basic friction angle at which sliding begins between core samples;

r and R are the rebound values of a Schmidt hammer test on a weathered, saturated joint surface and the corresponding unaltered dry rock respectively.

As all parameters of the above equations are easily measured in the lab, evaluation of the JRC for numerous fractures of various lithologies is limited only by the resources of the investigation. Not surprisingly, a representative profile corresponding to an index JRC has been compiled to estimate joint compressive strength in the field. While Barton et al. (1985) suggest a relationship between JRC, hydraulic aperture and mechanical aperture, there is no physical tie between the parameters that determine JRC and fluid flow.

To describe surface roughness numerically, I use a surface, calculated at the full scale of measure, to footprint ratio. While a relative incline does not impart roughness to a surface per se, for consistency among data sets I remove the planar trend of the form

$$z = a + bx + cy \tag{7.6}$$

from each, after the methodology of Stout et al. (2000) using my IDL program *Z_Trend_Remove.pro* (see Appendix B.8). For every four data points of the resulting surface elevations, two triangles can be defined without addition or loss of data (Figure

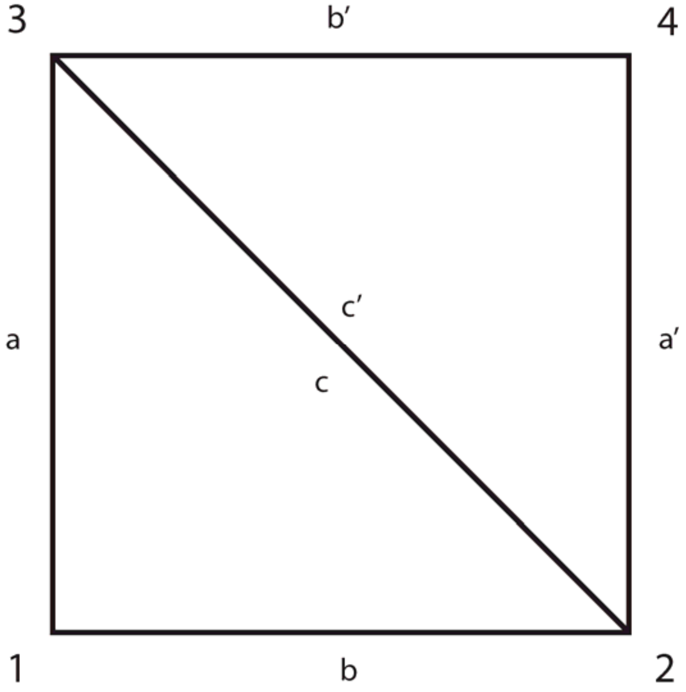

Figure 7.3 Every four elevation points from a surface data set define two triangles without addition or loss of data. The areas of these are accumulated over the sample to define the sample surface area.

7.3). Area is then accumulated by solving for the lengths of the sides and applying Heron's formula (Kung 1992):

$$A_{\Delta 1,\Delta 2} = \sqrt{s_1\left(s_1 - a\right)\left(s_1 - b\right)\left(s_1 - c\right)} + \sqrt{s_2\left(s_2 - a'\right)\left(s_2 - b'\right)\left(s_2 - c'\right)}, \tag{7.7}$$

such that:

$$S / S_0 = \frac{\sum A_{\Delta x_i x_j x_k}}{L \times W}. \tag{7.8}$$

This yields a dimensionless quantity $S/S_0 \geq 1$ which shows good discretization among the 25 surfaces studied and may be used in calculation of a friction factor tied to actual surface roughness.

7.3 Sample Data

The sample size and spacing information are found in Table 7.1. Samples El01 through El03 are cut from the same specimen to satisfy the CT size requirements. They are analyzed individually and then sized to match and taken as a unit. El03-sparse halves the data from the sample to approximate the spacing of the other two samples. The same process is repeated with the Pad sample to evaluate scale of measure on a coarse-grained weathered specimen.

7.4 Methodology for Investigating Roughness

To choose the surface sample for which roughness is to be determined, I interrogate raw CT data for the largest rectangular area that has rock at all points of the primary fracture surface. This is done to reduce artificial roughness caused by edge effects and to simplify the boundaries of the sample for consistent comparison.

Table 7.1 Sample names, spacing, and sizes included in the study

Sample Name	Δx,Δz (mm)	Δy (mm)	Pixels Wide	Pixels Long	Sample Area (cm^2)
El01	0.28	0.25	412	995	290.24
El02	0.28	0.25	454	992	318.86
El03	0.15	0.25	861	1000	319.51
El03-sparse	0.30	0.25	431	992	317.32
Fr-Wr	0.27	0.25	441	430	127.78
Fr-MnO	0.28	0.25	447	769	243.37
Pad	0.17	0.25	433	680	125.08
Pad-sparse	0.34	0.25	217	680	125.37
Pad-opposite	0.17	0.25	662	840	236.23
Calca-right	0.26	0.25	252	796	132.23
Oatman	0.25	0.2	240	350	42.00
Brushy	0.25	0.2	308	359	55.29
CC01-1	0.25	0.25	231	200	28.88
CC01-2	0.25	0.25	400	215	53.75
CC01-3top	0.30	0.25	381	561	162.81
CC01-3bot	0.30	0.25	381	561	162.81
CC02-1top	0.27	0.25	360	488	119.24
CC02-1bot	0.27	0.25	360	488	119.24
CC02-2top	0.23	0.25	401	603	141.68
CC02-2bot	0.23	0.25	401	603	141.68
YM-left top	0.23	0.25	820	1800	846.83
YM-left bot	0.23	0.25	820	1800	846.83

Figure 7.4 illustrates the edge effect roughness problem. The surface of interest is the leached weathering rind of the top, not the broken edge through two other fracture horizons. To aid respecting this possibility when choosing a sample surface, my algorithm *GetBotSurfOptimize.pro* (Appendix B.3) requires that the top surface be continuous along the full extent of the sample width (the x direction in Figure 7.5). While there are less restrictive ways to accomplish the surface pick, this serves as a quality control measure to avoid incorporating bad data into the analysis.

The idea of a Representative Elemental Surface for fractures implies that the statistics related to roughness are stationary. That is, no statistical moments vary in space (Manly 2009). To investigate this, I take samples sized 2^n x 2^n n=2, 3 … 9 (depending on the dimensions of the sample) across the complete rectangular surface, solve for S/S_0 as described in Section 7.1, and plot simple statistics of the samples by size.

The simple statistics used here include the first two moments of central tendency— the arithmetic mean and the variance— and the median. As the CT data incorporate the properties of continuous surfaces, I can define the equations using continuous notation. Starting with a probability function *f(z)* such that:

$$\int_{-\infty}^{+\infty} f(z)dz = 1, \tag{7.9}$$

then the arithmetic mean is:

$$\mu = \int_{-\infty}^{+\infty} zf(z)dz, \tag{7.10}$$

and the variance:

$$\sigma^2 = \int_{-\infty}^{+\infty} (z-\mu)^2 f(z)dz. \tag{7.11}$$

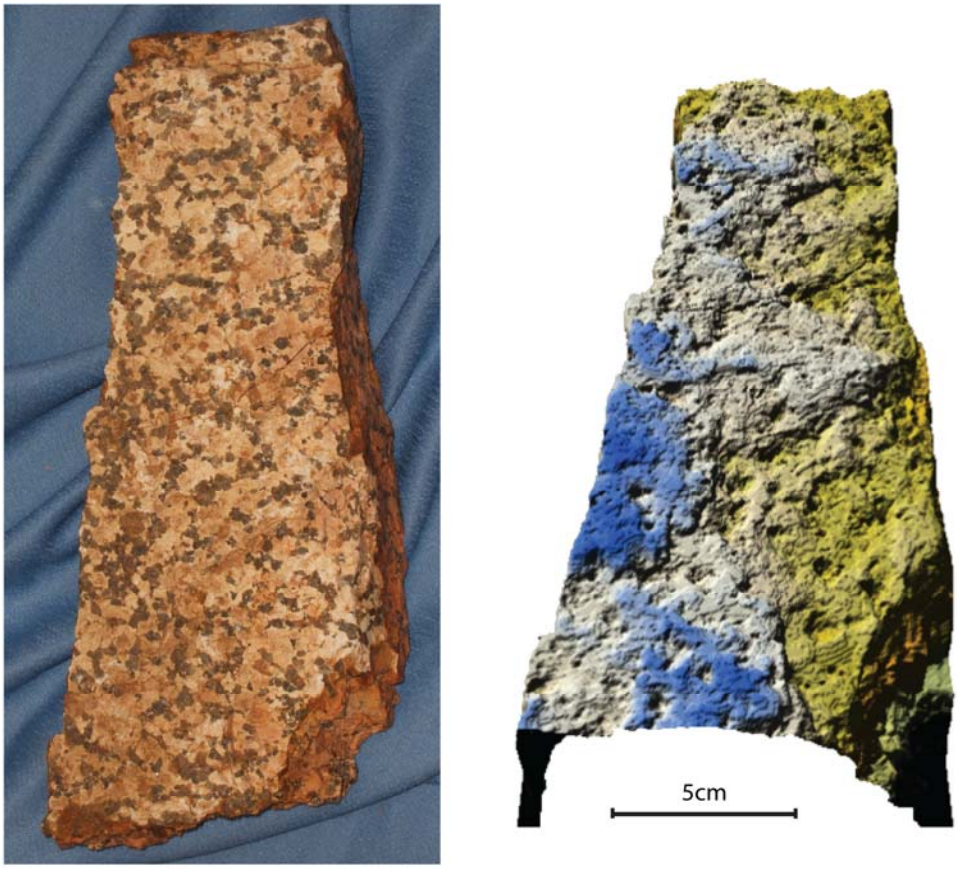

Figure 7.4 Calca Granite specimen on left. At right, digital representation of the Calca top surface. Inclusion of the lower right corner area would artificially roughen the surface of interest. Therefore, edges are systematically eliminated prior to surface sampling.

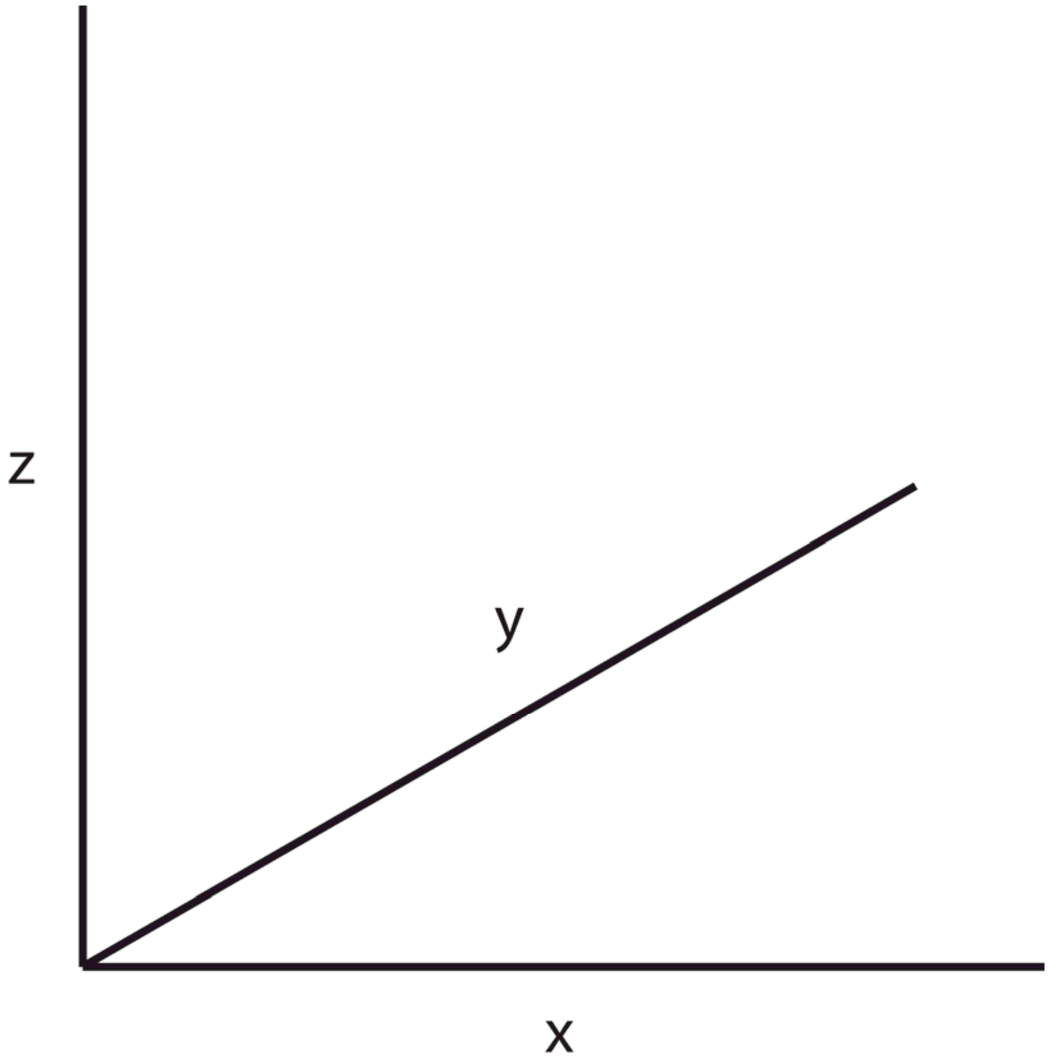

Figure 7.5 Common x y z coordinate system. For the purposes of discussing 3D arrays of CT data, this translates to array[x,z,y]. The array consists of y slices of x by z grayscale values. A surface array[x,y] of elevations remains after processing.

Samples are selected using *SampleGridVar.pro* (Appendix B.9), which converts the input surface to an array of *n* x *n* subsets evenly distributed across the original. While each arbitrarily rectangular surface is completely covered by 2^n sized square samples, overlap is kept to a minimum.

7.5 Results

Table 7.2 reports the S/S_0 values for 25 surface–spacing pairs used in this study and assigns a grouping to each that spans Very Smooth for an S/S_0 less than 1.03 through Very Rough with an S/S_0 greater than 1.20. Admittedly, the groupings are arbitrary at this point with a limited number of samples. However, three factors consistently influence roughness: 1) rock strength, 2) degree of weathering, and 3) surface coatings. For the purposes of this study, a fracture surface is classified as weathered if it exhibits visible degradation due to leaching or abrasion; fresh surfaces show no alteration products.

7.5.1 Closed Canyon samples

For the top surface of sample CC02-1 (Figure 7.6), the results of *SurfaceRoughness.pro* (Appendix B.10) are plotted in Figure 7.7 for sample sizes of 4 x 4 data points through 128 x 128 data points. These plots graphically illustrate the variation in S/S_0 across the sample width in the x direction. Each column of data represent the S/S_0 values for the *n* x *n* sized samples from the corresponding column of the sampled gridded surface. At a sample size of 11cm^2, the variance in the deviation from planarity across the surface is 4.1E-4. The black outline on Figure 7.8 describes the 11cm^2 sample size

Table 7.2 Sample names, rock type, skin type, total surface roughness and classification of all samples used in this study. *Notes:* *Fracture sample CC01-3 is inferred to be an impact fracture, not the result of an in situ stress regime, and is therefore rougher than expected for the welded tuff. +El03-sparse halves the data points of El03, reducing roughness by undersampling. #Paintbrush Tuff sample roughness is questionable due to multiple fracture horizons, increased roughness along the cut surface, and anomalous areas of CT numbers associated with x-ray deflection around mounting bolts and manometer ports.

Sample	Rock Type	Skin Type	S/S_0	Roughness Type
CC01-1	Welded Tuff	Fresh	1.045	Smooth
CC01-2	Welded Tuff	Weathered	1.062	Smooth
CC01-3top	Welded Tuff	Induced*	1.100	Moderate
CC01-3bot	Welded Tuff	Induced*	1.101	Moderate
CC02-1top	Semi-Welded Tuff	Weathered	1.104	Moderate
CC02-1bot	Semi-Welded Tuff	Weathered	1.103	Moderate
CC02-2top	Semi-Welded Tuff	Weathered	1.168	Rough
CC02-2bot	Semi-Welded Tuff	Weathered	1.167	Rough
Oatman top	Granite	Fresh	1.066	Smooth
Oatman bot	Granite	Fresh	1.059	Smooth
Fr-Wr	Granite	Weathered	1.179	Rough
Fr-MnO	Granite	Pyrolusite	1.047	Smooth
El01	Granite	Iron Oxide and clay	1.091	Moderate
El02	Granite	Iron Oxide and clay	1.098	Moderate
El03	Granite	Iron Oxide and clay	1.095	Moderate
El03-sparse+	Granite	Iron Oxide and clay	1.077	—
El-whole	Granite	Iron Oxide and clay	1.095	Moderate
Brushy top	Sandstone	Fresh	1.014	V. Smooth
Brushy bot	Sandstone	Fresh	1.019	V. Smooth
Pad	Green Granite	Weathered	1.221	V. Rough
Pad-sparse	Green Granite	Weathered	1.200	V. Rough
Pad opposite	Green Granite	Weathered	1.222	V. Rough
Calca	Granite	Weathered	1.200	V. Rough
YM left top#	Semi-Welded Tuff	Weathered	1.154	Rough
YM left bot#	Semi-Welded Tuff	Weathered	1.167	Rough

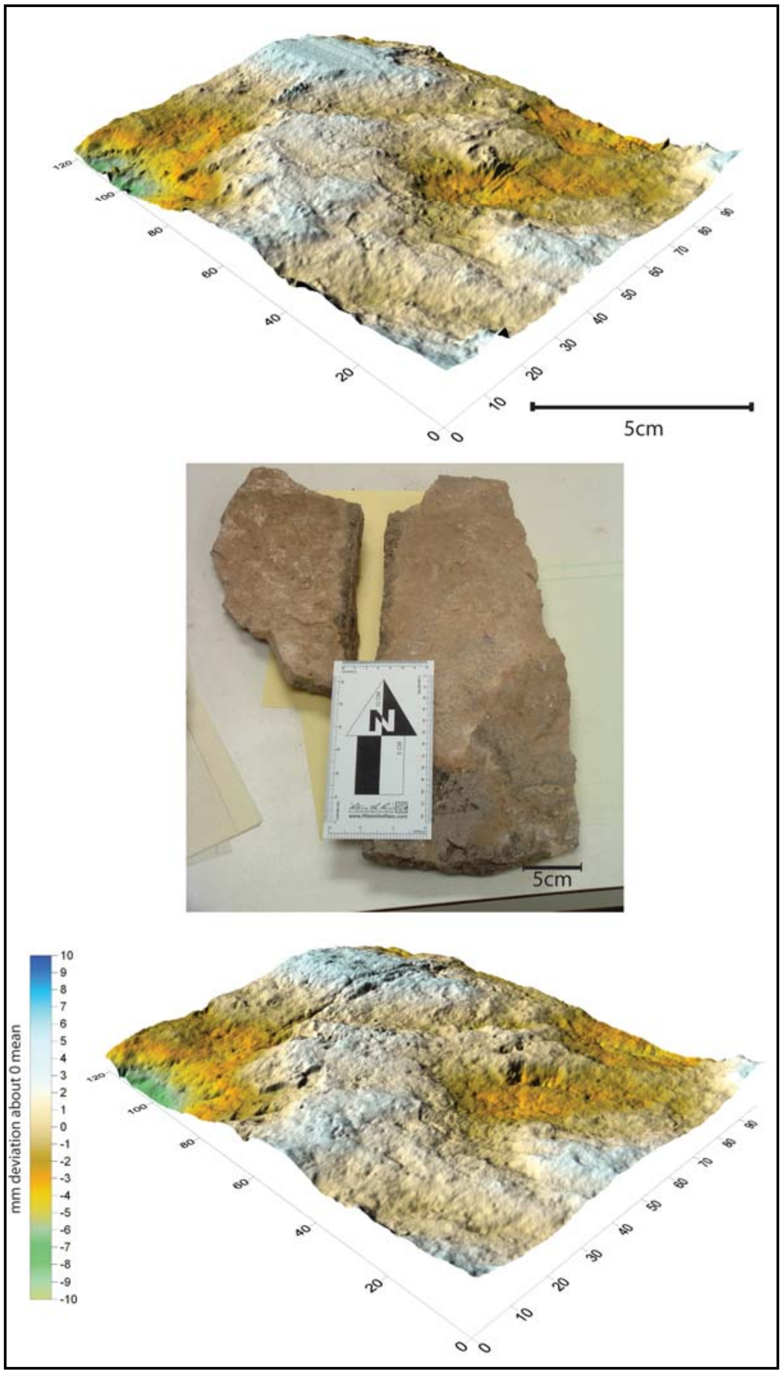

Figure 7.6 Specimen CC02-1 with visualizations of the zero mean top and bottom surfaces. Axes are in millimeters, and colors represent deviation in millimeters about the zero mean.

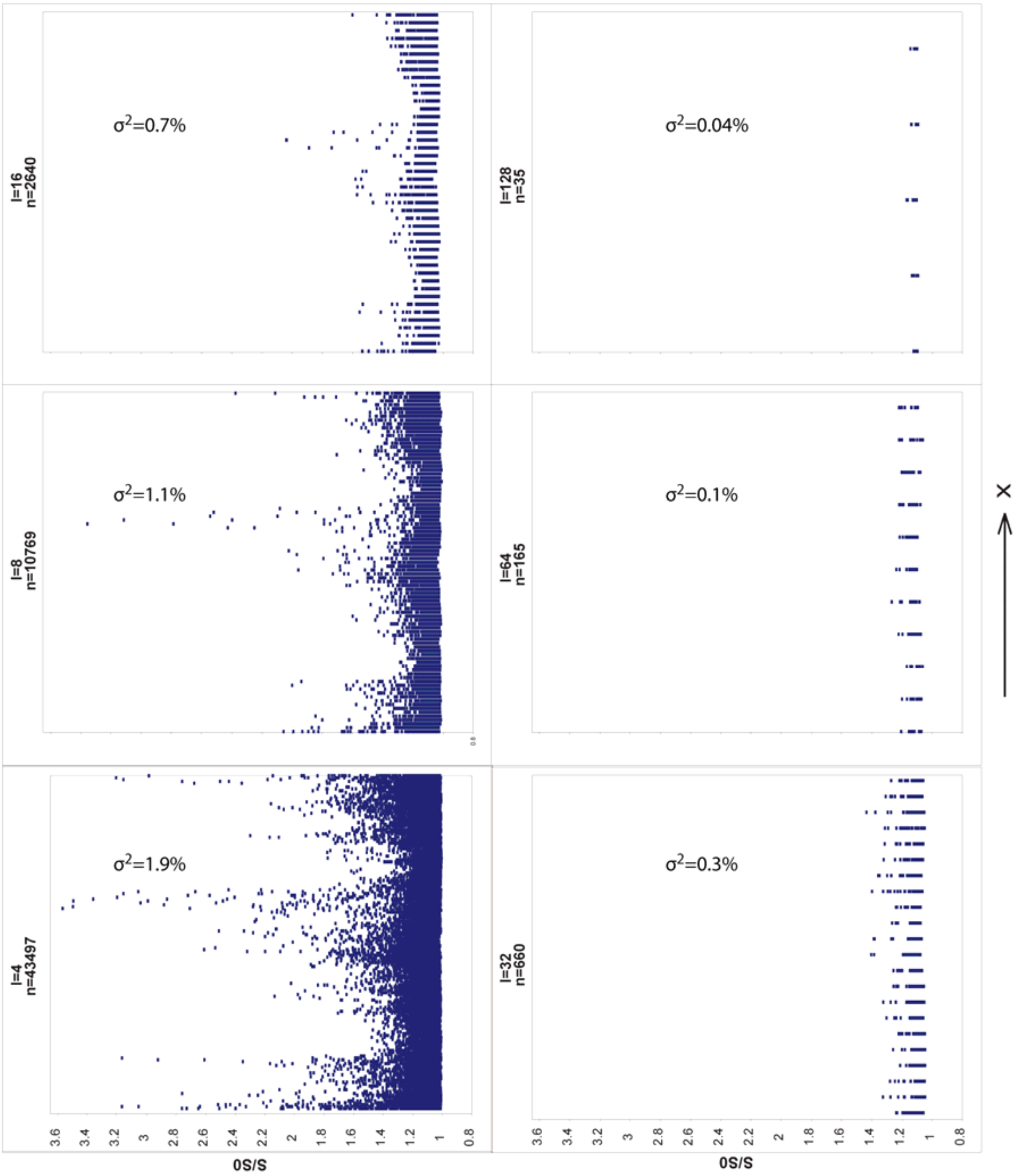

Figure 7.7 S/S$_0$ for sample CC02-1top with increasing sample size. Plots display the variation in roughness across the width of the sample. At a sample size of 11cm^2, corresponding to 128 x 128 pixels, the variance drops to 4.1E-4.

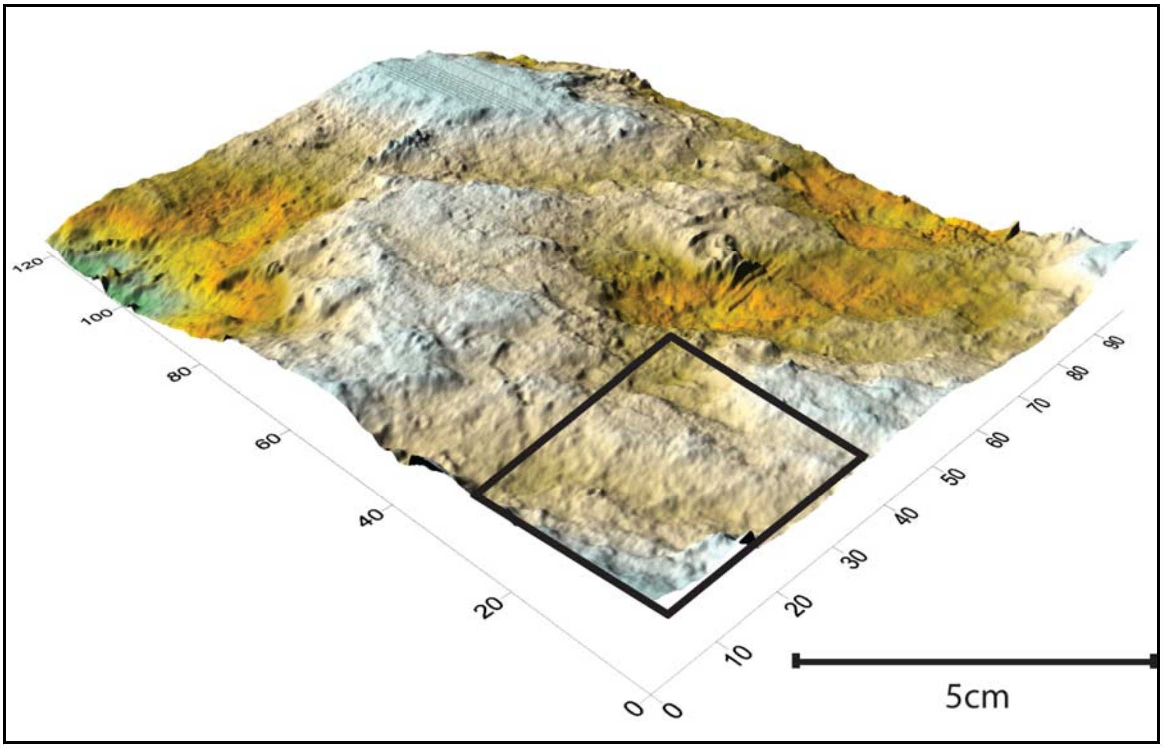

Figure 7.8 A Representative Elemental Surface for CC02-1top. Despite obvious inconstant undulation of the surface in its entirety, the roughness of the whole may be described from a much smaller sample.

relative to the whole surface. Further, the mean of all S/S_0 values at this sample size is indistinguishable from the entire surface roughness value of 1.111.

For a roughness metric to be useful on a wide scale, it should be applicable to the next fracture. For specimen CC02-2, the story is much the same. The 128 x 128 pixel sample corresponds to a 9.6cm^2 sample size. The mean value of S/S_0 is within 0.1% of the whole surface. The variance among the samples is 7.8E-4 for the top and 7.9E-4 for the bottom surface. However, the magnitude of S/S_0 is much different, 1.168 and 1.167 for top and bottom surfaces respectively. This disparity is inferred to be caused by the epoxy spray that preserved the surface roughness of CC02-2 through the sample preparation process.

The specimen CC01 consists of an unweathered fracture surface (CC01-1) subparallel with a weathered fracture surface (CC01-2) and a mated impact fracture (CC01-3) presumably from its fall to the floor of Closed Canyon. Calculation of S/S_0 for the transitional surfaces (Figure 7.9) yields anomalous results. The mean and median values for samples sized 4 x 4 pixels differ by 5.9%. At the 128 x 128 pixel sample size, the difference between mean and median is still 2.9%. This is due to the sampling of multiple fracture surfaces and is apparent by looking at the graphical results in Figure 7.10. The presence of a few samples of a given size that are inordinately rough can skew the mean noticeably higher than the median, but a difference of several percentage points over multiple sample sizes is a clear indicator that the surface sampled contains multiple fracture horizons.

The statistics of CC01-3 behave more regularly with variation in sample size (Figure 7.11). Of note is the roughness of this impact fracture compared to the natural

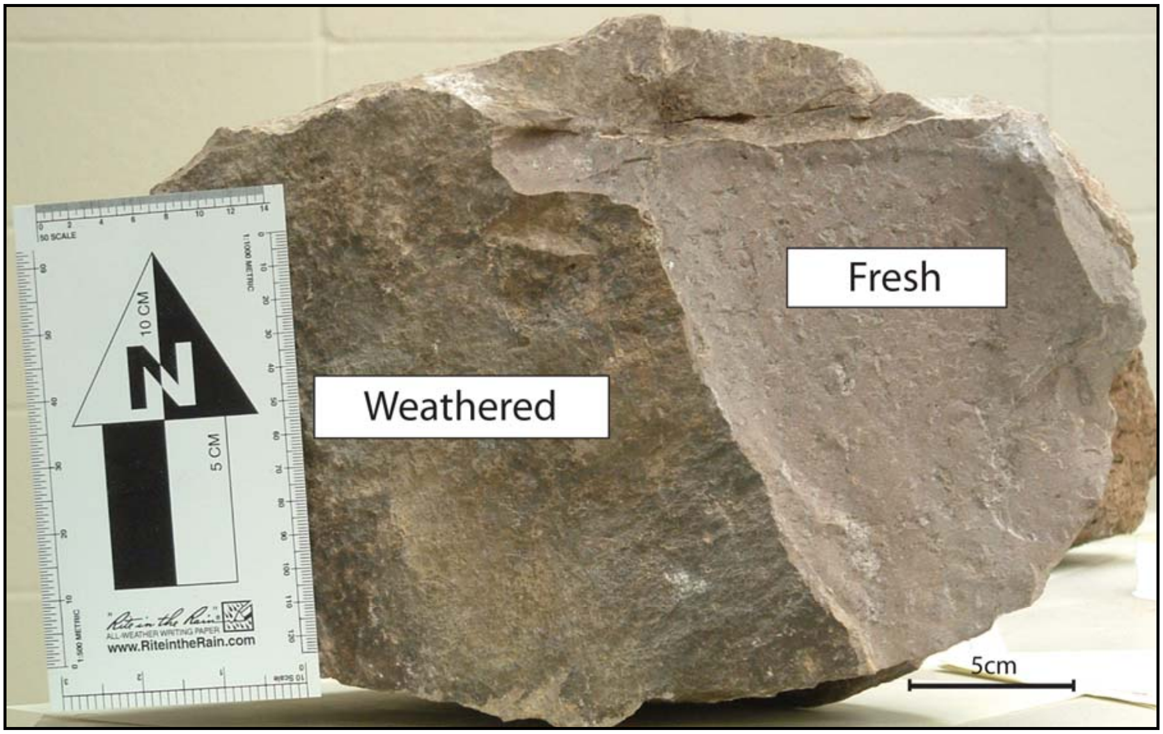

Figure 7.9 Specimen of welded Santana Tuff showing fracture surface samples CC01-1 (fresh surface) and CC01-2 (weathered surface).

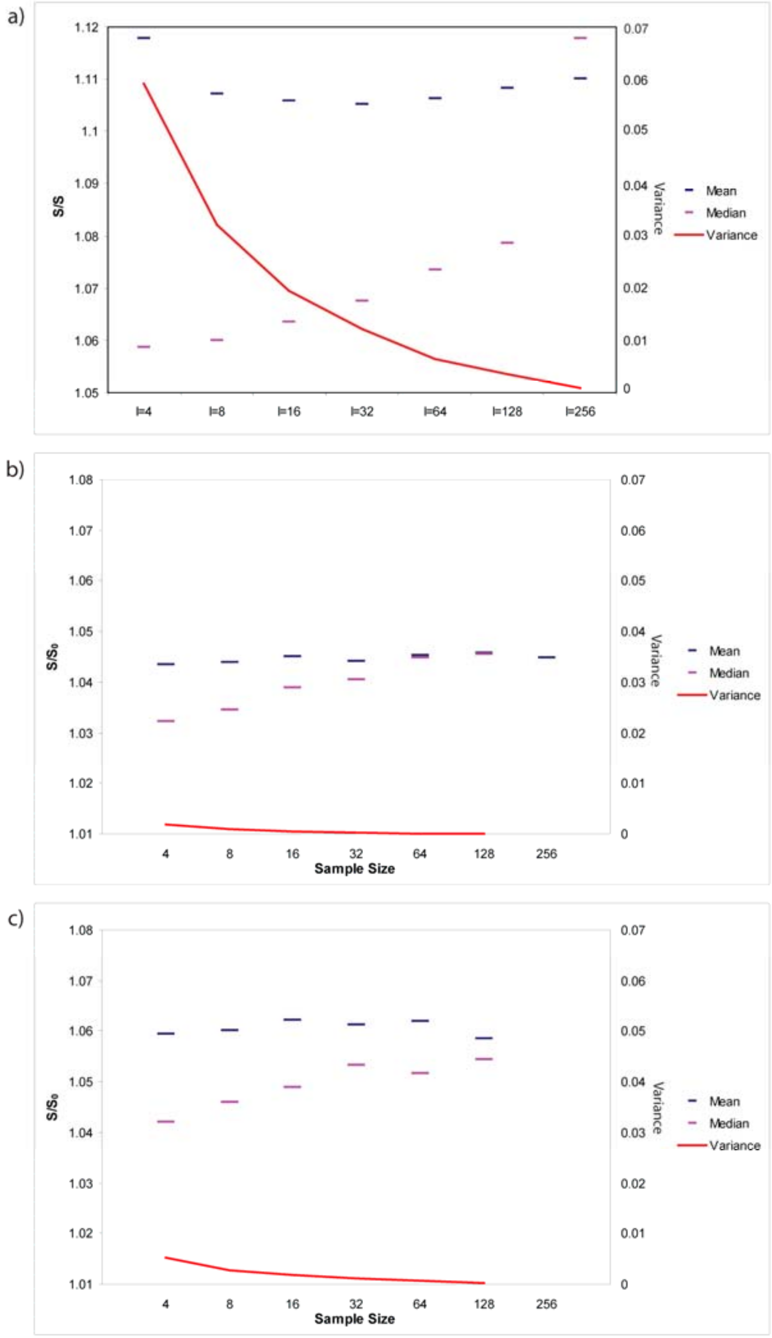

Figure 7.10 a) Variation in statistics with sample size for the slab containing fracture samples CC01-1 and CC01-2. b) Statistics of sample CC01-1 alone. c) Statistics of sample CC01-2 alone.

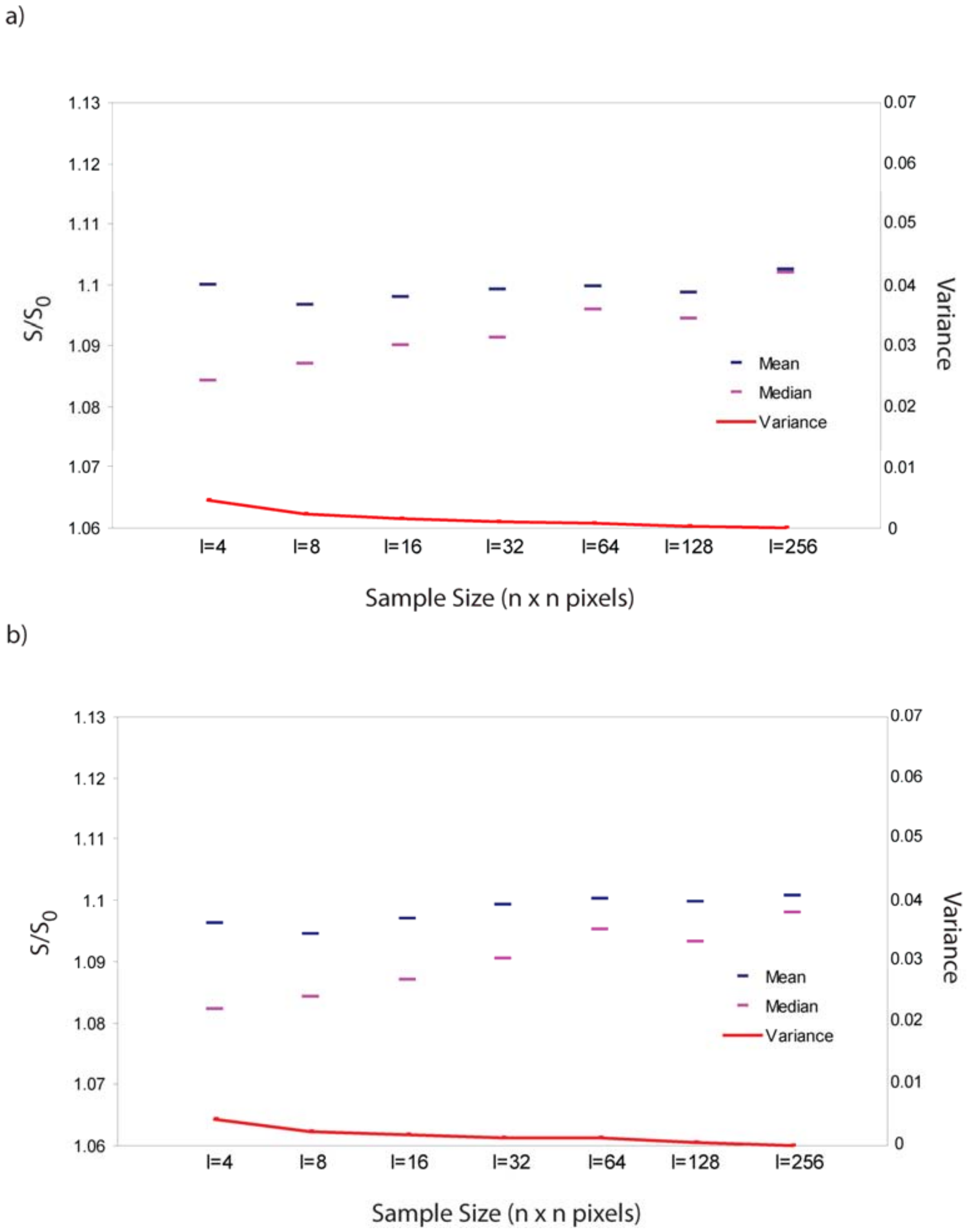

Figure 7.11 Variation in statistics with sample size for fracture sample CC01-3 top in a) and CC01-3 bottom in b).

fractures from the same specimen. I observe this roughness from induced fracturing in a number of granite samples and diorites in experiments that were designed to create my own fractures for flow testing. As the direction of this research followed the path of using natural fractures, I didn't pursue quantification of this effect. However, it is something to consider when encountering roughness measurements based on Brazil test type fractures. If natural fractures exhibit less roughness than that derived from induced fractures, the subsequent prediction of the effect of roughness on fluid flow through the naturally fractured media will be overestimated.

7.5.2 Town Mountain Granites

In addition to the Oatman Creek Granite fracture sample, two granitic fracture surfaces from the Llano uplift are included in this study. The Fr-Wr sample (Figure 7.12) has a 1cm weathering rind on the fracture surface of interest. A pyrolusite coating smoothes the surface of the Fr-MnO sample (Figure 7.13). These three samples provide a look at how skin type affects roughness on similar rock types.

The fresh surfaces of the Oatman Creek Granite fracture sample exhibit a S/S_0 of 1.066 for the top surface (Figure 7.14a) and 1.059 for the bottom (Figure 7.14b). As this fracture was originally oriented sub-horizontally, the disparity between the top and bottom surfaces may be attributed to breakage and mechanical weathering influenced by gravity. Although S/S_0 values in Table 7.2 are reported to 0.1% precision, discretizing roughness even to 1% increments in surface area may preclude grouping where otherwise it would seem appropriate. Variance among the samples at a size of 128 x 128 data

Figure 7.12 Town Mountain Granite fracture surface specimen Fr-Wr. The weathering rind induces significant roughness over what is observed on fresh surfaces.

Figure 7.13 Town Mountain Granite fracture specimen Fr-MnO. The pyrolusite coating smoothes the surface from the S/S_0 observed on fresh surfaces.

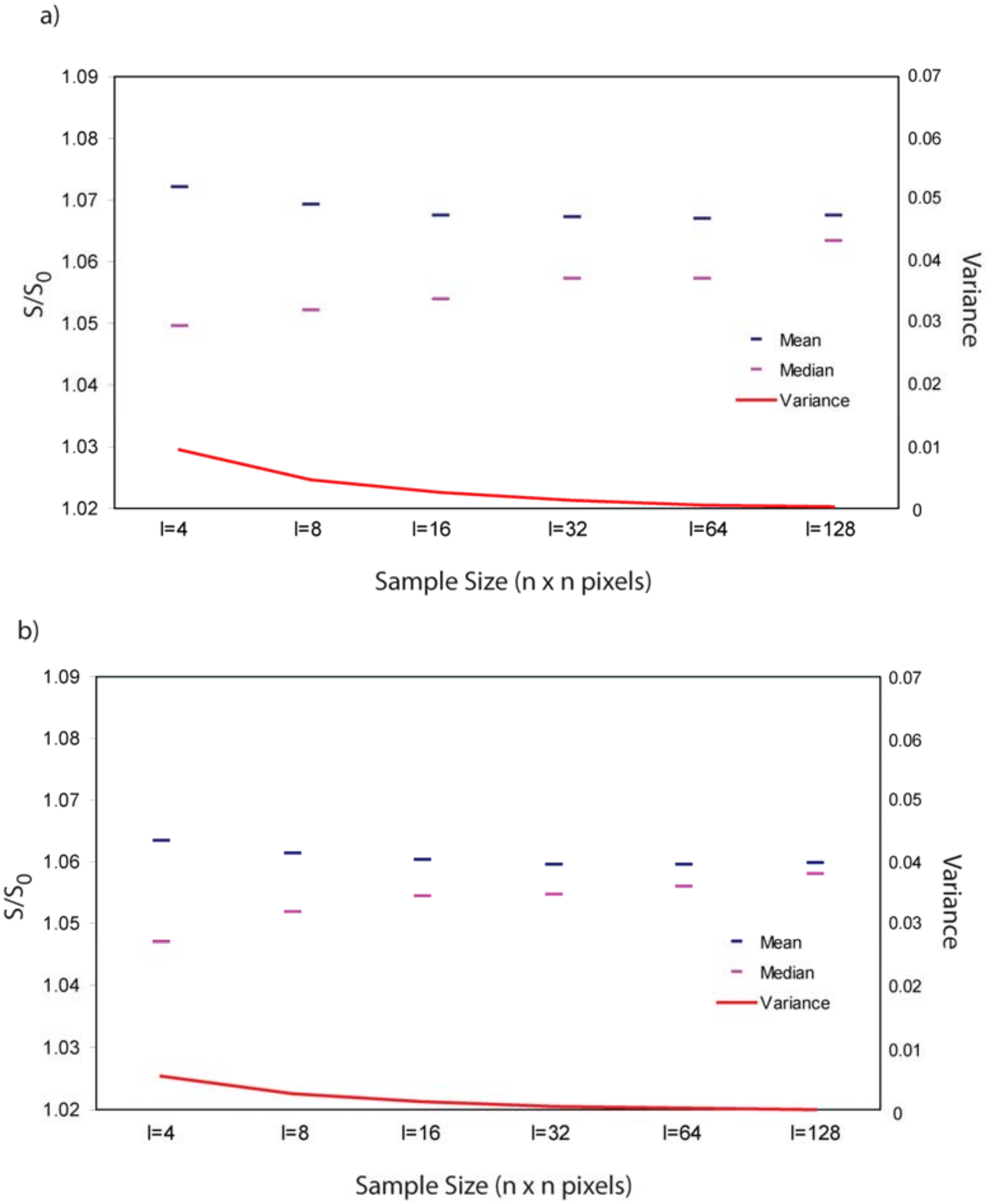

Figure 7.14 Variation in S/S_0 with increasing sample size for the Oatman Creek Granite sample a) top and b) bottom surfaces. At a sample size of 8.2cm^2, the variance among S/S_0 ratios is 2.5E-4 for the top surface with a whole surface roughness of 1.07, and 7.5E-5 for the bottom surface with a whole surface roughness of 1.06.

points, corresponding to 8.2cm^2, is 2.5E-4 and 7.5E-5 for top and bottom surfaces respectively.

Fracture sample Fr-Wr exhibits considerably greater roughness than the fresh surfaces from the Oatman Creek Granite sample. Figure 7.15, however, shows the same pattern of negligible variance among samples at a size of 128 x 128 data points. The S/S_0 ratio at this sample size, corresponding to 11.1cm^2 for the Fr-Wr spacing, is 1.176, while the whole surface S/S_0 is 1.179. Variance among samples at this size is 2.5E-4.

The pyrolusite coating on fracture surface sample Fr-MnO has a smoothing effect at the 0.25mm scale. Figure 7.16 shows the variation in S/S_0 statistics with increasing sample size. Among samples sized 11.6cm^2, the variance is 7.4E-4 and the mean S/S_0 is equal to that of the whole surface at 1.047.

The relative roughnesses of the Town Mountain Granite samples behave as hypothesized. The pyrolusite coatings are controlled by redox reactions and require loss of fluids (Garner 2007). Under these conditions, coatings will begin to form and spread at spill points, filling in lows, reducing roughness. The weathering surface results from leaching and differential mechanical weathering of the mineral constituents of the granite. Both of these processes remove material in a spatially variable manner and increase total surface roughness.

7.5.3 Elberton Granite

The Elberton Granite exfoliation joint specimen is pictured in Figure 7.17. The full-size specimen did not meet the requirements for CT imaging, so it was cut into three distinct samples (El01 through El03) for scanning and analysis. This specimen serves as

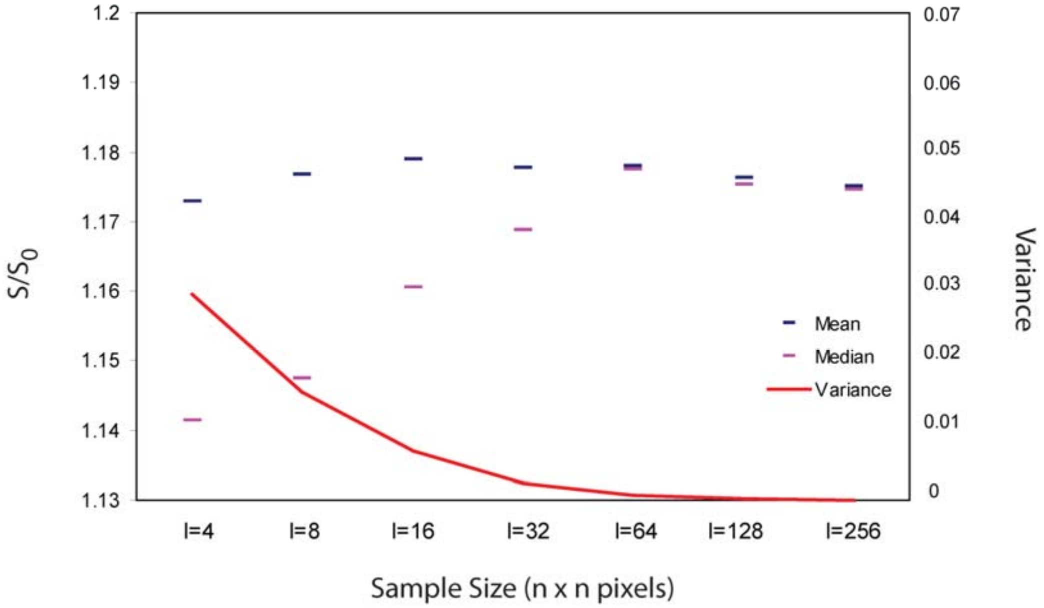

Figure 7.15 Variation in S/S_0 statistics with increasing sample size for Fr-Wr. At a sample size of 11cm^2, the variance among samples is 2.5E-4 and the mean is 1.176 compared to the whole surface S/S_0 of 1.179.

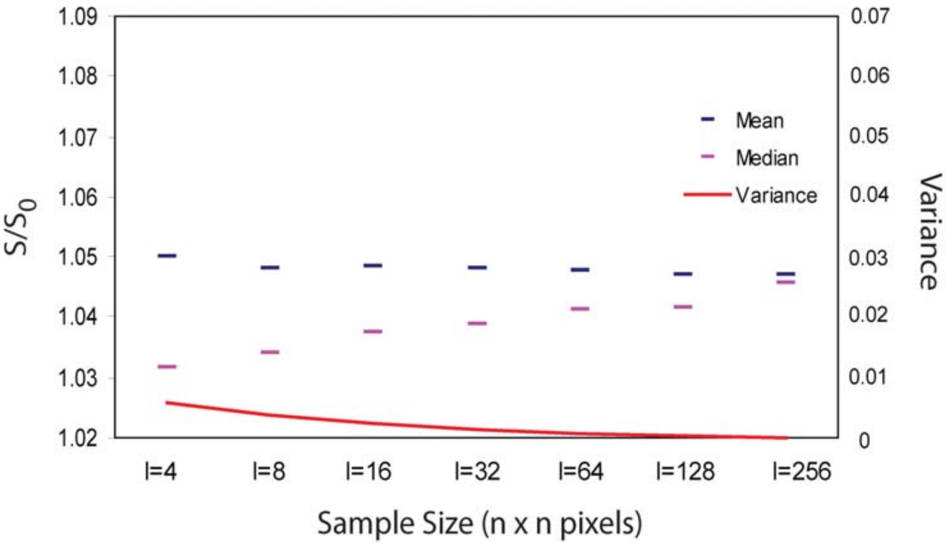

Figure 7.16 Variation in roughness statistics with increasing sample size for fracture surface sample Fr-MnO. At a sample size of 128 x 128 pixels corresponding to 11.6cm^2, the variance among sample roughness is 2.4E-4. The mean S/S_0 at this sample size is 1.047, as is that of the whole surface.

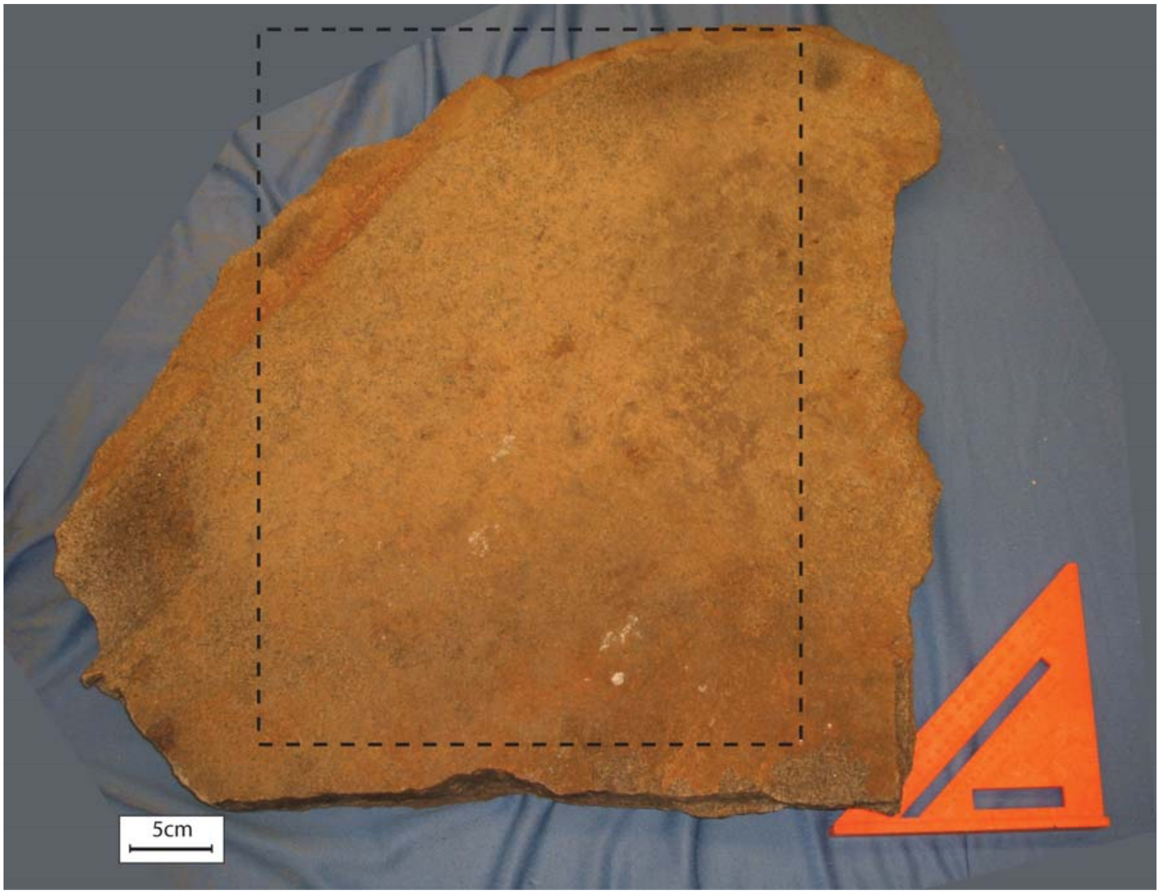

Figure 7.17 Elberton Granite exfoliation joint with clay and iron oxide coating. Dashed line is an approximation of the extent of samples El01 through El03. This specimen serves as a proof of concept for incorporating multiple samples into one roughness measurement.

proof of concept that multiple samples can be combined into a single surface for purpose of assigning a roughness.

The variation with sample size of the S/S_0 statistics for the three individual samples is presented in Figure 7.18. The S/S_0 roughness for the whole of El01 is 1.091, and 1.098 for El02. As the two samples do not line up perfectly due to missing material from the saw blade and possible variation in the orientation of the samples for CT imaging, it would be inappropriate to sample roughness across the boundary. I handle the bridging of samples with my overarching script, *WriteSurfRough.pro* (Appendix B.7) that writes the sample roughnesses for samples sized 4 x 4 through 2^n x 2^n, where

$$n = floor\left(\log_2\left(\min\left(S_{\text{dim}}\right)\right)\right), \tag{7.12}$$

and S_{dim} is the 2D dimensions of the sample. Where a sample crosses the user defined midpoint, one of three possibilities exists: 1) there is greater than one column of data on either side of the boundary; 2) the first column of the sample is the column before the boundary; or 3) the last column of the sample is the first column after the boundary. In the case of 2) or 3), roughness is undefined for the area of a line, and the roughness for that sample is the S/S_0 value of the remaining columns. Where there are at least two columns of data on both sides of the boundary, the roughness is assigned as the weighted roughness of each partial sample as:

$$S / S_0 = \frac{w_1}{2^n} \cdot \frac{S_1}{2^n \cdot \left(2^n - w_2\right)} + \frac{w_2}{2^n} \cdot \frac{S_2}{2^n \cdot \left(2^n - w_1\right)}. \tag{7.13}$$

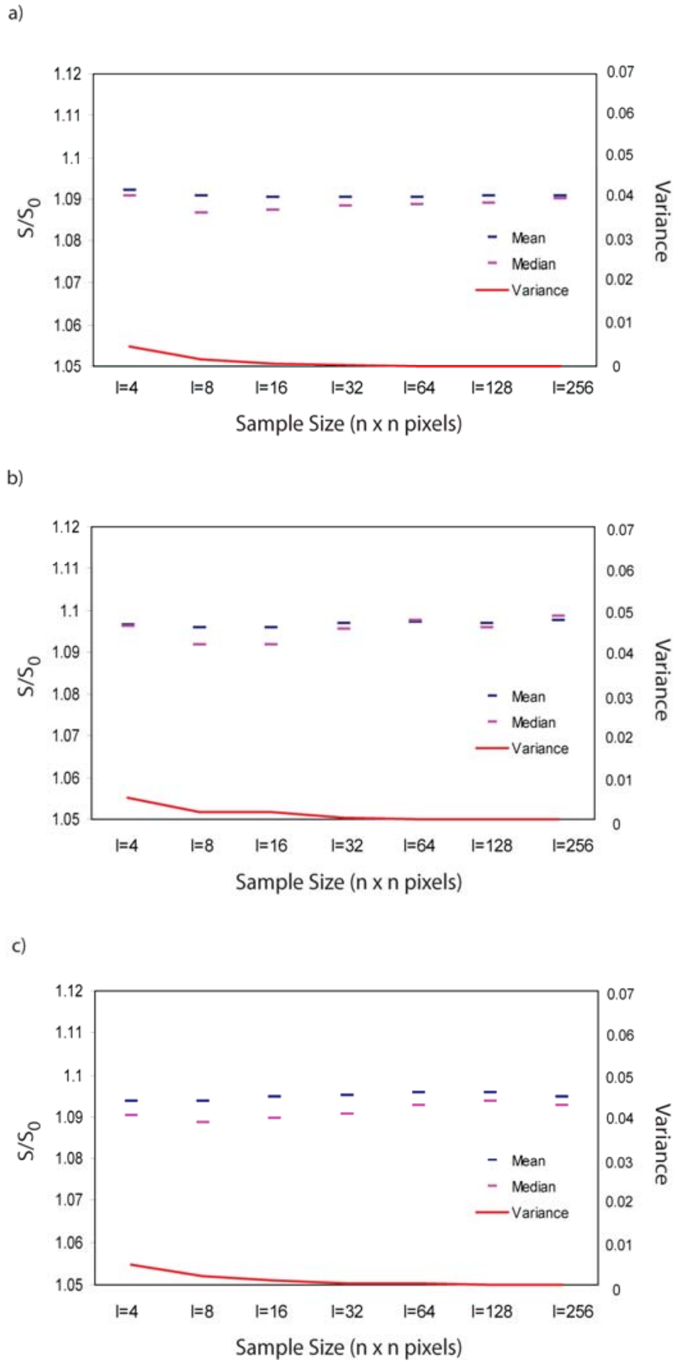

Figure 7.18 Variation of S/S_0 statistics with sample size for a) El01, b) El02, and c) El03. The whole surface roughness is 1.095. Roughnesses for the individual samples are 1.091, 1.098 and 1.095 for El01 through El 03 respectively. Variance is less than 1% for all sample sizes.

For the combination of the two surfaces, the 11.6cm^2, 128 x 128 data point sample mean roughness is 1.095, equal to the whole surface roughness, with a variance among samples of 5.8E-5.

Whether the difference in roughness between the Elberton Granite and the Town Mountain Granite is due to the nature of the clay and iron oxide coating or the fabric of the rock matrix is not identifiable from one Elberton sample; a fresh fracture surface would be required to discriminate a probable cause. What can be said is that the S/S_0 value for the Elberton Granite with coating is very similar to the roughnesses of the semi-welded tuff fracture sample, CC02-1, and the induced fracture in welded tuff, CC01-3.

The close match of the S/S_0 value for El03 to the other two Elberton Granite samples is misleading. The El03 CT scan output has 0.15mm horizontal resolution, as opposed to the 0.28mm horizontal spacing of the other two samples. Therefore, the expected roughness for El03 is greater than 1.095. However, the anomalous results are not attributed to variation in the rock fabric or coating of the original specimen. Figure 7.19 shows residual clay infilling on El03 not present on either El01 or El02, presumably resulting from incomplete rinsing of the sample after cutting the specimen to a size appropriate for CT imagery. Using a horizontal spacing of 0.30mm and calculating roughness on El03 yields a whole surface S/S_0 of 1.077. The difference between this and the 1.095 of the "clean" sample is very similar to that of the roughness of the pyrolusite coating on the Town Mountain Granite and the roughnesses of the fresh Oatman Creek Granite surfaces.

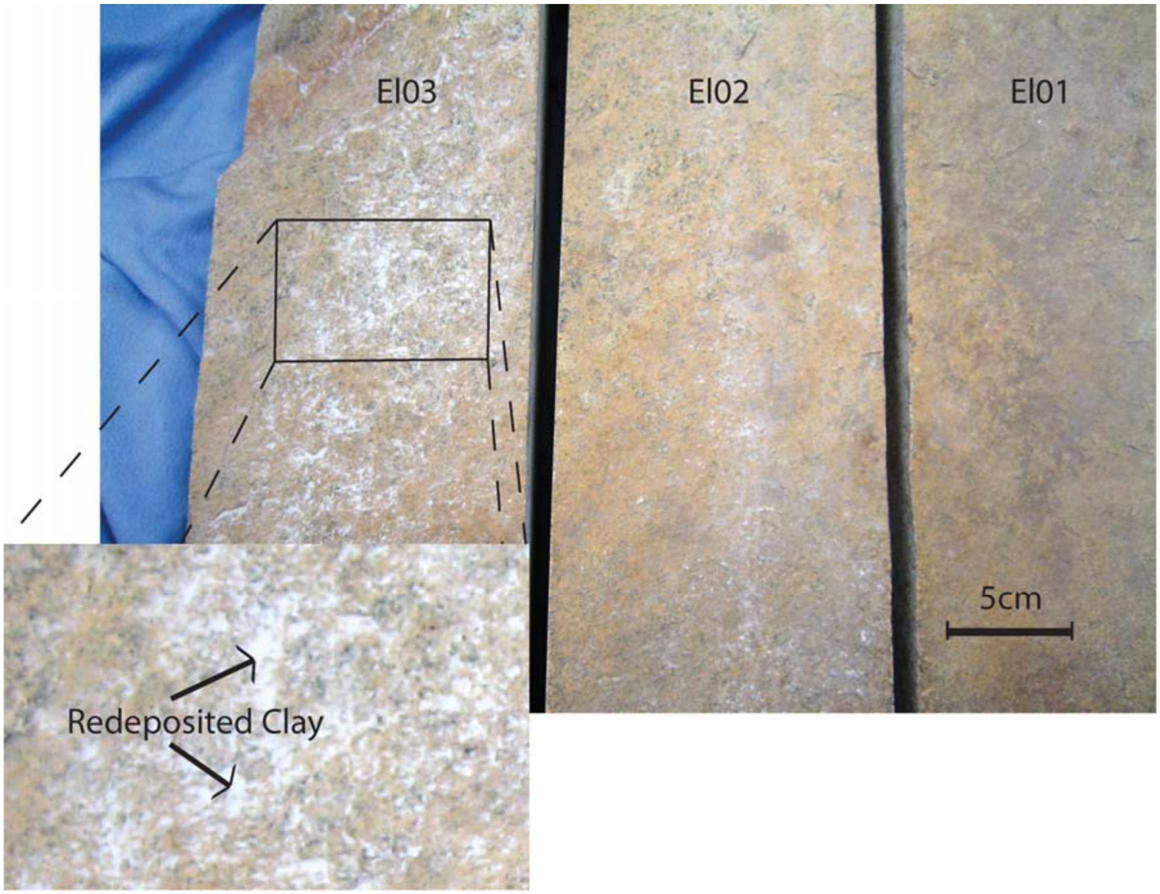

Figure 7.19 From left to right: fracture surface sample El03, El02, and El01. Notice the clay infilling on El03 not present on the other two fracture surfaces. This is attributed to recirculation of fine material through the pump supplying water to the saw used to cut the specimen to a size appropriate for CTimagery.

7.5.4 Calca Granite

The coarse-grained Calca Granite specimen consists of two weathered, vertical fracture faces; only the right fracture face provided a sufficiently large data set for inclusion here. The S/S_0 statistics variation with sample size is depicted in Figure 7.20. At a sample size of 10.8cm^2, the mean of the S/S_0 values is equal to that of the whole surface at 1.20. The variance among the roughnesses of these 128 x 128 data point samples is 0.13%, somewhat larger than is typical from the previous samples. The high variance is attributed to the high degree of weathering in this sample and the presence of sub-millimeter scale fractures intersecting the surface (Figure 7.21).

7.5.5 Padthaway Granite

Another coarse-grained, highly weathered granite from South Australia, the Marcollat green granite specimen from Padthaway provides two surfaces at a CT scanned resolution of 0.17mm in the x direction. One surface (Pad) is a continuous fracture surface evidenced by a sub-parallel fracture horizon adjacent to the weathering rind. The opposing side (Pad-opposite) is more ambiguous. While the surface is unbroken, the weathering rind is completely eroded from one corner (Figure 7.22); therefore, the surface cannot be considered as representing a single fracture.

Figure 7.23 displays the statistical results of sampling the two surfaces. The results of the Pad sample are similar to those for the Calca sample. Variance at a sample size of 128 x 128 data points is 0.12%; however, this corresponds to a sample size of 7.0cm^2. Picking a sparse data set and calculating the roughness statistics yields a whole surface roughness of 1.20, similar to that of the Calca sample, but the variance among

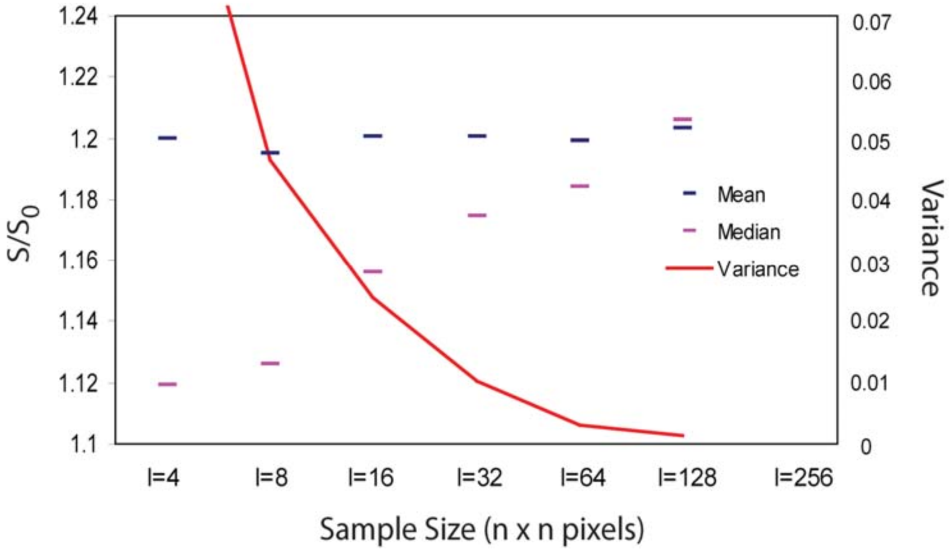

Figure 7.20 Variation in statistics with sample size for Calca Granite fracture surface sample. High degree of weathering and occurrence of intersecting fractures increases variance among samples, yet at a sample size of 128 x 128 data points, variance is still only 0.13%. Mean S/S_0 value at this size is 1.20, equivalent to that of the surface as a whole.

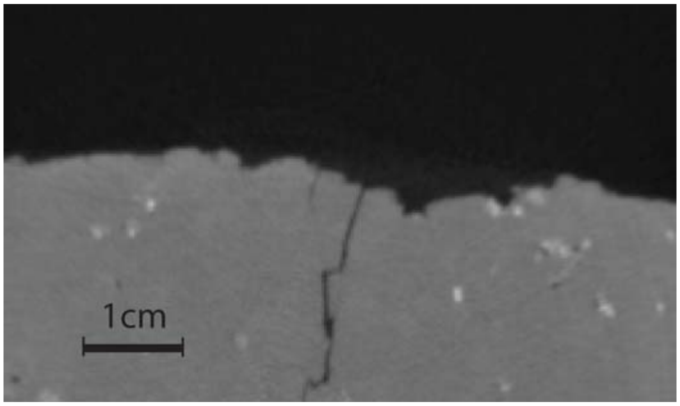

Figure 7.21 CT slice from Calca sample showing incidental sub-millimeter scale fractures intersecting the analyzed surface. The presence of such fractures within samples systematically increases S/S_0 values for those samples. This has the effect of increasing variance among samples of a particular size where the majority of samples do not have occurrence of such fractures.

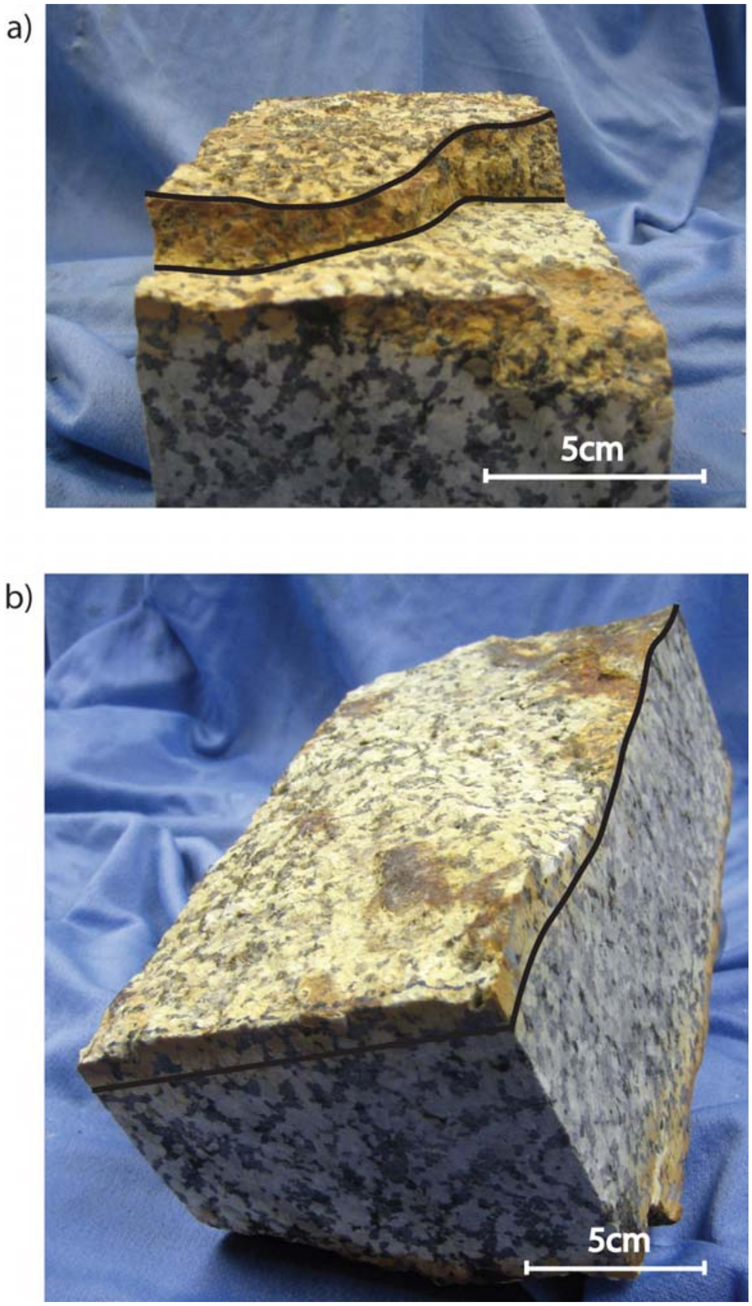

Figure 7.22 a) Fracture surface sample Pad with lines showing sub-parallel fracture planes. b) Pad-opposite displaying the erosion of the weathering rind toward the upper right corner. This differential weathering adds a component to roughness apparent from analysis of the statistical trend of S/S_0 values with increasing sample size.

a)

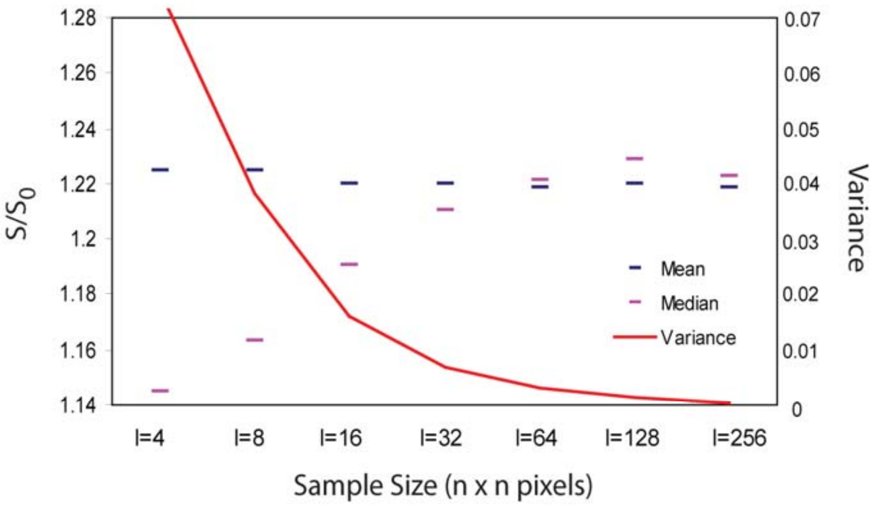

b)

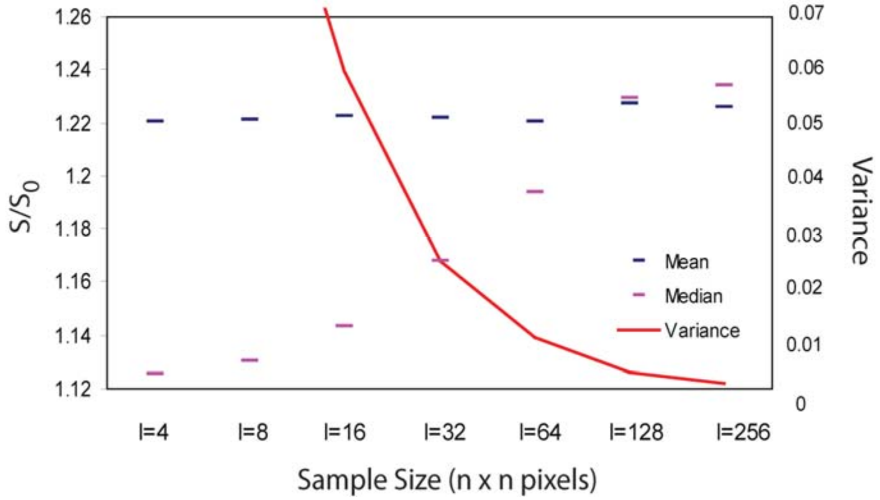

Figure 7.23 Variation in statistics with increasing sample size for a) Pad and b) Pad-opposite. For the Pad sample, using 128 x 128 data points, corresponding to a sample size of 7.0cm^2, the mean S/S_0 value is 1.22, equivalent to that of the whole surface, and the variance at that size is 0.12%. Pad-opposite has a mean sample roughness at 128 x 128 data points of 1.23, versus the whole surface roughness of 1.22. The variance among samples sized 7.0cm^2 is 0.3%.

samples of 128 x 128 data points, corresponding to 13.9cm^2, is 5.0E-4, more in keeping with the expected value for a single fracture surface.

For Pad-opposite, the differential weathering of the fracture surface produces variation in statistics with sample size resembling what would be expected from multiple fracture surfaces represented in a single sample. The gap between the median and the mean roughness values in general indicates that the sample size is insufficient to capture enough of the rough character of the overall surface. The failure of the median S/S_0 value to approach the mean through a sample size of 64 x 64 data points additionally points to a transitional surface that increases apparent roughness.

7.5.6 Paintbrush Tuff

YM-top and YM-bot comprise the data sets used from the Paintbrush Tuff specimen for this study. The S/S_0 values for both data sets fall in the range of the Santana Tuff sample with preserved clays (CC02-2) and the Town Mountain Granite with weathering rind. In this section, I describe these results and offer justification for accepting these values.

As described in Section 4.2.1, scanning the specimen with retaining bolts and copper manometer ports in place complicates accurate placement of the fracture surfaces. Figure 7.24 highlights the areas of the retaining bolts (red circles) and the manometer ports (black circles) in the top surface data set. While circular features on the surface are associated with the manometer ports, the retaining bolts make no apparent impression on the surface calculated from masked CT slices.

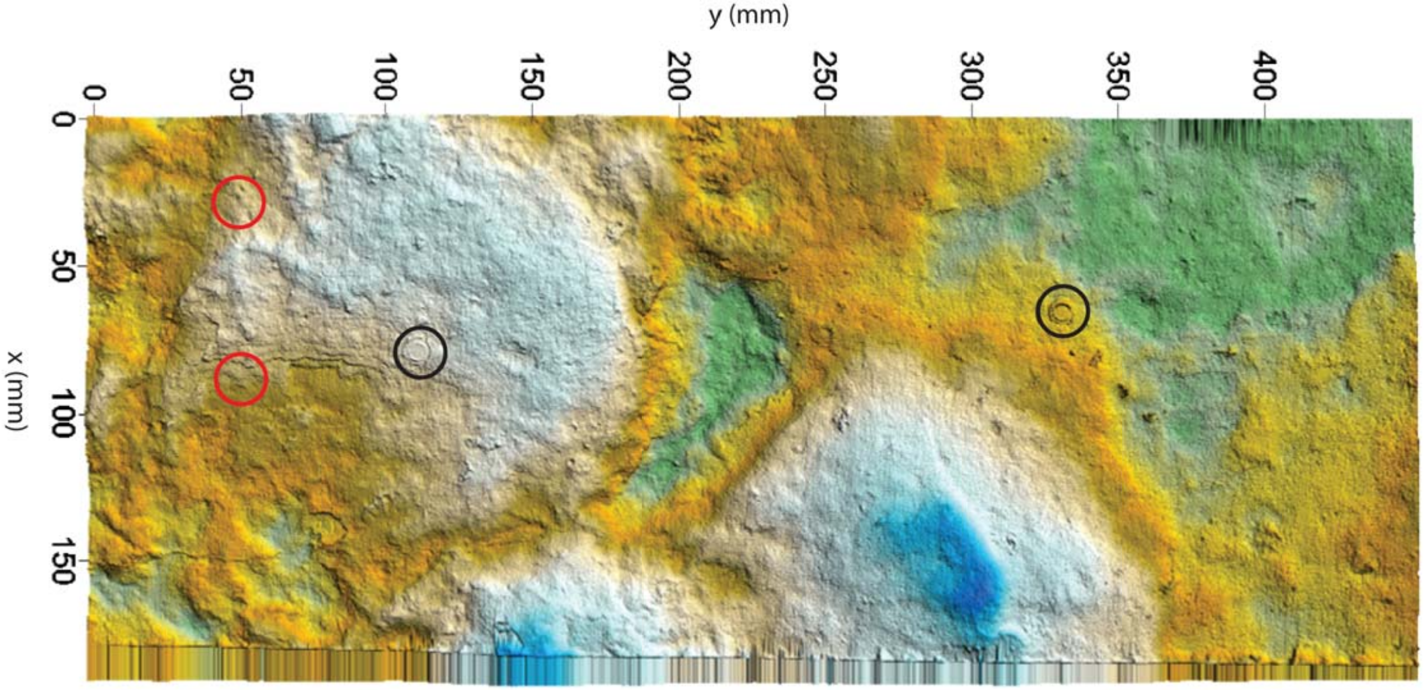

Figure 7.24 Top surface of left side of Paintbrush Tuff fracture specimen. Effects on surface due to copper manometer ports are circled in black. Areas of influence on surface by retaining bolts are circled in red, but not visible. Both these effects are insignificant to roughness measures compared to the area of zero aperture on the right side of the data set resulting from the non-vertical orientation of the sample during scanning.

More of an issue for roughness calculation and numerical modeling is the slight angle from vertical of the CT data set. Since the inlet and outlet conditioning reservoirs are connected to the fracture independently via retaining brackets, it was not deemed necessary to have the outlet directly opposite the inlet; it was sufficient that they be parallel and that the openings be the same length. This physical convenience produces the surface effect observed on the right side of Figure 7.24. This area is all systematically set to zero aperture in the procedure *GetVertCrackOptimize.pro*, but significantly increases roughness. Therefore, for the statistical treatment, only the maximum extent of rectangular data is included.

Figure 7.25 displays the variation in S/S_0 statistics with increasing sample size. The variance among samples sized 128 x 128 data points is 0.15% and 0.19% for the top and bottom surfaces of YM-left respectively. The individual roughness values at a sample size of 32 x 32 data points illustrate the variance nicely in Figure 7.26. The anomalous area in the upper left corner is attributed to contact and does not reflect surface roughness as the actual individual surfaces are not resolved. Likewise, the residual contact area on the lower left edge. Removing just these two points from calculation at the 9.4cm^2 sample size drops variance to 0.13% for the top surface.

7.5.7 Brushy Canyon Sandstone

While not suitable for flow testing, one soft rock fracture specimen was prepared and scanned, with data provided in Thompson (2005). In the case of the Brushy Canyon Sandstone fracture sample, S/S_0 values for the top and bottom whole surfaces are 1.01 and 1.02 respectively, equivalent to the mean value of samples sized 128 x 128 data

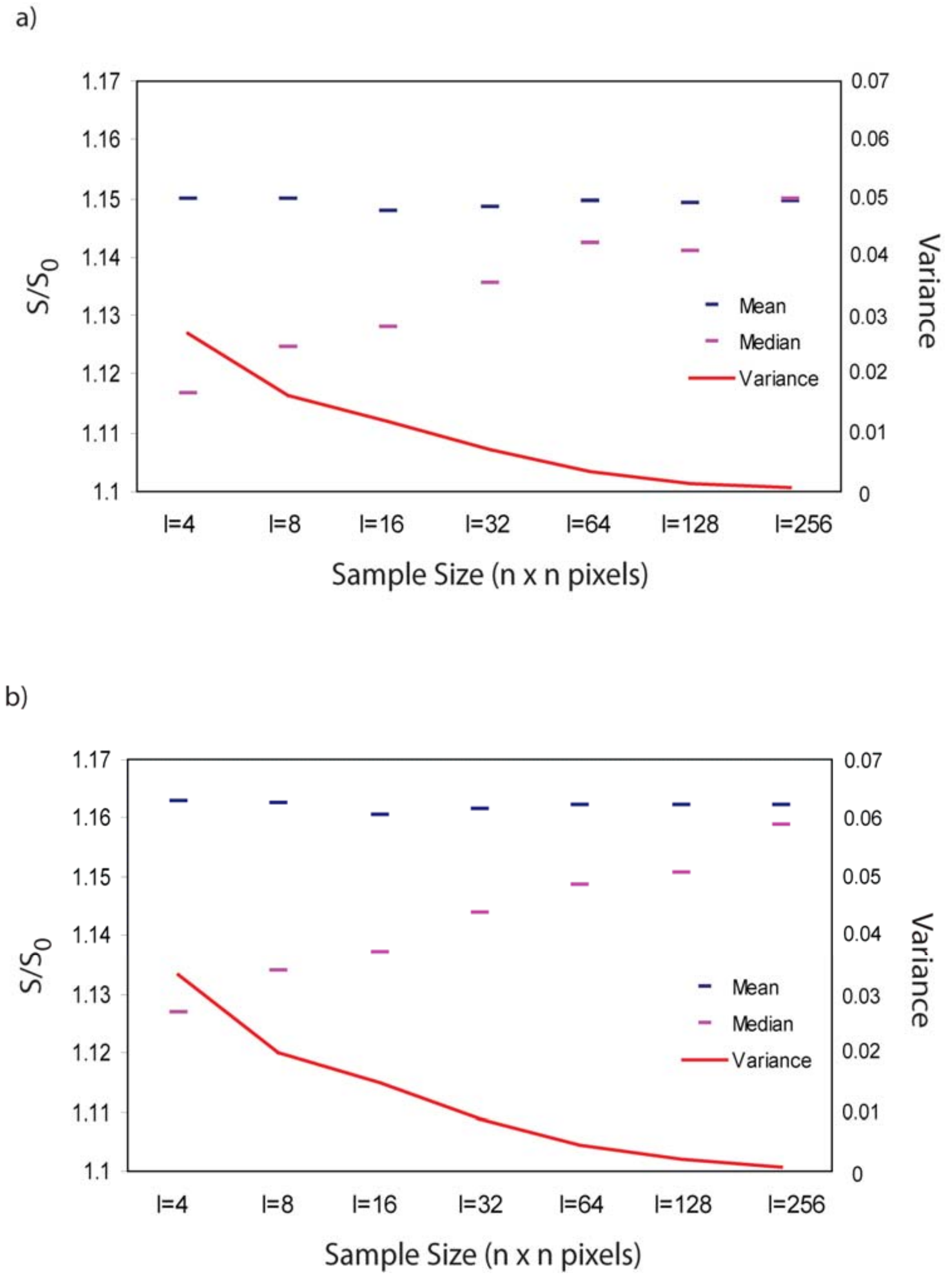

Figure 7.25 Variation in statistics with sample size for left side of Paintbrush Tuff fracture sample top (a) and bottom (b) surfaces. At a sample size of 9.4cm^2, the variances among the samples are 0.15% and 0.19% for the top and bottom surfaces respectively. The mean surface roughness at this 128 x 128 data point sample size is 1.15 for the top surface and 1.17 for the bottom surface

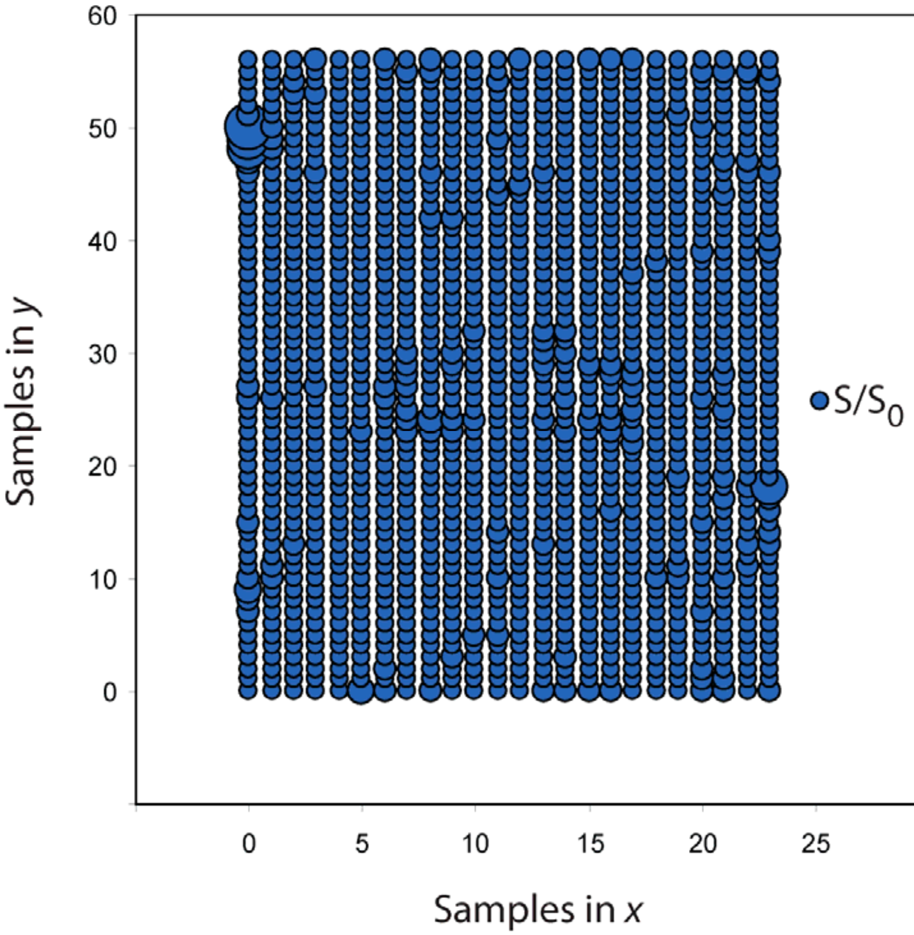

Figure 7.26 Variation in S/S_0 as a function of *x* and *y* at a sample size of 32 x 32 data points for the top surface of YM-left with the zero aperture columns on the right side removed. At this sample size the variance in the upper left due to the manner in which contact is resolved into surfaces is clearly illustrated. Comparing this figure with Figure 7.23, little effect on roughness can be attributed to either the manometer ports or the retaining bolts.

points (8.2cm^2). The variance among samples starts at a 10^{-4} order of magnitude at the 4 x 4 data point size, decreasing to 1.1E-5 and 2.8E-5 at the 8.2cm^2 sample size (Figure 7.27).

7.6 Discussion

Plotting the total surface roughnesses of all samples used in this study in Figure 7.28 illustrates some natural groupings. A roughness classification scheme from very smooth to very rough is proposed to take advantage of these groupings among rock types and surface coatings. Further refinement of these groupings with increased samples may allow an estimate of the effect of surface roughness on fluid flow with no requirement for gridded elevation data.

7.6.1 Very smooth

The fine-grained bedding plane fracture of the Brushy Canyon Sandstone specimen presents a very smooth surface. This is expected from the relative strength of the cement material compared to the strength of the quartz matrix; fracture propagation around grains that are roughly close-packed yields a sub-planar surface with roughness controlled by grain size. I place the boundary for very smooth fracture surfaces at an S/S_0 less than 1.03.

7.6.1 Smooth

The fracture surfaces within the range $1.03 \leq S/S_0 < 1.08$ are classified as smooth and include the samples Fr-MnO, CC01-1 and 2, and the fresh granite surfaces of the Oatman Creek fracture specimen. The nature of the growth of the pyrolusite coating, filling in lows from highs, is the control on roughness for the surface. Degree of welding

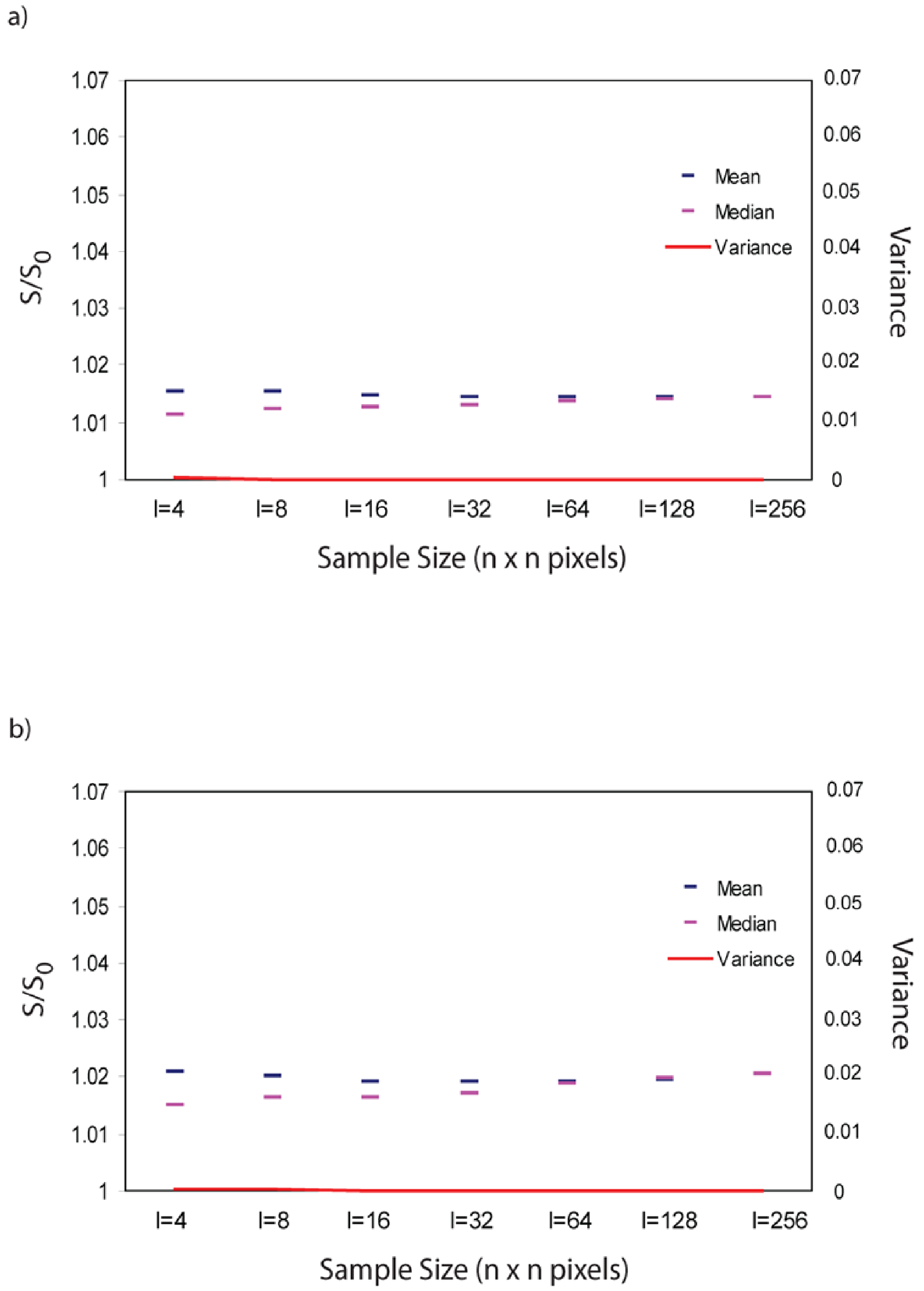

Figure 7.27 Variation in statistics with sample size for Brushy Canyon Sandstone fracture sample a) top and b) bottom. Variance among samples is less than 0.05% even at the 4 x 4 data point sample size, corresponding to $0.8mm^2$.

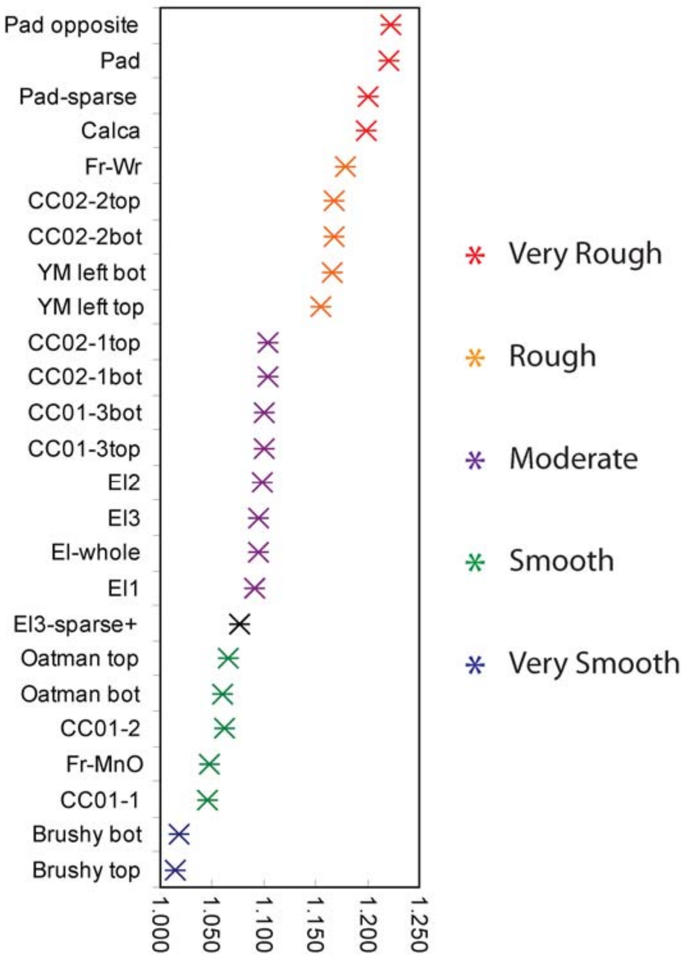

Figure 7.28 Grouping of similar S/S_0 surfaces into a classification ranging from very smooth at S/S_0 values less than 1.025 to very rough for S/S_0 values greater than or equal to 1.2.

influences the roughness of the Santana Tuff specimens. The welding process imparts a eutaxitic fabric to the tuff in response to viscous deformation of pyroclasts. This organized overprint to the ash flow material causes deposition parallel fractures to be less rough than vertical fractures through the unit. The roughness of the fine-grained Oatman Creek Granite is controlled by crystal size of the matrix material.

7.6.3 Moderately rough

Eight of the twenty-five surfaces fall within the range $1.091 \leq S/S_0 \leq 1.104$. However, for continuity, and recognizing that classification boundaries may change with additional data, roughnesses of $1.08 \leq S/S_0 < 1.13$ are classified as moderately rough. These surfaces include the individual Elberton Granite samples, the Elberton Granite surface as a whole, both surfaces from the impact fracture specimen CC01-3, and the surfaces from Santana Tuff fracture specimen CC02-1.

The fine-grained Elberton Granite sample surfaces exhibit considerably greater roughness than the surfaces of the lithologically similar Oatman Creek Granite specimen. While I have shown that infilling of clays is a smoothing process, chemical weathering is dominantly roughening. Therefore, the difference between the two specimens is inferred to be due to fresh versus weathered condition, rather than differences in composition or specimen size.

Two factors contribute to the roughness of CC01-3. The sudden failure of the solid due to impact imparts a measure of roughness at the sub-millimeter scale that would not be present had the fracture propagated on a long time scale. Additionally, the sub-vertical fracture cuts across the layered fabric of the welded tuff. Fracture propagation in a direction of weaker material strength occurs at lower stress anisotropy, creating conditions favorable for localized variation in propagation direction at the crack tip.

The fracture specimen CC02-1 is sub-vertical in a semi-welded tuff. Contributing to the roughness are its orientation across the fabric of the matrix and the effects of weathering. It is surmised that the effects on roughness due to weathering and differences in degree of welding between CC02-1 and CC01 are comparable to that attributable to sudden material failure.

7.6.4 Rough

Roughnesses in the range $1.13 \leq S/S_0 < 1.18$ are grouped and classified as rough. These surfaces include the top and bottom surfaces of the Paintbrush Tuff specimen, both surfaces of CC02-2, and the Town Mountain Granite with weathering rind. There are specific characteristics to each of these that contribute to increasing roughness over similar rock and fracture types described in Sections 7.6.2 and 7.6.3.

Although the orientation of the Paintbrush Tuff fracture is sub-horizontal as evidenced by the orientation of smeared pumice fragments within the matrix, the surfaces are considerably rougher than sub-horizontal fracture surfaces of Santana Tuff. This is attributed to compositional differences. The alkali-calcic Paintbrush Tuff chemically weathers much faster than the calcium poor Santana Tuff (Blum and Stillings 1995, Smyth-Boulton 1995). Presumably, under episodically saturated conditions, the rate limiting step to weathering of feldspathic materials being the dissolution of the feldspars themselves could account for increased roughness due to chemical weathering of the bottom surface relative to the top surface of this specimen.

As described in Section 3.1 and 7.5.1, the weathering products on the surfaces of fracture specimen CC02-2 were preserved through sample preparation. This is the inferred cause of the increase in roughness in CC02-2 relative to specimen CC02-1. Another likely possibility is that the sealed surface of CC02-2 did not allow flocculated clays to adhere during sample preparation. Then, the calculated roughness of CC02-1 represents an infilled surface, similar to that of sample El03, rather than one stripped of its weathered skin.

Calculated surface roughness of the medium-grained Town Mountain Granite with weathering rind specimen clearly demonstrates the effect of leaching on a fracture surface. No fresh medium-grained granite specimen is part of this study, so I use the roughness pair of CC02-1 and CC02-2 as an analogue for comparing the results of surface roughness calculation for Fr-Wr with the roughness of Fr-MnO.

Broadly speaking, a fresh rough surface can evolve along two paths. Figure 7.29 illustrates smoothing or roughening of a fresh surface over time. Thus, from the roughness results of CC02-1 and CC02-2, it makes little difference whether the disparity is due to weathering products being preserved on CC02-2 or infilling CC02-1 with detrital clays derived from sample preparation. Either provides a baseline for comparison with differences in the Town Mountain Granite roughness results.

With no apparent incidental fractures, either from the data or visual inspection of the sample, the roughness calculated for Fr-Wr is entirely due to mechanical and

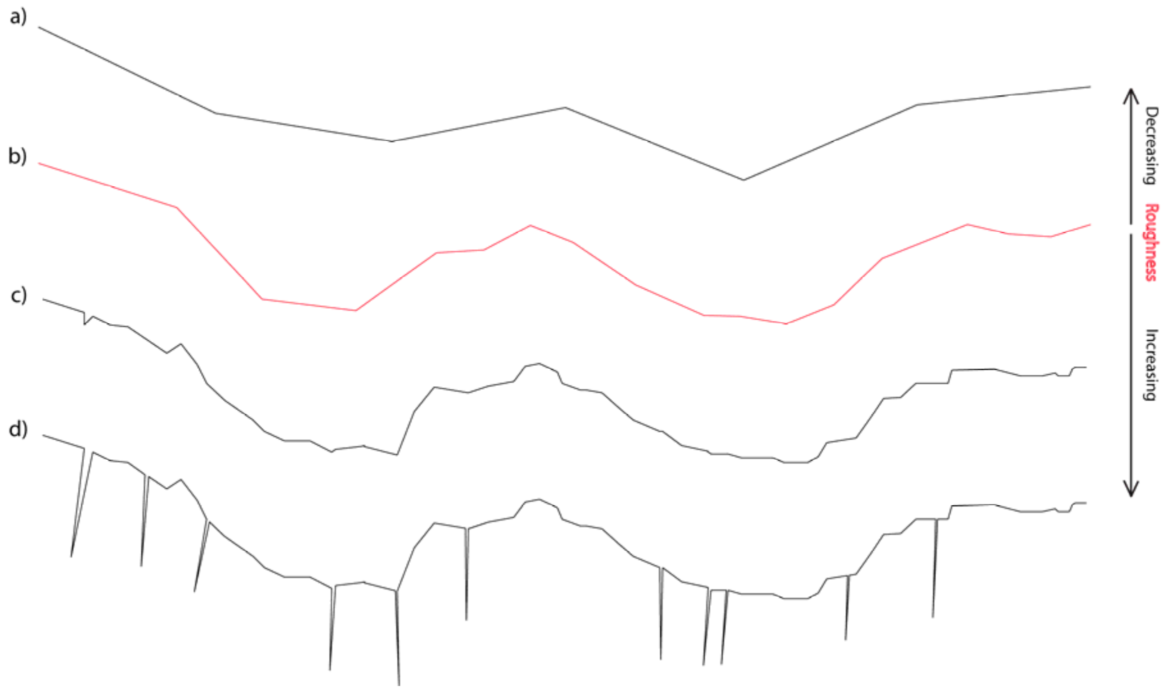

Figure 7.29 General forms of the evolution of a simulated fracture surface as detailed in this study. a) Infilling of fresh surface with non-bridging precipitate or detrital clays reduces fracture surface roughness. b) A fresh surface with roughness controlled by stress anisotropy, material toughness, and grain/crystal size. c) Chemical and physical weathering begins to pit fresh surface resulting in increased roughness. d) Rock begins to disintegrate in response to continuing chemical weathering, greatly increasing surface area per unit width (mechanical weathering at this stage compounds the fracture).

chemical weathering of one fracture surface superimposed on what would be expected of a fresh specimen of medium-grained Town Mountain Granite. The calculated value for Fr-Wr roughness exceeds that of Fr-MnO by over 13%. This difference is twice that between CC02-2 and CC02-1, supporting the progression of Figure 7.29.

7.6.5 Very rough

The sample surfaces from the two specimens from Australia exhibit a calculated roughness greater than or equal to 1.20, and are classified as very rough surfaces with calculated $S/S_0 \geq 1.8$. For the Calca sample, this extreme roughness is due to partial disintegration of the fracture surface in response to chemical weathering. The surface of the Marcollat Granite specimen has no obvious orthogonal breakage. Its roughness is controlled by crystal size and differential weathering of the constituent minerals.

7.6.6 Interpretation of results

Figure 7.30 displays the cumulative results of all samples less calca, which is omitted due to the influence of incidental sub-vertical weathering induced fractures on the median and variance. From Figure 7.30a, it is apparent that the mean of means is not a predictor for a representative surface size, or even a good indicator of multiple fracture surfaces (although the variation in means above a sample size of 64 x 64 data points does reflect a measure of oversampling related to the size of the whole surfaces sampled). The median value among samples of a particular size is a useful tool for determining possible influence on roughness of multiple fracture surfaces. Variance is the best indicator that a sample roughness sufficiently represents the whole surface. For the natural fracture surfaces analyzed in this study, a sample size of approximately 10cm^2 sufficiently characterizes the roughness of the entire fracture surface.

a) Mean Sample Roughness Relative to Whole Surface

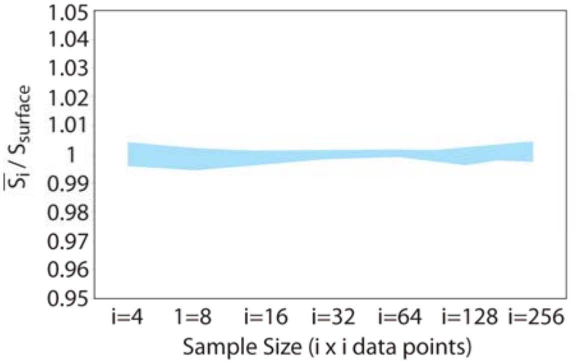

b) Median Roughness Relative to Whole Surface

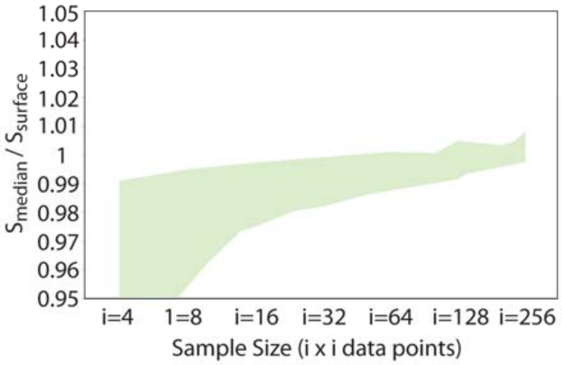

c) Variantion in Variance with Increasing Sample Size

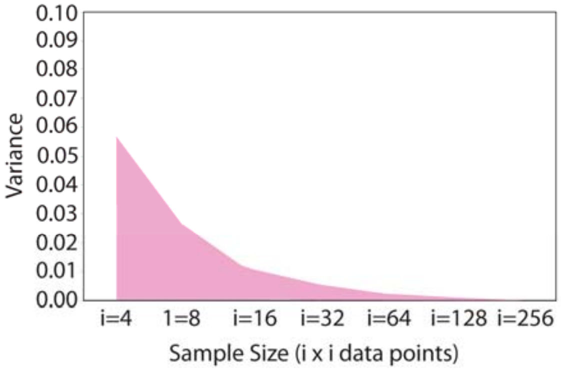

Figure 7.30 Variation in a) normalized mean, b) normalized median, and c) variance of roughnesses for all samples less Calca (which is omitted as the variance values are inflated and median values are deflated due to weathering consequent intersecting fractures) with increasing sample size. While the minimum variation of the mean occurs at a sample size of 64 x64 data points, all normalized median points at that sample size being less than 1.0 indicates that rough outliers skew the means to whole surface roughnesses.

8 REPRESENTATIVE ELEMENTAL VOLUME

Given the data requirement from Chapter 7 to establish an RES, does this requirement extend for mated fractures to a Representative Elemental Volume (REV)? The existence of an REV for discrete fractures may be specific to a particular fracture set and rock type due to roughness, and its corresponding effect on fluid flow, which is dependent on the stress regime that propagates the fractures. For such applications as modeling the response of a reservoir to stimulation by hydraulic fracturing, fluid flow behavior within an REV, established with a minimal investment in data acquisition, would be a valuable tool. In this chapter, I use the surface data from fracture sample CC02-2 to address this issue by modeling flow on subsets of the data and comparing with the results of the physical flow tests.

8.1 Methodology for Evaluating Discharge

The investigation into the existence of an REV for fractured media involves a choice of sample size, interpretation of the scaling relationship, and a method of comparison for the results of different sized samples. In this section, I discuss the limitations in the choice of data, difficulties inherent in scaling aperture, and my choice for comparing discharges from MODFLOW models with different dimensions.

Taking advantage of the RES data requirement discussed in Chapter 7, the search for an REV begins with a framework of 128 x 128 top and bottom surface data points. Twenty subsets of the surface data for fracture sample CC02-2 are selected using the IDL script *SampleGridVar.pro* as described in Appendix B and depicted in Figure 8.1. The

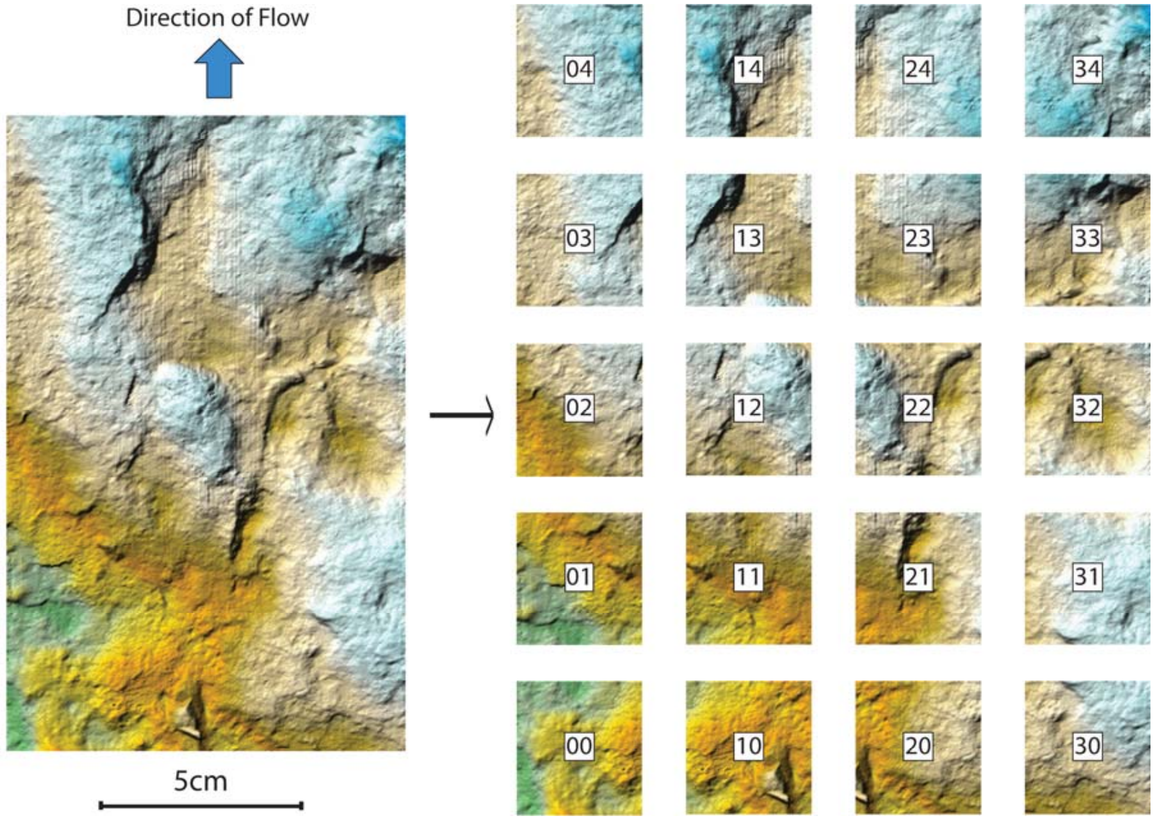

Figure 8.1 Fracture sample CC02-2 transformed into 20 discrete data sets. Transmissivity calculated from the aperture data from each of the 20 samples is used to populate the input array to a MODFLOW model to investigate the existence of a fracture REV. Samples are labeled using column-row notation starting from the lower left as pictured.

resulting data sets are labeled column-row (00–34) beginning with the data set corresponding to the leftmost upgradient portion of the physical configuration.

Modeling flow through a subset of the data smaller than 128 x 128 data points would provide little insight given the variation in roughness across each surface at such sizes. Further, using samples beyond the RES for this sample (which has well constrained physical flow test results) results in extensive overlap between adjacent samples, and does not contribute much to the discussion of a representative volume.

Each MODFLOW model is one layer of 128 rows by 128 columns spaced 0.024cm between adjacent rows and 0.025cm between adjacent columns. Columns 1 and 128 are defined as constant head, with a value of 0.272cm in column 1 and zero in column 128 corresponding to a hydraulic gradient of 0.08. Rows 1 and 128 are no flow boundaries. The transmissivity input parameter for each cell is set using aperture field data in Equation 5.10.

Two sets of data are processed for modeling for each subset. First, I used the aperture data from the flow test configuration to populate transmissivity fields for each subset. After consideration, I realized that the best fit configuration of the fracture specimens preserved from the field to flow testing did not necessarily correspond to an extrapolated fracture at field scale. Therefore, I modeled flow a second time on the aperture field calculated from *BestFit.pro* generated surfaces of each subset. It is from this basis that I draw my conclusions regarding the scaling of flow through discrete fractures.

Ordinarily, specific discharge *q*, defined as discharge per unit area normal to flow, would suffice to compare discharge values from different sized samples. However, as the use of a transmissivity field as input into MODFLOW reduces the dimensionality of a model layer to 2D by incorporating cell thickness into the parameter, dividing the model output discharge by the fracture output area does not reflect the model boundaries, and as no thickness is involved in the model calculations, specific discharge is explicitly undefined for model results. Therefore, I introduce a metric:

$$q_w = q \cdot b = Q / w, \tag{8.1}$$

or discharge per unit width of the model, to evaluate the subset modeling results.

8.2 Results of CC02-2 Subset Modeling

As each subset model is identical except for the input transmissivity field, the results are grouped and presented in this section. Neither the flow test configuration nor the best fit models behave in any consistent manner, let alone achieve the expected q_w of the entire fracture sample. However, examination of the best fit models does reveal end member properties that illustrate the hazards of extrapolating a limited fracture data set to any larger scale.

Figure 8.2a displays the q_w of each of the subset models in the flow test configuration. The values range from 0.044cm^2/s to 0.20cm^2/s, far from consistently matching the physical flow test result of 0.113cm^2/s. The spread of these results motivated the investigation of the best fit orientations of the subsets as I realized that the aperture distributions of the flow test configuration subsets, while matching the physical orientation of the surfaces they were meant to approximate, were not possible to replicate without knowledge of the whole. There is no *a priori* justification for mated surfaces with no contact points.

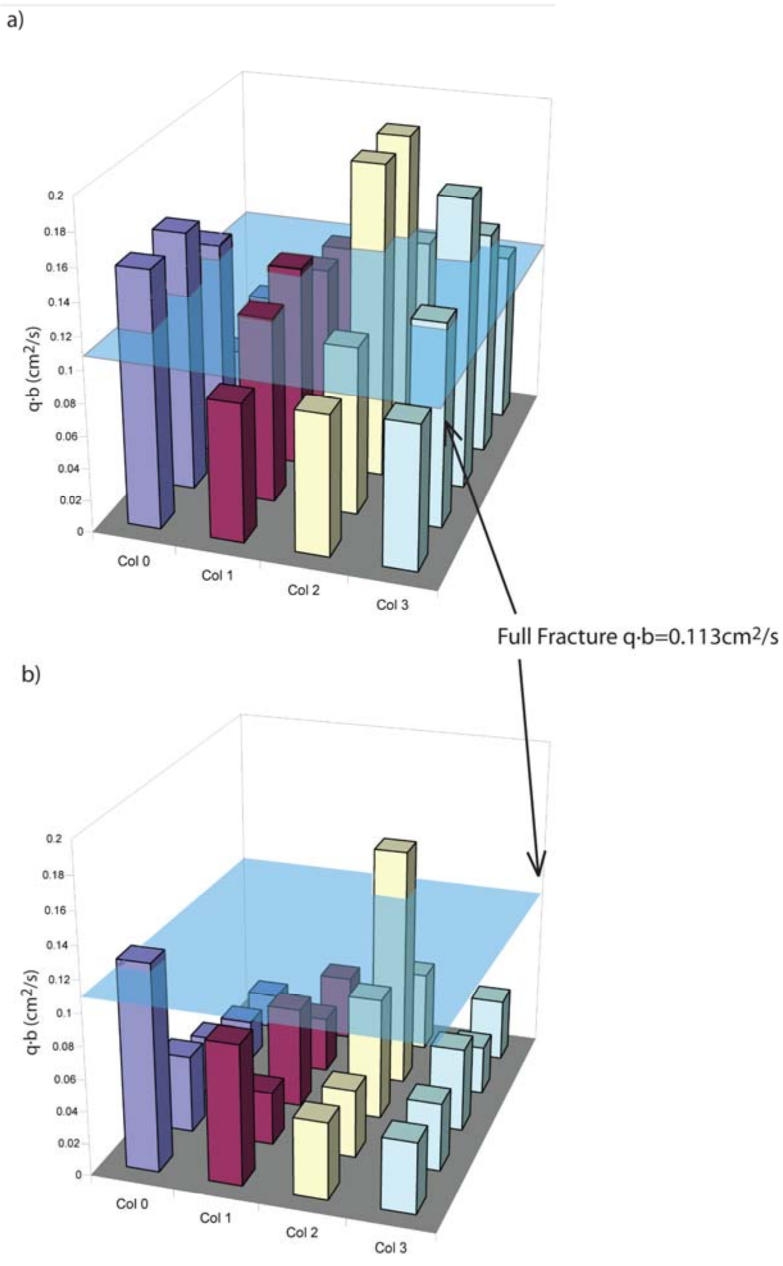

Figure 8.2 Discharge per unit width results of MODFLOW runs on 128 x 128 data point subsets of fracture sample CC02-2 in a) flow test configuration, and b) best fit configuration for each subset. The flow test results at a gradient of 0.08 yielded a discharge per unit width of 0.113cm^2/s versus a range of 0.044cm^2/s to 0.20cm^2/s for the models using the flow test configuration and a mean value of 0.055 for models using a best fit configuration.

Model results from the best fit configurations are depicted in Figure 8.2b. While overall the q_w values for all subsets are more consistent, they fall well below the physical flow test result of 0.113cm^2/s; 15 of the 20 values fall below the mean of 0.055cm^2/s.

MODPATH calculation of the paths of massless particles through four of the end member subsets reveals that the difference among the subsets is related to channeling. Figure 8.3b displays the particle tracks for subset 23, which form a dominant channel to the left downgradient corner of the model. The particle tracks for subset 00 (Figure 8.3a) also form a channel to the left downgradient corner that increases the discharge per unit width of the model beyond that of the physical flow test, though there are few slow flow paths present in this subset. Subsets 02 (Figure 8.3c) and 33 (Figure 8.3d) are two examples of particle tracks that highlight the reasons for low q_w for the majority of the subsets. Both subsets exhibit dominantly diffuse flow paths, and though subset 02 does form a late channel past 3seconds, its impact is not significant as the majority of particle times for the model of the whole fracture was less than 3.5seconds.

8.3 Implications for Scaling

Based on the results of twenty models of subsets of fracture sample CC02-2, no representative elemental volume exists for the 142cm^2 sample. Using the sample size of the RES of chapter 7, flow test configuration subset models fall short of accurately predicting the q_w of the full fracture sample (Figure 8.4). While many of the values do loosely approximate the target value, there is no justification for configuring the subsets in the actual flow test configuration without knowledge of the full sample. The results of best fit subset models followed one of two paths: 1) diffusive flow resulting in low q_w or

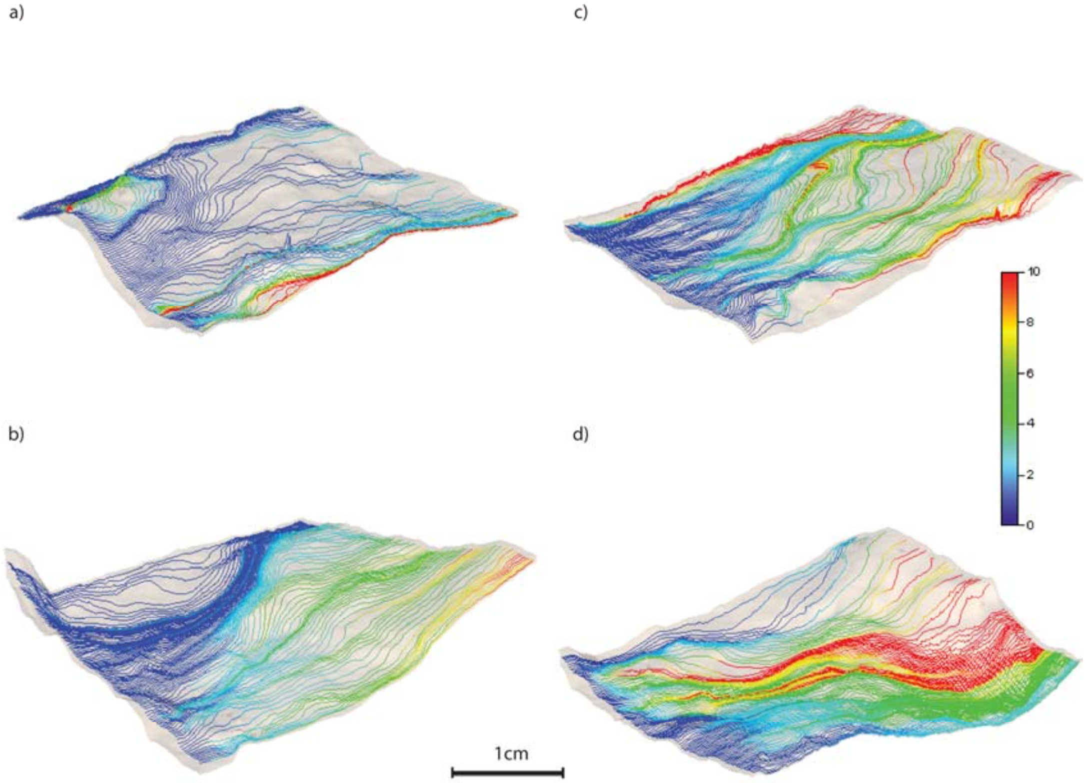

Figure 8.3 MODPATH particle tracks for models of subsets of fracture sample CC02-2. a) Subset 00 and b) subset 23 show distinct channel formation leading to a fast flow path dominating discharge through the model and a resultant high discharge per unit width not characteristic of the fracture as a whole. c) Subset 02 and d) subset 33 are two of many exhibiting diffuse flow paths resulting in very low discharge per unit width.

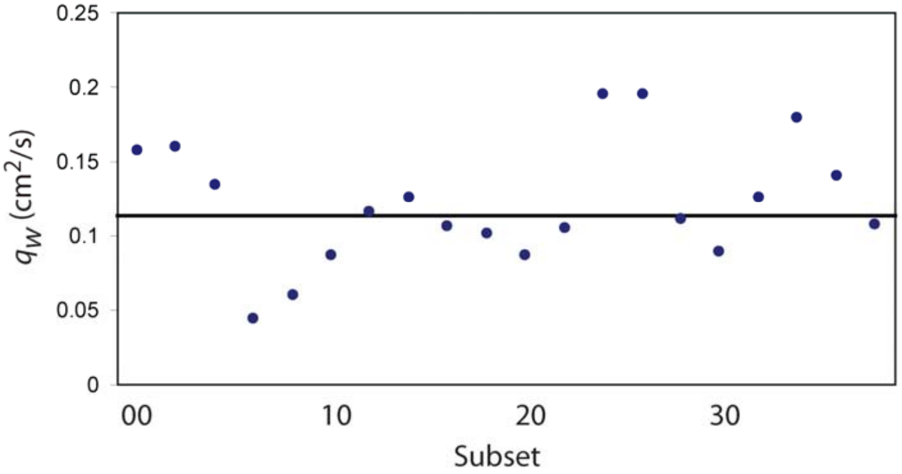

Figure 8.4 Discharge per unit width for MODFLOW models of twenty subsets of fracture sample CC02-2. Black line is at q_w=0.113cm^2/s, which represents the target value from physical flow test results.

2) a single channel dominating flow and causing significant increase to the model q_w. The binary nature of channeling at the scale of 10cm^2 transitioning to approximately five dominant channels at the scale of 100cm^2 (Figure 8.5) provides little confidence that the results of modeling the full CC02-2 sample can be extrapolated to represent the larger fracture of which it was a part. The difficulty in quantifying channeling at field scale precludes the development of a useful scaling parameter from hand samples to reflect the proportion of discharge via channels versus diffusive flow.

Therefore, I conclude that a representative fracture volume, should one exist, must be larger than the samples used in this study. This raises several logistical problems for further investigation: 1) discrete fractures of this size are difficult to find and collect; 2) confidently saturating a large fracture requires special consideration with regards to the mounting apparatus and equipment choice; 3) computed tomography imaging requires large fractures to be cut to an appropriate size, which introduces sources of error from the registration of multiple sets of mated surfaces; and 4) the method of digital reconstruction, including the handling of missing material and modeling across boundaries, challenges the assumption that the resultant model accurately describes the physical conditions of the full fracture. Despite these difficulties, the pursuit of a fracture REV continues to have merit.

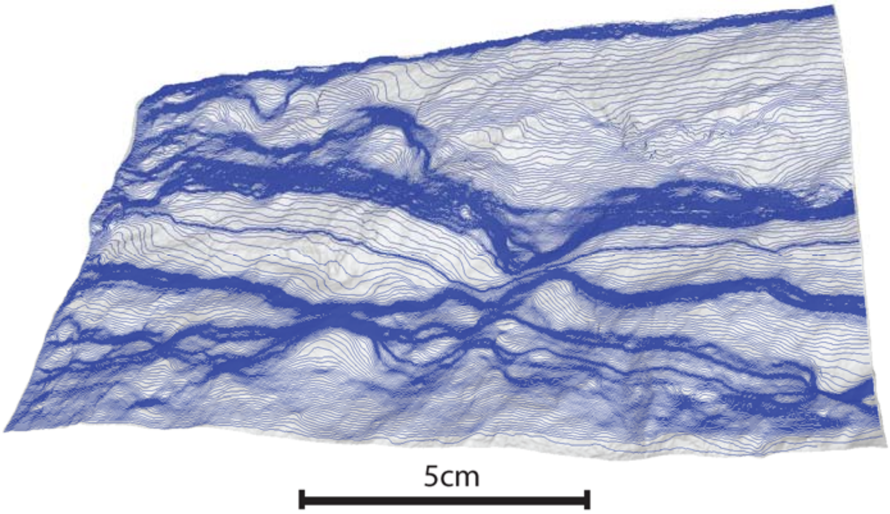

Figure 8.5 MODPATH particle tracks for the model of fracture sample CC02-2. At the tens of centimeters scale, multiple channels dominate flow.

9 CONCLUSIONS

Fractured rock systems and how to characterize fluid flow within them has been the subject of a number of relatively recent symposia in the fields of groundwater (e.g., Krasny and Sharp, 2007a) and petroleum geology (e.g., Petford and McCaffrey, 2003). For both water and hydrocarbons, however, there has long been interest in these settings (e.g., LeGrand, 1949; Davis and Turk, 1964; Trainer, 1988; Powers, 1932; Landes et al., 1960). Consequently, it would be valuable if data from studies at a small (e.g., hand sample or thin section) scale could be upcaled to well-field or regional systems. Scaling of permeability has been examined in karstic systems. Kiraly (1996) and Halihan et al. (1998) show that regional flow is dominated by conduits, flow to wells by fractures, and flow at the hand sample scale by the carbonate matrix. In fractured crystalline rocks, it is commonly assumed that this also holds as more permeable fractures should be encountered with increasing scale. However, Clauser (1990) suggests this need not always be the case. Indeed, he stated that permeability should upscale, but at very large scales would approach a constant. On the other hand, Krasny and Sharp (2007b) suggest that geomorphic and tectonic features need to be carefully evaluated to ascertain regional trends. Because of data limitations, a variety of mathematical upscaling approaches have been proposed to scale permeability in a variety of media, including power law distributions for fracture length and density (Blum et al., 2005), rock constitutive laws (Exadaktylos and Stavroploulou, 1997), multiple subregion models (Gong et al., 2008), and percolation probability (Masihi and King, 2008). However, in order to upscale the hydraulic properties of fractures, the properties must possess a relationship between fracture morphology and discharge that is either scale invariant or smoothly transformable (Sharp et al., 2008).

Conducting physical flow test experiments on discrete natural fractures, analyzing computed tomography derived surface and aperture data, and modeling fluid flow on the resultant aperture fields at varying scales and configurations, I conclude the following:

- the unmodified cubic law is valid for the range of gradients expected in the field,
- hydraulic aperture is best estimated by the geometric mean of areal aperture data,
- single measures of fracture aperture or estimates over a single along fracture scanline are not sufficient to estimate hydraulic aperture,
- fracture surface roughness can be adequately estimated from samples of 10 cm^2 for a variety of fracture surfaces, and
- upscaling of aperture from this same representative size is not feasible due to the dominant influence of the spatial distribution channeling and pinch out at small scales.

The classification of rough surfaces remains a promising line of research. However, roughness results must be paired with appropriate estimates of aperture distribution and regard for spatial arrangement of high transmissivity zones to be meaningful for prediction of fluid flow through fractured media from small investments in data acquisition. Further, continued modeling of mated surface data sets of varying lithologies is crucial to development of a useful channel scaling factor of the form:

$$I_{\omega} = C \cdot I_{0}^{\omega \cdot \gamma}, \tag{9.1}$$

where I_{w} represents the number of channels at some scale ω, and can be estimated by a constant multiple of the expected channels at the smallest representative size taken to a scaling exponent multiplied by the scale level. Until this relationship is sufficiently explored, forward prediction of flow through fractures will continue to be a best guess, uncertain exercise.

APPENDIX A—FLOW TEST DATA

Table A.1 Flow test results from parallel plate sample.

Trial	t(s)	Δh (mm)	i [-]	V_{out} (ml)	Q (ml/s)	T (^{o}C)	μ (cp)	ρ (g/ml)	b_e (mm)	Re [-]
1	27	10.86	0.07	200	7.41	23.25	0.93	0.96	1.06	151.26
2	60	10.65	0.07	515	8.58	23.25	0.93	0.96	1.12	175.27
3	23.5	13.85	0.09	189	8.04	23.25	0.93	0.96	1.01	164.23
4	26.63	11.40	0.08	227	8.52	23.25	0.93	0.96	1.10	174.06
5	26.57	12.25	0.08	239	9.00	23.25	0.93	0.96	1.09	183.68
6	25.15	11.72	0.08	217	8.63	23.25	0.93	0.96	1.09	176.19
7	28.57	11.72	0.08	235	8.23	23.25	0.93	0.96	1.07	167.96
8	28.56	11.40	0.08	231	8.09	23.25	0.93	0.96	1.08	165.16
9	28.6	11.72	0.08	231	8.08	23.25	0.93	0.96	1.07	164.93
10	27.93	11.93	0.08	227	8.13	23.25	0.93	0.96	1.06	165.96
11	27.31	11.72	0.08	227	8.31	23.25	0.93	0.96	1.08	169.73
12	27.81	11.50	0.08	223	8.02	23.25	0.93	0.96	1.07	163.74
13	32.69	14.38	0.09	227	6.94	24	0.91	1.03	0.92	154.13
14	26.72	10.65	0.07	205	7.67	24	0.91	1.03	1.05	170.29
15	27.84	10.65	0.07	214	7.69	24	0.91	1.03	1.05	170.62
16	25.47	10.65	0.07	190	7.46	24	0.91	1.03	1.04	165.58
17	26.00	10.65	0.07	197	7.58	24	0.91	1.03	1.05	168.18
18	17.03	19.17	0.13	217	12.74	24	0.91	1.03	1.03	282.83
19	17.85	17.04	0.11	212	11.88	24	0.91	1.03	1.04	263.62
20	19.60	17.04	0.11	226	11.53	24	0.91	1.03	1.03	255.94
21	15.65	18.64	0.12	193	12.33	24	0.91	1.03	1.02	273.73
22	16.03	18.64	0.12	194	12.10	24	0.91	1.03	1.02	268.63
23	20.37	18.11	0.12	244	11.98	24	0.91	1.03	1.02	265.88
24	21.13	17.04	0.11	245	11.59	24	0.91	1.03	1.03	257.37
25	15.35	18.11	0.12	187	12.18	24	0.91	1.03	1.03	270.41
26	17.68	18.11	0.12	227	12.84	24	0.91	1.03	1.05	284.99
27	12.10	31.42	0.21	241	19.92	24	0.91	1.03	1.01	442.09
28	45.34	31.42	0.21	953	21.02	24	0.91	1.03	1.03	466.55
29	11.00	33.02	0.22	235	21.36	24	0.91	0.98	1.03	451.37
30	34.09	5.86	0.04	222	6.51	24	0.91	0.98	1.24	137.59

Table A.2 Data for flow tests of Oatman Creek Granite reported in Thompson (2005).

Trial	t(s)	Δh (mm)	i[-]	V_{out} (ml)	Q (ml/s)	T (^{o}C)	μ (cp)	ρ (g/ml)	b_e (mm)	Re [-]
1	240	73.60	0.82	774	3.23	22.15	0.95	1.00	0.42	146.45
2	240	71.70	0.80	720.5	3.00	22.3	0.95	1.00	0.42	144.08
3	240	71.80	0.80	702.5	2.93	22.3	0.95	1.00	0.41	142.80
4	240	71.90	0.80	715.5	2.98	22.3	0.95	1.00	0.42	143.61
5	90	290.90	3.23	839	9.32	22.25	0.95	1.00	0.38	527.37
6	90	293.50	3.26	893.5	9.93	22.25	0.95	1.00	0.39	536.95
7	90	291.50	3.24	904.5	10.05	22.2	0.95	1.00	0.39	540.59
8	240	72.40	0.80	774	3.23	22.25	0.95	1.00	0.43	147.14
9	240	72.70	0.81	757.5	3.16	22.25	0.95	1.00	0.42	145.88
10	240	73.40	0.82	782	3.26	22.2	0.95	1.00	0.43	147.03
11	240	72.70	0.81	754.5	3.14	22.25	0.95	1.00	0.42	145.69
12	90	269.60	3.00	806	8.96	22.15	0.95	1.00	0.39	489.62
13	90	269.00	2.99	854.5	9.49	22.1	0.95	1.00	0.40	499.82
14	90	268.30	2.98	824	9.16	22.05	0.95	1.00	0.39	494.43
15	105	241.50	2.68	894	8.51	22.05	0.95	1.00	0.40	454.39
16	105	241.80	2.69	884	8.42	22	0.95	1.00	0.39	452.68
17	105	240.00	2.67	885	8.43	21.95	0.96	1.00	0.40	454.16
18	120	217.10	2.41	888	7.40	22	0.95	1.00	0.39	404.54
19	120	217.50	2.42	895	7.46	22	0.95	1.00	0.39	405.35
20	120	217.50	2.42	864.5	7.20	21.95	0.96	1.00	0.39	400.85
21	240	72.90	0.81	738.5	3.08	21.95	0.96	1.00	0.42	144.86
22	240	72.80	0.81	746.5	3.11	21.95	0.96	1.00	0.42	145.45
23	240	72.40	0.80	736	3.07	21.95	0.96	1.00	0.42	145.03
24	130	193.60	2.15	863	6.64	21.9	0.96	1.00	0.39	360.59
25	130	193.90	2.15	857	6.59	21.85	0.96	1.00	0.39	359.71
26	130	193.30	2.15	858	6.60	21.85	0.96	1.00	0.39	360.22
27	135	173.80	1.93	822	6.09	21.8	0.96	1.00	0.40	318.03
28	135	173.80	1.93	811.5	6.01	21.8	0.96	1.00	0.39	316.67
29	135	173.80	1.93	815	6.04	21.85	0.96	1.00	0.39	317.00
30	165	146.90	1.63	875	5.30	21.8	0.96	1.00	0.40	275.34
31	165	146.10	1.62	872	5.28	21.8	0.96	1.00	0.40	275.52
32	165	145.50	1.62	868	5.26	21.8	0.96	1.00	0.40	275.48
33	240	76.50	0.85	750	3.13	21.8	0.96	1.00	0.42	143.46
34	240	76.90	0.85	752	3.13	21.9	0.96	1.00	0.42	143.22
35	240	75.10	0.83	740	3.08	21.8	0.96	1.00	0.42	143.70
36	240	71.30	0.79	701.5	2.92	21.85	0.96	1.00	0.42	143.57
37	240	72.90	0.81	715	2.98	21.9	0.96	1.00	0.42	143.37
38	240	73.30	0.81	714.5	2.98	21.85	0.96	1.00	0.42	143.13
39	195	123.10	1.37	879.5	4.51	21.8	0.96	1.00	0.40	230.58
40	195	123.20	1.37	879.5	4.51	21.8	0.96	1.00	0.40	230.52

Table A.2 continued.

Trial	t(s)	Δh (mm)	i[-]	V_{out} (ml)	Q (ml/s)	T (^oC)	μ (cp)	ρ (g/ml)	b_e (mm)	Re [-]
41	195	121.50	1.35	864	4.43	21.8	0.96	1.00	0.40	230.22
42	225	97.90	1.09	830	3.69	21.85	0.96	1.00	0.40	186.12
43	225	97.90	1.09	846	3.76	21.85	0.96	1.00	0.41	187.31
44	225	97.30	1.08	832.5	3.70	21.8	0.96	1.00	0.41	186.77
45	240	72.60	0.81	689.5	2.87	21.85	0.96	1.00	0.41	141.89
46	240	74.00	0.82	691.5	2.88	21.85	0.96	1.00	0.41	141.13
47	240	73.20	0.81	688	2.87	21.85	0.96	1.00	0.41	141.46
48	240	72.50	0.81	648.5	2.70	21.9	0.96	1.00	0.40	139.03
49	240	72.80	0.81	647.5	2.70	21.95	0.96	1.00	0.40	138.71
50	240	72.70	0.81	643	2.68	21.95	0.96	1.00	0.40	138.45
51	360	59.90	0.67	822.5	2.28	22	0.95	1.00	0.41	116.66
52	360	59.80	0.66	822.5	2.28	22	0.95	1.00	0.41	116.73
53	360	58.90	0.65	802	2.23	22	0.95	1.00	0.41	116.34
54	420	49.70	0.55	809.5	1.93	22	0.95	1.00	0.41	93.85
55	420	50.00	0.56	800	1.90	22	0.95	1.00	0.41	93.29
56	420	49.50	0.55	786	1.87	21.95	0.96	1.00	0.41	93.09
57	480	44.50	0.49	831	1.73	21.9	0.96	1.00	0.41	82.27
58	480	44.20	0.49	807	1.68	21.9	0.96	1.00	0.41	81.65
59	480	43.90	0.49	810.5	1.69	21.85	0.96	1.00	0.41	81.99
60	240	73.50	0.82	644	2.68	21.9	0.96	1.00	0.40	138.08
61	240	72.90	0.81	639.5	2.66	21.9	0.96	1.00	0.40	138.13
62	240	72.60	0.81	624	2.60	21.85	0.96	1.00	0.40	137.25
63	540	36.90	0.41	813	1.51	21.85	0.96	1.00	0.42	71.67
64	540	36.50	0.41	786.5	1.46	21.8	0.96	1.00	0.41	71.17
65	540	36.70	0.41	795.5	1.47	21.8	0.96	1.00	0.41	71.31
66	600	30.50	0.34	723.5	1.21	21.75	0.96	1.00	0.41	59.15
67	600	30.10	0.33	705.5	1.18	21.75	0.96	1.00	0.41	58.91
68	600	29.70	0.33	692	1.15	21.75	0.96	1.00	0.41	58.80
69	720	23.80	0.26	667	0.93	21.75	0.96	1.00	0.41	47.07
70	720	25.10	0.28	710	0.99	21.75	0.96	1.00	0.41	47.22
71	720	24.60	0.27	701.5	0.97	21.8	0.96	1.00	0.41	47.33
72	240	73.00	0.81	601.5	2.51	21.8	0.96	1.00	0.39	135.38
73	240	73.20	0.81	602	2.51	21.8	0.96	1.00	0.39	135.30
74	240	73.10	0.81	602	2.51	21.8	0.96	1.00	0.39	135.36

Table A.3 Second suite of Oatman Creek Granite flow test data collected by Robertson (2006).

Trial	t(s)	Δh (mm)	i[-]	V_{out} (ml)	Q (ml/s)	T (^oC)	μ (cp)	ρ (g/ml)	b_e (mm)	Re [-]
1	33.28	33.02	0.37	100	3.00	24.25	0.91	0.99	0.54	109.02
2	31.94	33.02	0.37	97	3.04	24.25	0.91	0.98	0.54	109.79
3	33.78	33.02	0.37	102	3.02	24.25	0.91	0.98	0.54	109.15
4	38.79	33.02	0.37	118	3.04	24.50	0.90	0.99	0.54	110.96
5	36.06	33.02	0.37	110	3.05	24.75	0.90	0.99	0.54	112.41
6	22.25	53.78	0.60	108	4.85	25.25	0.89	0.98	0.53	179.36
7	20.59	53.78	0.60	102	4.95	25.50	0.88	0.98	0.53	182.97
8	22.69	53.78	0.60	111	4.89	26.00	0.87	0.97	0.53	182.60
9	19.58	53.78	0.60	96	4.90	25.75	0.88	0.98	0.53	183.00
10	22.12	53.78	0.60	109	4.93	26.00	0.87	1.00	0.53	188.17
11	19.38	75.62	0.84	126	6.50	24.63	0.90	0.98	0.53	236.33
12	23.41	76.68	0.85	147	6.28	24.50	0.90	0.99	0.52	229.24
13	20.81	76.68	0.85	132	6.34	24.25	0.91	0.98	0.52	229.17
14	20.85	76.68	0.85	131	6.28	24.25	0.91	0.98	0.52	227.49
15	18.47	76.68	0.85	115	6.23	24.00	0.91	0.99	0.52	224.43
16	20.44	76.68	0.85	128	6.26	24.25	0.91	0.98	0.52	224.86
17	44.97	21.30	0.24	73	1.62	24.63	0.90	0.97	0.51	58.35
18	35.47	21.30	0.24	57	1.61	25.00	0.89	0.97	0.50	58.36
19	46.38	21.30	0.24	75	1.62	25.00	0.89	0.98	0.50	59.16
20	38.25	21.30	0.24	62	1.62	25.00	0.89	0.96	0.51	58.23
21	33.28	21.30	0.24	55	1.65	25.00	0.89	0.97	0.51	59.96
22	59.91	5.33	0.06	51	0.85	24.50	0.90	0.98	0.65	30.83
23	60.35	6.39	0.07	38	0.63	24.75	0.90	0.98	0.55	23.07
24	62.28	7.46	0.08	47	0.75	25.00	0.89	0.97	0.56	27.29
25	60.47	7.46	0.08	56	0.93	25.38	0.88	0.99	0.59	34.47
26	58.82	7.08	0.08	55	0.94	25.38	0.88	0.96	0.61	33.83
27	60.21	10.65	0.12	65	1.08	25.88	0.87	0.97	0.55	39.95
28	60.03	9.58	0.11	59	0.98	25.88	0.87	0.98	0.55	36.77
29	60.34	9.58	0.11	59	0.98	25.75	0.88	0.98	0.55	36.54
30	59.97	9.58	0.11	58	0.97	25.88	0.87	0.97	0.55	35.91
31	58.04	9.58	0.11	59	1.02	26.13	0.87	0.98	0.56	38.11

Table A.4 Flow test data from Santana Tuff fracture sample CC02-1.

Trial	T(s)	Δh (mm)	i [-]	V_{out} (ml)	Q (ml/s)	T (^{o}C)	μ (cp)	ρ (g/ml)	b_e (mm)	Re [-]
1	164	16.0	0.15	116	0.71	22.5	0.94	0.95	0.38	14.04
2	149.13	15.7	0.15	101	0.68	22.5	0.94	0.98	0.38	13.78
3	222.28	15.7	0.15	137	0.62	22.5	0.94	0.98	0.36	12.61
4	221.28	15.7	0.15	136.5	0.62	22.5	0.94	0.98	0.36	12.62
5	151.82	15.7	0.15	102	0.67	22.5	0.94	0.98	0.37	13.71
6	222.59	15.7	0.15	147	0.66	22.5	0.94	0.98	0.37	13.52
7	164.35	14.9	0.14	98	0.60	22.5	0.94	0.98	0.37	12.15
8	300.34	14.9	0.14	172	0.57	22.5	0.94	0.98	0.36	11.74
9	163.53	14.7	0.14	93	0.57	22.5	0.94	0.98	0.36	11.60
10	164.78	14.4	0.14	81	0.49	22.5	0.94	0.97	0.35	9.99
11	308	16.0	0.15	169	0.55	22.5	0.94	0.98	0.35	11.24
12	150.03	29.5	0.28	103	0.69	23.75	0.92	0.98	0.30	14.49
13	151.12	29.5	0.28	103	0.68	23.75	0.92	0.99	0.30	14.43
14	300.72	29.5	0.28	206.5	0.69	23.75	0.92	0.99	0.30	14.55
15	301.52	29.5	0.28	209	0.69	23.75	0.92	0.98	0.31	14.66
16	300.25	22.0	0.21	220	0.73	23.75	0.92	0.99	0.34	15.51
17	299.09	21.7	0.21	225	0.75	23.75	0.92	0.98	0.35	15.87
18	150.25	24.2	0.23	123.5	0.82	23.75	0.92	0.99	0.34	17.46
19	300.53	14.3	0.14	129	0.43	23.75	0.92	0.98	0.33	9.06
20	339	14.3	0.14	144.5	0.43	23.75	0.92	0.98	0.33	9.01
21	150.15	14.3	0.14	63.5	0.42	23.75	0.92	0.99	0.33	8.96
22	150.19	14.3	0.14	63	0.42	23.75	0.92	0.98	0.33	8.87
23	709.6	5.0	0.05	96	0.14	24	0.91	0.97	0.32	2.84
24	307.25	5.0	0.05	41	0.13	24	0.91	0.97	0.32	2.78
25	686.81	4.0	0.04	73	0.11	23.75	0.92	0.99	0.32	2.26
26	702.22	7.5	0.07	129	0.18	24	0.91	0.98	0.31	3.89
27	393.19	7.5	0.07	71.5	0.18	24	0.91	0.97	0.31	3.83
28	1028.06	2.1	0.02	52	0.05	24	0.91	0.96	0.31	1.05
29	1251.06	2.1	0.02	57.5	0.05	24	0.91	0.98	0.30	0.98
30	301.41	12.2	0.12	95	0.32	24	0.91	0.98	0.31	6.70
31	618.56	12.2	0.12	185.5	0.30	24	0.91	0.99	0.31	6.39
32	121.37	12.2	0.12	37	0.30	24	0.91	0.96	0.31	6.34
33	323.03	9.7	0.09	78	0.24	24	0.91	0.98	0.31	5.12
34	632.81	9.6	0.09	150	0.24	24	0.91	0.98	0.31	5.03
35	95.88	10.1	0.10	23	0.24	24	0.91	0.96	0.31	4.98
36	349.38	13.8	0.13	143	0.41	24	0.91	0.98	0.33	8.69
37	539.09	16.5	0.16	227.5	0.42	24	0.91	0.98	0.31	8.89
38	460.03	16.5	0.16	188.5	0.41	24	0.91	0.98	0.31	8.71
39	1078.44	16.0	0.15	231	0.21	23.75	0.92	0.98	0.25	4.52
40	301.13	30.4	0.29	227	0.75	23.75	0.92	0.98	0.31	15.92

Table A.4 continued.

Trial	t(s)	Δh (mm)	i [-]	V_{out} (ml)	Q (ml/s)	T (^{o}C)	μ (cp)	ρ (g/ml)	b_e (mm)	Re [-]
41	241.06	33.5	0.32	204.5	0.85	23.75	0.92	0.98	0.31	17.95
42	150.53	55.9	0.53	208	1.38	23.75	0.92	0.98	0.31	29.23
43	150.22	56.1	0.54	205.5	1.37	23.75	0.92	0.99	0.31	28.97
44	150.65	46.1	0.44	171	1.14	23.75	0.92	0.98	0.31	23.90
45	180.28	46.1	0.44	203	1.13	23.75	0.92	0.98	0.31	23.76
46	180.37	49.7	0.47	197.5	1.09	23.75	0.92	0.99	0.30	23.18
47	210.09	49.7	0.47	227.5	1.08	23.75	0.92	0.98	0.30	22.88
48	250.1	38.7	0.37	212.5	0.85	24	0.91	0.99	0.30	18.09
49	230.97	44.3	0.42	219.5	0.95	24	0.91	0.98	0.30	20.21
50	151.25	44.3	0.42	143	0.95	24	0.91	0.98	0.30	20.08
51	153.28	58.3	0.56	225	1.47	24	0.91	0.98	0.31	31.15
52	142.38	58.3	0.56	207.5	1.46	24	0.91	0.98	0.31	30.99
53	78.57	134.2	1.28	238.5	3.04	24	0.91	0.98	0.30	64.49
54	82.12	134.5	1.28	247	3.01	24	0.91	0.98	0.30	63.91
55	68.19	133.7	1.28	203	2.98	24	0.91	0.98	0.30	63.31
56	60.5	153.4	1.46	201.5	3.33	24	0.91	0.98	0.30	70.78
57	74.78	153.4	1.46	241	3.22	24	0.91	0.98	0.29	68.45
58	70.1	153.4	1.46	225	3.21	24	0.91	0.98	0.29	68.12
59	70.56	155.5	1.48	227.5	3.22	24	0.91	0.98	0.29	68.56
60	54	203.4	1.94	233.5	4.32	24	0.91	0.98	0.30	91.95
61	53.6	203.4	1.94	232	4.33	24	0.91	0.98	0.30	91.79
62	35	308.3	2.94	215	6.14	24	0.91	0.98	0.29	130.62
63	42	305.7	2.92	231	5.50	23.25	0.93	0.99	0.28	115.27
64	43.72	305.1	2.91	239	5.47	23.25	0.93	0.98	0.28	114.18
65	42.57	309.1	2.95	230	5.40	23.25	0.93	0.98	0.28	112.77
66	43.97	305.9	2.92	234	5.32	23.25	0.93	0.98	0.28	111.21
67	47.84	302.5	2.89	239	5.00	23.25	0.93	0.99	0.27	104.70
68	47.47	300.9	2.87	233	4.91	23.25	0.93	0.98	0.27	102.52
69	49.03	305.3	2.91	240	4.89	23.25	0.93	0.99	0.27	102.51
70	46.03	328.0	3.13	245	5.32	23.25	0.93	0.98	0.27	111.17
71	44.09	337.6	3.22	237	5.38	23.25	0.93	0.99	0.27	112.69
72	44.22	339.7	3.24	237	5.36	23.25	0.93	0.98	0.27	112.02
73	42.03	358.4	3.42	237.5	5.65	23.25	0.93	0.99	0.27	118.26
74	42.25	358.9	3.43	238	5.63	23.25	0.93	0.98	0.27	117.60
75	40.91	384.5	3.67	239	5.84	23.25	0.93	0.98	0.26	122.18
76	41.06	384.8	3.67	240	5.85	23.25	0.93	0.98	0.26	121.83
77	42.72	383.4	3.66	236	5.52	23.25	0.93	0.99	0.26	115.61
78	45.87	364.0	3.47	239	5.21	23.25	0.93	0.98	0.26	108.83
79	47.72	368.0	3.51	245	5.13	23.25	0.93	0.98	0.26	107.06
80	53.03	336.0	3.21	241	4.54	23.25	0.93	0.99	0.25	95.09

Table A.4 continued.

Trial	t(s)	Δh (mm)	i [-]	V_{out} (ml)	Q (ml/s)	T (^{o}C)	μ (cp)	ρ (g/ml)	b_e (mm)	Re [-]
81	52.25	337.6	3.22	237	4.54	23.25	0.93	0.98	0.25	94.56
82	49.88	337.6	3.22	237	4.75	23.25	0.93	0.99	0.26	99.48
83	53.47	312.0	2.98	240	4.49	23.25	0.93	0.98	0.26	93.72
84	52.35	312.0	2.98	233	4.45	23.25	0.93	0.98	0.26	93.00
85	57.28	312.6	2.98	242	4.22	23.25	0.93	0.98	0.25	88.30
86	58.1	286.5	2.73	235	4.04	23.25	0.93	0.98	0.26	84.49
87	60.09	286.5	2.73	242	4.03	23.25	0.93	0.98	0.26	84.06
88	58.37	297.9	2.84	242	4.15	23.25	0.93	0.98	0.26	86.61
89	61	272.1	2.60	239	3.92	23.25	0.93	0.99	0.26	81.97
90	64.47	272.1	2.60	249	3.86	23.25	0.93	0.98	0.26	80.59
91	66.32	260.6	2.49	244	3.68	23.25	0.93	0.99	0.26	76.97
92	66.13	260.6	2.49	243	3.67	23.25	0.93	0.98	0.26	76.74
93	72.56	236.1	2.25	247	3.40	23.25	0.93	0.98	0.26	71.08
94	71.63	235.4	2.25	241	3.36	23.25	0.93	0.98	0.26	70.28
95	70.03	247.9	2.37	245	3.50	23.25	0.93	0.98	0.26	72.74
96	71.69	247.6	2.36	247	3.45	23.25	0.93	0.98	0.26	71.68
97	73.22	248.1	2.37	240	3.28	23	0.93	0.98	0.25	68.01
98	74.25	248.1	2.37	238	3.21	23	0.93	0.98	0.25	66.50
99	180.12	99.3	0.95	247	1.37	23	0.93	0.99	0.26	28.53
100	159.43	106.7	1.02	240	1.51	23	0.93	0.98	0.26	31.25
101	180.59	93.9	0.90	239	1.32	23	0.93	0.98	0.26	27.39
102	184.1	93.7	0.89	241	1.31	23	0.93	0.98	0.26	27.13
103	155.16	114.0	1.09	237	1.53	23	0.93	0.99	0.25	31.79
104	159.59	114.0	1.09	243	1.52	23	0.93	0.98	0.25	31.52
105	137	140.0	1.34	247	1.80	23	0.93	0.99	0.25	37.53
106	133.57	139.5	1.33	241	1.80	23	0.93	0.98	0.25	37.47
107	154.06	118.2	1.13	238	1.54	23	0.93	0.98	0.25	32.04
108	160.44	118.2	1.13	246	1.53	23	0.93	0.98	0.25	31.83
109	149.66	131.3	1.25	248	1.66	23	0.93	0.98	0.25	34.43
110	149.91	131.3	1.25	247	1.65	23	0.93	0.98	0.25	34.16
111	127.91	153.7	1.47	245	1.92	23	0.93	0.98	0.25	39.66
112	128.25	153.7	1.47	242	1.89	23	0.93	0.99	0.25	39.27
113	111.09	173.6	1.66	239	2.15	23	0.93	0.98	0.25	44.69
114	122.65	160.5	1.53	245	2.00	23	0.93	0.98	0.25	41.36
115	109.09	181.1	1.73	240	2.20	23	0.93	0.98	0.24	45.72
116	113	187.4	1.79	245	2.17	23	0.93	0.99	0.24	45.11
117	108.59	186.4	1.78	241	2.22	23	0.93	0.98	0.24	46.03
118	101.25	197.6	1.89	235	2.32	23	0.93	0.98	0.24	48.24
119	87.19	225.0	2.15	241	2.76	23	0.93	0.98	0.25	57.31
120	92.62	213.0	2.03	241	2.60	23	0.93	0.98	0.25	54.08

Table A.5 Flow test data from Santana Tuff fracture sample CC02-2.

Trial	t(s)	Δh (mm)	i [-]	V_{out} (ml)	Q (ml/s)	T (°C)	μ (cp)	ρ (g/ml)	b_e (mm)	Re [-]
1	1080.5	1.60	0.01	193	0.18	23	0.93	0.98	0.60	3.86
2	300.4	1.60	0.01	50	0.17	23	0.93	0.97	0.59	3.54
3	1629.09	1.60	0.01	243	0.15	23	0.93	0.99	0.56	3.23
4	191.28	6.07	0.04	101	0.53	23	0.93	0.98	0.55	11.42
5	300.28	6.07	0.04	157.5	0.52	23	0.93	0.99	0.55	11.38
6	467.21	6.07	0.04	244	0.52	23	0.93	0.99	0.55	11.32
7	186.81	12.78	0.08	199	1.07	23	0.93	0.99	0.54	23.13
8	226.19	12.78	0.08	241	1.07	23.5	0.92	0.99	0.54	23.38
9	151.66	12.78	0.08	162	1.07	23.5	0.92	0.98	0.54	23.35
10	145.78	20.98	0.13	248	1.70	23.5	0.92	0.98	0.53	37.25
11	120.4	20.98	0.13	205	1.70	23.5	0.92	0.98	0.53	37.26
12	143.19	20.98	0.13	243	1.70	23.5	0.92	0.98	0.53	37.15
13	95.41	32.70	0.20	245	2.57	23.5	0.92	0.98	0.53	56.15
14	96.41	32.70	0.20	247	2.56	23.5	0.92	0.98	0.53	56.12
15	90.31	32.70	0.20	233.5	2.59	23.5	0.92	0.99	0.53	56.70
16	58.47	55.70	0.35	243	4.16	23.5	0.92	0.98	0.52	91.05
17	58.47	55.70	0.35	243	4.16	23.5	0.92	0.98	0.52	90.86
18	45.31	55.70	0.35	187.5	4.14	23.5	0.92	0.99	0.52	90.77
19	85.47	37.28	0.23	245.5	2.87	23.5	0.92	0.98	0.53	62.94
20	83.21	37.28	0.23	237.5	2.85	23.5	0.92	0.99	0.52	62.59
21	77.94	42.07	0.26	239	3.07	23	0.93	0.98	0.52	66.35
22	300.03	41.54	0.26	901.5	3.00	23	0.93	0.98	0.52	65.02
23	71.4	47.93	0.30	243	3.40	23	0.93	0.98	0.51	73.60
24	73.45	47.93	0.30	250	3.40	23	0.93	0.98	0.51	73.55
25	113.06	29.29	0.18	247	2.18	23	0.93	0.98	0.52	47.28
26	49.78	70.61	0.44	236	4.74	23	0.93	0.98	0.50	102.61
27	51.28	70.61	0.44	243	4.74	23	0.93	0.98	0.50	102.26
28	207.49	71.36	0.45	981	4.73	23	0.93	0.98	0.50	102.20
29	58.41	61.77	0.39	239	4.09	23	0.93	0.98	0.50	88.31
30	58.43	61.77	0.39	237	4.06	23	0.93	0.98	0.50	87.75
31	57.56	61.77	0.39	233	4.05	23	0.93	0.98	0.50	87.71
32	47.91	83.07	0.52	246	5.13	23	0.93	0.98	0.49	111.06
33	48.18	82.01	0.51	246	5.11	23	0.93	0.98	0.49	110.44
34	38.28	105.44	0.66	247.5	6.47	23	0.93	0.98	0.49	140.04
35	38.56	105.44	0.66	248.5	6.44	23	0.93	0.98	0.49	139.42
36	32	127.80	0.80	246.5	7.70	23	0.93	0.98	0.49	166.63
37	32	127.80	0.80	247	7.72	23	0.93	0.98	0.49	166.90
38	27.87	151.76	0.95	250	8.97	23	0.93	0.98	0.48	194.08
39	27.37	151.76	0.95	246	8.99	23	0.93	0.98	0.48	194.49
40	28	151.76	0.95	250	8.93	23	0.93	0.98	0.48	193.10

Table A.5 continued.

Trial	t(s)	Δh (mm)	i[-]	V_{out} (ml)	Q (ml/s)	T (^{o}C)	μ (cp)	ρ (g/ml)	b_e (mm)	Re [-]
41	24.84	174.34	1.09	248.5	10.00	23	0.93	0.98	0.48	216.34
42	24.75	174.34	1.09	247	9.98	23	0.93	0.99	0.48	216.33
43	22.81	195.43	1.22	251	11.00	23	0.93	0.98	0.47	238.39
44	21.88	195.43	1.22	239	10.92	23	0.93	0.98	0.47	236.26
45	20.54	217.26	1.36	245.5	11.95	23	0.93	0.98	0.47	258.52
46	20.69	217.26	1.36	246.5	11.91	23	0.93	0.98	0.47	257.93
47	18.87	241.01	1.51	242.5	12.85	23.25	0.93	0.98	0.47	280.00
48	70.09	241.01	1.51	898	12.81	23.25	0.93	0.98	0.47	278.71
49	17.63	263.06	1.64	243.5	13.81	23.25	0.93	0.99	0.46	301.20
50	17.88	263.06	1.64	248	13.87	23.25	0.93	0.98	0.46	301.94
51	17.6	263.06	1.64	243	13.81	23.25	0.93	0.98	0.46	300.33
52	16.5	286.49	1.79	243	14.73	23.25	0.93	0.99	0.46	321.03
53	16.79	286.49	1.79	247	14.71	23.25	0.93	0.98	0.46	320.49
54	15.65	309.92	1.94	245.5	15.69	23.25	0.93	0.98	0.46	341.86
55	15.69	309.92	1.94	245	15.62	23.25	0.93	0.98	0.46	340.00
56	60.66	308.32	1.93	918.5	15.14	22	0.95	0.98	0.46	320.24
57	15.59	337.07	2.11	245	15.72	22.25	0.95	0.98	0.45	333.95
58	57.47	337.07	2.11	902.5	15.70	22.25	0.95	0.98	0.45	333.60
59	15.09	360.50	2.25	247	16.37	22.25	0.95	0.98	0.44	348.17
60	56.78	360.50	2.25	931	16.40	22.25	0.95	0.98	0.45	348.27
61	14.18	383.93	2.40	243	17.14	22.25	0.95	0.98	0.44	364.26
62	57.25	383.93	2.40	976	17.05	22.25	0.95	0.98	0.44	362.29
63	13.81	407.58	2.55	246	17.81	22.25	0.95	0.98	0.44	379.03
64	54.16	407.36	2.55	961	17.74	22.25	0.95	0.98	0.44	377.57
65	13.25	430.26	2.69	245	18.49	22.375	0.95	0.98	0.44	394.42
66	52.91	430.26	2.69	975.5	18.44	22.375	0.95	0.98	0.44	393.53
67	68.19	56.45	0.35	249	3.65	22.5	0.94	0.98	0.50	78.05
68	63.12	60.71	0.38	245.5	3.89	22.5	0.94	0.98	0.50	83.21
69	54.69	72.63	0.45	245.5	4.49	22.5	0.94	0.98	0.49	96.04
70	217.07	70.29	0.44	949.5	4.37	22.5	0.94	0.98	0.49	93.51
71	55.45	76.15	0.48	251	4.53	22.5	0.94	0.98	0.49	96.49
72	61.68	66.88	0.42	252	4.09	22.5	0.94	0.98	0.49	87.38
73	77.68	49.52	0.31	243	3.13	22.5	0.94	0.98	0.50	66.83
75	18.65	290.21	1.81	239	12.82	23	0.93	0.99	0.44	278.00
76	18.71	290.21	1.81	240	12.83	23	0.93	0.99	0.44	278.28
77	19.66	266.25	1.66	240.5	12.23	23	0.93	0.99	0.44	265.06
78	19.81	266.25	1.66	242	12.22	23	0.93	0.98	0.44	264.27
79	20.9	243.89	1.52	239	11.44	23	0.93	0.98	0.45	247.44
80	19.97	267.85	1.67	243	12.17	23	0.93	0.99	0.44	264.14

Table A.5 continued.

Trial	t(s)	Δh (mm)	i [-]	V_{out} (ml)	Q (ml/s)	T (^{o}C)	μ (cp)	ρ (g/ml)	b_e (mm)	Re [-]
81	21.78	242.82	1.52	247	11.34	23	0.93	0.98	0.45	245.62
82	23.43	220.99	1.38	248.5	10.61	23	0.93	0.99	0.45	230.02
83	22.91	220.99	1.38	243	10.61	23	0.93	0.98	0.45	229.48
84	24.06	211.94	1.32	246	10.22	23	0.93	0.98	0.45	221.43
85	26.12	189.57	1.18	245	9.38	23	0.93	0.98	0.46	202.87
86	25.03	187.97	1.17	243.5	9.73	23	0.93	0.98	0.46	210.65
87	25.28	198.62	1.24	245	9.69	23	0.93	0.99	0.45	210.05
88	27.88	176.26	1.10	248.5	8.91	23	0.93	0.99	0.46	193.14
89	27.13	176.79	1.10	240.5	8.86	23	0.93	0.98	0.46	191.51
90	29.31	168.27	1.05	247.5	8.44	23	0.93	0.98	0.46	182.82
91	32.66	144.31	0.90	243.5	7.46	23	0.93	0.98	0.46	161.31
92	34.15	144.31	0.90	245.5	7.19	22.75	0.94	0.98	0.46	154.52
93	32.4	153.36	0.96	244	7.53	22.75	0.94	0.98	0.45	162.12
94	32.53	152.83	0.96	246	7.56	22.75	0.94	0.98	0.46	162.48
95	37.09	128.65	0.80	245	6.61	22.75	0.94	0.98	0.46	141.45
96	36.75	128.44	0.80	242	6.59	22.75	0.94	0.98	0.46	141.74
97	39.19	120.35	0.75	242	6.18	23	0.93	0.98	0.46	133.76
98	46.63	97.13	0.61	237	5.08	23	0.93	0.98	0.46	110.06
99	43.94	106.50	0.67	242	5.51	23	0.93	0.98	0.46	119.25
100	45.16	106.50	0.67	248	5.49	23	0.93	0.99	0.46	119.09
101	55	84.14	0.53	247	4.49	23	0.93	0.98	0.47	97.19
102	55	84.14	0.53	247	4.49	23	0.93	0.98	0.47	97.27
103	61.63	73.80	0.46	247.5	4.02	23	0.93	0.98	0.47	86.95
104	71.5	62.84	0.39	245	3.43	23.25	0.93	0.98	0.47	74.21
105	77.12	57.51	0.36	246	3.19	23.25	0.93	0.98	0.47	69.43
106	85.63	50.59	0.32	242	2.83	23.25	0.93	0.99	0.47	61.60
107	82.28	53.78	0.34	245.5	2.98	23.25	0.93	0.98	0.47	64.97
108	96.5	44.20	0.28	243	2.52	23.25	0.93	0.98	0.48	54.84
109	107.78	40.47	0.25	248	2.30	23.25	0.93	0.98	0.48	50.09
110	122.03	34.61	0.22	241	1.97	23.25	0.93	0.98	0.48	42.92
111	180.13	23.43	0.15	245	1.36	23.25	0.93	0.98	0.48	29.62
112	129.19	32.48	0.20	248	1.92	23.25	0.93	0.98	0.48	41.82
113	129	32.48	0.20	247.5	1.92	23.25	0.93	0.98	0.48	41.78
114	168.09	23.96	0.15	247.5	1.47	23.25	0.93	0.98	0.49	32.05
115	363.66	11.72	0.07	243	0.67	23.25	0.93	0.98	0.48	14.55
116	620.31	6.82	0.04	243	0.39	23.25	0.93	0.98	0.48	8.53

Table A.6 Flow test data for fracture sample of Paintbrush Tuff.

Trial	t(s)	Δh (mm)	i [-]	V_{out} (ml)	Q (ml/s)	T (^{o}C)	μ (cp)	ρ (g/ml)	b_e (mm)	Re [-]
1	1052	329.44	0.52	20000	19.01	23.5	0.92	0.98	0.52	132.82
2	1097	317.64	0.50	20000	18.23	23.5	0.92	0.98	0.52	127.63
3	1228	296.60	0.47	20000	16.29	23.5	0.92	0.96	0.51	111.59
4	982	292.88	0.46	16000	16.29	23.5	0.92	0.98	0.51	113.31
5	945	282.49	0.44	15000	15.87	23.5	0.92	0.98	0.51	110.95
6	796	266.62	0.42	12000	15.08	23.5	0.92	0.98	0.51	104.85
7	990	247.51	0.39	14000	14.14	23.5	0.92	0.98	0.52	98.81
8	935	225.35	0.35	12000	12.83	23.5	0.92	0.98	0.52	89.43
9	591	205.23	0.32	7000	11.84	23.5	0.92	0.98	0.52	82.38
10	431	186.80	0.29	4000	9.28	23.5	0.92	0.98	0.49	64.55
11	1565	163.74	0.26	12000	7.67	23.5	0.92	0.98	0.48	53.20
12	1854	129.18	0.20	12000	6.47	23.5	0.92	0.98	0.49	45.07
13	1326	116.09	0.18	8000	6.03	23.5	0.92	0.98	0.50	42.02
14	1373	83.23	0.13	6000	4.37	23.5	0.92	0.98	0.50	30.43
15	1195	61.61	0.10	4000	3.35	23.5	0.92	0.98	0.51	23.36
16	3293	33.28	0.05	6000	1.82	23.5	0.92	0.98	0.51	12.68
17	861	10.65	0.02	463	0.54	23.5	0.92	0.99	0.49	3.78
18	631	7.40	0.01	193	0.31	23.5	0.92	0.99	0.46	2.15
19	1021	5.33	0.01	223.5	0.22	23.5	0.92	0.99	0.46	1.54
20	1702.51	58.04	0.09	4468	2.62	23.5	0.92	0.99	0.47	18.54
21	1604	111.83	0.18	8000	4.99	23.5	0.92	0.98	0.48	34.66
22	1033	153.68	0.24	7000	6.78	23.5	0.92	0.98	0.47	47.27
23	638	143.24	0.23	4000	6.27	23.5	0.92	0.98	0.47	43.83
24	37	158.69	0.25	249	6.73	23.5	0.92	0.99	0.46	47.53
25	1366	203.95	0.32	12000	8.78	23.5	0.92	0.98	0.47	61.52
26	555	247.61	0.39	6000	10.81	23.5	0.92	0.98	0.47	75.71
27	459	291.81	0.46	6000	13.07	23.5	0.92	0.98	0.47	91.55
28	389	335.16	0.53	6000	15.42	23.5	0.92	0.98	0.48	107.56
29	502	377.76	0.59	9000	17.93	23.5	0.92	0.98	0.48	125.36
30	399	414.82	0.65	8000	20.05	23.5	0.92	0.98	0.49	140.19
31	259	473.93	0.75	6000	23.17	23.5	0.92	0.97	0.49	159.66
32	627.57	472.86	0.74	15000	23.90	23.5	0.92	0.98	0.49	166.86
33	597.46	388.19	0.61	12000	20.09	23.5	0.92	0.98	0.50	140.44
34	660.09	349.32	0.55	12000	18.18	23.5	0.92	0.98	0.50	127.31
35	499.46	306.72	0.48	8000	16.02	23.5	0.92	0.98	0.50	111.99

Table A.6 continued.

Trial	t(s)	Δh (mm)	i [-]	V_{out} (ml)	Q (ml/s)	T (^{o}C)	μ (cp)	ρ (g/ml)	b_e (mm)	Re [-]
36	574.67	263.69	0.41	8000	13.92	23.5	0.92	0.98	0.50	97.34
37	514.86	218.86	0.34	6000	11.65	23.5	0.92	0.98	0.50	81.48
38	24.67	177.64	0.28	246	9.97	23.5	0.92	0.99	0.51	70.34
39	425.21	177.64	0.28	4000	9.41	23.5	0.92	0.98	0.50	65.78
40	575.95	129.40	0.20	4000	6.95	23.5	0.92	0.98	0.50	48.56
41	680.57	82.01	0.13	3000	4.41	23.5	0.92	0.98	0.50	30.82
42	1029.43	35.68	0.06	2000	1.94	23.5	0.92	0.98	0.51	13.58
43	1033	35.68	0.06	2000	1.94	23.5	0.92	0.98	0.51	13.54
44	1382.6	105.44	0.17	8000	5.79	23.5	0.92	0.98	0.51	40.46
45	434	177.00	0.28	4000	9.22	23.5	0.92	0.98	0.50	64.44
46	324.2	242.82	0.38	4000	12.34	23.5	0.92	0.98	0.50	86.27
47	379.42	309.60	0.49	6000	15.81	23.5	0.92	0.98	0.50	110.75
48	419.42	372.22	0.59	8000	19.07	23.5	0.92	0.98	0.50	133.58
49	573.95	413.22	0.65	12000	20.91	23.5	0.92	0.98	0.49	146.42
50	629.2	473.93	0.75	15000	23.84	23.5	0.92	0.98	0.49	166.96
51	508.53	473.93	0.75	12000	23.60	23.5	0.92	0.98	0.49	165.26
52	756.75	391.39	0.62	15000	19.82	23.5	0.92	0.98	0.49	138.82
53	261.15	309.06	0.49	4000	15.32	23.5	0.92	0.98	0.49	107.27
54	704.31	219.39	0.34	8000	11.36	23.5	0.92	0.98	0.50	79.36
55	882.1	127.80	0.20	6000	6.80	23.5	0.92	0.98	0.50	47.64
56	530.37	35.68	0.06	1000	1.89	23.5	0.92	0.98	0.50	13.20
57	592.87	127.80	0.20	4000	6.75	23.5	0.92	0.98	0.50	47.17
58	360.04	219.39	0.34	4000	11.11	23.5	0.92	0.98	0.49	77.80
59	262.37	309.92	0.49	4000	15.25	23.5	0.92	0.98	0.49	106.77
60	613.68	396.18	0.62	12000	19.55	23.5	0.92	0.98	0.49	136.94
61	518.23	474.46	0.75	12000	23.16	23.5	0.92	0.98	0.49	162.16
62	521.95	473.93	0.75	12000	22.99	23.5	0.92	0.98	0.49	161.01

APPENDIX B—IDL PROGRAMS

Interactive Data Language (IDL) is a fourth generation programming language that provides excellent data and image processing capabilities using array based processing algorithms similar to MatLab. A good reference for the use of the language is written by Gumley (2002). While many compiled programs populate this study, IDL provides easy access to data with an interactive workbench environment. This allows quick visualization of large amounts of data to aid in maintaining consistent orientations, troubleshooting algorithms, building figures, et cetera. In this Appendix, I describe the logic and the mathematics involved in picking surfaces from CT data, the sampling procedures used, and manipulating large data sets. Note that formatting for ease of reading demands that these scripts are not syntactically correct. IDL uses semicolons to differentiate comments and '$' to break commands across lines. These conventions are removed here.

B.1 Mated Fracture Surface Selection

Distinguishing the boundary between rock and air where two surfaces are in close proximity is the subject of this section. As described by Equation 4.7, I use a missing attenuation method to define the extent of the void space, and thus the elevations of the top and bottom surfaces. The algorithm requires one pixel per line of data points that describe a rock-air-rock sequence have a grayscale value below the midpoint between all air and all rock. A contact point is defined where a line of data points has no such pixel. This section includes the algorithms *GetVertCrackOptimize.pro* and *FixSlope.pro* that handle these issues.

B.1.1 GetVertCrackOptimize.pro

GetVertCrackOptimize.pro handles primary selection of surfaces for fractures. It uses a missing attenuation method (MA) to pick a top and bottom surface from a three dimensional array of grayscale values corresponding to CT output. In this application the top and bottom surfaces are selected as the first occurrence from the minimum grayscale value that crosses the rock/air boundary.

This procedure uses a histogram of each slice to determine the appropriate values for RockGray and AirGray (minGray here). It uses the procedure FixSlope to account for points of contact and bridging precipitates. Stack is a series of 2D slices. Xyz is the 2 element array of spacing information. Top, bot, and aper are keywords set to the appropriate arrays in the calling function or procedure. Arrays are defined (col,row).

```
Pro GetVertCrackOptimize, stack, xyz, top=topSurf, bot=botSurf, aper=aperture,
        rock, air
```

Matrices to hold results

```
 sz = Size(stack)
 topSurf = FltArr(sz[1],sz[3])
 botSurf = topSurf
 midSurf = topSurf
 aperture = topSurf
 if ~arg_present(rock) || ~arg_present(air) then begin
```

Do a histogram calculation to infer rock grayscale

```
   hist=histogram(stack,binsize=1000,min=0)
   plot,hist
   rock=long(0)
   air=rock
   catch, err
   if err ne 0 then print, '***FORMAT: integer, integer***'
   read,prompt='Enter onset of full rock grayscale, maximum of all air (int,int):',
      rock,air
   catch, /cancel
   catch,err
   if err ne 0 then print,'***Format: y,Y or n,N***'
   response=''
   read,prompt='Is the sample masked? (y/n):  ',response
```

```
   response=strmid(string(response),0,1)
if response eq 'y' || response eq 'n' || response eq 'Y' || response eq 'N' then
        catch,/cancel else response[1]=''

case response of
            'Y': mask=1
            'y': mask=1
            else: mask=0
endcase
if mask then begin
```

Create a smooth gradient between the number of values in the bin 1000 below the mask value and 1000 above the mask value.

```
    maskcount=max(hist,maxPt)
rockGray=(total(stack*(stack gt rock)*(stack lt 1000*maxPt)) + total(stack*(stack ge
            1000*(maxPt+1))) + 1000.0*maxPt*(hist[maxPt+1]+(hist[maxPt-1]-
            hist[maxPt+1])/2))/(total(hist[rock/1000:maxPt-1])+
            total(hist[maxPt+1:n_elements(hist)-1]) +hist[maxPt+1]+(hist[maxPt-1]-
            hist[maxPt+1])/2
    endif else begin
```

Use the total grayscale values

```
      rockGray=(total(stack*(stack ge rock))/total(stack ge rock))
     endelse
     minGray=total(stack*(stack le air))/total(stack le air)
   endif else begin
      rockGray=rock & minGray=air
   endelse
   midGray=(rockGray+minGray)/2
  Flag=[0,0]
```

Set on contact point/section to the location of initial contact so surfaces can be set using FixSlope upon encountering next opening.

```
            for j=0,sz[3]-1 do begin
              for i=0,sz[1]-1 do begin
                line = float(Reform(stack[i,*,j]))
                minVal = Min(line, minPt)
                if minval gt midgray then begin
                  if Flag[0] eq 0 then Flag=[1,i]
                  continue
                endif else begin
```

Ascribes the aperture as the ratio of the difference from full rock in the aperture to that if only air were in the aperture voxels. Each surface is picked independently accounting for different grayscale values at the boundaries.

```
           upPt=minPt
           repeat begin
            repeat upPt++ until line[upPt] ge midGray
           endrep until line[upPt+1] gt midGray
           downPt=minPt
           repeat begin
            repeat downPt-- until line[downPt] ge midGray
           endrep until line[downPt-1] gt midGray
           aper=(indgen(upPt-(downPt)+1))+downPt
           halfap=where(aper LT minPt, halfapcount)
           if halfapcount NE 0 then slicepos = 1.0*minPt -
((halfapcount+0.5)*(line[aper[0]-1])-total([line[aper[halfap]],0.5*line[minPt]])) /
                                    (line[aper[0]-1]-minGray)      all air
            else slicepos = 1.0*minPt - 0.5
           botSurf[i,j] = slicePos * xyz[0]
           halfap=where(aper GT minPt, halfapcount)
           if halfapcount NE 0 then slicepos = 1.0*minPt +
             ((halfapcount+0.5)*(line[max(aper)+1])-
              total([line[aper[halfap]],0.5*line[minPt]])) /
              (line[max(aper)+1]-minGray)
           else slicepos = 1.0*minPt + 0.5

           topSurf[i,j] = slicePos * xyz[0]

           midSurf[i,j] = (topSurf[i,j] + botSurf[i,j])/2.0
           aperture[i,j] = topSurf[i,j] - botSurf[i,j]
           if Flag[0] eq 1 then
              FixSlope,Flag=Flag,botsurf=botsurf,topsurf=topsurf,
                midsurf=midsurf,aperture=aperture,i,j
          endelse
        endfor
        if Flag[0] eq 1 then
FixSlope,Flag=Flag,botsurf=botsurf,topsurf=topsurf,midsurf=midsurf,aperture=
aperture,i,j,/ENDOFROW
       endfor
      End
```

B.1.2 FixSlope.pro

FixSlope.pro is called from *GetVertSurfaceOptimize.pro* for handling points of contact. While useful for modeling purposes, the smoothing of surfaces one slice of CT data at a time has an anomalous effect on roughness as described in Section 7.5.6.

This procedure "fills in" values for the surfaces where there is contact via surface to surface or bridging precipitation. Aperture is set to 0 for these areas, and Flag is reset. Three possible scenarios exist in the procedure: Flag is set at the beginning of the slice, in which case the surfaces will be set to the midpoint of the first open space at i; there is an opening before and after the blockage, in which case the surfaces are set to the line connecting the midpoints of the preceding opening at Flag[1] and the calling opening at i; and the end of the slice is reached before a new opening is found, in which case the remaining surfaces are set to the midpoint of the preceding opening at Flag[1].

```
Pro FixSlope, Flag=Flag, botsurf=botsurf, topsurf=topsurf, midsurf=midsurf,
aperture=aperture, i, j, ENDOFROW=ENDOFROW, ZERO=ZERO

 Set the length of contact segment for slope calculation.
   range=i-Flag[1]+1

Contact at beginning of slice, opening at aperture[i,j].
   if Flag[1] eq 0 then begin
     B=midsurf[i,j]
     A=B
   endif else begin
     A=midsurf[Flag[1]-1,j]
     if Keyword_Set(ENDOFROW) then begin
Added Keyword ZERO to ease stitching multiple samples together.
       if Keyword_Set(ZERO) then A=0
       B=A
     endif else B=midsurf[i,j]
   endelse

   slope=(B-A)/range
   h=0
   for k=Flag[1],i-1 do begin
     h++
     topsurf[k,j]=A+h*slope
     midsurf[k,j]=topsurf[k,j]
     botsurf[k,j]=midsurf[k,j]
```

```
    aperture[k,j]=0
  endfor

Reset Flag and ENDOFROW.
  Flag=[0,0]
  ENDOFROW=0
End
```

B.2 Single Fracture Surface Selection

An easier prospect than automatically finding a continuous fracture and defining the top and bottom surfaces is that for defining the boundary of a fracture surface to air. My algorithm *GetBotSurfOptimize.pro* uses a bimodal distribution of grayscale values to determine appropriate values for all air and all rock. Setting the surface involves determining the partial contribution of rock in the pixel that crosses the air/rock boundary.

This procedure interrogates a 3D stack of CT slices to reduce the data set to a surface. It uses the average of the low grayscale values for Air Gray and that of the high grayscale values for Rock Gray. It requires the stack be formatted with air at "top" and that each profile on a slice contains a pixel with a grayscale value greater than (RockGray+AirGray)/2. As a reminder, B3D_ReadTiffs.pro returns data [left to right, bottom to top, front to back].

```
Pro GetBotSurfOptimize, stack, xyz, bot=botSurf
```

Matrices to hold results.

```
  sz = Size(stack)
  botsurf = FltArr(sz[1],sz[3])
```

Do a histogram calculation to infer rock grayscale.

```
  hist=histogram(stack,binsize=1000)
  szhist=size(hist,/dimensions)
  rockGray=total(stack*(stack GT 10000))/total(hist[10:szhist-1])
  minGray=total(stack*(stack LE 10000))/total(hist[0:9])
  midGray=(rockGray+minGray)/2

  for j=0,sz[3]-1 do begin
   for i=0,sz[1]-1 do begin
      line = float(Reform(stack[i,*,j]))
```

temp var to fill bottom air with average rock gray value.

```
      k = 0
      while (line[k] LT midGray) do begin
        line[k]=rockGray
        k+=1
      endwhile
```

```
      minVal = Min(line, minPt)
Start in air.
      k = minPt
Find bottom boundary.
      while (line[k] LT midGray) do k--
If line[k] =midGray, then the boundary lies in the middle of the pixel.
      slicePos = 0.5+1.0*k + (midGray - line[k])/(minGray - line[k])
      botSurf[i,j] = slicePos * xyz[0]
    endfor
  endfor
End
```

B.3 Fitting Unregistered Surfaces

Creating mated surfaces from digital data sets of natural fracture surfaces that are scanned in an unregistered configuration is a considerable challenge. In fact, I have yet to discover a reasonable solution. Too few data points match due to inherent differences between the two surfaces as well as the complications discussed in Section 4.1 defeat face recognition software. I chose to assume a close fit and shift the surfaces relative to each other to minimize mean aperture as a proxy of registration. This process is detailed in the algorithm *FitSurface.pro.* The associated procedures *GetNode.pro, Halve.pro, Expand_2.pro, Expand_3.pro, and WriteTree.pro* are included.

B.3.1 GetNode.pro

Integral to FitSurface, GetNode assigns initial values to new nodes of search path. Structure of node described below.

```
Function GetNode, name, top, bot, bmean, bmax, spacing, level, parent
  node=ptr_new({name:",top:[0,0,0,0],bot:[0,0,0,0],bmean:0.0,bmax:0.0,
minval:1B,mindir:ptr_new(),spacing:0,level:0,parent:ptr_new(),child:ptrarr(9)})

  (*node).name=name & (*node).top=top & (*node).bot=bot &
  (*node).bmean=bmean  (*node).bmax=bmax & (*node).mindir=node &
  (*node).spacing=spacing & (*node).level=level  &  (*node).parent=parent
  return,node

End
```

B.3.2 FitSurface.pro

FitSurface takes two arrays of non overlapping elevations and searches for a best fit by utilizing BestFit.pro and manipulating the data set through moving first the top surface relative to the bottom surface in a square circle radius of 1, then recursing if a minimum separation is found at one of those steps until a "best fit" of the original data is found. The data set is then doubled using bilinear interpolation and the new data set is manipulated in the same manner. If no new minimum is found, the original data set is tripled and the process repeated for a final time. If a minimum separation is found by shifting the doubled data set, an *attempt to refine this shift is made by tripling the original data set and exploring the direction of minimum separation such that 8 calls are made to BestFit at each step, for a minimum of 25 calls assuming the surfaces are best referenced at the start. Developed by Donald T. Slottke 03-09-2009.*

*To call this function, top and bot are equal sized 2D arrays of elevations, xyz is a 2 element array of del x and del y spacing, newtop is the handle for the final best fit top surface, newbot is the handle for the final bottom surface should expansion of the data set result in a minimum separation. Path is a pointer to the root of the linked list of BestFit results returned at completion of the function. It is used in the call for recursion purposes only. The structure of *path is: {name:'',top:intarr(4),bot:intarr(4),bmean:0.0,bmax,0.0,minval:0B, mindir:ptr_new(), spacing:0,level:0,parent:ptr_new(),child:ptrarr[9]}, which defines:*
{name:'name of shift',top:[4 element array of offsets from [0,sz[0],0[sz[1]] of the data set, bot:[same as top],bmean:mean separation of top and bot,bmax:maximum separation of top and bot,minval:flag set to one for each node until a lower mean separation is found subordinate to it,mindir:pointer to the subodinate node with a lower mean separation,spacing:'radius' of search square,level:multiple of original data set,parent:pointer to superior node,child:ptrarr[9] where [0:7] hold the best fit search inputs and results and [8] is a copy of the current node used at expansion of the data set}.

```
Function FitSurface,top,bot,xyz,path,newtop=fit,newbot=retbot

  sz=size(top,/dimensions)
  temp=size(bot,/dimension)
  top=size(top,/type) eq 4 ? top : float(top)
  bot=size(bot,/type) eq 4 ? bot : float(bot)
```

Only 2D arrays are valid for fitting.

```
  if n_elements(sz) ne 2 then begin
    print,'***Invalid input!***'
      print,'result=FitSurface(top{r,c],bot[r,c],xyz[del r,del c])'
    return,-1
  endif
```

Top and Bottom surfaces must have equal dimensions

```
  if sz[0] ne temp[0] || sz[1] ne temp[1] then begin
    print,'***Invalid input!***'
    print,'Surface arrays must be equal sizes'
    return,-1
  endif
```

Set the 24 possible direction names and dimension modifications in structures. Bounds are rotated from row arrays to columns to allow appending.

```
  u2l2={name:'up 2 left 2',bounds:rotate([[2,-1,0,-3],[0,-3,2,-1]],4)}
  ul2={name:'up left 2',bounds:rotate([[2,-1,0,-2],[0,-3,1,-1]],4)}
  l2={name:'left 2',bounds:rotate([[2,-1,0,-1],[0,-3,0,-1]],4)}
  dl2={name:'down left 2',bounds:rotate([[2,-1,1,-1],[0,-3,0,-2]],4)}
  d2l2={name:'down 2 left 2',bounds:rotate([[2,-1,2,-1],[0,-3,0,-3]],4)}
  u2l={name:'up 2 left',bounds:rotate([[1,-1,0,-3],[0,-2,2,-1]],4)}
  ul={name:'up left',bounds:rotate([[1,-1,0,-2],[0,-2,1,-1]],4)}
  l={name:'left',bounds:rotate([[1,-1,0,-1],[0,-2,0,-1]],4)}
  dl={name:'down left',bounds:rotate([[1,-1,1,-1],[0,-2,0,-2]],4)}
  d2l={name:'down 2 left',bounds:rotate([[1,-1,2,-1],[0,-2,0,-3]],4)}
  u2={name:'up 2',bounds:rotate([[0,-1,0,-3],[0,-1,2,-1]],4)}
  u={name:'up',bounds:rotate([[0,-1,0,-2],[0,-1,1,-1]],4)}
  d={name:'down',bounds:rotate([[0,-1,1,-1],[0,-1,0,-2]],4)}
  d2={name:'down 2',bounds:rotate([[0,-1,2,-2],[0,-1,0,-3]],4)}
  u2r={name:'up 2 right',bounds:rotate([[0,-2,0,-3],[1,-1,2,-1]],4)}
  ur={name:'up right',bounds:rotate([[0,-2,0,-2],[1,-1,1,-1]],4)}
  r={name:'right',bounds:rotate([[0,-2,0,-1],[1,-1,0,-1]],4)}
  dr={name:'down right',bounds:rotate([[0,-2,1,-1],[1,-1,0,-2]],4)}
  d2r={name:'down 2 right',bounds:rotate([[0,-2,2,-1],[1,-1,0,-3]],4)}
  u2r2={name:'up 2 right 2',bounds:rotate([[0,-3,0,-3],[2,-1,2,-1]],4)}
  ur2={name:'up right 2',bounds:rotate([[0,-3,0,-2],[2,-1,1,-1]],4)}
  r2={name:'right 2',bounds:rotate([[0,-3,0,-1],[2,-1,0,-1]],4)}
  dr2={name:'down right 2',bounds:rotate([[0,-3,1,-1],[2,-1,0,-2]],4)}
  d2r2={name:'down 2 right 2',bounds:rotate([[0,-3,2,-1],[2,-1,0,-3]],4)}

  ispath=n_params() eq 4?1 : 0
```

Testing fit of nodes to nodes, or at a distance of a 1 "radius" square from a real data node, counterclockwise starting from "down".

```
  if ~ispath || (*path).spacing le 1 then begin
    namestr=[d.name,dr.name,r.name,ur.name,u.name,ul.name,l.name,dl.name]
```

Append 8 directional bounds and reform bounds array to [4,2,8] dimensionality.

```
bounds=reform(rotate([d.bounds,dr.bounds,r.bounds,ur.bounds,u.bounds,ul.bounds,l.bounds,dl.bounds],4),4,2,8)
```

Fit of top to bot surface with no shift done only once with original input surfaces.

```
    if ~ispath then begin
      fit=BestFit(top,bot,xyz)
```

If surfaces overlap, BestFit prints an error message and returns -1, so all that is needed here is a pass through of -1. Size function is used with the type switch set to differentiate between return of normal array of float elevations and overlap condition with integer -1 return value.

```
      if size(fit,/type) eq 2 then return,-1
```

```
   retbot=bot
   path=GetNode('root',[0,0,0,0],[0,0,0,0],mean(fit-bot),
         max(fit-bot),0,1,ptr_new())
   print,(*path).name,(*path).bmean
  endif
```

Shift top surface relative to bot surface in direction specified by namestr[i] then BestFit.

```
  for i=0,n_elements(namestr)-1 do begin
   temptop=top[bounds[0,0,i]:sz[0]+bounds[1,0,i],
           bounds[2,0,i]:sz[1]+bounds[3,0,i]]
   tempbot=bot[bounds[0,1,i]:sz[0]+bounds[1,1,i],
            bounds[2,1,i]:sz[1]+bounds[3,1,i]]
   temp=BestFit(temptop,tempbot,xyz)
```

NaN is supplied as mean and max separation if any overlap exists in the shift to avoid setting mindir to an invalid surface configuration.

```
   newnode=GetNode(namestr[i],bounds[*,0,i],bounds[*,1,i],
           size(temp,/type) eq 2 ? !values.F_NAN : mean(temp-tempbot),
           size(temp,/type) eq 2 ? !values.F_NAN : max(temp-
             tempbot),1,(*path).level,path)
   (*path).child[i]=newnode
```

If a new minimum separation is found, clear the minval flag and set mindir to point at the new node.

```
   if (*newnode).bmean lt (*(*path).mindir).bmean then begin
    (*path).minval=0B
    (*path).mindir=newnode
         fit=temp
         retbot=tempbot
   endif
```

Print progress in form of last search direction, mean separation and current minimum separation direction.

```
   print,(*(*path).child[i]).name,(*(*path).child[i]).bmean
   print,string(9b),(*(*path).mindir).name,string(10b)
  endfor
 endif
```

*For full spacing, if (*path).minval not set then recurse with top and bot shifted appropriately or expand.*

```
 if ~(*path).spacing then begin
  if ~(*path).minval then begin
   tbound=[0,sz[0],0,sz[1]]+(*(*path).mindir).top
   bbound=[0,sz[0],0,sz[1]]+(*(*path).mindir).bot
```

```
      (*(*path).mindir).spacing=0
      (*(*path).mindir).name+='-new root'
      temp=FitSurface(top[tbound[0]:tbound[1],tbound[2]:tbound[3]],
        bot[bbound[0]:bbound[1],bbound[2]:bbound[3]],xyz,(*path).mindir,
        newtop=fit,newbot=retbot)
      return,path
    endif else begin
      Expand_2,top,newarr=top2 & Expand_2,bot,newarr=bot2
      (*path).child[8]=GetNode('Expand 2', [0,0,0,0], [0,0,0,0], (*path).bmean,
                                                   (*path).bmax,1,2,path)
      temp=FitSurface(top2,bot2,xyz/2,(*path).child[8],newtop=fit,newbot=retbot)
      return,path
    endelse
  endif
```

After searching the double data set, original top and bottoom surfaces are pulled out then tripled. Search proceeds for the last time appropriately regarding the current minimum direction.

```
  if (*path).level eq 2 then begin
    Halve,top,newarr=origtop & Halve,bot,newarr=origbot
    Expand_3,origtop,newarr=top3 & Expand_3,origbot,newarr=bot3
    sz=size(top3,/dimensions)
    if (*path).minval then begin
      (*path).child[8]=GetNode('Expand 3', [0,0,0,0], [0,0,0,0],(*path).bmean,
                                                  (*path).bmax,1,3,path)
      temp=FitSurface(top3,bot3,xyz/3,(*path).child[8],newtop=fit,newbot=retbot)
      return,path
    endif else begin
      (*path).child[8]=GetNode('Expand 2 '+(*(*path).mindir).name, [0,0,0,0],
                                                    [0,0,0,0], (*(*path).mindir).bmean,
                                                    (*(*path).mindir).bmax,1,3,(*path).mindir)
```

Set the parameters of the search path for best fit.

```
     switch (*(*path).mindir).name of
        'down': namestr=[l.name,dl.name,d2l.name,d.name,
                                     d2.name,r.name,dr.name,d2r.name]
        'down':
bounds=reform(rotate([l.bounds,dl.bounds,d2l.bounds,d.bounds,d2.bounds,
                           r.bounds,dr.bounds,d2r.bounds],4),4,2,8)
        'down': break
        'down right': namestr=[d.name, d2.name, r.name, dr.name, d2r.name,
                                              r2.name, dr2.name, d2r2.name]
        'down right':
bounds=reform(rotate([d.bounds,d2.bounds,r.bounds,dr.bounds,d2r.bounds,
                           r2.bounds,dr2.bounds,d2r2.bounds],4),4,2,8)
```

```
    'down right': break
    'right': namestr=[u.name,d.name,ur.name,r.name,dr.name,
                     ur2.name,r2.name,dr2.name]
    'right':
bounds=reform(rotate([u.bounds,d.bounds,ur.bounds,r.bounds,dr.bounds,
            ur2.bounds,r2.bounds,dr2.bounds],4),4,2,8)
    'right': break
    'up right': namestr=[u2.name,u.name,u2r.name,ur.name,r.name,
                        u2r2.name,ur2.name,r2.name]
    'up right':
bounds=reform(rotate([u2.bounds,u.bounds,u2r.bounds,ur.bounds,r.bounds,
            u2r2.bounds,ur2.bounds,r2.bounds],4),4,2,8)
    'up right': break
    'up': namestr=[u2l.name,ul.name,l.name,u2.name,u.name,
                  u2r.name,ur.name,r.name]
    'up':
bounds=reform(rotate([u2l.bounds,ul.bounds,l.bounds,u2.bounds,u.bounds,
            u2r.bounds,ur.bounds,r.bounds],4),4,2,8)
    'up': break
    'up left': namestr=[u2l2.name,ul2.name,l2.name,u2l.name,
                       ul.name,l.name,u2.name,u.name]
    'up left':
bounds=reform(rotate([u2l2.bounds,ul2.bounds,l2.bounds,u2l.bounds,ul.bounds,
            l.bounds,u2.bounds,u.bounds],4),4,2,8)
    'up left': break
    'left': namestr=[ul2.name,l2.name,dl2.name,ul.name,
                    l.name,dl.name,u.name,d.name]
    'left':
bounds=reform(rotate([ul2.bounds,l2.bounds,dl2.bounds,ul.bounds,l.bounds,
            dl.bounds,u.bounds,d.bounds],4),4,2,8)
    'left': break
    'down left': namestr=[l2.name,dl2.name,d2l2.name,l.name,
                         dl.name,d2l.name,d.name,d2.name]
    'down left':
bounds=reform(rotate([l2.bounds,dl2.bounds,d2l2.bounds,l.bounds,dl.bounds,
            d2l.bounds,d.bounds,d2.bounds],4),4,2,8)
   endswitch
```

Shift top surface relative to bot surface in direction specified by namestr[i] and BestFit.

```
   for i=0,n_elements(namestr)-1 do begin
    temptop=top3[bounds[0,0,i]:sz[0]+bounds[1,0,i],bounds[2,0,i]:sz[1]+
            bounds[3,0,i]]
    tempbot=bot3[bounds[0,1,i]:sz[0]+bounds[1,1,i],bounds[2,1,i]:sz[1]+
             bounds[3,1,i]]
```

```
    temp=BestFit(temptop,tempbot,xyz/3)
```

NaN is supplied as mean and max separation if any overlap exists in the shift to avoid setting mindir to an invalid surface configuration.

```
    newnode=GetNode(namestr[i],bounds[*,0,i],bounds[*,1,i],
            size(temp,/type) eq 2 ? !values.F_NAN:mean(temp-tempbot),
            size(temp,/type) eq 2 ? !values.F_NAN:
            max(temp-tempbot),2,(*(*path).child[8]).level,(*path).child[8])
    (*(*path).child[8]).child[i]=newnode
    if (*newnode).bmean lt (*(*(*path).child[8]).mindir).bmean then begin
     (*(*path).child[8]).minval=0B
     (*(*path).child[8]).mindir=newnode
     fit=temp
     retbot=tempbot
    endif
    print,(*(*(*path).child[8]).child[i]).name,
         (*(*(*path).child[8]).child[i]).bmean
    print,string(9b),(*(*(*path).child[8]).mindir).name,string(10b)
   endfor
  endelse
 endif
 return,path
End
```

B.3.3 Computing multiples of a data set

In this section are the procedures *Halve.pro, Expand_2.pro,* and *Expand_3.pro*. To halve the data, I simply sample every other point. Expansions are done using a bilinear interpolation.

B.3.3.1 Halve.pro

Halve reduces a 2D array by half. Used in FitSurface

```
Pro Halve,array,newarr=newarr
 sz=size(array,/dimensions)
 if n_elements(sz) ne 2 then begin
  print,'     ***Invalid input***'
  print,' Array must have 2 dimensions.'
  return
 endif
 newsz=sz/2+1
 newarr=fltarr(newsz)
```

```
  for i=0,newsz[0]-1 do $
    for j=0,newsz[1]-1 do $
      newarr[i,j]=array[2*i,2*j]
End
```

B.3.3.2 Expand_2.pro

Expand_2 doubles a 2D data set using bilinear interpolation.

```
Pro Expand_2,array,newarr=newarr
  sz=size(array,/dimensions)
  if n_elements(sz) ne 2 then begin
    print,'      ***Invalid input***'
    print,' Array must have 2 dimensions.'
    return
  endif
  newsz=(sz-1)*2+1
  newarr=fltarr(newsz)
  for i=0,sz[0]-1 do $
    for j=0,sz[1]-2 do begin
      newarr[2*i,2*j]=array[i,j]
      newarr[2*i,2*j+1]=.5*array[i,j]+.5*array[i,j+1]
    endfor
  index=indgen(sz[0])*2
  newarr[index,newsz[1]-1]=array[*,sz[1]-1]
  for j=0,newsz[1]-1 do $
    for i=1,newsz[0]-2,2 do $
      newarr[i,j]=.5*newarr[i-1,j]+.5*newarr[i+1,j]
End
```

B.3.3.3 Expand_3.pro

Expand_3 triples a 2D data set using bilinear interpolation. Every third row is fixed first, then intermediate column values are computed.

```
Pro Expand_3,array,newarr=newarr
  sz=size(array,/dimensions)
  if n_elements(sz) ne 2 then begin
    print,'      ***Invalid input***'
    print,' Array must have 2 dimensions.'
    return
  endif
  newsz=(sz-1)*3+1
  newarr=fltarr(newsz)
  for i=0,sz[0]-1 do $
    for j=0,sz[1]-1 do $
```

```
      newarr[3*i,3*j]=array[i,j]
  for i=0,newsz[0]-1,3 do begin
    for j=0,newsz[1]-4,3 do begin
      newarr[i,j+1]=2*newarr[i,j]/3 + newarr[i,j+3]/3
      newarr[i,j+2]=newarr[i,j]/3 + 2*newarr[i,j+3]/3
    endfor
  endfor
  for j=0,newsz[1]-1 do begin
    for i=0,newsz[0]-4,3 do begin
      newarr[i+1,j]=2*newarr[i,j]/3 + newarr[i+3,j]/3
      newarr[i+2,j]=newarr[i,j]/3 + 2*newarr[i+3,j]/3
    endfor
  endfor
End
```

B.3.4 WriteTree.pro

WriteTree takes the search path returned by FitSurface and writes directions, mean separations and maximum separations to a user specified file. If the file exists, it is overwritten.

```
Pro WriteTree,path,filename=filename

  if ~keyword_set(filename) then begin
    print,'***Usage:  WriteTree,path,filename=filename***'
    return
  endif

  catch,error
  if error ne 0 then begin
    print,'***Error message:  ',!error_state.msg,'***'
    return
  endif

  openw,fp,filename,/get_lun,error=err
  if float(err) then begin
    print,'***Error:',!error_state.msg,'***'
    return
  endif

  printf,fp,''
  printf,fp,string(9b),'Summary of Results for BestFit Search Path'
  printf,fp,''
  ptr=path
  while (*ptr).mindir ne ptr || (*ptr).child[8] do begin
```

```
    printf,fp,format='(a20,a10,f8.5,a10,f8.5)',(*ptr).name,'  mean:',(*ptr).bmean,'
max:',(*ptr).bmax
    for i=0,7 do $
      printf,fp,format='(a20,a10,f8.5,a10,f8.5)',(*(*ptr).child[i]).name,'
mean:',(*(*ptr).child[i]).bmean,'  max:',(*(*ptr).child[i]).bmax
    printf,fp,"
    ptr=(*ptr).child[8]?(*ptr).child[8]:(*ptr).mindir
  endwhile
  flush,fp
  close,fp

End
```

B.4 Digital Best Fit

The best fit configuration is defined as a point of contact in three different quadrants. It is computed by subtracting a wedge oriented at a particular angle from the top data set. This wedge is determined from binomial search in *BestFit.pro* and constructed using *GetWedge.pro* described in this section. *GetQuadrant.pro* and *Vec2Arr.pro* are associated algorithms and also included.

B.4.1 BestFit.pro

BestFit.pro takes two equal element arrays of non-overlapping surface elevations and removes a plane from "top" that produces 3 points of contact corresponding to minimum separation. This is accomplished by first assigning a quadrant to the point of minimum separation between the surfaces, subtracting that value from the top to produce a point of contact, then folding the top surface closed relative to the bottom surface using a binary search for the angle until a second point of contact is achived in another quadrant. A zero line is computed between these two points and the top surface is rotated again along this axis until a third point of contact is achieved. This top surface is returned as a best fit between the two surfaces. For convenience sake, quadrants will be numbered:

I--[0:sz[0]/2-1,0:sz[1]/2-1]
IV--[sz[0]/2:sz[0]-1,0:sz[1]/2-1]
III--[sz[0]/2:sz[0]-1,sz[1]/2:sz[1]-1]
II--[0:sz[0]/2-1,sz[1]/2:sz[1]-1]

```
*******************
*        *        *
*   II   *  III   *
*        *        *
*******************
*        *        *
*   I    *   IV   *
*        *        *
*******************
```

```
Function BestFit,top,bot,xyz

   !except=0
   inf=!values.f_infinity

   sz=size(top,/dimensions)
   temp=size(bot,/dimensions)

   if ~array_equal(sz,temp) then begin
      print, '      ***Bad Aruguments***'
      print, 'Surfaces must have equal dimensions.'
      return,-1
   endif
```

Provide placeholders for procedure calls

```
   x0=0 & x1=0 & x2=0 &y0=0 &y1=0 & y2=0 & qs=0 & maxdist=0

   ptlate=-1
   diff=top-bot
   mindiff=min(diff)
   if mindiff lt 0 then begin
     print, '      ***Invalid Surfaces***'
     print, '        No overlap allowed.'
     return,-1
   endif
   temp1=where(diff eq mindiff,count)
```

If there are 3 or more points of initial minimum separation, no further reduction can be made using this algorithm.

```
   if count gt 2 then return,top-mindiff

   if count eq 1 then begin
      vec2arr,temp1,sz,x=x0,y=y0
      q0=GetQuadrant([x0,y0],sz)
   endif else begin
```

If two minimum points exist, separate the Where result into distinct x and y's.

```
      vec2arr,temp1[0],sz,x=x0,y=y0
      vec2arr,temp1[1],sz,x=x1,y=y1
      q0=GetQuadrant([x0,y0],sz)
      q1=GetQuadrant([x1,y1],sz)
      if q0 ne q1 then begin
         pt0=temp1[0]
         pt1=temp1[1]
         goto, point3
      endif
```

Use the point closest to the center of the sample.

```
   if abs(x1-sz[0]/2) lt abs(x0-sz[0]/2) then begin
      x0=x1 & y0=y1 & q0=q1 & temp1=shift(temp1,1)
   endif
endelse
pt0=temp1[0]
```

temptop holds partial results of minimization

```
temptop=top-mindiff
```

worktop is changed with each iteration looking for the best fit angle.

```
worktop=temptop
col=intarr(sz[1])
col[*]=1
row=indgen(sz[0])*xyz[0]
if q0 eq 3 || q0 eq 4 then row=rotate(row,2)
row-=(row[x0])[0]
high=5
angle=double(1)
low=0
```

Do a binary search for the best fit axial angle.

```
while 1 do begin
   wedge=float(row*sin(angle/!radeg)#col)
   worktop-=wedge
   diff=worktop-bot
   mindiff=min(diff)
   temp2=where(diff eq mindiff,count)
   if mindiff eq 0 then begin
      if count gt 2 then return,worktop
      if count eq 2 then begin
         pt1=(temp2[where(temp2 ne pt0)])[0]
         vec2arr,pt1,sz,x=x1,y=y1
         q1=GetQuadrant([x1,y1],sz)
         if q1 ne q0 then goto, point3   $
         else begin
            x0=x1 & y0=y1 & pt0=pt1
            row=indgen(sz[0])*xyz[0]
            if q0 eq 3 || q0 eq 4 then row=rotate(row,2)
            row-=(row[x0])[0]
            high=5 & angle=1 & low=0 & temptop=worktop
            continue
         endelse
      endif
   endif
```

```
      if mindiff lt 0 then begin
         high=angle
         angle-=(angle-low)/2.
      endif else begin
         low=angle
         angle+=(high-angle)/2
      endelse
      worktop=temptop
   endwhile

Point3:
```

Find bounding points for the zero line and direction of third point

```
   halfarea=(sz[0]-1)*(sz[1]-1)/2
   m=float(y0-y1)/(x0-x1)
   if m eq inf then begin
      b=x0
      goto, Fold
   endif
   b=y0-m*x0
   ylo=b
   yhi=m*sz[0]-1+b
   xlo=-b/m
   xhi=(sz[1]-1-b)/m
```

Account for the zero line sectioning each of the four courners or a slope of 0.

```
   if (ylo le 0 && yhi le sz[1]-1) || (ylo le sz[1]-1 && yhi le 0) ||
     (m eq 0 && b lt sz[1]/2) then upLeft=1
   else if (xlo le 0 && xhi le sz[0]-1) || (xhi ge 0 && xlo ge sz[0]-1) ||
           (m eq 0 && b ge sz[1]/2) then upLeft=0
```

Handle the cases of the zero line bridging the entire sample

```
   else if b gt 0 then begin
      lowarea=m gt 0 ? (.5*(yhi-ylo)+ylo)*(sz[0]-1) :
                       (.5*(ylo-yhi)+yhi)*(sz[0]-1)
      upLeft=(lowarea le halfarea) ? 1 : 0
   endif else begin
      leftarea=m gt 0 ? (.5*(xhi-xlo)+xlo)*(sz[1]-1) :
                        (.5*(xlo-xhi)+xhi)*(sz[1]-1)
      upLeft=(leftarea le halfarea) ? 0 : 1
   endelse

Fold:
   temptop=worktop
   low=0
   angle=double(1)
```

```
  high=5
  wedge=fltarr(sz[0],sz[1])
  while 1 do begin
    GetWedge,wedge,b,angle,xyz,m,sz
    worktop-= upLeft ? float(wedge) : float(-wedge)
    diff=worktop-bot
    mindiff=min(diff)
    temp=where(diff eq mindiff,count)
    if mindiff eq 0 && count ge 3 then begin
      pts=(temp[where((temp ne pt0 and temp ne pt1) eq 1,count)])
      for i=0,count-1 do begin
        vec2arr,pts[i],sz,x=xtemp,y=ytemp
        qtemp=getquadrant([xtemp,ytemp],sz)
        if qtemp ne q0 && qtemp ne q1 then qs=3
        tempdist=m eq inf ? abs(xtemp-x0) : abs(ytemp-(m*xtemp+b))
        if tempdist gt maxdist then begin
          maxdist=tempdist & pt2=pts[i] & x2=xtemp &
          y2=ytemp & q2=qtemp
        endif
      endfor
      if ptlate eq pt0 || ptlate eq pt1 || qs eq 3 then return,worktop
      if q2 eq q0 then begin
        x0=x2 & y0=y2 & pt0=pt2
      endif else begin
        x1=x2 & y1=y2 & pt1=pt2
      endelse
      ptlate=pt2
      goto, Point3
    endif
    if mindiff lt 0 then begin
      high=angle
      angle-=(angle-low)/2.
    endif else begin
      low=angle
      angle+=(high-angle)/2
    endelse
    worktop=temptop
  endwhile

End
```

B.4.2 GetWedge.pro

Populate the given wedge of xyz spacing with elevations calculated from the given angle about a zero line defined by the slope m and y intercept b. sz used only when the zero line is vertical

```
Pro GetWedge,wedge,b,angle,xyz,m,sz
  if m eq !values.f_infinity then begin
    row=indgen(sz[0])*xyz[0]*sin(angle/!radeg)
    col=replicate(1,sz[1])
    wedge=row#col
    if b lt sz[0]/2 then wedge-=row[b]
      else wedge=rotate(wedge-row[sz[0]-b-1],2)
    return
  endif
  tgamma=tan(angle/!radeg)
  calpha=cos(atan(m))
  for i=0,sz[0]-1 do begin
    h=b+i*m
    for j=0,sz[1]-1 do begin
        a=abs(j-h)*calpha*sqrt(xyz[0]*xyz[1])
        wedge[i,j]=(j gt h) ? a*tgamma : -a*tgamma
    endfor
  endfor
End
```

B.4.3 GetQuadrant.pro

GetQuadrant.pro uses a 2 element array for a point and calculates the appropriate quadrant from the size of the data set.

```
Function GetQuadrant, loc, sz
   Vert=sz[0]/2
    Horiz=sz[1]/2
    if loc[0] lt Vert then
        if loc[1] lt Horiz then
            return,1
        else return,2
        else if loc[1] lt Horiz then
            return,4
        else return,3
End
```

B.4.4 Vec2Arr.pro

Vec2Arr.pro separates a one dimensional subscript into x and y coordinates.

```
Pro Vec2Arr,point,sz,x=x,y=y
   x=(point mod sz[0])[0]
   y=(point/sz[0])[0]
End
```

B.6 Surface Roughness

The overarching algorithm for calculating surface roughness from a 2D data set is *WriteSurfRough.pro* which interrogates the data set starting with samples of 4 x 4 data points and increasing by powers of 2 until the sample size is greater than one dimension of the data set. To accomplish this task, I also wrote *Z_Trend_Remove.pro, SampleGridVar.pro,* and *SurfaceRoughness.pro.* These algorithms are presented in this section.

B.6.1 WriteSurfRough.pro

WriteSurfRough.pro takes a 2D surface array, an output directory, a base filename, a 2 element spacing array, with parameters available for 1 or 2 intermediate points that define where multiple data sets have been spliced.

```
Pro WriteSurfRough,array,dir,basefile,xyz,midpoint=midpoint,
         thirdpoint=thirdpoint
```

Set maximum sample size to a power of two not greater than the minimum dimension of the data set.

```
maxsz=2^floor(alog(min(size(array,/dimensions)))/alog(2))
i=4
while i LE maxsz do begin
  temp=SampleGridVar(array,i)
  sz=size(temp,/dimensions)
  dim=size(sz,/dimensions)
```

there are multiple samples in both dimensions

```
  if dim EQ 4 then begin
      roughness=fltarr(sz[2],sz[3])
      maxcol=sz[3]-1
      maxrow=sz[2]-1
  endif else begin
      maxcol=0
```

the data set is exactly maxsz wide

```
      if dim EQ 3 then begin
          roughness=fltarr(sz[2])
          maxrow=sz[2]-1
```

only one roughness value sent to WriteVector

```
      endif else begin
```

This necessitates adding a unity row that must be deleted from the text file.

```
      roughness=[[0],[1.0]]
      maxrow=0
    endelse
  endelse
  if Keyword_Set(MIDPOINT) then begin
   midcol=''
   for j=0,maxrow do for l=0,i-2 do
    if temp[l,0,j,0] eq array[midpoint-1,0] &&
      temp[l+1,0,j,0] eq array[midpoint,0] then
     if n_elements(midcol) eq 1 then midcol=[l,j]
     else midcol=rotate([rotate(midcol,4),rotate([l,j],4)],4)
   mids=n_elements(midcol)/2
   for k=0,maxcol do begin
    if mids then begin
     for j=0,midcol[1,0]-1 do
roughness[j,k]=SurfaceRoughness(temp[*,*,j,k],xyz)
     for l=0,mids-1 do begin
      if midcol[0,l] eq 0 then
roughness[j,k]=SurfaceRoughness(temp[1:i-1,*,j,k],xyz)
      else if midcol[0,l] eq i-1 then
roughness[j,k]=SurfaceRoughness(temp[0:i-2,*,j,k],xyz)
      else roughness[j,k]=float(midcol[0,l]+1)/i*
SurfaceRoughness(temp[0:midcol[0,l],*,j,k],xyz) +
float(i-midcol[0,l]-1)/i*SurfaceRoughness(temp[midcol[0,l]+
1:i-1,*,j,k],xyz)
      j++
     endfor
     while j le maxrow do begin
      roughness[j,k]=SurfaceRoughness(temp[*,*,j,k],xyz)
      j++
     endwhile
    endif else for j=0,maxrow do for k=0,maxcol do
roughness[j,k]=SurfaceRoughness(temp[*,*,j,k],xyz)
   endfor
  endif else for j=0,maxrow do for k=0,maxcol do
roughness[j,k]=SurfaceRoughness(temp[*,*,j,k],xyz)
  WriteVector,roughness,[1,1],dir,basefile+strtrim(string(i),1)+'.txt'
  i*=2
endwhile

End
```

B.6.2 SampleGridVar.pro

Use at least 2x2 grid for expected results. Returns 3D array for dimension equal to one dimension of input grid. Returns 2D array for dimension equal to the square input grid. Breaks grid into variable dimension subsets and returns them in an 4D array in the form [dim,dim,wide,long]. Grid formatted [col,row]
Verified by Donald T. Slottke 5 March, 2007.

```
Function SampleGridVar, grid,dimension

   ON_ERROR,2
   catch, err
   if err NE 0 then begin
     print, "
     print, '    Bad Argument',err,!ERROR_STATE.MSG
     print, "
   catch, /CANCEL
   endif

   sz=size(grid,/dimensions)
   if sz[0] lt dimension || sz[1] lt dimension then begin
     print, "
     print, '   Sample too small for this procedure!!', sz
     print, "
     return, grid
   endif

   w=0
   l=0
```

Number of samples wide.

```
   i=ceil(sz[0]/float(dimension))
```

Number of samples long.

```
   j=ceil(sz[1]/float(dimension))
```

Spacing between samples.

```
   w_offset=(i gt 1) ? (sz[0]-dimension)/(i-1) : 0
   l_offset=(j gt 1) ? (sz[1]-dimension)/(j-1) : 0
   array=fltarr(dimension,dimension,i,j)
```

For odd cases--dimension x dimension, dimension x ?, ? x dimension

```
   if i eq 1 then begin
      if j eq 1 then goto, LastPiece
      for l=0,j-2 do
         array[*,*,0,l]=extrac(grid,0,l*l_offset,dimension,dimension)
      goto, LastPiece
   endif
   if j eq 1 then begin
      for w=0,i-2 do
```

```
        array[*,*,w,0]=extrac(grid,w*w_offset,0,dimension,dimension)
      goto, LastPiece
   endif

   for w=0,i-2 do begin
      array[*,*,w,j-1]=extrac(grid,w*w_offset,sz[1]-
dimension,dimension,dimension)
      for l=0,j-2 do begin
        if w EQ 0 then
          array[*,*,i-1,l]=extrac(grid,sz[0]-
dimension,l*l_offset,dimension,dimension)

array[*,*,w,l]=extrac(grid,w*w_offset,l*l_offset,dimension,dimension)
      endfor
   endfor
```

Extract final subset of grid.

```
LastPiece:
   array[*,*,w,l]=extrac(grid,sz[0]-dimension,sz[1]-
dimension,dimension,dimension)
   return, array
End
```

B.6.3 SurfaceRoughness.pro

Returns ratio of area of sampled surface to planar reference surface S0. Assuming the surface defined by each set of three 'nearest neighbor' grid points is planar, the sum of the surface areas of the thus defined triangles will approximate the actual surface area. 'surf' is the input surface in [col,row] format. 'xyz' is a 2 element array of the sample spacing.

```
Function SurfaceRoughness, surf, xyz

   sz=size(surf, /dimensions)
   S0=(sz[0]-1)*xyz[0]*(sz[1]-1)*xyz[1]
   S=0
   for i=0,sz[0]-2 do begin
     for j=0, sz[1]-2 do begin
```

Define points of two triangles comprising surface between sampling points.

```
       a=sqrt(xyz[1]^2+(surf[i,j]-surf[i,j+1])^2)
       b=sqrt(xyz[0]^2+(surf[i,j+1]-surf[i+1,j+1])^2)
       c=sqrt(sqrt(xyz[0]^2+xyz[1]^2)^2+(surf[i,j]-surf[i+1,j+1])^2)
       d=sqrt(xyz[1]^2+(surf[i+1,j]-surf[i+1,j+1])^2)
       e=sqrt(xyz[0]^2+(surf[i,j]-surf[i+1,j])^2)
```

Define semiperimeters of triangles.

```
       s1=(a+b+c)/2
       s2=(c+d+e)/2
```

```
Add incremental areas using heron's formula.
              S=S+sqrt(s1*(s1-a)*(s1-b)*(s1-c))+sqrt(s2*(s2-c)*(s2-d)*(s2-e))
            endfor
          endfor
        return, S/S0

        End
```

B.6.4 Z_Trend_Remove.pro

While not strictly necessary as a planar trend through an entire data set does not impart roughness, all data sets in this study have the planar trend removed for comparison purposes as spacing and sampling issues present otherwise. This procedure was written using the equation provided for planar trend removal given in Stout et al. (2000).

```
Procedure to remove planar trend from 3D data set.
Planar trend in the form of z'=a+bx=cy is subtracted
from the input array z with the result placed in the
array assigned the tag newarr by the calling program.
Written and verified by Donald Slottke 26Feb09.
        Pro Z_Trend_Remove,z,xyz,newarr=z__,newxyz=newxyz

         if n_params() ne 2 || n_elements(xyz) ne 2 ||
          ~arg_present(z__) then begin

          print,'***Usage:  Z_Trend_Remove,2D input array,
           2 element spacing array [delta x, delta y],
           newarr=result***'

          print,'  Note:  result need not be a defined variable
           prior to running routine.'

          return
         endif

         sz=size(z,/dimensions)
         if size(sz,/dimensions) ne 2 then begin
          print,'***Invalid input for 3D trend removal.***'
          z__=-1
          return
         endif
```

```
x=findgen(sz[0])*xyz[0]
xbar=mean(x)
y=findgen(sz[1])*xyz[1]
ybar=mean(y)
zbar=mean(z)
```

Fill arrays of size sz with appropriate variables...

```
a=0 & b=0 & c=0
x_=replicate(1,sz[1])
y_=replicate(1,sz[0])
x__=x # rotate(x_,4)
y__=y_ # rotate(y,4)
```

thereby allowing use of array math instead of nested loops.
LSE Plane equations from Stout et al. (2000).

```
 b=total(x__*(z-zbar))/total(x__*(x__-xbar))
 c=total(y__*(z-zbar))/total(y__*(y__-ybar))
 a=zbar-b*xbar-c*ybar
 print,'a=',a,'  b=',b,'  c=',c

 if arg_present(newxyz) then
newxyz=[sqrt((b*xyz[0]*sz[0])^2+(sz[0]*xyz[0])^2)/sz[0],sqrt((c*xyz[1]*
sz[1])^2+(sz[1]*xyz[1])^2)/sz[1]]

 z__=z-(a+b*x__+c*y__)

End
```

B.7 Masking Voids

The variability of the void space in the data from the Paintbrush Tuff sample inspired the creation of an interactive procedure that delivers a data set suitable as input to *GetVertCrackOptimize.pro.* To accomplish this, the algorithm searches for anomalous areas, offers several choices for how they should be handled, and displays the results for verification before moving on to the next 2D slice. In this section, I present *AutoMaskStack.pro* and the associated procedure *Write_Anomaly.pro.*

B.7.1 AutoMaskStack.pro

AutoMaskStack requires limited user input to process 3D CT imagery that yields a data set from which fracture surfaces can be picked. Stack is the grossly masked data set. Mask is a pseudo-random slice of all rock that is used to assign visually appealing areal masks to stack. MidGray defines a limit whereby a pixel contains both rock and air. If the next pixel also exceeds this value a boundary is assigned. The threshold parameter defines the expected maximum distance between the minimum values of adjacent pixels within a fracture. Adjacent minimum values that exceed this distance are subjected to possible masking by this procedure.

```
Pro AutoMaskStack,stack,mask,midGray,threshold,first=first
  sz=size(stack,/dimensions)
```

Array maps are generated for the minimum value of each line in all slices of the CT volume, the locations within the line of these minimum values, and the distance between a given minimum value and the minimum of the immediately preceding adjacent line. The differences that exceed the threshold are then indexed for possible masking.

```
minpos=intarr(sz[0],sz[2]) & minval=minpos & diff=minval
for i=0,sz[0]-1 do begin
  for j=0, sz[2]-1 do begin
    minval[i,j]=min(stack[i,*,j],temp)
    minpos[i,j]=temp[0]
  endfor
endfor
diff[1:sz[0]-1,*]=minpos[1:sz[0]-1,*]-minpos[0:sz[0]-2,*]
highindex=where(diff gt threshold)
highs=where(minval[highindex] lt midGray)
maxs=rotate([[highindex[highs] mod
        sz[0]],[minpos[highindex[highs]]],[highindex[highs]/sz[0]]],4)
lowindex=where(diff lt -threshold)
lows=where(minval[lowindex] lt midGray)
mins=rotate([[lowindex[lows] mod
        sz[0]],[minpos[lowindex[lows]]],[lowindex[lows]/sz[0]]],4)
```

i is the first slice that contains anomalous minimum values.
imax is the last slice containing anomalies.

```
i=Keyword_Set(first) ? first :
                        min([rotate(mins[2,*],4),rotate(maxs[2,*],4)])
imax=max([rotate(mins[2,*],4),rotate(maxs[2,*],4)])
```

For each anomaly with a slice one of six possible actions are user selected. First, the position may simply be skipped if the minimum value lies within the fracture or if the area in question is too complicated for this algorithm, e.g. where the copper sampling ports create linear artifacts through both matrix and air indiscriminately. Second, if the anomalous area *lies completely outside the fracture, the area bounded by pixels with grayscale values greater than midGray is masked from the jump out of the fracture to the next jump. Third, if the anomalous area grades into the fracture a mask is first placed in the jump line to account for possible continuity of the fracture with a minimum grayscale somewhat greater than the minimum of the line. Then the following lines are evaluated and masked until only one section of the line has values below midGray. Fourth, for minimums that trend out of the fracture, the jump is encountered back into the fracture. In this case the preceding procedure is followed starting with line immediately preceding the jump and worked back until only one segment of values below midGray exists on a line. One of two possibilities remains: either the jump is into the fracture due to an area of contact; or the area is too complicated to be handled by this procedure, in which case it is logged for manual attention.*

```
  anomalies=[-1,-1,-1]
  while i le imax do begin
    indexmin=where(mins[2,*] eq i,countmin)
    indexmax=where(maxs[2,*] eq i,countmax)
    if countmin ne 0 and countmax  ne 0 then begin
      array=[[mins[0:1,indexmin]],[maxs[0:1,indexmax]]]
      array=array[*,sort(array[0,*])]
    endif else begin
      if countmin gt 0 then array=mins[0:1,indexmin]
      if countmax gt 0 then array=maxs[0:1,indexmax] else begin i++ &
continue & endelse
    endelse
```

one of four? options: in fracture, out of fracture, grade into fracture, grade out of fracture

```
    indexmax=countmin+countmax-1
    index=0
```

For reference, the current slice is written to the default directory.

```
;   write_tiff,'current slice.tif',rotate(stack[*,*,i],7),/short
    tempslice=stack[*,*,i]
    print,'******SLICE '+string(i,format='(I04)')+'******'
    repeat begin
      cur=array[*,index]
      index++
      next=array[*,index gt indexmax ? indexmax : index]
      err=0
      catch,err
      if err then message,/reset
      response=0
      print,'6 options: 1-in fracture,check for back fill;'
      print,'          2-out of fracture completely, fill anomaly to next;'
      print,'          3-grade into fracture, fill until line has only one minimum
                segment;'
```

```
print,'          4-grade out of fracture, fill backwards until line has one
          minimum segment;'
print,'          5-in fracture, no back fill;'
print,'          6-skip anomaly and log.'
window,/free,ysize=sz[1],xsize=51
tv,tempslice[cur[0]-25:cur[0]+25,*]*float(255)/
               max(tempslice[cur[0]-25:cur[0]+25,*])
wait,2.5
wdelete
print,'Given the current and next jumps as:'
print,cur,next
read,prompt='What should I do?',response
if response ne 1 && response ne 2 && response ne 3 && response ne
     4 && response ne 5 && response ne 6 then response[1]=''
if (response eq 2 || response eq 3) && cur[0] eq next[0] then begin
  temp=0
  read,prompt='Input next line in fracture:',temp
  next[0]=temp
endif
if response eq 3 then begin
  temp=0
  read,prompt='Input location of fracture at next line:',temp
  next[1]=temp
endif
switch response of
  1:  if cur[0] ne 0 then begin
        k=cur[0]-1
        temp=where(stack[k,*,i] le midGray, linecount)
        mintemp=min(stack[k,*,i],mintemppos)
        while mintemp le midGray &&       $
                (abs(mintemppos-minpos[cur[0],i]) gt threshold) &&
                (stack[k,cur[1],i] gt midGray || linecount ne
                   temp[n_elements(temp)-1]-temp[0]+1) do begin
          top=mintemppos & bot=top
          repeat top++ until stack[k,top,i] gt midgray
          repeat bot-- until stack[k,bot,i] gt midgray
          stack[k,bot:top,i]=mask[k,bot:top]
          k--
          temp=where(stack[k,*,i] le midGray, linecount)
          mintemp=min(stack[k,*,i],mintemppos)
        endwhile
      endif
  1:  break
  2:  k=cur[0]
```

```
    2:  repeat begin
          top=(where(stack[k,*,i] eq min(stack[k,*,i])))[0] & bot=top
          repeat top++ until stack[k,top,i] gt midgray
          repeat bot-- until stack[k,bot,i] gt midgray
          stack[k,bot:top,i]=mask[k,bot:top]
          k++
        endrep until k ge next[0] || minval[k,i] gt midGray ||
                (abs(minpos[k,i]-minpos[k-1,i]) gt threshold)
    2:
    2:  break
    3:  k=cur[0]
    3:  linehigh=max([cur[1],next[1]],min=linelow)+5
    3:  linelow-=5
    3:  Repeat begin
          top=(where(stack[k,*,i] eq min(stack[k,*,i])))[0] & bot=top
          repeat top++ until stack[k,top,i] gt midGray
          repeat bot-- until stack[k,bot,i] gt midGray
          stack[k,bot:top,i]=mask[k,bot:top]
          temp=where(stack[++k,linelow:linehigh,i] lt midGray, linecount)
        endrep until linecount eq temp[n_elements(temp)-1]-temp[0]+1
    3:  break
    4:  k=cur[0]
    4:  linehigh=max([cur[1],minpos[--k,i]],min=linelow)+5
    4:  linelow-=5
    4:  Repeat begin
          top=(where(stack[k,*,i] eq min(stack[k,*,i])))[0] & bot=top
          repeat top++ until stack[k,top,i] gt midGray
          repeat bot-- until stack[k,bot,i] gt midGray
          stack[k,bot:top,i]=mask[k,bot:top]
          temp=where(stack[--k,linelow:linehigh,i] lt midGray, linecount)
        endrep until linecount eq temp[n_elements(temp)-1]-temp[0]+1
    5:  break
    6:  if max(anomalies) lt 0 then anomalies=[cur,i]
        else anomalies=rotate([rotate(anomalies,4),rotate([cur,i],4)],4)
  endswitch
endrep until index gt indexmax
window,xsize=820,ysize=180,xpos=100,ypos=400
tv,stack[*,*,i]*float(255)/max(stack[*,*,i])
wait,2.5
wdelete
read,prompt='Is this OK?  (1 for yes)  ',response
if response ne 1 then begin
  stack[*,*,i]=tempslice
  continue
endif
```

```
    mask=shift(mask,50*randomu(seed))
    i++
  endwhile
```

If there exist areas in the stack that cannot be handled properly by this algorithm, they are written to file anomalies.txt in the default directory.

```
  if max(anomalies) ne -1 then write_anomaly,anomalies,[-1,-1,-1]
End
```

B.7.2 Write_Anomaly.pro

```
Pro Write_Anomaly,mins,maxs,filename=filename
  if keyword_set(filename) then begin
    openw,fp,filename,/get_lun,error=err
    if err ne 0 then return
  endif else begin
    openw,fp,'anomalies.txt',/get_lun,error=err
    if err ne 0 then begin
      print,'***Check Default Path***'
      return
    endif
  endelse

  i=min([rotate(mins[2,*],4),rotate(maxs[2,*],4)])
  imax=max([rotate(mins[2,*],4),rotate(maxs[2,*],4)])

  while i le imax do begin
    indexmin=where(mins[2,*] eq i,countmin)
    indexmax=where(maxs[2,*] eq i,countmax)
    i++
    if countmin ne 0 and countmax  ne 0 then begin
      array=[[mins[*,indexmin]],[maxs[*,indexmax]]]
      array=array[*,sort(array[0,*])]
    endif else begin
      if countmin gt 0 then array=mins[*,indexmin]
      if countmax gt 0 then array=maxs[*,indexmax] else continue
    endelse
    printf,fp,array
    printf,fp
  endwhile

  close,fp
  free_lun,fp

End
```

References

Atkinson, J.T.N., 1982, Corrosion and its control: an introduction to the subject: Houston, National Association of Corrosion Engineers, 202p.

Barton, N., 1973, Review of a new shear-strength criterion for rock joints: Engineering Geology, v. 7, p. 287-332.

Barton, N., Bandis, S., and Bakhtar, K., 1985, Strength, deformation and conductivity coupling of rock joints: International Journal of Rock Mechanics and Mining Sciences & Geomechanics Abstracts, v. 22, p. 121-140.

Barton, N., and Choubey, V., 1977, The shear strength of rock joints in theory and practice Rock Mechanics, v. 10, p. 1-54.

Bendat, J.S., and Piersol, A.G., 1986, Random Data--Analysis and Measurement Procedures: New York, Wiley & Sons, 566 p.

Blum, A.E., and Stillings, L.L., 1995, Feldspar dissolution kinetics: in (White, A.F., and Brantley, S.L., eds.) Chemical Weathering Rates of Silicate Minerals, Volume 31: Reviews in Mineralogy: Washington, D. C., Mineralogical Society of America, p. 291-352.

Blum, P., Mackay, R., Riley, M.S., and Knight, J.L., 2005, Performance assessment of a nuclear repository, upscaling coupled hydro-mechanical properties for far-field transport analysis: International Journal of Rock Mechanics and Mining Science, v. 42, p. 781-792.

Brown, S.R., 1987, Fluid flow through rock joints: the effect of surface roughness: J. Geophys. Res., v. 92, p. 1337-1347.

Brown, S.R., and Scholz, C.H., 1985, Broad bandwidth study of the topography of natural rock surfaces: J. Geophys. Res., v. 90, p. 12,575-12,582.

Budd, A.R., Wyborn, L. A. I., Bastrakova, I.V. 2001, The metallogenic potential of Australian Proterozoic granites: Summary Volume Geoscience Australia, 152p.

Byers Jr., F.M., Carr, W.J., Orkild, P.P., Quinlivan, W. D., Sargent, K. A. 1976, Volcanic suites and related cauldrons of Timber Mountain-Oasis Valley Caldera Complex, southern Nevada: USGS professional paper, p. 83.

Cardenas, M.B., Slottke, D.T., Ketcham, R.A., and Sharp, J.M., Jr., 2007, Navier-Stokes flow and transport simulations using real fractures shows heavy tailing due to eddies: Geophysical Research Letters, v. 34, L14404.

Chae, B.G., Ichikawa, Y., Jeong, G.C., Seo, Y.S., and Kim, B.C., 2004, Roughness measurement of rock discontinuities using a confocal laser scanning microscope and the Fourier spectral analysis: Engineering Geology, v. 72, p. 181-199.

Clauser, C., and Villinger, H., 1990, Analysis of conductive and convective heat-transfer in a sedimentary basin, demonstrated for the Rheingraben: Geophysical Journal International, v. 100, p. 393-414.

Conrad, P., 1982, Uranium in the Oatman Creek Granite of Central Texas and its Economic Potential: unpub. MS thesis, Texas A&M University, 120 p.

Davis, S.N., and Turk, L.J., 1964, Optimum depths of wells in crystalline rocks: Ground Water, v. 2, p. 6-11.

Drexel, J.F., and Preiss, W.V., 1995, The geology of South Australia, Volume 2 - The Phanerozoic: Volume Bull. 54, Geological Survey of South Australia, 347p.

Exadaktylos, G., and Stavropoulou, M., 1997, A specific upscaling theory of rock mass parameters exhibiting spatial variability: analytical relations and computational scheme: International Journal of Rock Mechanics and Mining Science, v. 45, p. 1102-1125.

Garner, T.T., 2007, Characterization of Transport Properties in Granitic Rock Fractures with Skins: unpub. Ph.D. dissertation, The University of Texas at Austin, 191p.

Ge, S., 1997, A governing equation for fluid flow in rough fractures: Water Resour. Res., v. 33, p. 53-61.

Griffiths, A.A., 1920, The phenomena of rupture and flow in solids: Philisophical Trans. of the Royal Soc. of London, Series A, v. 221, p. 163-198.

Gumley, L.E., 2002, Practical IDL programming: creating effective data analysis and visualization applications: San Francisco, Morgan Kaufmann, 508 p.

Halihan, T., Wicks, C.M., and Engeln, J.F., 1998, Physical response of a karst drainage basin to flood pulses: example of the Devil's Icebox cave system (Missouri, USA): Journal of Hydrology, v. 204, p. 24-36.

Harbaugh, A.W., Banta, E.R., Hill, M.C., and McDonald, M.G., 2000, MODFLOW-2000, The U.S. Geological Survey modular ground-water model—user guide to modularization concepts and the ground-water flow process: USGS, 121 p.

Irwin, G.R., 1958, Fracture I, in Flugge, S., ed., Handbuch der Physik VI: New York, Springer-Verlag.

Johns, R.A., Steude, J.S., Castanier, L.M., and Roberts, P.V., 1993, Nondestructive Measurements of Fracture Aperture in Crystalline Rock Cores Using X-Ray Computed-Tomography: Journal of Geophysical Research-Solid Earth, v. 98, p. 1889-1900.

Keller, A., 1998, High resolution, non-destructive measurement and characterization of fracture apertures: International Journal of Rock Mechanics and Mining Sciences, v. 35, p. 1037-1050.

Ketcham, R.A., and Carlson, W.D., 2001, Acquisition, optimization and interpretation of x-ray computed tomographic imagery: applications to the geosciences: Computers & Geosciences, v. 27, p381-400.

Ketcham, R.A., Slottke, D.T., and Sharp, J.M. Jr., submitted, Three-dimensional measurement of fractures in heterogeneous materials using high-resolution X-ray CT: submitted for publication to Geosphere.

Kiraly, B., 1976, Kinematic examination of constraint systems realized on pairs of surfaces in contact: Acta Technica Academiae Scientiarum Hungaricae, v. 82, p. 401-415.

Krasny, J., and Sharp, J.M., Jr., (eds.), 2007a, Groundwater in Fractured Rocks: Selected Papers 9, International Association of Hydrogeologists, Taylor & Francis, London, 646p.

Krasny, J., and Sharp, J.M., Jr., 2007b, Hydrogeology of fractured rocks from particular fractures to regional approaches: State-of-the-art and future challenges: in Krasny, J., and Sharp, J.M., Jr., eds.), Selected Papers, International Association of Hydrogeologists: Groundwater in Fractured Rocks, Taylor & Francis, London, p. 1-32.

Kung, S.H., 1992, Another elementary proof of Heron's Formula: Mathematics Magazine, v. 65, p. 337-338.

Lamb, H., 1932, Hydrodynamics: NY, Dover, 738p.

Landes, K.K., Amoruso, J.J., Charlesworth, L.J., Heaney, F., and Lesperance, P.J., 1960, Petroleum resources in basement rocks: American Assoc. Petroleum Geologists Bull., v. 44, p. 1682-1691.

LeGrand, H.E., 1949, Sheet structure, a major factor in the occurrence of ground water in granites of Georgia: Economic Geology, v. 44, p. 110-118.

Lomize, B.M., 1951, Fil’tratsiia v treshchinovatykh porodakh (Fractured Rock Permeability), (in Russian), Gosenergoizdat, Moscow, 127p.

Louis, C., 1969, Study of groundwater flow in jointed rock and its influence on the stability of rock masses, Rock Mechanics Research Report No. 10, Imperial College, London, 90p.

Manly, B.F.J., 2009, Statistics for Environmental Science and Management: Boca Raton, FL, Chapman & Hall, 312p.

Masihi, M., and King, P.R., 2008, Connectivity prediction in fractured reservoirs with variable fracture size: analysis and validation: SPE Journal, v. 13, p. 88-98.

Méheust, Y., and Schmittbuhl, J., 2000, Flow enhancement of a rough fracture: Geophysical Research Letters, v. 22, p. 2989-2992.

Nicholl, M.J., Rajaram, H., Glass, R.I., and Detwiler, R., 1999, Saturated flow in a single fracture: evaluation of the Reynolds Equation in measured aperture fields: Water Resour. Res., v. 35, p. 3361-3373.

Olson, J.E., Laubach, S.E., and Lander, R.H., 2009, Natural fracture characterization in tight gas sandstones: integrating mechanics and diagenesis: AAPG Bulletin, v. 93, p. 1535-1549.

Patek, J., Hruby, J., Klomfar, J., SouCkova, M., and Harvey, A.H., 2009, Reference correlations for thermophysical properties of liquid water at 0.1 MPa: Journal of Physical and Chemical Reference Data, v. 38, p. 21-29.

Perez, N., 2004, Fracture Mechanics: Boston, Kluwer Academic Publishers, 284 p.

Petford, N., and McCaffrey, K.J.W., 2003, Hydrocarbons in Crystalline Rocks: Geological Society Special Publication No. 214, The Geological Society, London, 242p.

Philip, Z.G., Jennings, J.W., Jr., Olson, J.E., Laubach, S.E., and Holder, J., 2005, Modeling coupled fracture-matrix fluid flow in geomechanically simulated fracture networks: SPE Reservoir Evaluation & Engineering, v. 8, p. 300-309.

Pinskii, F.S., Orlov, S.B., and Vorontsova, N.I., 1969, Method for raising the precision in reading scales of measuring instruments: Measurement Techniques, v. 12, p. 12-15.

Rasband, W., 2006, ImageJ http://rsb.info.nih.gov/ij, National Institutes of Health, USA.

Sharp, J.M., Jr., Slottke, D.T., Ketcham, R.A., and Cardenas, M.B., 2008, Evaluating the effects of fracture roughness on fluid flow and solute transport: is scaling possible?: Geo. Soc. America, Abs. with Programs (North-Central Section Mtg.), v. 40, p. 13.

Slottke, D.T., Ketcham, R.A., Cardenas, M.B., and Sharp, J.M., Jr., 2008, Roughness effects on flow and transport: implications for predictive modeling, Presented at 33d Intl. Geol. Congress: Oslo, Norway.

Smyth-Boulton, R.C., 1995, Porosity and permeability controls in the Santana Ash-Flow Tuff, Trans-Pecos Texas: unpub. MA thesis, The University of Texas at Austin, 100p.

Stout, K.J., Blunt, L., Mainsah, E., Luo, N., Dong, W.P., Mathia, T., Sullivan, P.J., and Zahouani, H., 2000, Development of methods for the characterisation of roughness in three dimensions: Penton Press, 358p.

Thomas, T.R., 1998, Trends in surface roughness: International Journal of Machine Tools and Manufacture, v. 38, p. 405-411.

Thompson, C., 2005, Investigation of surface roughness of natural rock fractures using high-resolution x-ray computed tomography and laboratory flow test measurements: unpub. MS thesis, The University of Texas at Austin, 262p.

Trainer, F.W., 1988, Plutonic and metamorphic rocks: in (Back, W., Rosenshein, J.S., and Seaber, P.R., eds.) Hydrogeology, Volume 0-2, Geol. Soc. America, Boulder, Colorado, p. 367-381

Tsang, Y.W., and Tsang, C.F., 1987, Channel Model of Flow through Fractured Media: Water Resources Research, v. 23, p. 467-479.

Westergaard, H.M., 1939, Bearing pressures and cracks: J. Applied Mech., v. G1, p. A49-A53.

Witherspoon, P.A., Wang, J.S.Y., Iwai, K., and Gale, J.E., 1980, Validity of cubic law for fluid flow in a deformable rock fracture: Water Resour. Res., v. 16, p. 1016-1024.

Zimmerman, R.W., and Bodvarsson, G.S., 1996, Hydraulic conductivity of rock fractures: Transport in Porous Media, v. 23, p. 1-30.

VITA

Donald Timothy Slottke graduated from Sam Houston High School, Arlington,Texas. He served in the United States Navy as a Data Systems Technician during Operation Desert Storm. After a number of years working in various areas of construction, he returned to college at Wichita State University in 1998. He received a Bachelor of Science degree for Computer Science in 2003. In the process of pursuing this degree, he acquired a taste for geology, continuing at Wichita State University for a second Bachelor of Science awarded in 2004. In August of 2004, he enter the Graduate School at The University of Texas at Austin.

Permanent Address: 1516 Lawrence St., Houston, Texas 77008

This manuscript was typed by the author.